INVESTIGATION OF OPTICAL MEMORY TECHNIQUES FINAL REPORT

October 1970

Prepared under Contract No. NAS 12-2200 by

ELECTRO-OPTICS CENTER
RADIATION INCORPORATED
Ann Arbor, Michigan 48106

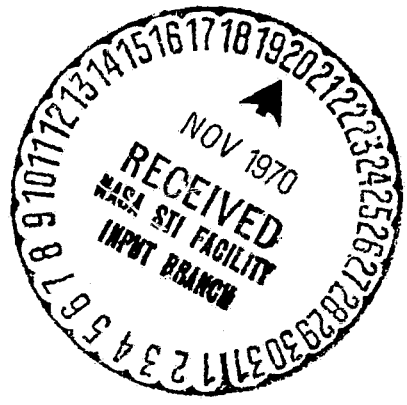

Marshall Space Flight Center

INVESTIGATION OF
OPTICAL MEMORY TECHNIQUES
FINAL REPORT

October 1970

Prepared under Contract No. NAS 12-2200 by

ELECTRO-OPTICS CENTER
RADIATION INCORPORATED
Ann Arbor, Michigan 48106

Marshall Space Flight Center

NATIONAL AERONAUTICS AND SPACE ADMINISTRATION

TABLE OF CONTENTS

TABLE OF CONTENTS (continued)

TABLE OF CONTENTS (continued)

TABLE OF CONTENTS (continued)

TABLE OF CONTENTS (continued)

LIST OF ILLUSTRATIONS

LIST OF ILLUSTRATIONS (continued)

LIST OF ILLUSTRATIONS (continued)

LIST OF ILLUSTRATIONS (continued)

LIST OF ILLUSTRATIONS (continued)

LIST OF TABLES

FOREWORD

This report was prepared by the Electro-Optics Center of Radiation Incorporated, under National Aeronautics and Space Administration Contract NAS 12-2200, and covers the work performed between 1 July 1969 and 30 June 1970. The contract was monitored by G. A. Bailey, Jr. of the NASA Marshall Space Flight Center, Huntsville, Alabama; in the initial stages the contract was monitored by N. G. Patt of the NASA Electronics Research Center, Cambridge, Massachusetts.

The principal investigator on this project was A. A. Friesem. Other contributors were M. O. Greer, G. E. Hoffmann, A. Kozma, W-H. Lee, E. N. Leith, H. N. Roberts, A. Vander Lugt, and R. G. Zech. This report was prepared under the direction of A. Vander Lugt, Research Manager.

The contractor's report number is EOC-8101-12-F.

SUMMARY

The objective of this investigation is to study the feasibility of using holographic techniques for a 10^{10} to 10^{12} bit read/write optical memory, having no moving parts. Although the main objective is to evaluate various holographic techniques and to determine a suitable storage material, other components of the system such as the block data composer, the photodetector array, the deflection and scanning devices, and the coherent light source are also investigated.

Techniques for holographically recording and retrieving information with adequate signal-to-noise ratio and error rates are investigated. It is shown that 10^5 bits of information can be retrieved from each 1 mm^2 hologram with a 20 dB signal-to-noise ratio and a 10^{-7} error rate. By recording 20 holograms at each storage location in a 10^6 array, it is possible to achieve a total capacity of 10^{11} bits. Each storage location can be addressed with an acousto-optic deflector and each hologram can be independently retrieved by using the properties of a thick recording material and a multiwavelength laser. Following a general classification of holograms and their properties, we discuss the noise characteristics, the exposure sensitivities, the diffraction efficiencies, and the angular orientation and the wavelength discrimination of different types of recording materials. The results are used to develop a model of thin absorptive recording materials used to simulate nonlinear and film-grain noise effects. We use a computer to assist in analyzing the imaging properties of holograms.

Several approaches and designs for implementing the major elements of the system are suggested. After selecting promising approaches, two specific holographic memory designs of 10^9 and 10^{10} bits total capacities and 10^8 bits/second data rates are described. The major differences between the two designs are that one uses a thin storage material such as photoplastic or MnBi whereas the other uses a thick phase storage material

and a multiwavelength laser. Both designs use input block data composers and photodetector arrays containing 256 x 256 elements and acousto-optic beam deflectors.

Finally, a list of requirements for a suitable storage material and recommendations for future development of the holographic memory system are given.

SECTION I

INTRODUCTION

Some techniques for implementing medium to large scale bulk data storage systems are highly developed (for example, discs, cores, etc.) and are in commercial use, while others (ferrites, integrated circuits, thin films, etc.) are under development and hold promise for future use in applications where small, high-speed memories are necessary. However, if the storage requirement exceeds 10^9 bits, the limited storage density and the interconnection problem of these memories become limiting factors so that memories using optical techniques then seem feasible.

Optical storage techniques using photosensitive materials can store vast quantities of data. For example, it is conceivable that 10^8 bits of information could be stored on a square centimeter of high-resolution film. However, conventional optical techniques, at these storage densities, require (among other things) great precision in the readout optics, a storage material with virtually no surface defects, and great care in handling the stored data since dust and scratches could easily obscure large portions of the recorded data. Conventional optical storage techniques have therefore found little use in practice.

Holographic storage techniques, on the other hand, can have the high storage capabilities associated with conventional optical techniques without the problems stated above. A brief review of the advantages of the use of holography in optical memories is useful as a background for the more detailed discussions given in the text. The advantages to be gained from the use of holography are:

1. Each hologram if properly illuminated, projects a real image which can be detected without the use of imaging optics; each hologram stores both an array of data and the optical imaging properties of a lens.

2. Several holograms can be stored so that the real image from each hologram will appear in a fixed position; if each hologram is read out separately, only one detector array is required and the need for a mechanical transport of the stored data is eliminated.

3. Image resolution can be as good as the diffraction limit imposed by the size of the hologram; aberrations, which occur with imaging lenses, can be avoided in hologram imaging.

4. Since information stored in the hologram is not localized but can be unfocused, diffused and distributed, the hologram record is relatively insensitive to dust or scratches. Because a distribution of the stored data implies redundancy, a greater tolerance in registering the hologram with respect to the readout beam is obtained.

5. The data can be stored at high density on the hologram while the readout can have a relatively low density; this alleviates the readin/readout registration problems.

6. The hologram may be formed on nonabsorbing materials (phase materials); Schlieren imaging techniques are not needed to reconstruct an image from the stored data.

7. Holograms may be superimposed unambiguously by forming them in a thick medium, thus increasing the capacity of the memory.

These are compelling reasons to study the use of holographic techniques for an optical memory. However, to gain the full use of these advantages requires careful system design, since various holographic parameters must be carefully controlled to realize optimum performance.

The purpose of this study is to investigate the feasibility of using holographic techniques for a read/write optical memory, having no moving parts, which is capable of storing 10^{10} to 10^{12} bits. The main objective is

to evaluate various holographic techniques and to determine what storage material is most suitable. Other components of the system such as the block data composer, output detector array, beam deflection and scanning devices, coherent light sources, etc. are also investigated.

In Section II we discuss some fundamental holographic techniques and we summarize our investigations of using Fresnel and Fourier transform holograms for recording digital arrays. We then discuss our experiments on the incoherent addition of signals and our experimental results which demonstrate the effectiveness of storing a multiplicity of images in a thick material by means of wavelength variation.

In Section III we begin with a review of the fundamental properties of recording materials as they relate to holographic storage systems, and we consider the problems of measuring and evaluating these properties for a general class of recording materials. The characteristics of a representative set of holographic recording materials are described along with the procedures for testing these materials and our experimental results. We then discuss the noise characteristics of recording materials and determine their effect on the behavior of the holographic storage system. The analytical results of the noise characteristics study are extended to show the effects of the signal-to-noise ratio on the achievable error rates and on the capacity of a holographic memory system.

In Section IV we describe the results of a computer assisted study in which we simulate the response of recording materials to a given signal and analyze the effects of the intermodulation noise and the grain noise of the recording material on the reconstructed image of this signal. We also show how the computer can be used to analyze the imaging properties of holograms.

In Section V we consider each of the major components of the system and suggest promising approaches for implementing them in practice. Included are considerations of the following elements: (1) a read/write storage material, (2) the block data composer, (3) the laser, (4) the beam deflection

device, (5) the readout detector array, and (6) the associated drive, synchronization and data conditioning electronics.

A set of general relations to guide the overall system design are developed in Section VI; these relations are then used to synthesize two holographic memories. For each memory we select a hologram format and specific techniques for the major components; we then design the memory and establish performance criteria for the storage material and each major component.

Finally, in Section VII we give recommendations for further work for the development of holographic mass memory systems. These recommendations are based partly on the results of our studies during the past year and partly on our assessment of state-of-the-art technology in several key areas. We also include a list of requirements to aid in developing a suitable storage material for the final system.

SECTION II

BASIC HOLOGRAPHIC TECHNIQUES

2.1 INTRODUCTION

In this section we discuss some fundamental holographic storage techniques. Since the basic theory of holography is well known (Refs. 1 and 2), we will deal with the techniques that are pertinent to the design of a holographic memory system.

The use of holograms as high density information storage and retrieval devices is one of the more promising applications of holography. A holographic storage and retrieval system stores a large block of data in each hologram location. Since the access to each hologram is achieved by deflecting a laser beam, the holographic system can achieve both a large total capacity and fast access times.

Information is introduced into a holographic memory in an array format; each element in the array corresponds to a binary unit of the input data block. A light wave, modulated by such an array, interferes with a coherent reference beam and the resulting pattern is recorded to form a hologram which stores the block of data. This hologram, generally of small physical dimensions, is part of a larger array of separate holograms forming the memory; each hologram in the array stores a unique block of data. The information is retrieved by addressing any particular hologram with a light beam which is a replica of the reference beam used in the recording. A reconstructed image is then projected onto a photodetector array which, in turn, produces an electrical output signal. Thus, by illuminating any one hologram storage location, we transfer a large block of information from the storage location to the readout matrix.

Both the recording and the readout of the information must be accomplished so that there is little or no interaction between the reconstructed images from any two holograms. This condition is satisfied if

each hologram in the array is recorded with sufficient separation so that each can be independently addressed, or by using thick storage materials so that each hologram can be independently addressed by angular or wavelength variations in the readout beam.

Several holographic memory systems have been reported in recent years (Ref. 3). The essential features of all holographic storage systems can be described with the aid of Fig. 2-1. Figure 2-1(a) shows the recording arrangement in which the reference beam, derived from a laser, passes through an x-y deflector to address a specific hologram storage location. Simultaneously, another beam, derived from the same laser passes through a data composer which spatially modulates the beam in accordance with a binary bit pattern derived from an electrical input signal. Since the data composer receives the input in time sequence and since the block of data must fill the array before the hologram is recorded, the data composer must act as a buffer store as well as a spatial modulator. The modulated signal beam produces a diffraction pattern at the storage location which interferes with the reference beam; this interference pattern is recorded to form a hologram. The remaining holograms in the array are formed in the same fashion.

The readout arrangement is shown in Fig. 2-1(b). Random access to any hologram in the array is achieved by passing the readout beam through a suitable x-y deflector. Each addressed hologram generates a light pattern, which is the real image of the input data array at the readout plane where a photodetector array is located. The photodetector array connects the light pattern to an electrical signal. Since information about each bit in the input array is spread over the entire area of the hologram, the sensitivity of the system to dust particles and scratches is significantly reduced. Dust and scratches will reduce the signal-to-noise ratio for each bit slightly but none of the information will be completely destroyed. Furthermore, the exact positioning and the uniformity of illumination of the hologram are not very critical.

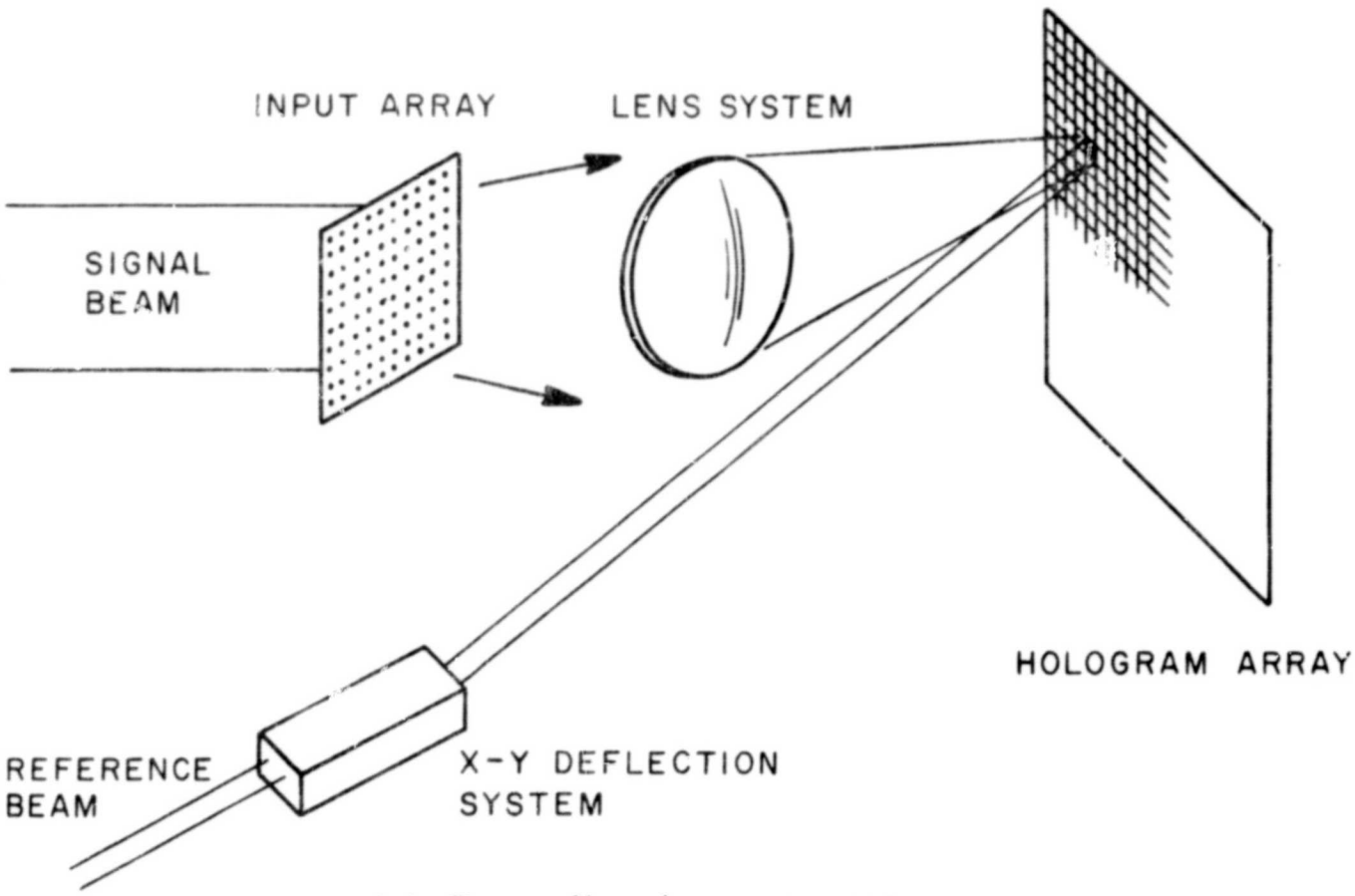

(a) Recording Arrangement

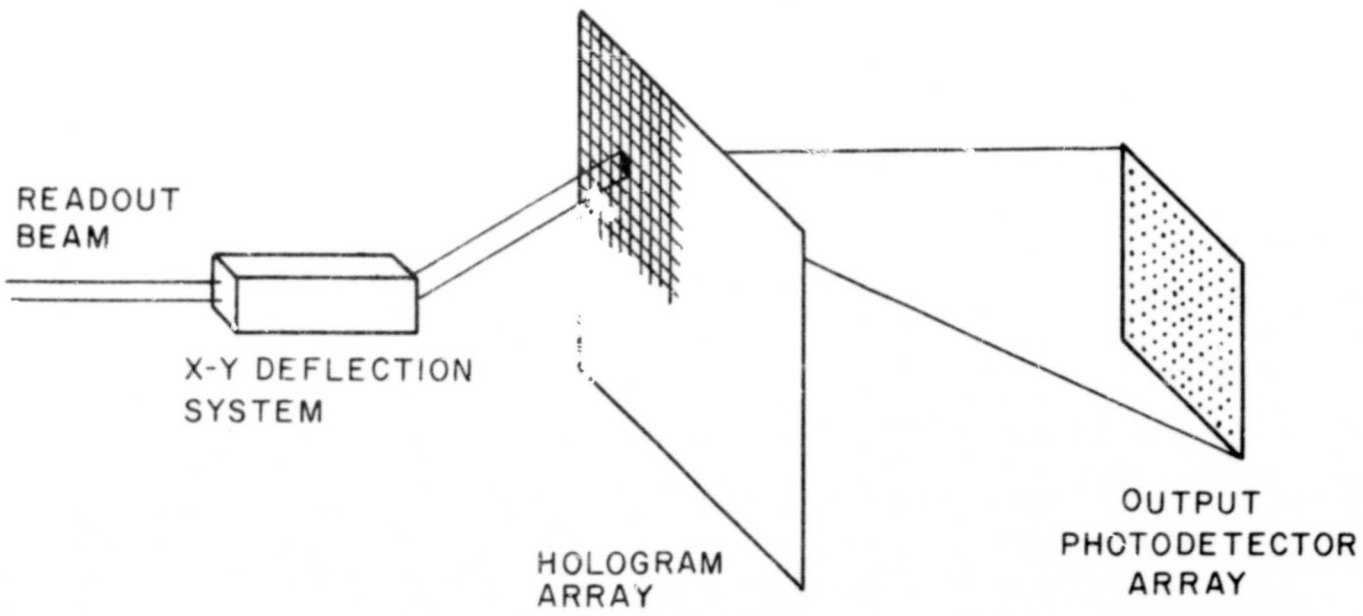

(b) Readout Arrangement

FIGURE 2-1. HOLOGRAPHIC MEMORY

Of the many types of holograms that can be used for storing and retrieving information, the Fresnel and Fourier transform holograms appear to be the most suitable for the holographic memory. The Fresnel type of hologram is the most straightforward; an illustrative arrangement for recording and retrieving information of Fresnel holograms is shown in Fig. 2-2. In the recording step, the signal is usually diffusely illuminated so that the information about each input bit is distributed over a large area in the hologram plane. The reference beam is directed onto the hologram plane at some angle relative to the signal beam. It is possible to form holograms with a reference beam having an arbitrary wavefront; the only requirement is that it be coherent with the signal beam. For the readout step we use a reconstructing beam that is conjugate to the reference beam. An undistorted aerial image of the input signal appears behind the hologram as shown in Fig. 2-2. Although the Fresnel transform hologram is the simplest type, it is wasteful of laser power because only a small fraction of the total light at the hologram plane is used to form each hologram in the array. For this reason the Fourier transform hologram (or near Fourier transform hologram) approach is potentially very promising. Both the information packing density and the light intensity is highest in the Fourier transform plane so that the space-bandwidth product of the recording medium can be used most efficiently and the laser power is conserved. An illustrative arrangement for recording and retrieving information of Fourier transform holograms is shown in Fig. 2-3. The input signal is placed in the front focal plane of a lens so that each signal point produces a parallel beam of light incident on a small region of the photographic plate. The reference beam is a plane wave which impinges on the hologram plane at some angle relative to the signal beam. If the hologram is located at the back focal plane of the lens, it will record an exact Fourier transform hologram of the data. As we will show in subsequent sections, it is sometimes advantageous to locate the hologram at some plane which is displaced from the Fourier transform plane of the lens. We refer to holograms formed with such an arrangement as near

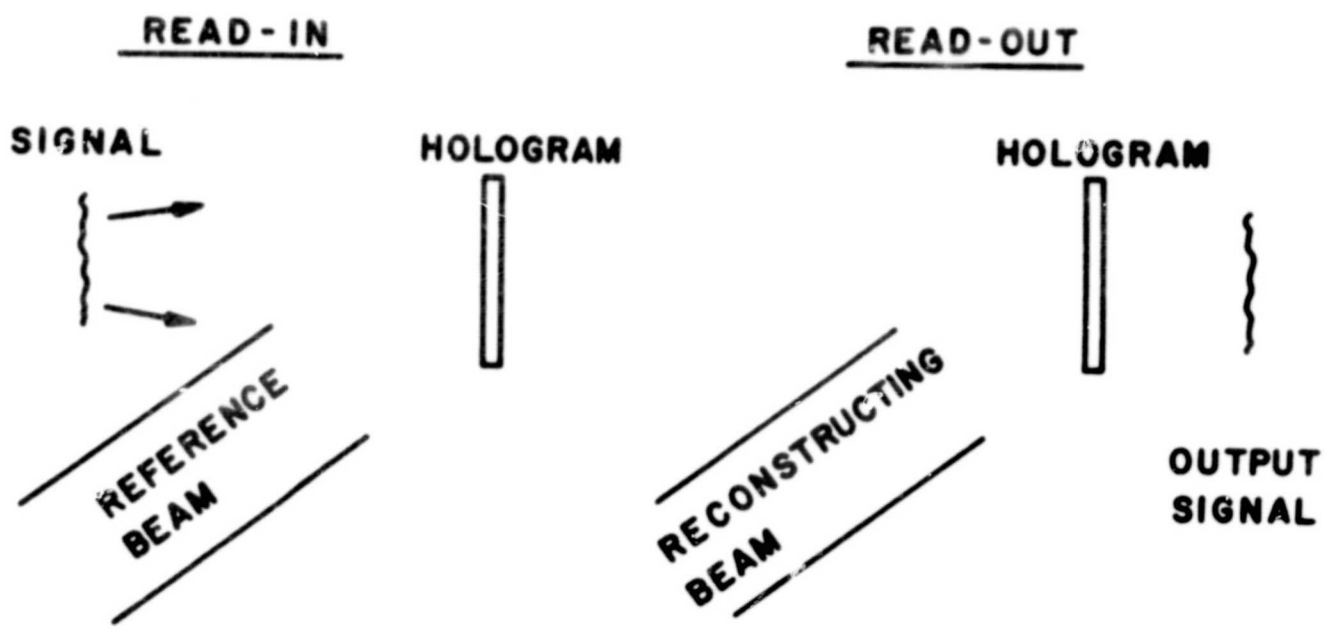

FIGURE 2-2. READIN AND READOUT ARRANGEMENTS FOR FRESNEL HOLOGRAMS

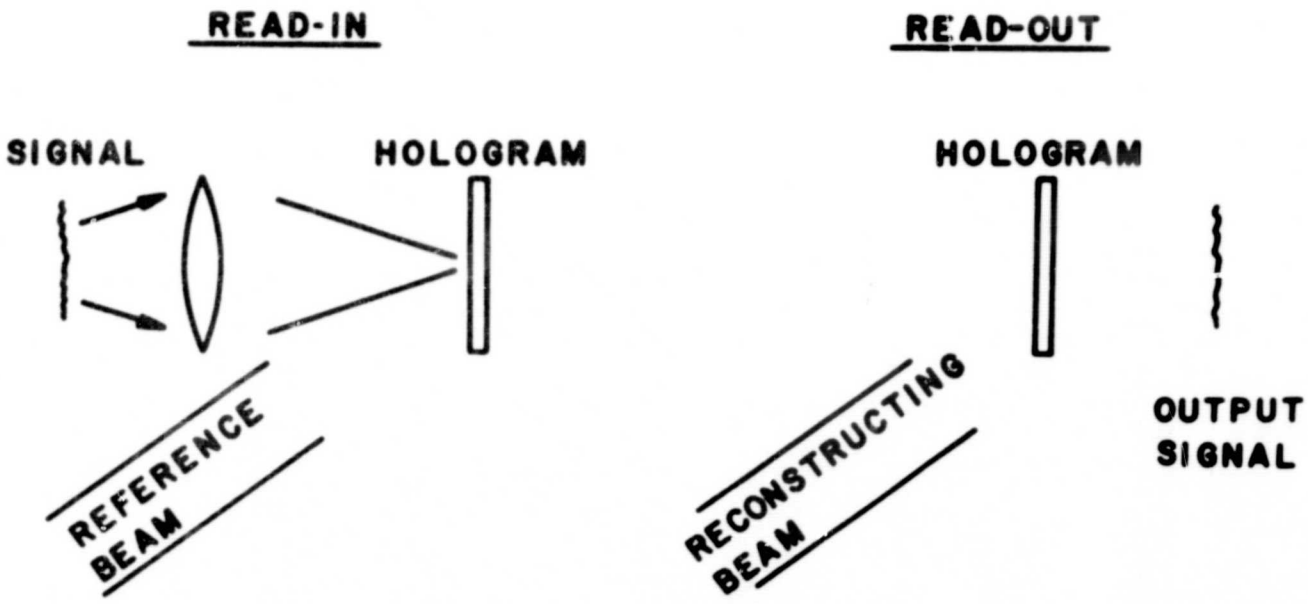

FIGURE 2-3. READIN AND READOUT ARRANGEMENTS FOR FOURIER TRANSFORM HOLOGRAMS

Fourier transform holograms.

In the remainder of this section we present our investigations on recording holograms of digital arrays and discuss the merits of Fresnel and Fourier transform in more detail. We then discuss our experiments of incoherent additions of signals and our experimental results which demonstrate that thick storage materials can be used to independently retrieve only one image from a composite hologram having a multiplicity of stored images.

2.2 HOLOGRAPHIC STORAGE OF DIGITAL DATA

We performed a series of experiments in which we holographically recorded digital information from an N by N array. Both Fresnel holograms and Fourier transform holograms were investigated; the recording materials were conventional photographic emulsions and dichromated gelatin. The emphasis in these experiments is on determining the best format for the digital data and the effects of the nonlinearities of the recording medium on the reconstructed image.

2.2.1 Input Data Format

The basic data mask is a 100 x 100 element array in which the presence or absence of an element corresponds to a value of 1 or 0 at a given position. The digital information contained in the data mask is generated by a computer and plotted on a Calcomp plotter. The data mask is then photographically reduced to a 25 mm x 25 mm transparency. The pattern of dots can be described by a function f(x, y):

$$f(x,y) = \sum_n \sum_m a(n,m)\, \delta(x-nd-\Delta_n \cdot y-md-\Delta_m) \ * \ g(x,y) \qquad (2\text{-}1)$$

$$\text{where } g(x,y) = \begin{cases} 1 \text{ for } |x| \le \frac{1}{2}b;\ |y| \le \frac{1}{2}b;\ b < d, \\ 0 \text{ otherwise} \end{cases}$$

* denotes convolution, $a(n,m) = 0$ or 1, and $\delta(x,y)$ is a two-dimensional Dirac delta function. The constant d is the basic period of the elements of the array and b is a parameter that is related to the duty cycle of the dots. The constants Δ_n and Δ_m are shifting parameters which move a dot from its nominal position by a small amount. We used three types of data masks:

Type 1 $\quad b = \frac{1}{2}d;\ \Delta_n = \Delta_m = 0.$

Type 2 $\quad b = \frac{1}{3}d;\ \Delta_n = \Delta_m = 0$

Type 3 $\quad b = \frac{1}{3}d;$ The values of Δ_n and Δ_m are chosen at random from the set $\{-\frac{1}{7}d,\ 0,\ +\frac{1}{7}d\}$.

The array in Type 3 is called a jittered array because each element in the array is positioned randomly about its nominal position in the array. The other two arrays are called regular arrays and have duty cycles of $\frac{1}{2}$ and $\frac{1}{3}$. Small sections of the three different types of data format are shown in Fig. 2-4, where Fig. 2-4(a), 2-4(b), and 2-4(c) shows the 1/2 duty cycle, the 1/3 duty cycle and the jittered array, respectively; Fig. 2-4(d) shows the complete array of 10^4 points.

2.2.2 Fourier Transform Holograms

The major difficulty encountered in recording a Fourier transform hologram is the large difference between the intensity of the signal at zero spatial frequency and at higher spatial frequencies. This, together with the finite dynamic range of the recording material, prevents a linear recording of the Fourier transform hologram with high efficiency. In studying the effects of film nonlinearities on Fourier transform holograms, we find that the image reconstructed from a "jittered array" is often better than the regular array. We cannot detect any false images due to film nonlinearities when we use a properly chosen small area of the hologram that is very close to zero spatial frequency (d. c.) of the Fourier transform.

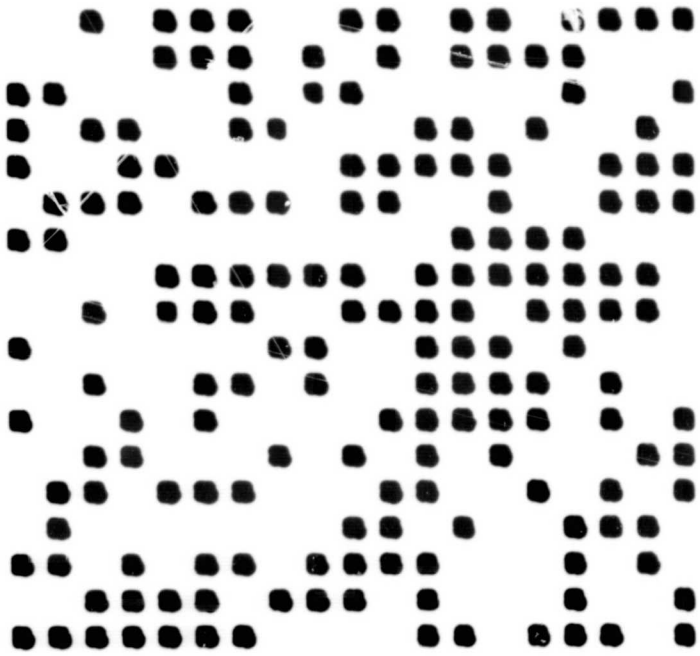

(a)

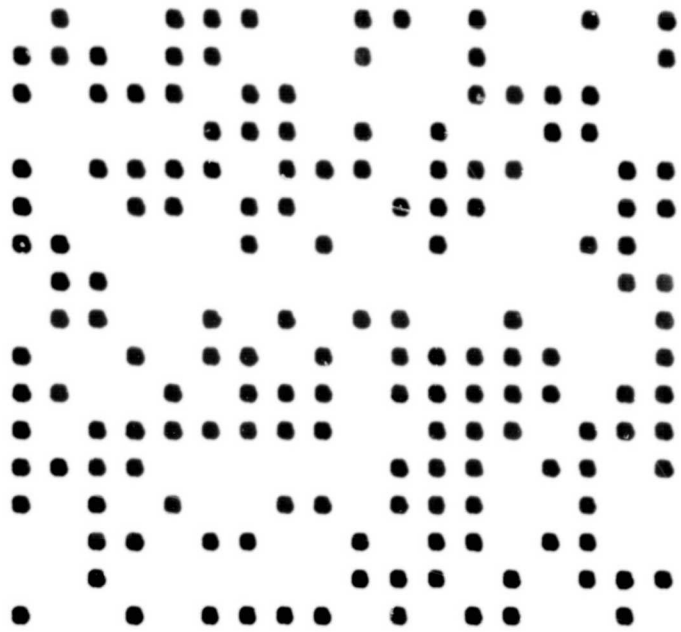

(b)

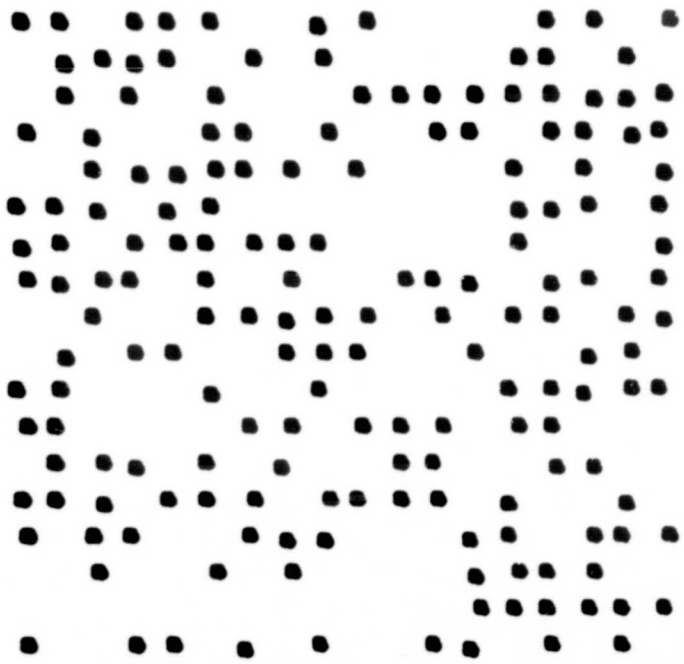

(c)

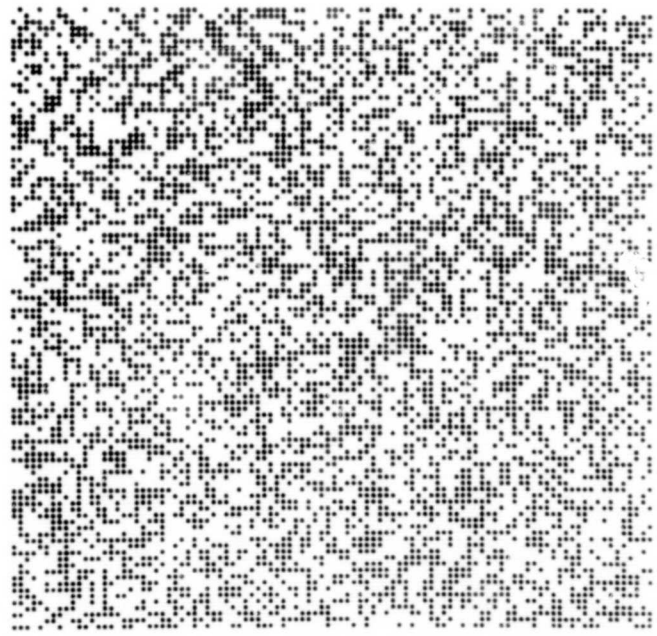

(d)

FIGURE 2-4 INPUT DATA FORMATS

Usually the region in the Fourier transform close to the d.c. produces the greatest film nonlinearity noise. The advantage of the jittered array is that it has a more uniform spectrum than a regular array. We shall briefly analyze the spectrum of a one-dimensional jittered array of f(x):

$$f(x) = \left\{ \sum_n a(n)\, \delta(x-nd-\Delta_n) \right\} * g(x), \tag{2-2}$$

where $g(x) = \begin{cases} 1 & |x| \le \frac{1}{3} d \\ 0 & \text{otherwise} \end{cases}$

and $\Delta_n = -\frac{1}{7} d,\ 0,$ or $+\frac{1}{7} d.$ We can decompose the function f(x) into three components:

$$f(x) = f_1(x) + f_2(x) + f_3(x),$$

where

$$\begin{aligned} f_1(x) &= \left[\sum_n a_1(n)\, \delta(x-nd - \tfrac{1}{7} d) \right] * g(x) \\ f_2(x) &= \left[\sum_n a_2(n)\, \delta(x-nd) \right] * g(x), \\ f_3(x) &= \left[\sum_n a_3(n)\, \delta(x-nd + \tfrac{1}{7} d) \right] * g(x) . \end{aligned} \tag{2-3}$$

Because Δ_n is chosen at random from the set of three numbers, the energy of each component is about $\frac{1}{3}$ of the total energy of the function f(x). The Fourier transform of f(x) is equal to

$$F(u) = F_1(u) e^{-j\frac{2\pi}{7} du} + F_2(u) + F_3(u) e^{+j\frac{2\pi}{7} du}, \tag{2-4}$$

where $F_i(u)$ is the Fourier transform of $f_i(x)$. The linear phase factors

associated with $F_1(u)$ and $F_3(u)$ are generated by the shift parameters. In a region close to zero spatial frequency the effect of the linear phase factor is small. The Fourier spectrum of the jittered array in that region, therefore, is similar to that of a regular array. However, at higher spatial frequencies the phase factor generated by the shifting of the dots will prevent the Fourier transforms $F_i(u)$ from adding coherently to form high intensity in the spectrum. Because the shifting parameter is chosen to be $\frac{1}{7}$ d, the spectrum of the jittered array is a period function with period $\frac{7}{d}$. Fig. 2-5(a) and 2-5(b) show scans of the spectrum of the regular array and the jittered array. Note that, in the region enclosed by the circle, the spectrum of the jittered array has a relatively smaller dynamic range.

We purposely recorded the Fourier transform holograms of the data mask so that the zero spatial frequency and most of the low spatial frequencies were recorded nonlinearly. Because the intensity of the spectrum decreases at high spatial frequencies, some of the spectrum will be recorded linearly. The results of these experiments are shown in Figs. 2-6 and 2-7. The image shown in Fig. 2-6(a) is reconstructed from the Fourier transform hologram of a regular array, using a 2 mm diameter reconstruction beam. The main effect of the nonlinearity of the film is the suppression of the low spatial frequency content of the image and the generation of spurious images. As a result, we only observe the edges of the dots seen in the original data mask. If we use a smaller beam (1 mm or $\frac{1}{2}$ diameter), the dots in the data mask cannot be reconstructed from a region near the optical axis because the hologram is completely saturated in that region. However, as we move the small beam away from zero spatial frequency, we start to see both distorted and spurious images as shown in Fig. 2-6(b). If we move the beam sufficiently far away from zero spatial frequency, the effect of film nonlinearity disappears completely; the ratio of the reference beam to the signal intensity becomes larger at higher spatial frequencies and the recording is therefore linear. The reconstructed image shown in Fig. 2-6(c) is obtained from a region of the hologram which is linearly recorded.

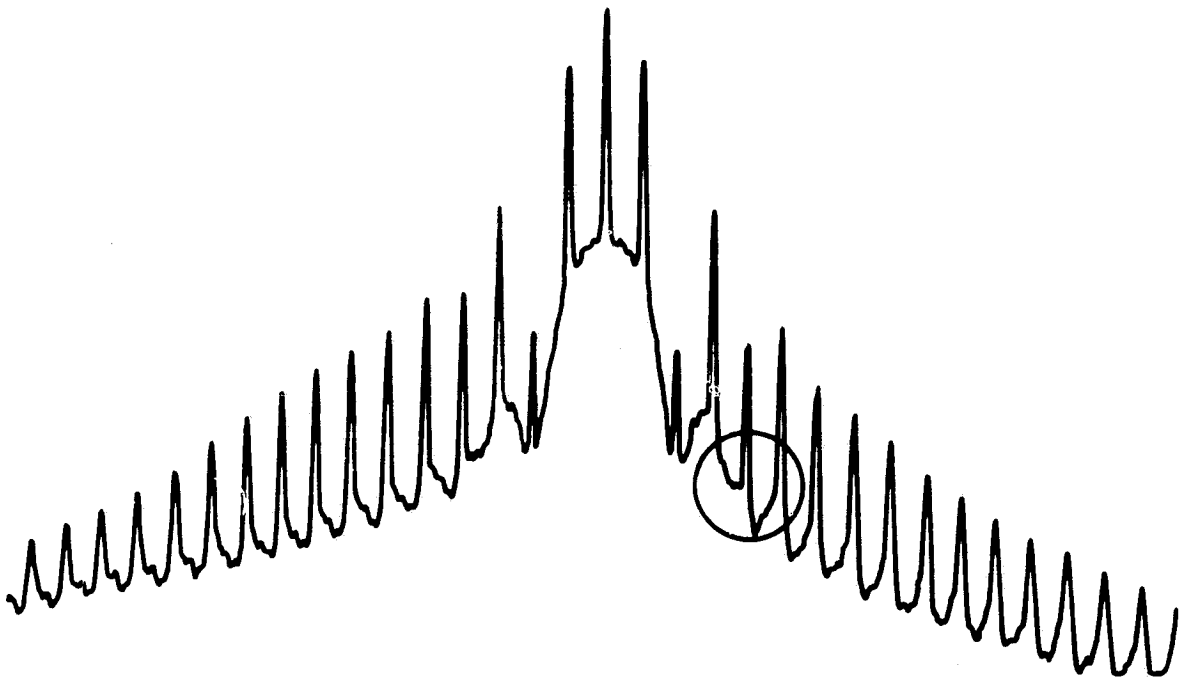

(a)

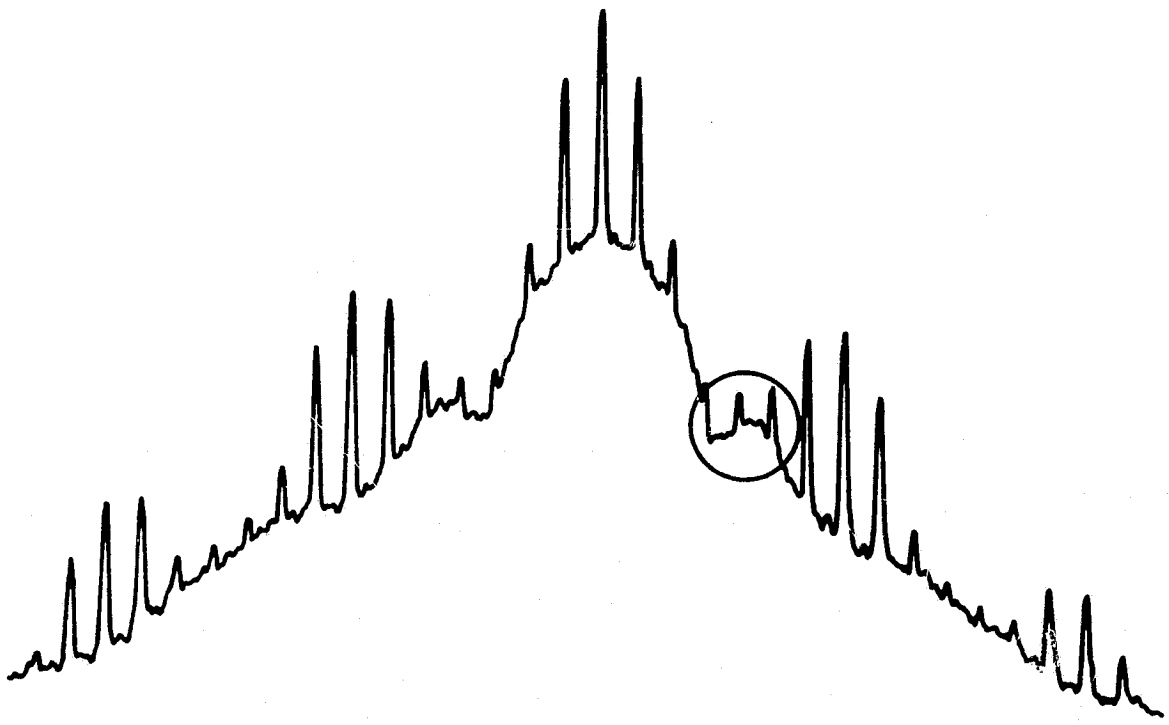

(b)

FIGURE 2.5. SPECTRUM OF INPUT SIGNALS

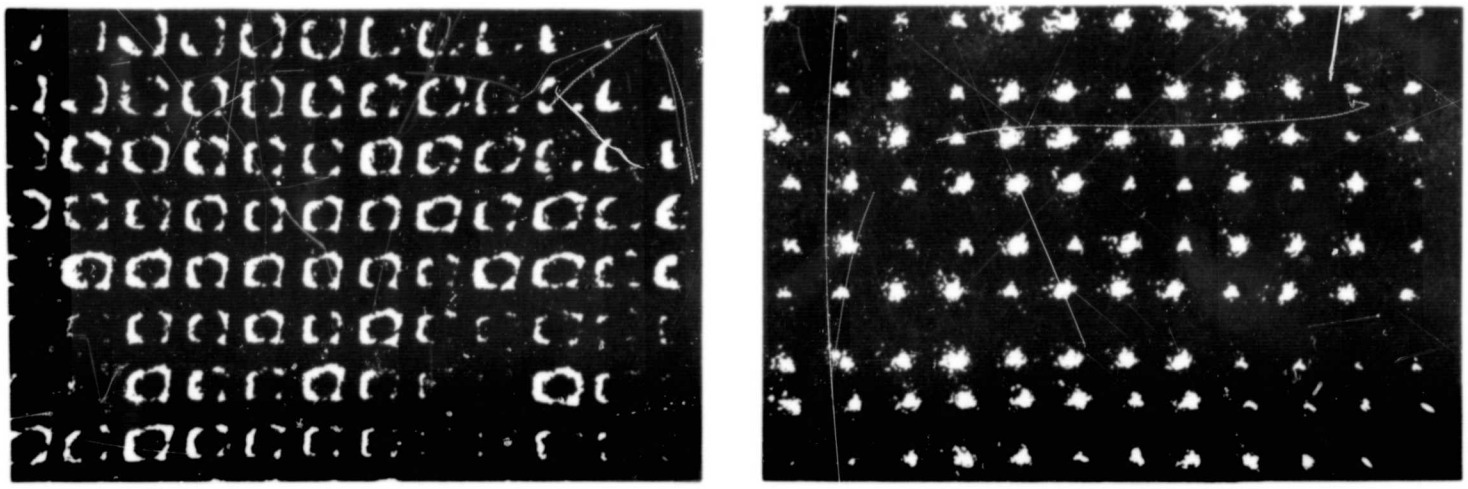

(a) (b)

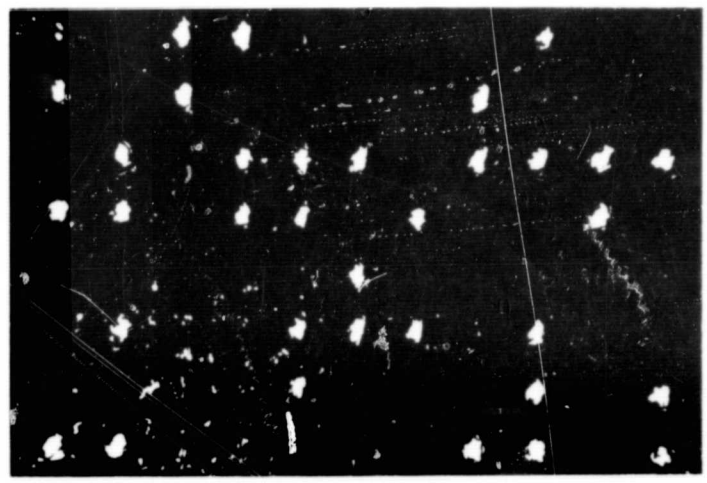

(c)

FIGURE 2-6 REGULAR ARRAY RECONSTRUCTED FROM THREE REGIONS OF A FOURIER TRANSFORM HOLOGRAM.

To demonstrate the differences between the jittered array and the regular array, we show in Fig. 2-7 the images reconstructed from a hologram of the jittered array under the same conditions used to obtain the images from the hologram of a regular array. Note that linear recording in the Fourier transform of the jittered array near the zero spatial frequency is more uniform than that of the regular array. Fig. 2-8 illustrates the regions of the spectrum from which the images shown in Figs. 2-6 and 2-7 are obtained.

Figure 2-9 shows the dependence of the reconstructed image on the size of the hologram aperture. The images were obtained in a region of the hologram sufficiently far from the zero spatial frequency to avoid the film nonlinearity effect. Note that the size of each dot increases as the aperture of the hologram decreases. An aperture greater than or equal to $2\lambda F/d$ should fully resolve the dots, where F is the focal length of the lens, λ is the wavelength of light, and d is the distance between the adjacent dots in the data mask. We used He-Ne laser ($\lambda = 6328\text{Å}$), a 50 mm focal length lens, and a value of d = 0.25 mm to make the Fourier transform hologram. Therefore, the theoretical minimum aperture of the hologram is about 0.25 mm which is in close agreement with the experimental results shown in Fig. 2-9.

When we used a 1 mm diameter reconstruction beam, displaced from the optical axis, to illuminate the Fourier transform, we noted that the reconstructed image is an array of smaller dots which contained the same digital information as the original array. All elements in this array are shifted by a distance equal to $\frac{1}{2}$ d and this property, as explained below, is possessed by both the regular array and the jittered array.

For a data mask of type 1, the Fourier transform of f(x, y) is equal to

$$F(u, v) = \sum \sum F_1\left(u - \frac{n}{d}, v - \frac{n}{d}\right) G(u, v), \qquad (2\text{-}5)$$

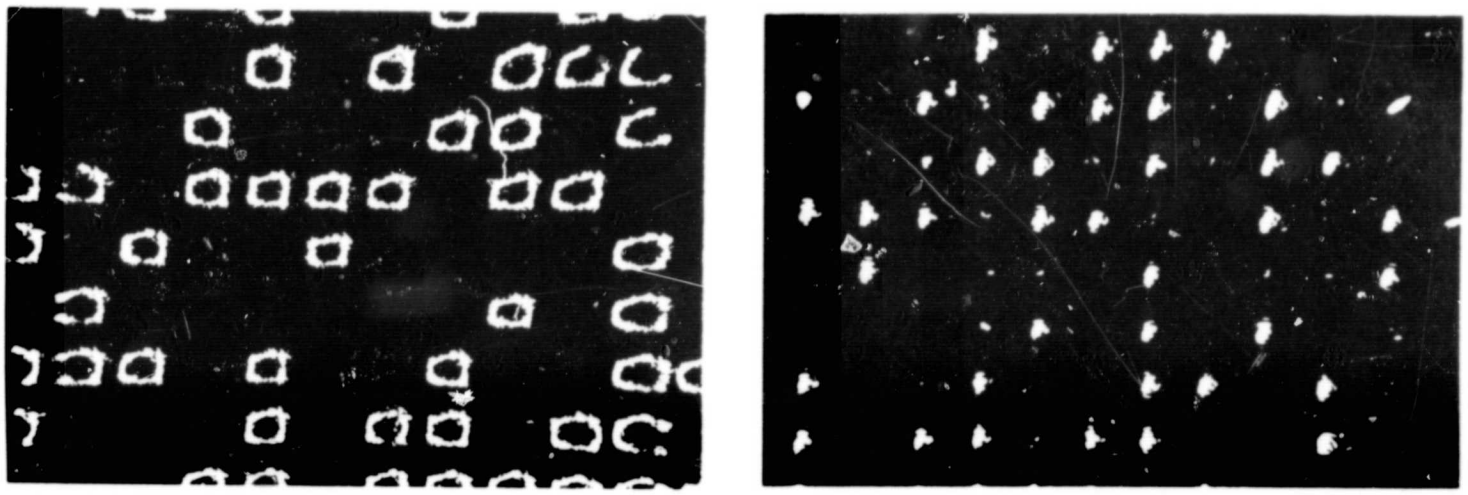

(a) (b)

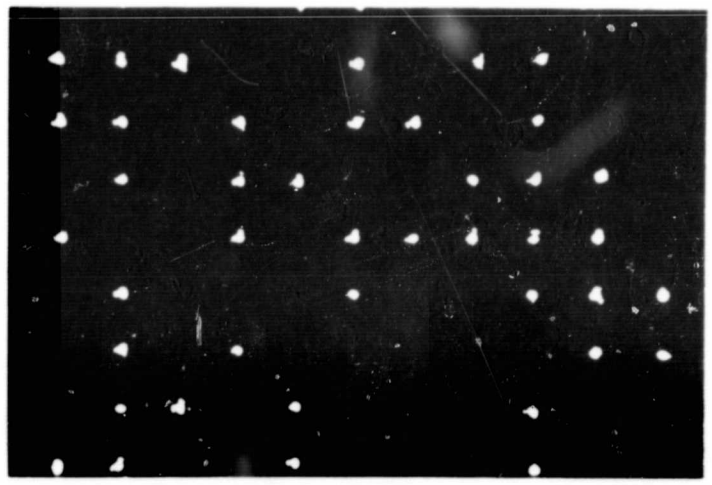

(c)

FIGURE 2-7 JITTERED ARRAY RECONSTRUCTED FROM THREE REGIONS OF A FOURIER TRANSFORM HOLOGRAM.

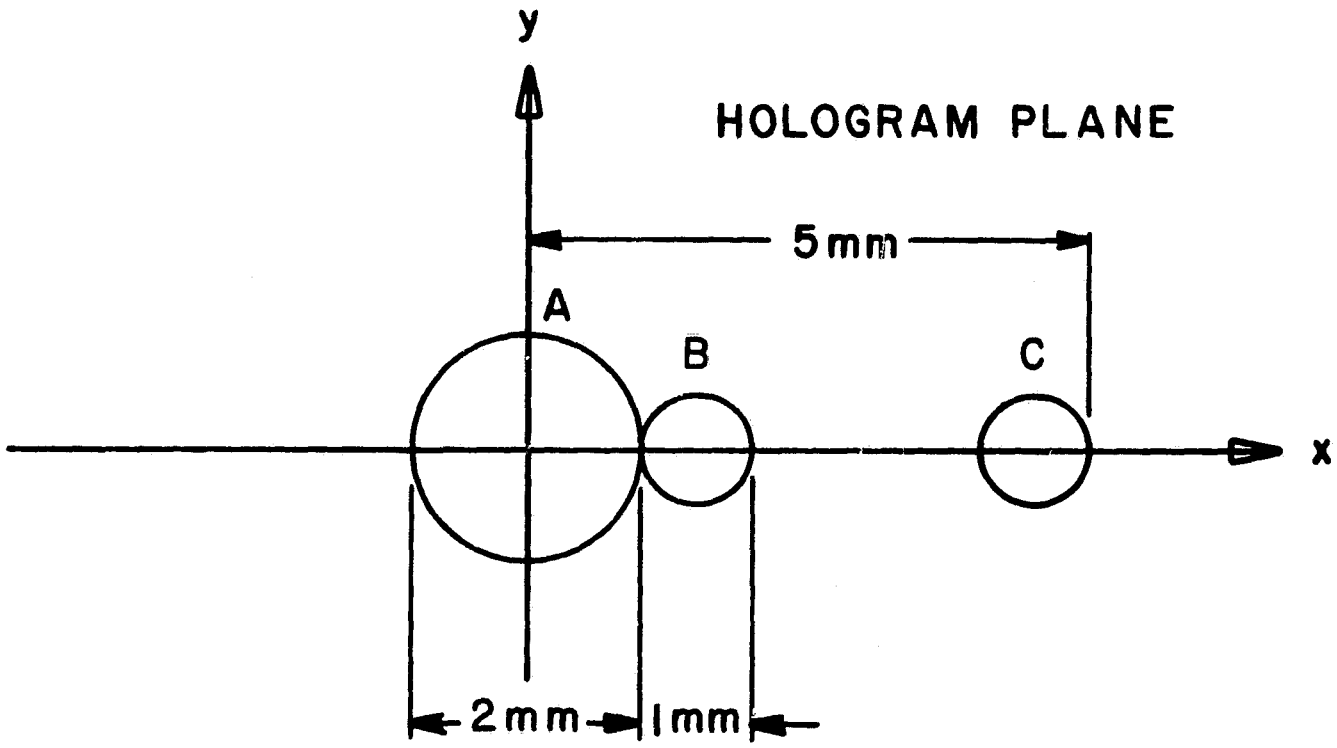

FIGURE 2.8. REGIONS OF THE FOURIER TRANSFORM HOLOGRAM USED FOR RECONSTRUCTIONS.

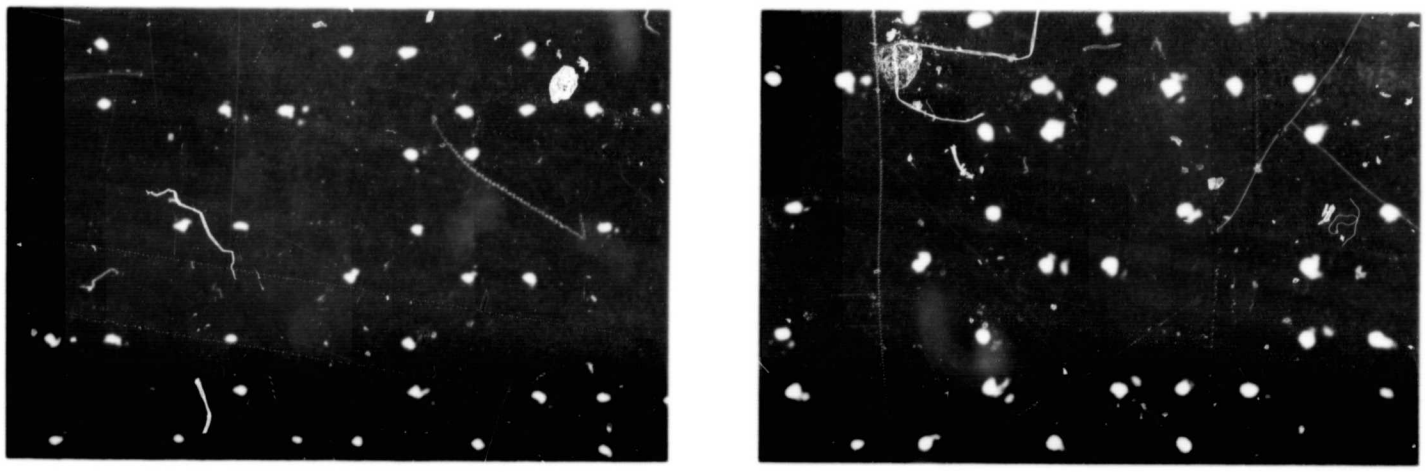

(a) (b)

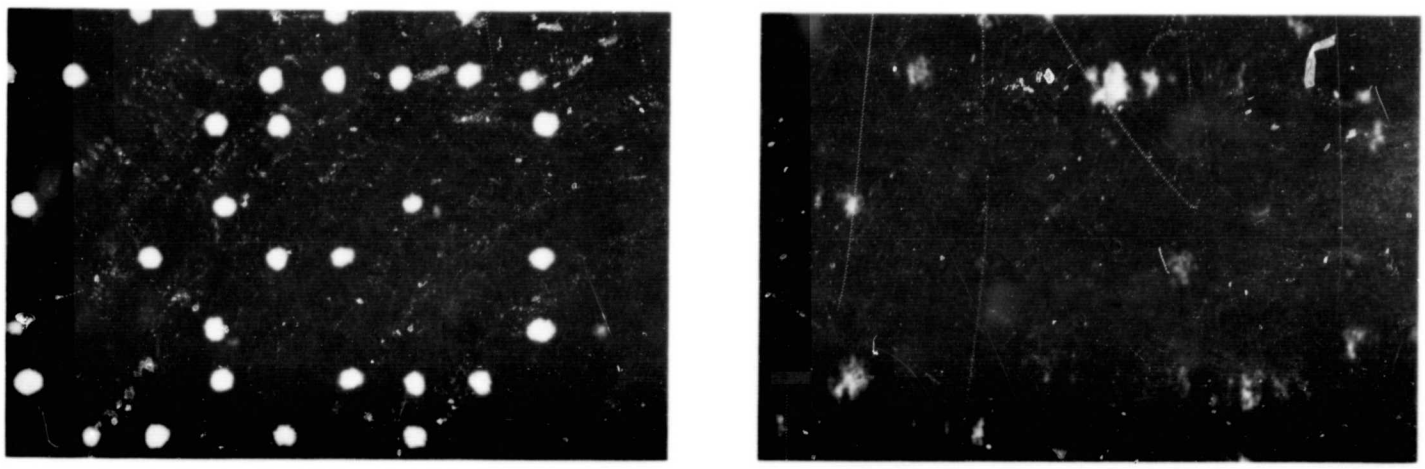

(c) (d)

FIGURE 2-9 EFFECTS OF HOLOGRAM APERTURES ON IMAGE RESOLUTION FOR FOURIER TRANSFORM HOLOGRAM (a) 1.5 mm, (b) 1 mm, (c) .5 mm, (d) .2 mm.

85671-6

where $G(u,v) = \text{sinc}(\pi du)\ \text{sinc}(\pi dv)$

and $F(u,v) = \sum\sum a(n,m)e^{-j\frac{2\pi}{d}(nu+mv)}$ for $|u| \le \frac{1}{2d}$, $|v| \le \frac{1}{2d}$.

The function $G(u,v)$ is an envelope function produced by the square dots. For sidelobes sufficiently far from the main lobe the sidelobes of $G(u,v)$ vary almost sinusoidally. For simplicity we shall perform the analysis in one-dimensional notation. The function $F(u)$ can then be approximated by

$$F'(u) = \sum_{n=N_1}^{N_2} (-1)^n F(u - \frac{n}{d}). \tag{2-6}$$

When we perform the inverse Fourier transform on $F'(u)$, we obtain

$$f'(x) = f(x) \sum_{n=N_1}^{N_2} e^{j2\pi n(\frac{x}{d} - \frac{1}{2})} \tag{2-7}$$

Therefore,

$$|f'(x)|^2 = |f(x)|^2 k^2(x), \tag{2-8}$$

where

$$k(x) = \frac{\sin[\pi(N_1 - N_2)(\frac{x}{d} - \frac{1}{2})]}{\sin\pi(\frac{x}{d} - \frac{1}{2})} \tag{2-9}$$

The function $k(x)$ is a series of pulses separated by a distance d. The width of each pulse depends on $(N_2 - N_1)$ and the center of the pulse is shifted by a

distance $\frac{1}{2}$ d from the origin. Depending upon which area of the hologram is illuminated, the pulse is shifted to the right or left, up or down. Fig. 2-10 shows the images of the digital array obtained from two different regions in the sidelobes. In Fig. 2-10(a), the reconstructing beam is shifted along the x-axis while in Fig. 2-10(b) the beam is shifted along the y-axis. This same property of the digital array can be observed when an off-axis aperture is used at the Fourier transform plane in an ordinary coherent imaging system so that it is not uniquely caused by the holographic process.

2.2.3 Fresnel Holograms

We performed experiments to determine how the noise is related to the number of active elements in the array, the duty cycle, and the degree of nonlinearity. We give experimental results for Fresnel transform holograms recorded on either absorptive or phase materials. The representative absorptive material is high resolution 649F photographic emulsions, while the representative phase material is dichromated gelatin.

The input signals were the diffusely illuminated data masks shown in Fig. 2-4. The data mask was located a distance Z = 50 mm from the hologram plate. We made a series of holograms for each signal with a different reference-to-signal beam intensity ratio, and the holograms were sufficiently large so that we could show the effect of variations in aperture size on the signal-to-noise ratio of the reconstruction. The effect of the aperture size on the signal-to-noise ratio for Fresnel holograms is shown in Fig. 2-11. The minimum hologram aperture required to resolve the bits is given by $A = 2\lambda Z v$; for $\lambda = 632.8$ nm, $Z = 50$ mm, and $v = 4$ lines/mm, the minimum aperture for a 10^4 bits array is 0.25 mm. Note, however, that an aperture of about twice the theoretical minimum is necessary to reduce the variance of the signal to an acceptable level.

We performed experiments to determine the dependence of spurious images (or noise) on the number of elements contained in the array and the

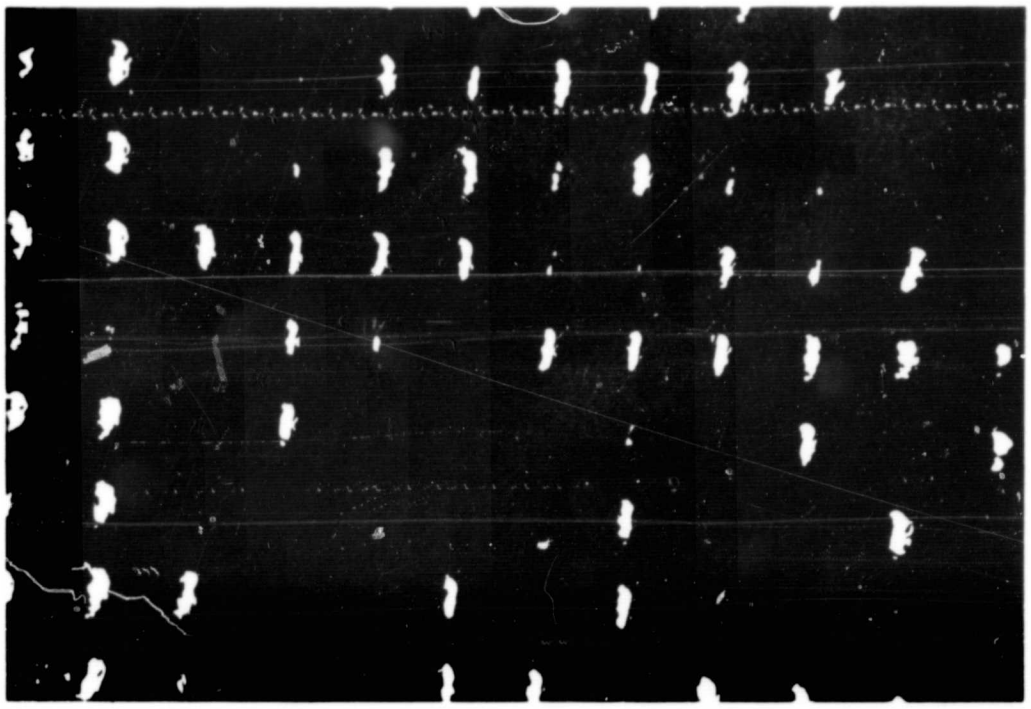

(a)

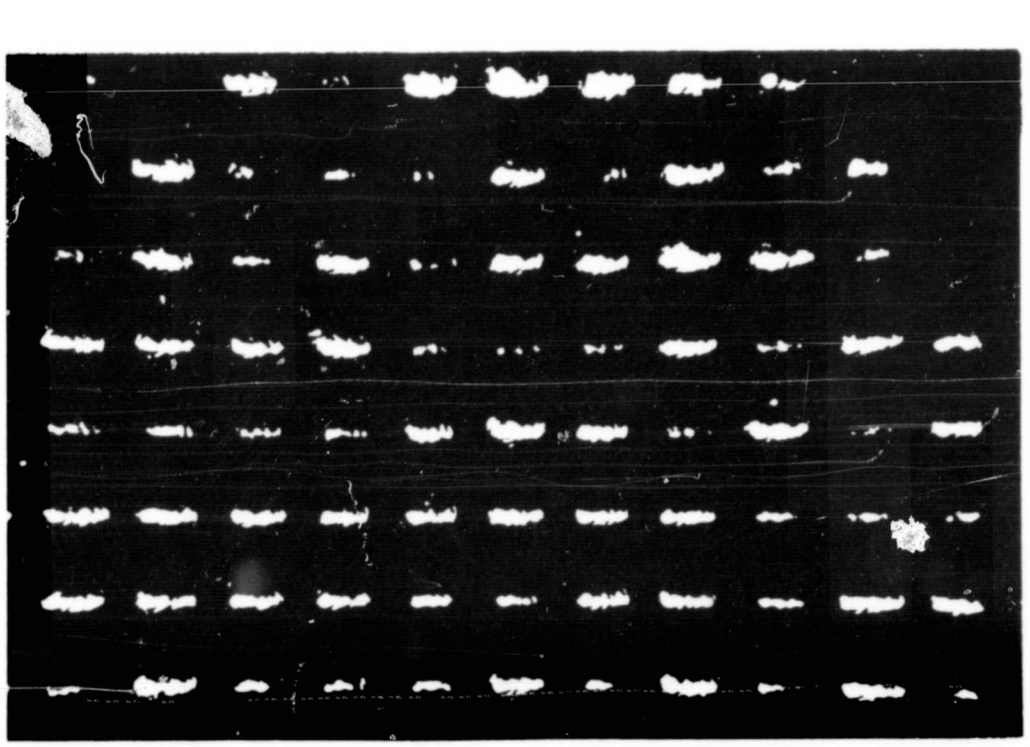

(b)

FIGURE 2-10 SIDEBAND RECONSTRUCTION OF A FOURIER TRANSFORM HOLOGRAM. (a) Along x-axis, (b) Along y-axis.

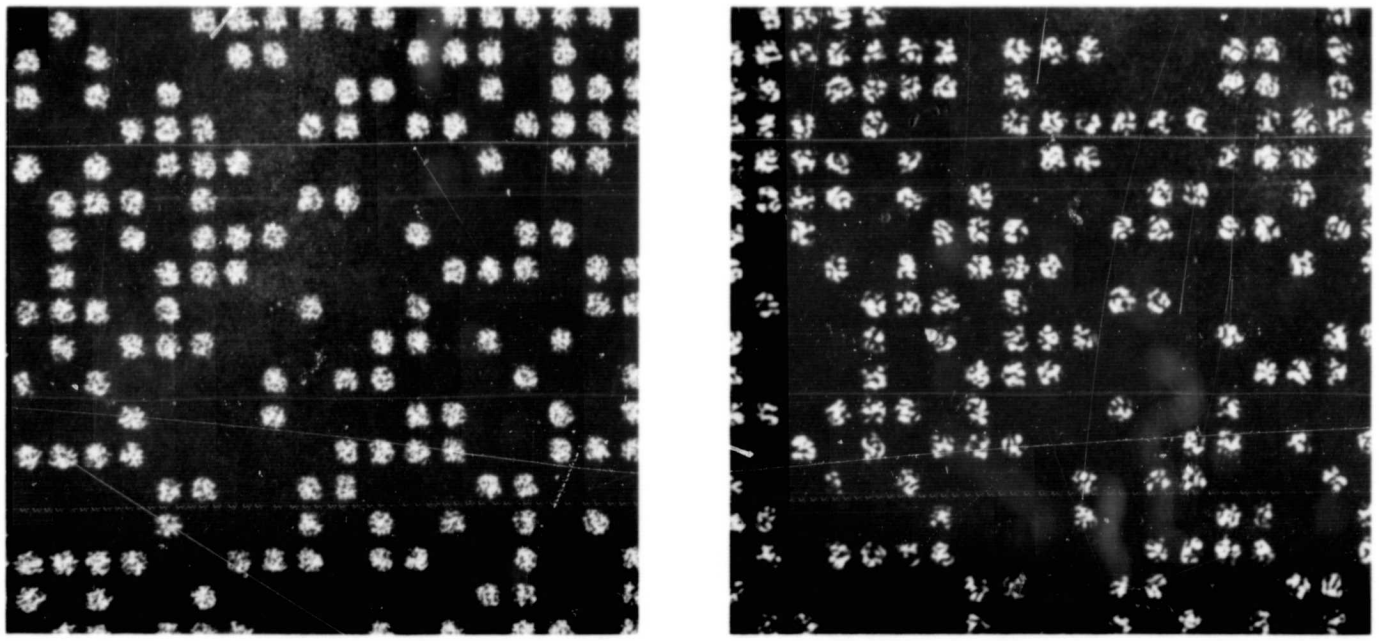

(a)

(b)

(c)

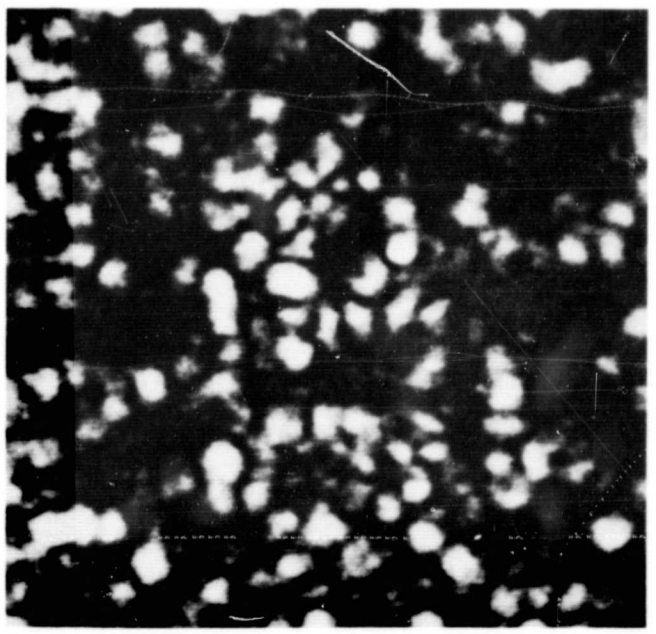

(d)

FIGURE 2-11 EFFECTS OF HOLOGRAM APERTURE ON IMAGE RESOLUTION FOR FRESNEL HOLOGRAM. (a) 1.5 mm, (b) 1 mm, (c) .5 mm, (d) .2 mm.

85671-5

duty cycle of the array. Some holograms were made from arrays having a fixed duty cycle but different numbers of total elements. Others were made from arrays where the duty cycle was varied while the number of points remained constant. All holograms were purposely recorded non-linearly so that the intermodulation terms should appear in the reconstructed image. Fig. 2-12 shows reconstructed images of arrays having duty cycles of 1/2, 1/3, and 1/4; the total number of elements in each array, however, was the same. Note that the spurious images become more distinct as the duty cycle becomes smaller. Fig. 2-13 shows reconstructed images of arrays having different numbers of bits. The spurious images are less distinct when there are more dots in the data mask. These results are expected because, if the input array contains enough resolvable points, the noise due to spurious images is generally negligible in comparison to the film grain noise.

We also recorded holograms on dichromated gelatin, varying the exposure and the reference-to-signal beam intensity ratio. The holograms were sufficiently large so that we could show the effect of a variation in the aperture size of the holograms on the signal-to-noise ratio of the reconstructed image. The holograms were recorded with 488 nm light and an exposure of about 30 mJ/cm^2.

We determined the relative signal-to-noise ratio as a function of the hologram aperture and the signal-to-reference beam intensity ratio. Fig. 2-14 shows the relative intensities of the diffracted, transmitted, and reflected light of a dichromated gelatin hologram, measured for a 1 mm diameter hologram; the intensity of the absorbed and scattered light is about equal to the diffracted light. Fig. 2-15 shows the relative signal-to-average noise intensity ratio I/I_n as a function of the exposure; this ratio was measured by using a photo multiplier scanner. In comparing Fig. 2-14 with Fig. 2-15 we see that at high exposures, where the diffraction efficiency is increasing, the signal-to-noise ratio is decreasing.

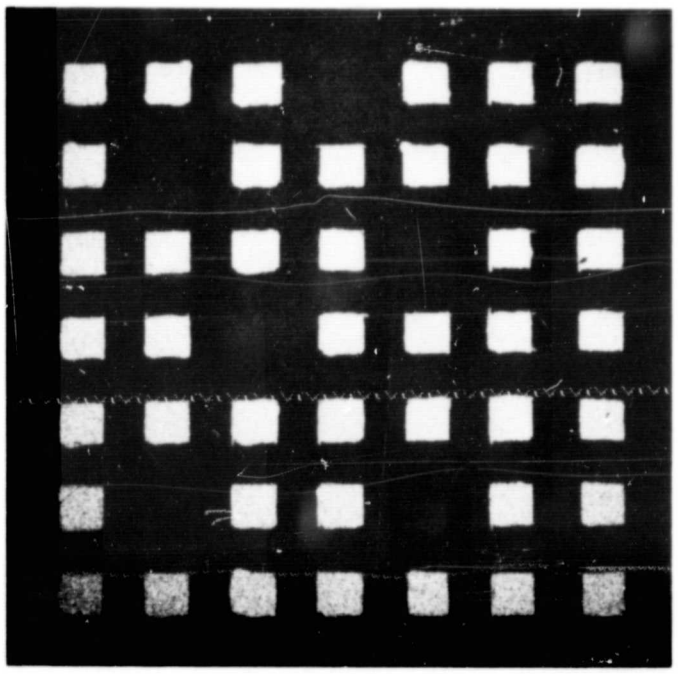

(a)

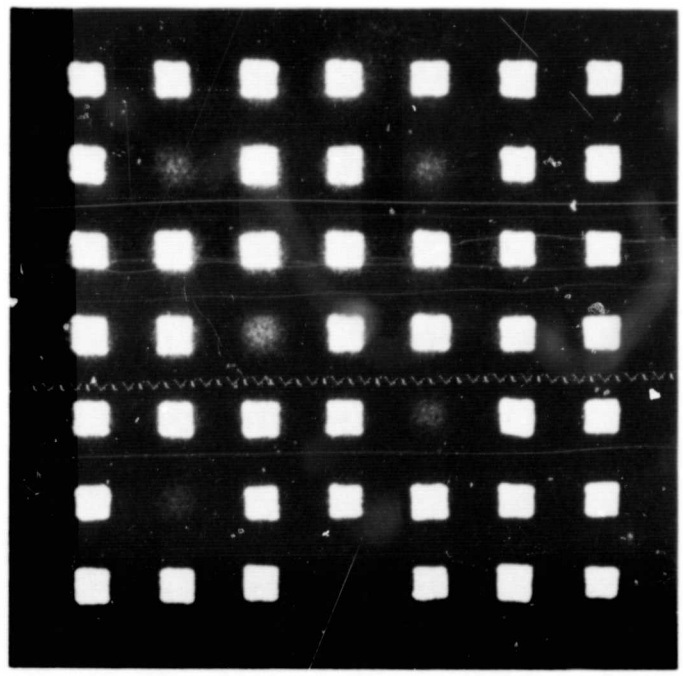

(b)

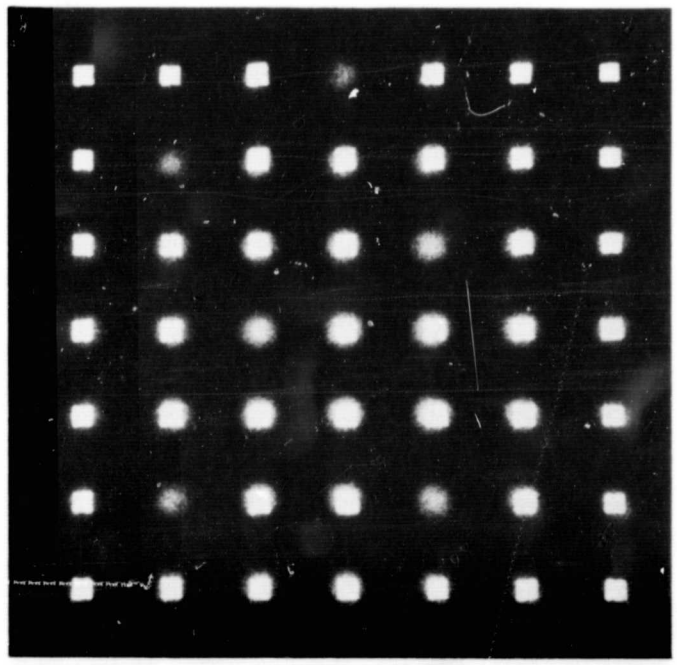

(c)

FIGURE 2-12 EFFECTS OF FILM NONLINEARITY FOR THREE DIFFERENT DUTY CYCLES

85671-1

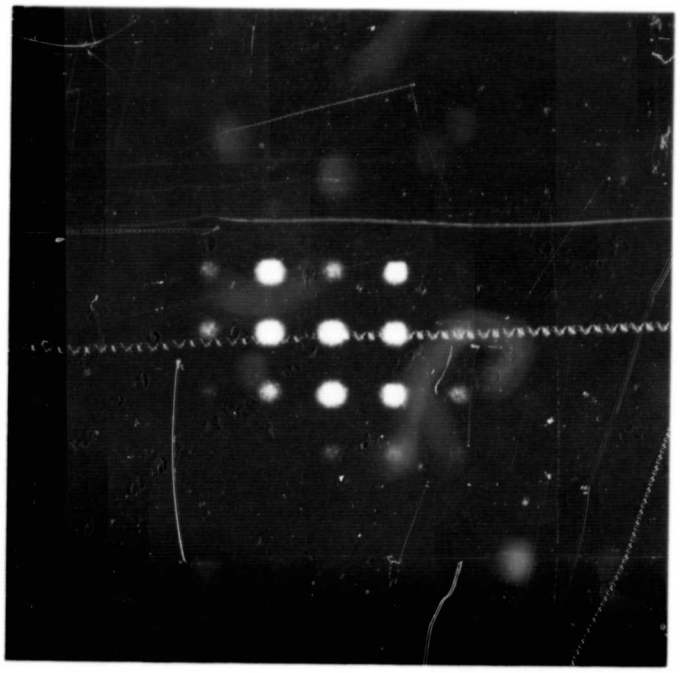

(a)

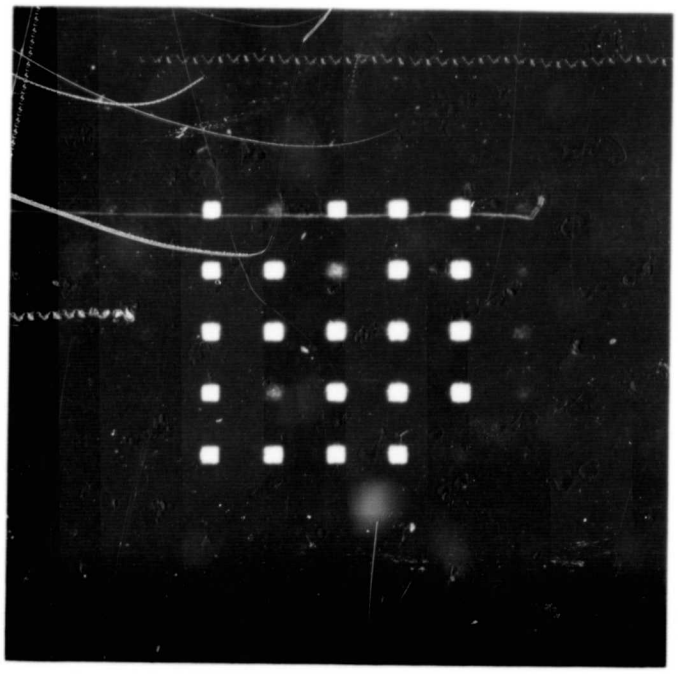

(b)

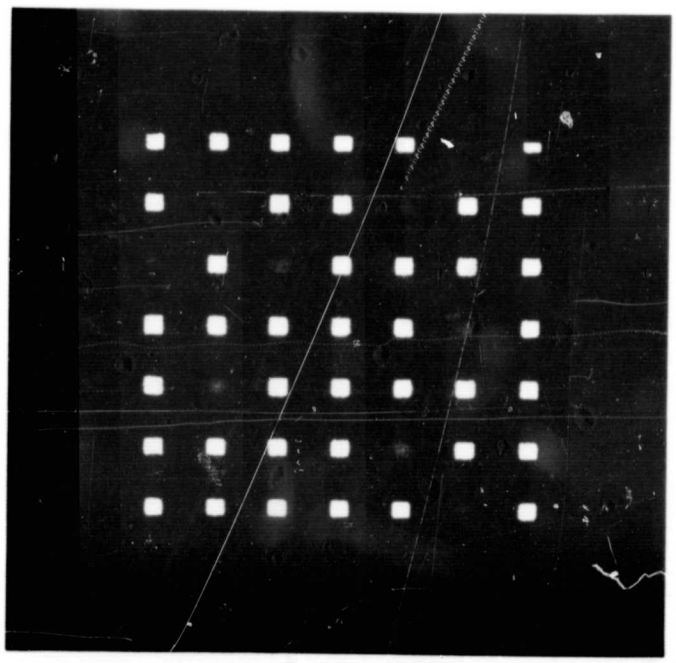

(c)

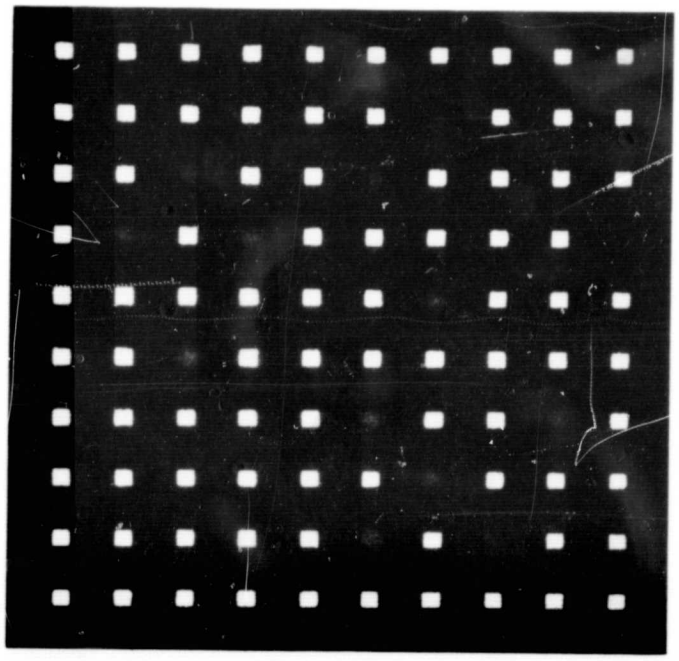

(d)

FIGURE 2-13 EFFECTS OF FILM NONLINEARITIES FOR DIFFERENT ARRAYS.

85671-2

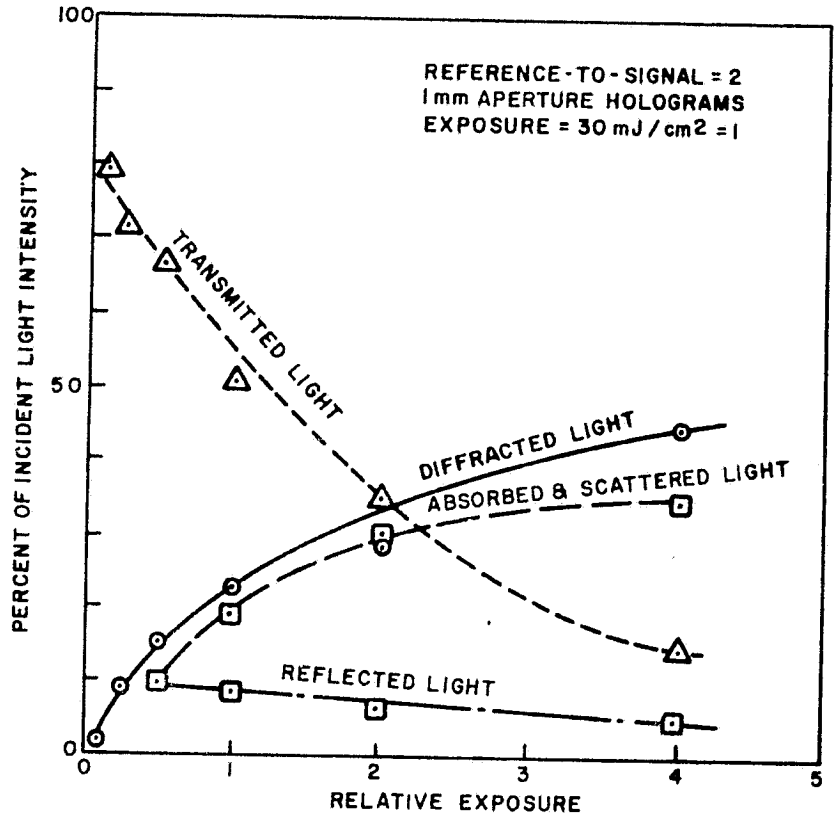

FIGURE 2-14. LIGHT DISTRIBUTION OF A DICHROMATED GELATIN HOLOGRAM VERSUS EXPOSURE

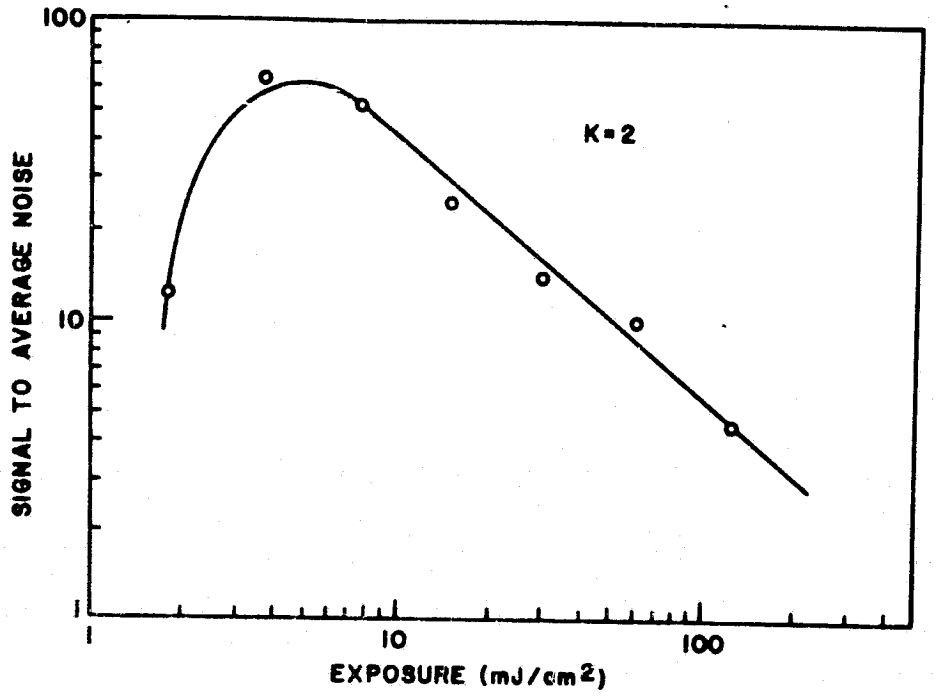

FIGURE 2-15. SNR VERSUS EXPOSURE

Fig. 2-16 shows the effect of the reference-to-signal beam intensity ratio on the diffraction efficiency. The diffraction efficiency of dichromated gelatin does not decrease as rapidly with increasing reference-to-signal beam ratios as it does for 649F film. Fig. 2-17 shows the signal-to-average noise intensity ratio as a function of reference-to-signal beam ratio; these curves suggest that there may be a trade-off in exposure and reference-to-signal beam to obtain the optimum performance of the dichromated gelatin in terms of signal-to-noise ratio.

2.2.4 Comments

From the results of these experiments we determined that the signal-to-average noise intensity ratio is maximized when the number of bits per unit area on the hologram is selected to balance the effects of film grain noise against the effects of the film nonlinearity noise. We also found that, for a given hologram aperture, the quality of the image reconstructed from a Fourier transform hologram is better than that from a Fresnel hologram. Furthermore, we demonstrated that the quality of the Fourier transform hologram can be improved if the input data mask is made of a jittered array.

2.3 EXPERIMENTS WITH INCOHERENT ADDITIONS OF SIGNALS

As part of our investigation of holographic techniques, we experimentally investigated the degradation of signal-to-noise ratio (SNR) due to the incoherent addition of holograms. The output SNR is a parameter of major importance since it determines both the usable storage capacity and error rate of an optical memory. The study of holographic data storage technique using the incoherent addition of holograms is motivated by a desire to achieve the highest packing densities possible for a given error rate. For example, suppose a prescribed error rate permits some fraction of the maximum storage capacity of a recording material to be used. Then, if the optical system can achieve the maximum available capacity, a single hologram

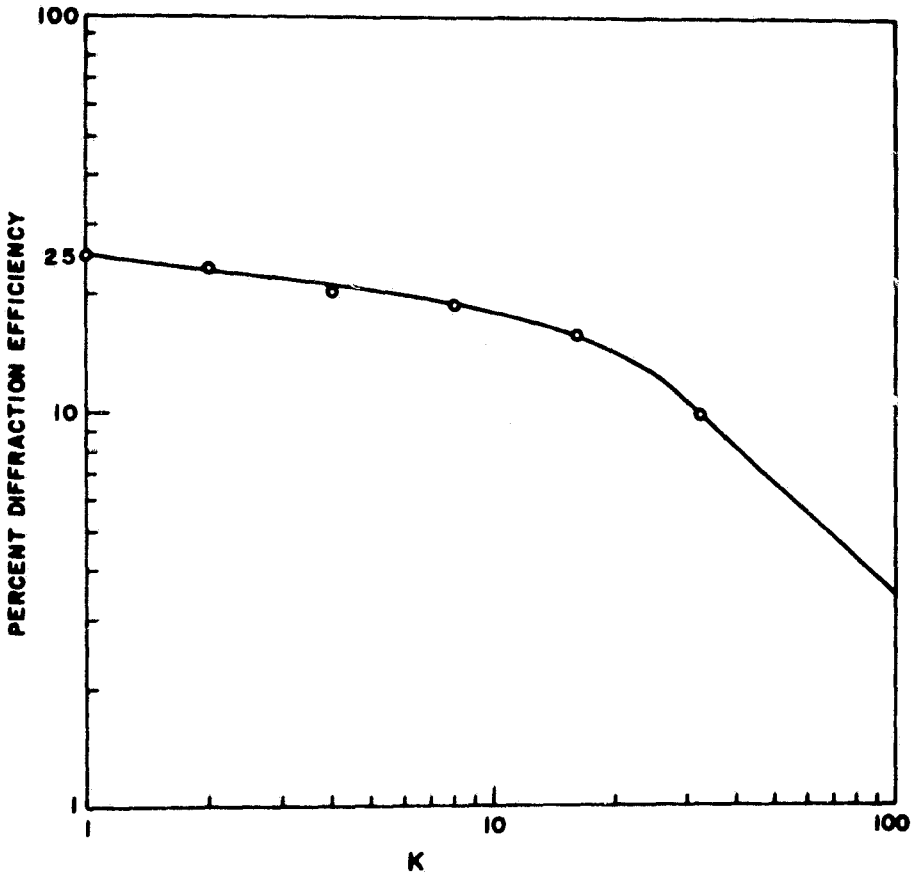

FIGURE 2-16. DIFFRACTION EFFICIENCY VERSUS BEAM RATIO K

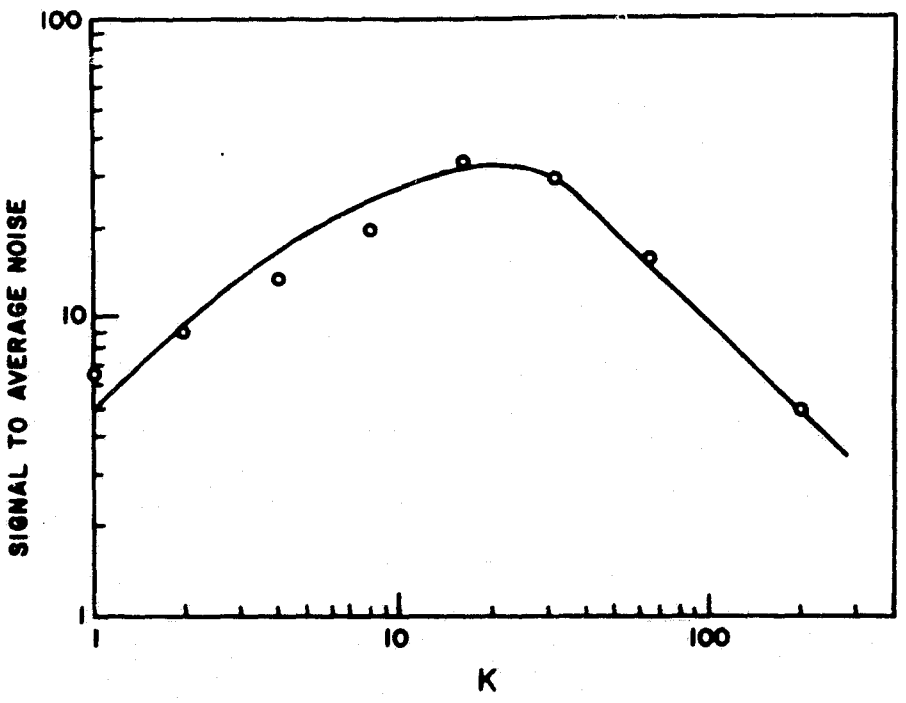

FIGURE 2-17. SNR VERSUS BEAM RATIO K

recording suffices. However, if the optical system (or limitations on its major components) limits the capacity to a value less than the maximum, incoherent addition of holograms becomes an attractive technique for making use of the available storage capacity. Bragg storage by either angular or wavelength discrimination or both is an example of this technique.

Data storage techniques using incoherent addition are generally considered inferior to coherent addition techniques. It is generally believed that an incoherent addition technique causes the SNR per hologram to decrease inversely as the square of the number of signals incoherently added. By way of comparison, the SNR for the coherent addition case falls off only inversely as the number of signals added. This factor is significant even when the number of signals becomes modestly large. For example, for ten additions, the SNR for the incoherent addition case is already 10 dB less than for the corresponding coherent addition case. In the remainder of this section we present the experimental results showing that Bragg storage may under certain conditions, improve the SNR of incoherently added signals.

2.3.1 Experimental Geometry

Figure 2-18 shows the geometry used in our experimental work. An argon laser operating in a single longitudinal and transverse mode at 488 nm is used as a coherent light source. The output beam of the laser is split into two parts, the signal and the reference beam. The signal beam is used to illuminate an input data mask which is a square piece of ground glass having a small opaque square in the center, positioned parallel to the hologram recording plane and at a distance of 100 mm. The clear area of the data mask is 350 mm^2. The reference beam is a plane wave and the average offset angle between the reference and the reference and the input signal beam is 40°. The reference-to-signal beam intensity ratio K is maintained at 10. A 1 cm diameter aperture, placed in the hologram recording plane, shields stray light; this aperture also determines the area of the hologram.

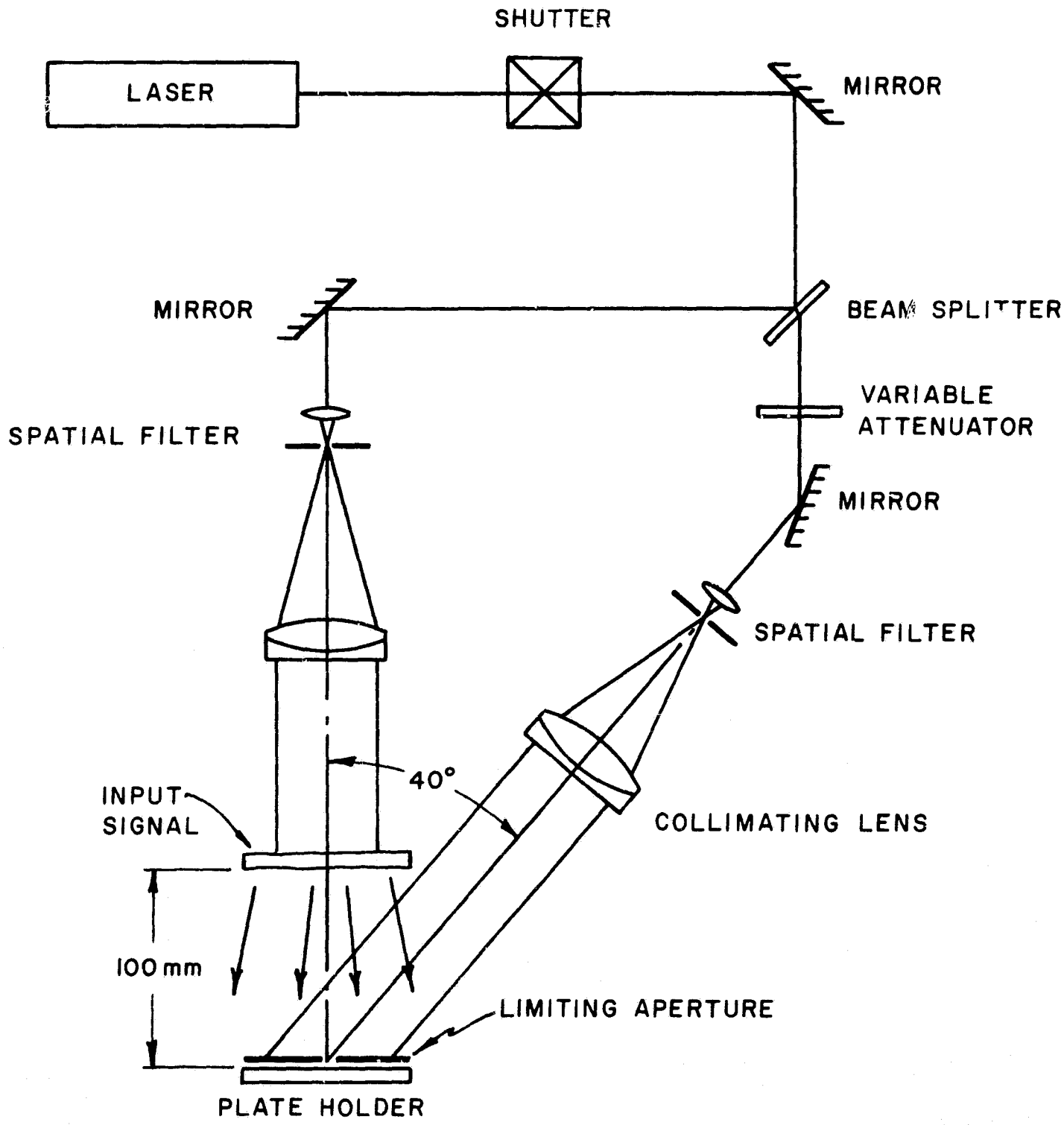

FIGURE 2-18. EXPERIMENTAL SETUP FOR INCOHERENT ADDITION TECHNIQUES

There are 10^7 resolution elements in the signal using this experimental arrangement.

2.3.2 Experimental Procedure

To determine the SNR for each hologram individually we spatial-frequency multiplexed the holograms so that the reconstructed images are spatially separated. We implemented the frequency multiplexing by rotating the plateholder about an axis normal to the hologram plane; this is illustrated in Fig. 2-19, together with a spatial frequency domain representation of the recorded information.

A series of holograms having 1, 2, 4, 8, 16 and 32 incoherent additions was recorded on Kodak HR emulsions, Agfa Lippmann emulsions, and on dichromated gelatin. After each exposure the recording material was rotated. When the prescribed number of incoherent additions was completed, the recording material was translated and the process repeated; the total exposure was fixed. Hence, the exposure per hologram was the total exposure divided by the number of incoherent additions.

After appropriate development, we illuminated each composite hologram with a readout beam and separately measured the amplitude transmittance T_a, the diffraction efficiency η, the signal-to-noise ratio SNR and the standard deviation of the noise σ_N. The experimental arrangement and procedure for measuring these parameters are described in Section 3.

2.3.3. Experimental Results

The data obtained from our measurements is given in both tabular and graphic form. In Tables 2-1, 2-2, and 2-3 we list the measured quantities for each material and for each hologram. Figs. 2-20(a), 20(b), 20(c) are plots of SNR for the first hologram recorded in each sequence versus the number of incoherent additions for each of the three recording materials used. In the reconstruction, the hologram aperture was reduced so that

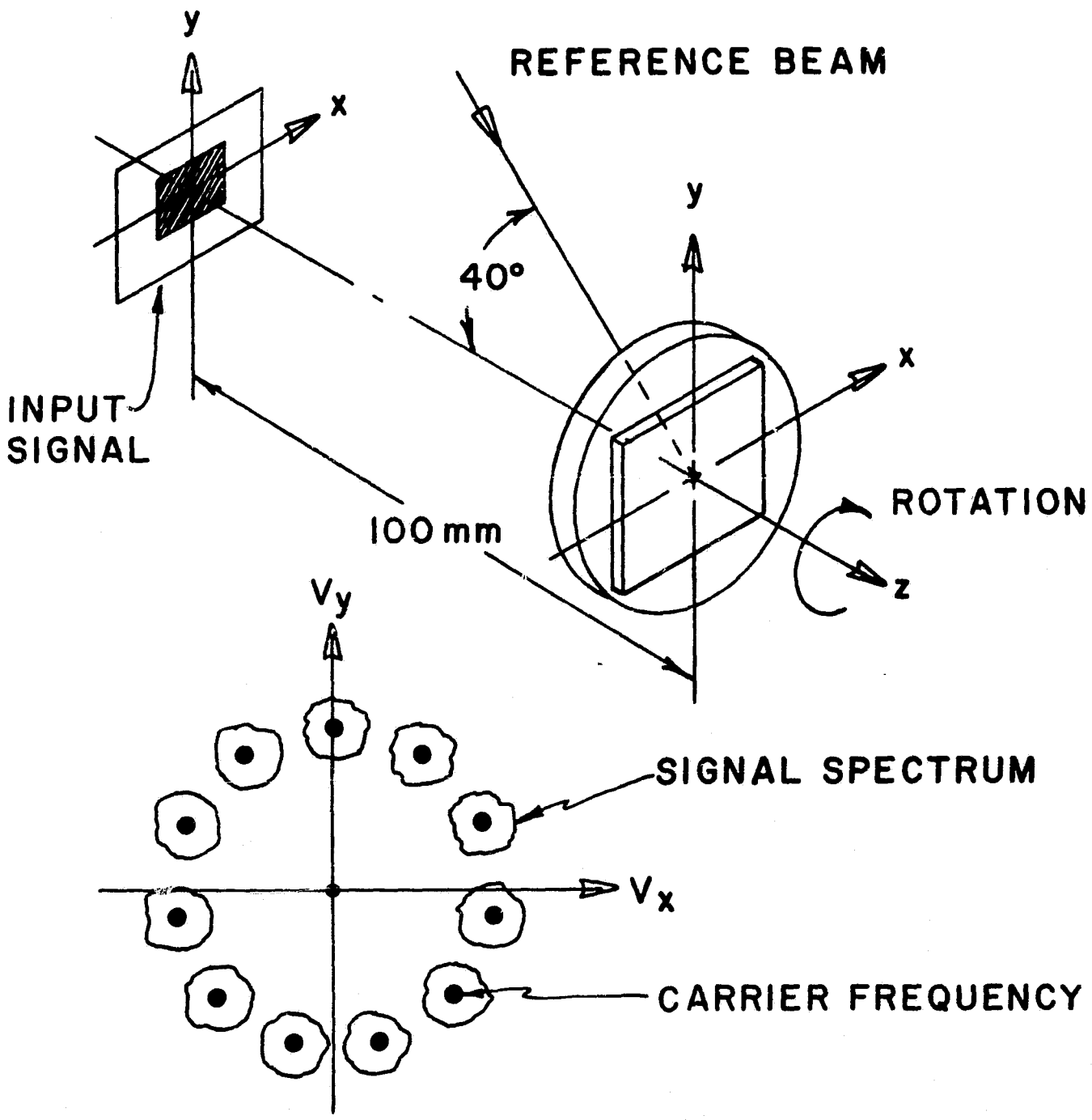

FIGURE 2-19. SPATIAL FREQUENCY MULTIPLEXING TECHNIQUE AND CORRESPONDING FREQUENCY DOMAIN REPRESENTATION

No. of Incoherent Additions	Hologram No.	$< T_a >$	Percent	SNR (dB)	σ_N(dB)
1	1	.242	.32	15.	5.
2	1	.247	.16	15.2	3.5
	2		.075	13.4	3.2
4	1	.288	.011	14.	2.8
	2		.0425	10.4	2.8
	3		.0355	9.	3.2
	4		.0210	6.2	3.2
8	1	.316	.045	10.8	3.3
	5		.010	3.4	3.
	8		.0150	6.5	3.2
16	1	.336	.020	5.9	3.1
	9		.0155	4.3	3.2
	16		.013	3.7	3.2
32	1	.419	.015	3.1	3.2
	17		.0125	--	--
	32		.01	--	--

TABLE 2-1 KODAK HR EMULSION

No. of Incoherent Additions	Hologram No.	$<T_a>$	Percent	SNR (dB)	σ_N(dB)
1	1	.335	.115	14.6	2.8
2	1	.335	.130	17.5	2.9
	2		.038	13.8	2.7
4	1	.335	.065	15.	2.8
	2		.045	14.7	2.9
	3		.043	14.4	2.8
	4		.043	14.	2.8
8	1	.338	.0230	12.8	2.8
	5		.010	8.2	2.9
	8		.010	9.5	2.9
16	1	.316	.0075	8.4	3.0
	9		.005	6.5	2.9
	16		.006	6.5	3.0
32	1	.264	.0036	3.7	2.8
	17		.0030	3.1	2.8
	32		.0026	2.2	2.7

TABLE 2-2 AGFA LIPPMANN EMULSION

No. of Incoherent Additions	Hologram No.	Percent	SNR (dB)	σ_N (dB)
1	1	.05	9.0	3.2
2	1	.1	11.5	4.0
	2	.15	13.6	4.5
4	1	.05	15.0	4.5
	2	.046	9.5	4.2
	3	.046	10.6	4.6
	4	.045	8.8	4.9
8	1	.021	11.0	4.7
	5	.008	8.4	4.8
	8	.012	8.7	4.4
16	1	.012	11.6	4.6
	9	.01	4.4	4.4
	16	.013	8.1	4.5
32	1	.005	9.0	4.8
	17	.004	2.2	4.2
	32	.004	6.2	4.5

TABLE 2-3 DICHROMATED GELATIN

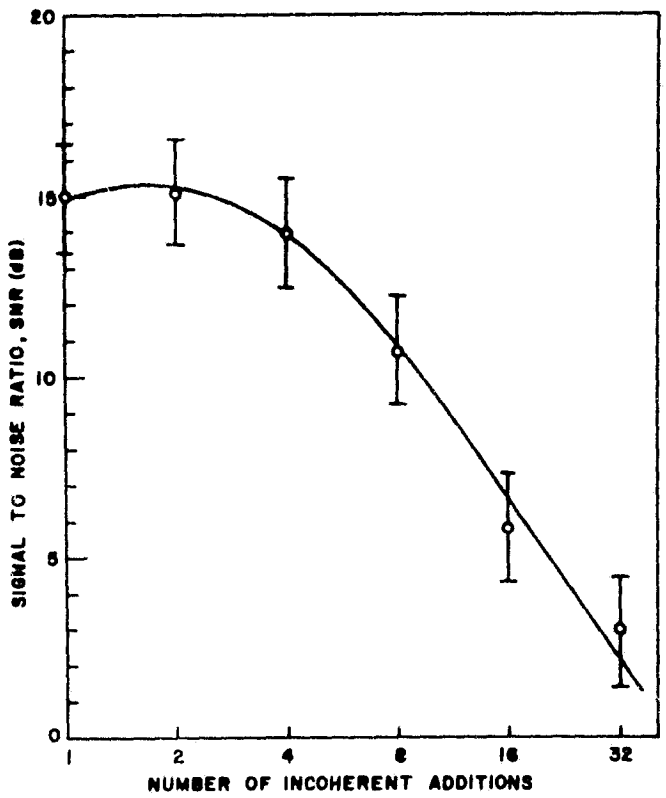

(a) HR Plate

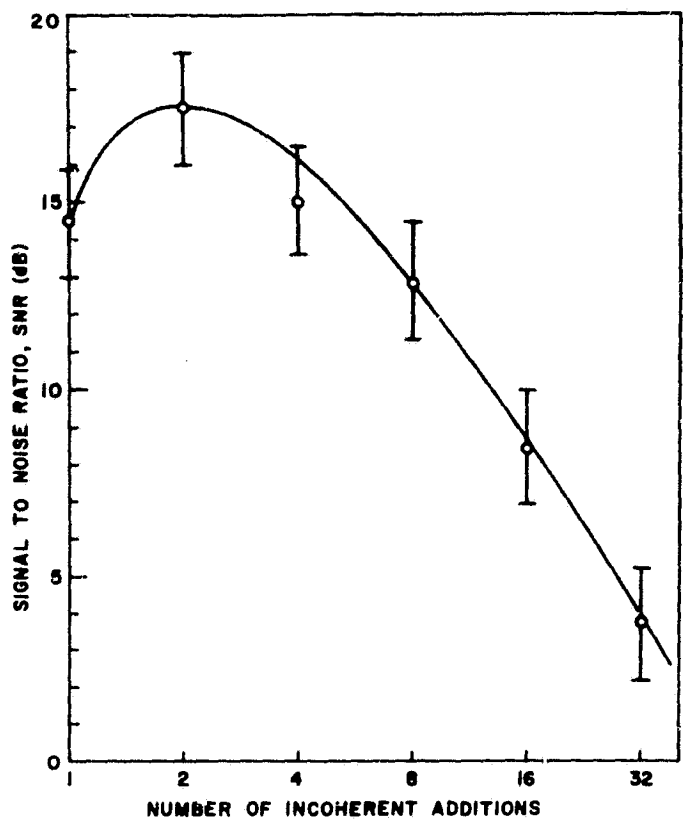

(b) Lippmann Emulsion

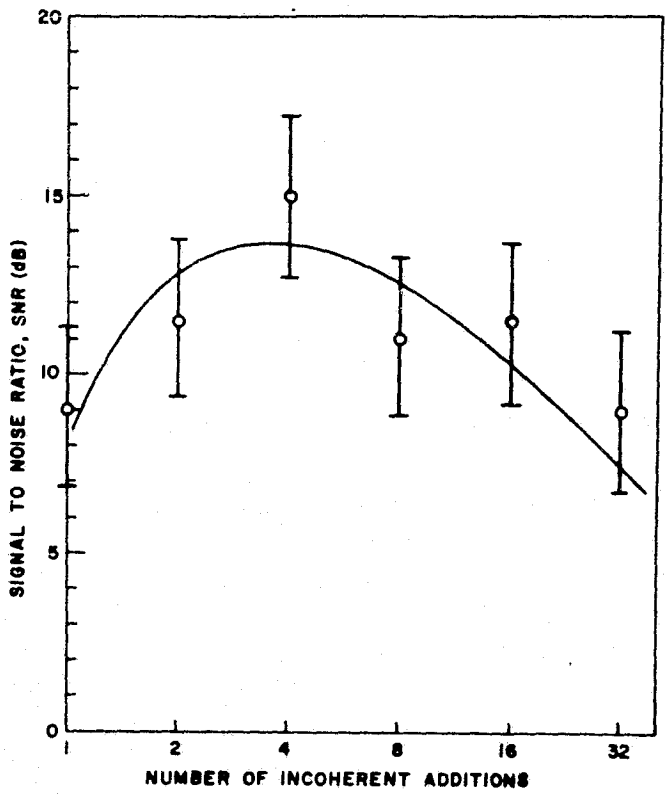

(c) Dichromated Gelatin

FIGURE 2-20. SNR VERSUS NUMBER OF INCOHERENT ADDITONS: SPATIAL FREQUENCY MULTIPLEXING

the image contained 1.6×10^6 resolution elements.

The peak SNR for the recording materials used in this investigation are 15 dB, 17.5 dB, and 15 dB for the HR emulsion, the Lippmann emulsion, and the dichromated gelatin, respectively. For more than about four incoherent additions, the SNR decreases at a rate somewhere between 10 dB per decade and -20 dB per decade. In this region, the main source of noise is the fine structure within the volume of the recording material. In the case of photographic emulsions the noise is caused by the silver halide grains, while for dichromated gelatin a probable source is precipitated gelatin resulting from rapid dehydration by alcohol during processing. The SNR reaches a maximum value at approximately four incoherent additions and then decreases This behavior is due to the fact that two sources of noise are present: scattering noise as discussed above and nonlinear noise. The nonlinear noise is associated with the hologram recording process and arises because the response of the recording medium is not strictly linear.

2.3.4 Discussion

The data presented in the preceeding section merits some discussion because incoherent addition of holograms should cause the SNR per hologram to decrease inversely as the square of the number of incoherent additions (at -20 dB per decade). However, our results show that this functional relationship is not always satisfied. This suggests that the Bragg effect influences the SNR when incoherent addition recording techniques are used.

An analysis of the situation reveals the following:

1. the total modulation of the hologram M_T is

$$M_T = \frac{2\sqrt{K}}{(K+1)\sqrt{n}} \left[1 + \frac{\sigma_s^2}{2K \langle I_s \rangle^2} \right]^{\frac{1}{2}}$$

and

2. the modulation per hologram, M_H is

$$M_H = \frac{2\sqrt{K}}{(K+1)n} \left[1 + \frac{\sigma_s^2}{2K<I_s>^2}\right]^{\frac{1}{2}} = \frac{M_T}{\sqrt{n}}$$

where $K = \frac{I_R}{<I_s>}$ is the reference to signal beam intensity ratio, n is the number of incoherent additions, $<I_s>$ is the average signal beam intensity, and σ_s^2 is the variance of the signal beam intensity. We have assumed that the reference beam intensities are constant and that the various signal beam intensities are statistically independent random variables having equal means and variances. Since the diffraction efficiency (and therefore the intensity) of the reconstructed signal beams is a function of the modulation, we expect from theoretical considerations that the SNR per hologram will decrease as $1/n^2$ for thin holograms.

We have experimentally verified that for a thin hologram the signal intensity per hologram decreases as $1/n^2$ while the total signal intensity falls as $1/n$. We did this by measuring the diffraction efficiency of two Fourier transform holograms of a diffusely-illuminated transparency. The first hologram was made with a single exposure. The second was recorded by partitioning the transparency and then making 18 incoherent additions.

For thick holograms, the problem is somewhat more complicated. To further investigate the anomalous results of our experiments we did the following:

1. We reconstructed each hologram with a normally incident plane wave, taking advantage of the symmetry of the frequency multiplexing format used for the recording process. This permitted n images at a time to be reconstructed. We measured diffraction efficiency as before and found that the signal intensity still decreased at a rate less than $1/n^2$. Moreover, the

diffracted intensity in this mode of readout was of the same order of magnitude as that obtained for the original measurements.

2. Using the same experimental geometry as before we repeated the initial experiment. However, this time, we did not rotate the plateholder, but instead introduced a random phase to each input signal by translating a piece of ground glass between exposures. We measured the intensity of each output signal as before. The results of these measurements are shown in Fig. 2-21. The $1/n$ dependence for the total signal intensity is clearly exhibited. This implies that each component hologram contributes $1/n^2$ of the diffracted intensity and taking them n at a time yields a net $1/n$ dependence.

3. We repeated the original experiment using both spatial frequency multiplexing and randomization of the input signal. The intensity of the diffracted signal beams again decreased at a rate less than $1/n^2$.

In every experiment we have performed where the Bragg effect was present and the incoherently superimposed holograms could be separated for individual measurement, we have found that the SNR per hologram falls off at a rate between $1/n$ and $1/n^2$.

We do not fully understand yet the reason why the decrease should not be exactly $1/n^2$ for incoherent additions of signals. It appears that the Bragg effect plays an essential role. The situation is extremely complicated since we must take into account the interactions between the reconstructing light field and the various allowed Bragg diffraction modes associated with each of the stored signals. Further analysis and experimentation are required before any conclusion can be reached.

2.4 MULTIPLE SIGNAL STORAGE BY VARYING THE WAVELENGTH OF THE RECORDING BEAMS

One of the distinctive properties of holograms recorded in three-dimensional media, when compared with conventional planar holograms, is that their inherent high angular and wavelength sensitivities provide high

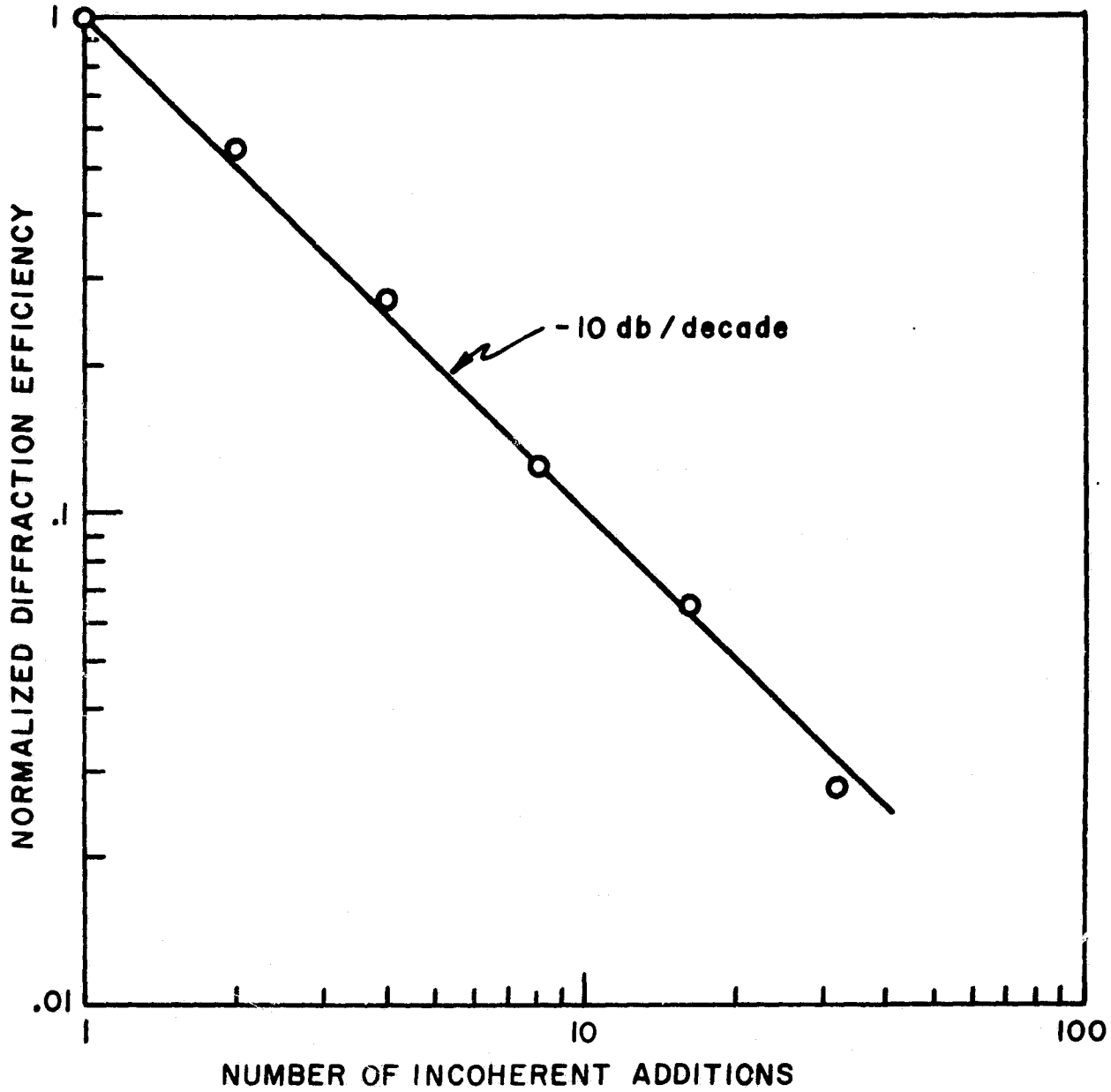

FIGURE 2-21. SNR VERSUS NUMBER OF INCOHERENT ADDITIONS: WITHOUT SPATIAL MULTIPLEXING

data storage capabilities. Both of these parameters can be effectively used to construct holograms which store a multiplicity of images, each separately stored uniformly throughout the recording medium. In the past we demonstrated (Ref. 5) the angular sensitivities of thick materials by holographically recording and subsequently retrieving 100 separate images with little or no interaction in between them. Here we report on recent experiments in which we used the wavelength sensitivity property of thick materials to holographically record a multiplicity of signals.

2.4.1 Experimental Procedure and Results

The experimental setup for recording and for readout of the holograms is similar to that shown in Fig. 2-18. The illumination source was an argon laser with a wavelength selector that gives a convenient adjustment for getting five discrete wavelengths from the laser (λ_1 = 457.9 nm, λ_2 = 476.5 nm λ_3 = 488 nm, λ_4 = 496.5 nm and λ_5 = 514.5 nm). Five different 35 mm photographic transparencies served as the input signals. Each of the signals was diffusely illuminated with a different wavelength and holographically recorded in a silver-halide photochromic glass (1.6 mm thick). Figure 2-22 shows the five input signals, with their corresponding recording wavelengths, used in making the holograms.

We made five superimposed recordings sequentially and arranged them so that upon reconstruction, each image is formed in the same location. After each recording the laser wavelength was changed and the corresponding input signal was inserted into the signal path. We then illuminated the composite hologram successively with five collinear reconstructing beams, each of a different wavelength (as in recording). Two examples of the reconstructed imagery are shown in Fig. 2-23. These images are of high quality and, if the recording and readout arrangements are identical, each can be observed only when it is illuminated by the same wavelength that was used in the recording. The ghost images and attendant detrimental effects,

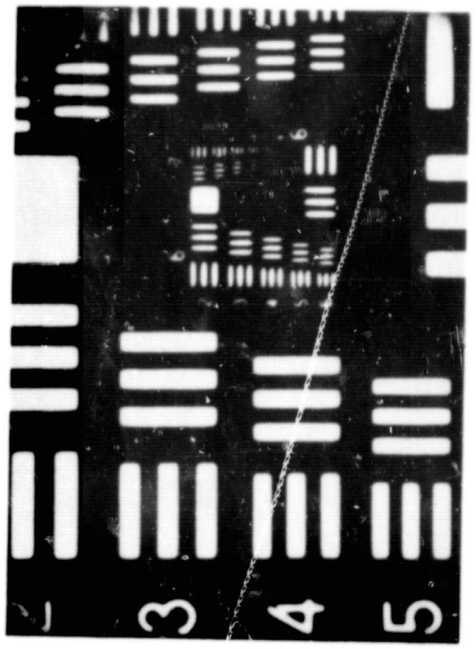

λ_1

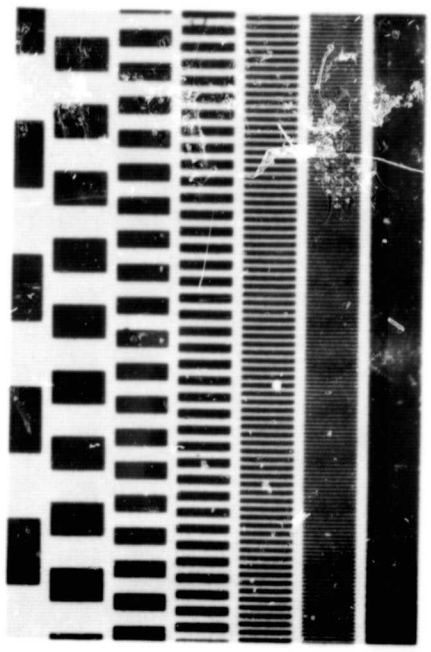

λ_2

λ_3

λ_4

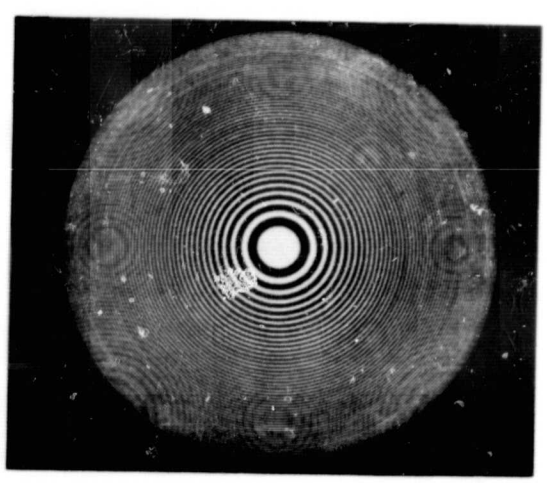

λ_5

FIGURE 2-22 ORIGINAL INPUT SIGNALS

85671-3

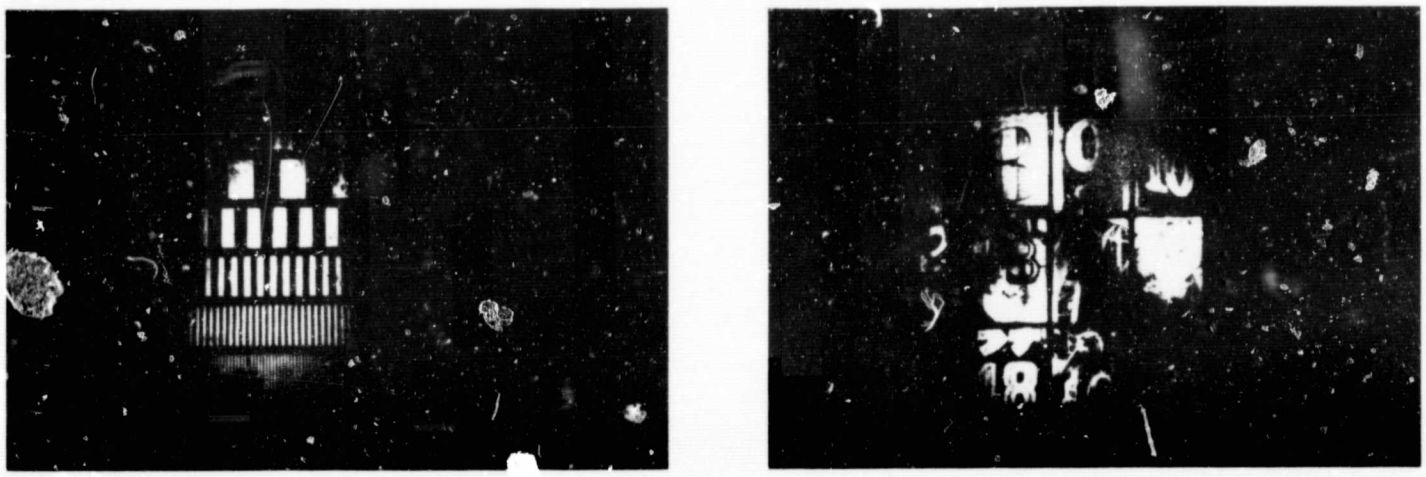

FIGURE 2-23 RECONSTRUCTED IMAGES FROM THICK HOLOGRAMS.

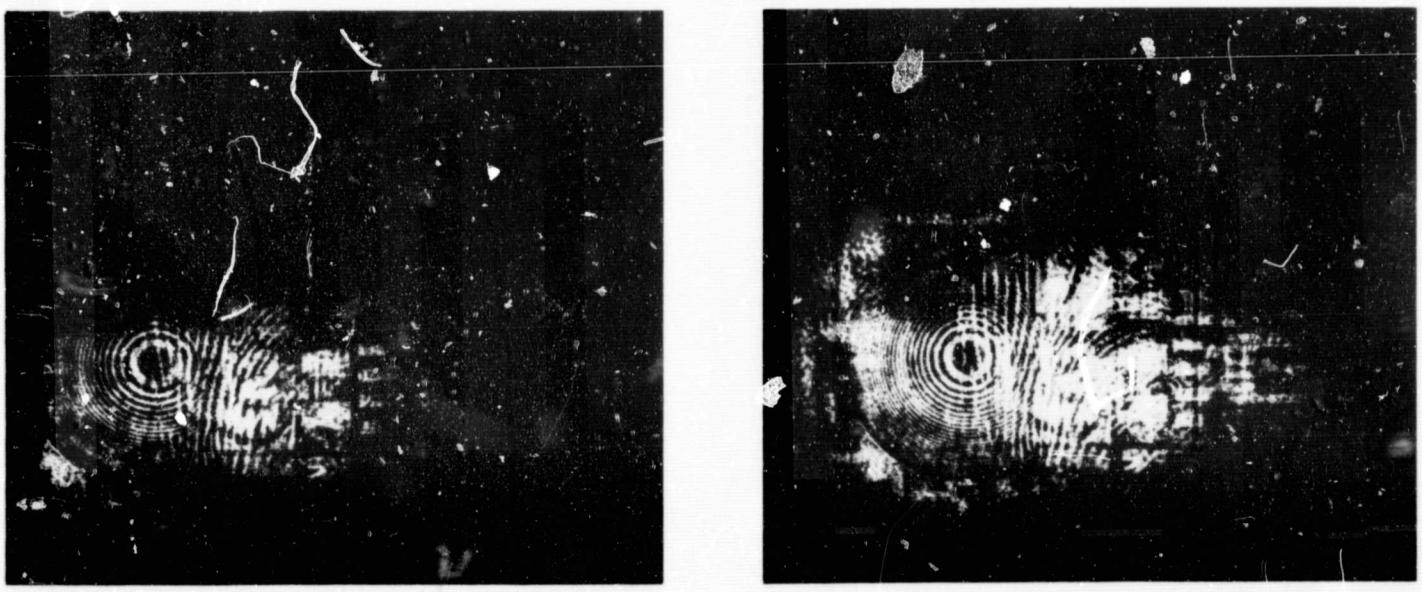

FIGURE 2-24 RECONSTRUCTED IMAGES FROM THIN HOLOGRAMS.

85671-4

normally associated with thin materials, are completely suppressed by the effect of the thick recording medium. For comparison, we used the same experimental setup to construct a similar composite hologram with relatively thin photographic plates (6 microns thick). As shown in the two photographs of Fig. 2-24, each reconstructed image contains four spurious images; these images overlap the desired image, producing a relatively poor reconstruction.

These results show that thick emulsions are needed if this type of data storage is to be useful.

SECTION III

HOLOGRAPHIC STORAGE MATERIALS

3.1 INTRODUCTION

In this section we review the fundamental properties of recording materials as they relate to a holographic storage system and we consider the problems of measuring and evaluating these properties for a general class of recording materials. These include both phase and absorptive materials which can be either thin or thick. We discuss the differences between the various types of materials and the merits of each one in an effort to find the most suitable material for our application.

The characteristics of a representative set of holographic recording materials are described in paragraph 3.3; we also present the procedures for testing these materials and our experimental results. Although we do not expect to use any of these materials in the final system, some of them have properties that make them useful as interim devices to check the other components of the optical memory.

In paragraph 3.4 the noise characteristics and their effects on the behavior of the holographic storage system are discussed in greater detail. In order to make the noise characteristics amenable to analysis, we develop a model for analytically determining the signal-to-noise ratio (SNR) of the recording material. By way of an example we use thin photographic emulsions as the recording materials and support the analysis with extensive experimental results.

The analytical results of the noise characteristics of photographic emulsions are then extended to show the effects of the SNR on the achievable error rates and capacity in a holographic memory system. The theoretical development, which is presented in paragraph 3.4, assumes that the

hologram produces additive noise which can be represented by a complex Gaussian process with independent real and imaginary parts. The error rates and storage capacity are calculated as functions of the SNR and input data formats.

3.2 GENERAL DISCUSSION

We consider some fundamental properties of recording materials as they relate to holographic storage. These properties are (1) exposure sensitivity and spectral response, (2) diffraction efficiency, (3) resolution, (4) noise characteristics, and (5) angular orientation and wavelength discriminations. All of these must be measured and evaluated to determine the suitability of any recording material for use in a holographic storage system. In the following sections we describe the nature of these properties, their impact on the holographic process and methods for quantitatively measuring them; the results of the measurement programs are reported in the following section.

3.2.1 Exposure Sensitivity and Spectral Response

A basic property of recording materials is that exposure to suitable radiation produces a physical change. A photochromic crystal, for example, which is normally transparent, darkens when exposed to ultraviolet light; the darkening, or absorption, is a function of the exposure. Information is stored holographically as a spatial variation of absorption in the volume of the photochromic crystal. A more subtle change occurs for a phase material such as lithium niobate; in these materials exposure to light does not produce an effect that is visible by ordinary means. Changes in the index of refraction occur instead of darkening so that the information stored holographically is due to a spatial variation of refractive index in the volume of the crystal. It is important, therefore, to be able to specify the behavior of the recording material in terms of the resultant variation of either

absorption or index of refraction as a function of exposure.

The exposure sensitivity of the recording materials depends on factors such as (1) the type of material, (2) the wavelength of the exposing light, (3) the temperature, and (4) the intensity of the exposing light. The latter factor is important because some recording materials exhibit reciprocity failure. The exposure sensitivity of a recording material can be determined by direct experimental measurements. For an absorption material, such as a photochromic crystal, the procedure is (1) to expose the material with laser light of constant intensity for uniformly increasing time intervals, and (2) to measure the absorptance with low intensity laser light having the same wavelength as that used for the exposure. The same procedure is followed for different laser wavelengths to determine the spectral response of the material. These data, displayed graphically as absorptance versus exposure with wavelength as a parameter, are sufficient to specify the exposure sensitivity and spectral response of the recording material.

Reciprocity failure is investigated by exposing the recording materials with laser light at various intensity levels; the exposure time is varied so that the total exposure is constant. The variation of absorptance with intensity provides the required data for specifying reciprocity failure effects.

For phase materials, an indirect approach is required. We follow exactly the same procedures as outlined for the absorption materials but we use diffraction efficiency as the dependent variable instead of absorptance. To do this, simple grating holograms made by recording the interference pattern of two plane waves are recorded in the phase materials with fixed offset angles between the beams and a fixed reference-to-signal beam ratio. Each hologram is recorded with a different exposure and the corresponding diffraction efficiency is measured. With this modification in procedure, exposure sensitivity, spectral response, and reciprocity effects can be evaluated.

For this holographic storage application, we require that the recording material be sensitive to light of a relatively large number of discrete wavelengths. It might seem desirable that the sensitivity of the recording material should be the same for all wavelengths. Under actual operating conditions, however, it is preferable to match the response of the recording medium to the wavelengths and the intensity levels of available lasers so that better balance can be achieved.

3.2.2 Diffraction Efficiency

Diffraction efficiency is defined as the ratio of the reconstruction beam power that is diffracted by the hologram to the effective incident beam power. The effective beam power is obtained from the total incident beam power by subtracting light losses caused by reflection, by absorption, or by other factors extraneous to the essential nature of the hologram itself. The diffraction efficiency is a basic hologram parameter which is particularly important in the optical memory application, since it directly influences the power of the light source needed to obtain adequate output brightness.

To describe the diffraction process in thin recording materials we first characterize these materials in terms of their complex amplitude transmittance T_a versus exposure E. For a thin hologram amplitude grating the values of T_a are limited to the range of $0 \leq T_a \leq 1$. A sinusoidal grating is defined by the transmittance function

$$T_a(x) = \frac{1}{2} + \frac{m}{2} \cos\left(\frac{2\pi}{a} x\right) \qquad (3\text{-}1)$$

where m represents the peak to peak change of amplitude transmittance and a is the grating period.

If the grating represented by Eq. (3-1) is illuminated by a monochromatic plane wave normal to the grating, it will diffract equally into two orders.

The amplitude of each diffracted order is one fourth of the incident wave times the modulation factor, m. The corresponding efficiency is

$$D.E. = \frac{I_{diffracted}}{I_{incident}} = \left(\frac{m}{4} \right)^2$$

Since the range of m is confined to $0 \leq m \leq 1$, the maximum diffraction efficiency for a sinusoidal amplitude grating is 1/16 or 6.25 percent.

A sinusoidal thin phase grating is mathematically described by the transmittance function

$$T_a(x) = \exp\left\{ -j \left[\phi_0 - \phi_1 \cos\left(\frac{2\pi}{\alpha} x \right) \right] \right\} \qquad (3\text{-}2)$$

where ϕ_0 represents the average phase delay through the grating and ϕ_1 represents the amplitude of the fluctuating phase delay.

If the grating represented by Eq. (3-2) is illuminated by a monochromatic plane wave normal to the grating, it will diffract into many orders. However, only the wave diffracted into order one (or minus one) is of primary interest in holography, since only this wave contributes to the reconstruction of the original wavefront.

The analysis can be simplified by use of the identity

$$\exp\left(j\phi_1 \cos \frac{2\pi}{\alpha} x \right) = \sum_{n=-\infty}^{\infty} j^n J_n(\phi_1)\, e^{jn \frac{2\pi}{\alpha} x} \qquad (3\text{-}3)$$

where J_n is the Bessel function of order n. From Eq. (3-3) we find that the amplitude of either of the first diffracted orders is given by $J_1(\phi_1)$. The maximum of $J_1(\phi_1)$ occurs at $\phi_1 = 1.9$ and is given by $J_1(1.9) = .582$. The

maximum diffraction efficiency of a thin sinusoidal phase grating is then given by $(.582)^2 = .339$ or 33.9 percent.

The diffraction process of holograms recorded in thick media is more complex than for conventional holograms recorded in thin media. Thick holograms reconstruct with maximum efficiency only if the reconstructing wave is incident from a direction satisfying the Bragg condition which, for fringes normal to the hologram surface, gives the required angle of incidence θ as

$$\sin \theta = \lambda / 2d$$

where λ is the illumination wavelength and d is the period of the fringe surfaces. For light incident at this angle, we can derive the diffraction efficiency relations for both thick absorption and phase recording media.

For the case of simple grating holograms recorded as a fluctuation of the absorption coefficient (such as thick photographic emulsions and photochromic crystals) the diffraction efficiency can be given as (Ref. 6)

$$\eta = \exp (\mu_0 t_0 / \cos\theta) \sinh^2 (\mu_1 t_0 / 2 \cos\theta) \qquad (3\text{-}4)$$

where $\mu_0 / 2$ is the average absorption, μ_1 is the amplitude of the sinusoidal absorption fluctuations, and t_0 is the thickness of the recording medium. The maximum diffraction efficiency is obtained when $\mu_0 / 2 = \mu_1$, i.e., when the hologram is completely transparent at the absorption minima. Using this condition in Eq. (3-4), we can show that the maximum theoretical diffraction efficiency is 1/27 (3.7 percent). We have experimentally achieved this maximum diffraction efficiency with thick photographic emulsions

For the case of simple grating holograms recorded as fluctuations of the index of refraction in phase materials such as dichromated gelatin and lithium niobate crystals, the diffraction efficiency is given as (Ref. 7)

$$\eta = \sin^2\left(\frac{\pi n_1 t_o}{\lambda \cos\theta}\right) \tag{3-5}$$

where n_1 is the fluctuation of the index of refraction. Eq. (3-5) shows that thick phase holograms can achieve a theoretical maximum diffraction efficiency of 100 percent when $n_1 t_o = \frac{1}{2}\lambda \cos\theta$. We have achieved experimentally measured efficiencies of 95 percent in holograms recorded in a thick phase material such as dichromated gelatin.

Besides allowing high diffraction efficiencies, the low absorption of phase materials is advantageous because they can be illuminated non-destructively with high intensity readout beams. This is particularly important in recording formats where each hologram is small and a high output intensity is required. For example, an illumination energy of 200 millijoules on a 1 mm hologram may destroy the information if the recording media is highly absorptive.

The diffraction efficiencies discussed above are for simple holograms in which both the reference and signal beams are plane waves. The situation is more complicated when the signal is made up of many plane waves, as would be the case for a coherently illuminated digital array. The situation is even more complex when we incoherently record a number of such signals in one hologram. The diffraction efficiency is reduced and the high values noted earlier can no longer be achieved.

To experimentally evaluate the diffraction efficiency of the recording media for this application we record simple interference gratings using plane waves for both reference and signal beams, and vary the following

recording parameters: (1) the illumination wavelength, (2) the ratio of the reference beam intensity to object beam intensity, and (3) the exposure levels. We then measure the diffraction efficiency as a function of these recording parameters. Using the results of these preliminary experiments, we can determine the diffraction efficiency, for different wavelengths, using transparencies of digital arrays as the input objects while maintaining an optimum ratio of reference beam to signal beam intensities and the best exposure level.

3.2.3 Resolution

Two aspects of resolution merit discussion: recording material resolution and holographic image resolution. We will discuss their meanings separately.

The resolution of the recording material is a partial measure of the ultimate storage capacity of the recording material. In a physical sense, it is a measure of the finest spatial variation of intensity to which the recording material responds with an unambiguous change in either absorptance or index of refraction. Finally, the resolution of a recording material is determined solely by the physical characteristics of the material, it is not a function of external system configurations.

Recording material resolution is usually evaluated by imaging sine wave gratings having different spatial frequencies and contrast ratios onto the material. This approach can be used for spatial frequencies up to about 1000 lines/mm to determine the modulation transfer function (MTF) of the material. However, holography often requires a recording material whose frequency response extends to 3,000 lines/mm or more. Obviously, the usual methods for measuring the MTF are inadequate. Hence, we evaluate the resolution of recording material by using plane wave gratings because (1) the spatial frequency of the grating can be varied by changing the offset

angle between the beams or by changing the wavelength, (2) very high spatial frequencies can be generated, and (3) the variations of the measured diffraction efficiency with spatial frequency gives a direct measure of resolution. The relationship between the spatial frequency and the angle between the two beams is $\nu = 2 \sin(\theta/2)/\lambda$ where ν is the spatial frequency, θ is the offset angle, and λ is the recording wavelength. If, for example, θ is 60° and λ is 500 nm, then ν is 2,000 lines/mm. The diffraction efficiency depends on the effective modulation level which, in turn, depends upon the resolution of the recording material; thus, diffraction efficiency is a direct measure of the resolution of the material.

In the experimental procedure we (1) construct an experimental configuration for producing two uniform plane waves, (2) record grating holograms with increasing spatial frequencies by varying the offset angle between the beams, and (3) measure the diffraction efficiency of each of the holograms. Care is taken to provide a constant exposure for each hologram and the input modulation level is held constant. A plot of diffraction efficiency as a function spatial frequency is generated to specify the recording material resolution.

The resolution of the reconstructed image (as distinguished from the resolution of the recording material) is a function of recording geometry and the resolution and size (aperture) of the holographic recording material. By image resolution we mean the finest detail which can be observed in a projected holographic image. Noise generated by the recording and reconstruction processes and by the recording material also affects image resolution. We evaluate image resolution by holographically storing an Air Force resolution target in the recording materials. The real image of the resolution target is projected onto a viewing screen. Image resolution is studied as a function of (1) type of material, (2) wavelength,

(3) ambient light level, (4) image brightness level, (5) type of viewing screen, and (6) hologram recording geometry.

3.2.4 Noise Characteristics

The quality of the image reconstructed from a hologram is dependent on the characteristics of the noise generated by the recording material. Noise from two sources is commonly observed in the image. One type of noise, which is random in nature, is the scattered light caused by the recording material. For photographic emulsion, the scattering of light is due to the granular structure of the silver halide particles in the emulsion (Ref. 8). Similar scattering noise is produced by photochromic materials as well as by dichromated gelatins and other phase materials. The second type of noise is produced by the nonlinearities of the recording materials (Ref. 9); this noise depends on the exposure characteristics of the recording material, the reference-to-signal beam ratio and the specific objects recorded in the recording material. These two types of noises are present in all reconstructed images; however, their severity can usually be controlled by an appropriate selection of the recording parameters.

A measure of the severity of the noise in the reconstructed image is given by the signal-to-noise ratio, defined as the ratio of the average energy of the image to the variance of the fluctuation of the noise processes. In using coherent optical systems, we find that a better measure is given by the ratio of the signal intensity to the average noise intensity, because this ratio can be conveniently measured experimentally.

To experimentally measure the signal-to-average noise intensity ratio, we holographically record a test signal which is located approximately 50 mm from the hologram. A series of holograms is recorded at various exposure levels, different reference-to-signal beam intensity ratios, and different angles between the reference and signal beams.

Two kinds of test signals are generally used in these experiments. One is a point object, obtained by focusing a collimated beam onto a pinhole. In using this test signal, the only noise process affecting the reconstructed image is the scattering of the light by the recording material. Thus, we can determine the ratio of the signal intensity to the average intensity of scattered noise. To study the combined effects of the two noise processes, we use a diffusely illuminated aperture with an opaque area in the center as the test signal. In the readout process, a scanner-photomultiplier assembly is used to detect the real image of the test signal; the output from the photomultiplier is then recorded on a chart recorder. From these experimental data we can obtain the signal-to-average noise intensity ratio as a function of exposure, of reference-to-signal beam ratio, and of the angle subtended by the reference and signal beams.

We have successfully used this procedure to measure the noise characteristics of photographic emulsions and dichromated gelatins. From the experimental results we found that we could predict not only the severity of the noise in the reconstructed image, but also the storage capacity of the photographic emulsion due to the limitation of the noise.

3.2.5 Angular Orientation and Wavelength Discrimination

For holograms recorded in thin media, a change in the readout beam wavelength or angle of incidence generally results in aberrations, distortions, and a displacement of the reconstructed image. The intensity of the diffracted image is relatively constant over a wide range of wavelengths and angular orientations. Thus, when a multiplicity of images are holographically stored in one location, we cannot selectively readout one hologram without interacting with the others. Such interaction causes degradation of the SNR of any one reconstructed image.

For holograms recorded in thick media, however, a change in the wavelength or the direction of the readout beam produces a change in the diffraction intensity from a hologram. These parameters can therefore be used to construct a hologram which stores a multiplicity of images, each image stored uniformly throughout the recording medium.

The angular discrimination available from thick holograms imposes a limitation on the number of holographically stored signals. A measure of the angular orientation sensitivity is the angular width between the half power points of the curve of diffracted intensity versus readout beam angle. An expression for this angular width, derived by adapting existing X-ray diffraction theory, is given by (Ref. 6)

$$\Delta\theta_{\frac{1}{2}} = \sqrt{\frac{\ell n 2}{\pi}} \; \frac{2\lambda}{t_o} \; \frac{(n^2 - \sin^2\theta_r)^{\frac{1}{2}} (n^2 - \sin^2\theta_s)^{\frac{1}{2}}}{\cos\theta_r [\sin\theta_s (n^2 - \sin^2\theta_r)^{\frac{1}{2}} + \sin\theta_r (n^2 - \sin^2\theta_s)^{\frac{1}{2}}]} \qquad (3\text{-}6)$$

where n is the index of refraction, t_o is the thickness, λ is the wavelength of the illumination, and the incidence angles of the reference and signal beams relative to the hologram are denoted by θ_r and θ_s, respectively. This equation can be used to calculate the angular orientation sensitivity as a function of hologram thickness and as a function of reference beam and signal beam orientations.

We have experimentally tested the angular discrimination of photographic emulsions, photochromics and ferroelectric materials, and have found that the results are in agreement with calculated values derived from Eq. (3-6). Photographic plates having an emulsion thickness of 15μ require an average change of orientation of 10° between each successive image to prevent significant interaction between images. The angular orientation sensitivity is quite low for small offset angles but increases with larger

offset angles. Since the available angular orientation for recording a conventional hologram is 180°, we cannot store more than 18 images without interference.

The number of stored images can be increased by two or three orders of magnitude with existing photochromic and ferroelectric materials because of their greater thicknesses. We have demonstrated the feasibility of this technique by holographically recording a multiplicity of diffusely illuminated transparencies on a photochromic sample and reconstructing them with essentially no interference. Typical results indicate that separate images can be holographically recorded in a 4 mm thick crystal merely b rotating the plate two minutes of arc between each recording.

A measure of wavelength discrimination is the wavelength bandwidth between the half-power points on the curve of diffracted intensity versus readout wavelength. An expression for this bandwidth was derived by adapting existing X-ray diffraction theory and is given by (Ref. 6).

$$\Delta\lambda_{\frac{1}{2}} = \frac{\sqrt{\frac{\ell n 2}{\pi}}\ \lambda^2 (n^2 - \sin^2\theta_s)^{\frac{1}{2}}}{t_o\left[n^2 - (n^2 - \sin^2\theta_s)^{\frac{1}{2}} (n^2 - \sin^2\theta_r)^{\frac{1}{2}} + \sin\theta_s \sin\theta_r \right]} \qquad (3-7)$$

where the various parameters were defined earlier. Eq. (3-7) can be used to calculate the wavelength sensitivity as a function of hologram thickness and as a function of reference beam and signal beam orientations.

The wavelength sensitivity of thick holograms was used successfully to reconstruct multicolor signals with no degrading ghost images. Although we used only five primary wavelengths in the experimental demonstration, we have calculated that independent images can be recorded by varying the wavelength for each exposure by only a few angstroms. The development of frequency-tunable lasers has progressed sufficiently so that the wavelength

sensitive property of thick holograms is very attractive for dense holographic storage.

A problem related to the angular and wavelength discrimination properties is the shrinkage of the three-dimensional recording media. Shrinkage generally causes a change in both the orientation and the spacing of the fringe surfaces in the hologram so that either the orientation or the wavelength of the reconstructing beam must be altered to maximize the diffracted intensity. In both instances, the location of the reconstructed image also changes. In photographic materials, shrinkage is caused by chemical processing. In photochromic crystals shrinkage occurs when the read-in and read-out operations are performed at different temperatures.

In earlier investigations we found that the required reorientation is not a function of crystal thickness; however, the thickness parameter does play an important role. When complex gratings containing many fringe systems are recorded, the shrinkage effects vary the fringe spacings so that the Bragg relation cannot be simultaneously satisfied for all fringe systems, resulting in a nonuniform image intensity. As the thickness of the crystal is increased, this problem is more severe because the angular orientation sensitivity increases.

3.3 EXPERIMENTAL INVESTIGATIONS OF HOLOGRAPHIC RECORDING MATERIALS

In this section we give a summary of the properties of several holographical materials which we have considered in the course of this contract. These materials include thick photographic emulsions, thick dichromated gelatins, photochromics, ferroelectric crystals, manganese bismuth, photopolymers, photoresist and photoplastics. Although none of these materials possess the necessary characteristics to be useful in the final system, most can be used as interim devices or as aids in testing other components of the system.

In the following paragraphs we list the advantages and current disadvantages of each of these materials, with particular emphasis on those properties that have been discussed in paragraph 3.2. Along with these lists we also present the results of our experiments which were primarily designed to test the exposure characteristics, diffraction efficiency and angular discrimination of these materials.

We start by describing the general procedures of our experiments and then separately discuss the merits and the experimental results for each recording material. In general, the experiments were not exhaustive but were designed to give accurate indications of the behavior of the materials for holographic applications.

3.3.1 Experimental Procedures

We have performed experiments to test the basic properties of some recording materials such as the exposure characteristics, diffraction efficiency and angular discrimination. The procedures for obtaining these measurements are described in the following paragraphs.

3.3.1.1 Experimental Procedure for Determining Exposure Sensitivity

To determine exposure characteristics of absorptive recording materials, we begin by uniformly exposing the materials through a 1 cm diameter aperture. A series of exposures, with different exposure levels or wavelengths or both was made for each material. After appropriate development, each exposed area was again illuminated with a uniform beam and we measured the incident beam I_i, the transmitted beam I_t, and the extraneous beam I_e. The extraneous beam is reflected and absorbed light. We then determined the optical density and the amplitude transmittance of the materials by using the following relations

$$\text{Optical Density} = D \triangleq -\log_{10} \frac{I_t}{I_i - I_e}$$

and

$$\text{Amplitude Transmittance} = T_A \triangleq \left(\frac{I_t}{I_i - I_e}\right)^{\frac{1}{2}}$$

By plotting either of these parameters as a function of exposure we obtain a characterization of the exposure sensitivities.

3.3.1.2 Experimental Procedure for Determining Diffraction Efficiency

To obtain the desired quantitative data, we recorded simple interference gratings by using monochromatic plane waves for both the reference and the signal beam. Depending on the recording material, we used the 363.8 nm and 488 nm lines of the argon laser of the 632.8 nm line of the He-Ne laser for both recording and readout.

The basic experimental setup is shown in Fig. 3-1. Light from the laser is divided by the beam splitter; one path is the reference beam having intensity I_r and the other path is the signal beam having intensity I_s. The pinhole assemblies and the collimating lenses are used to expand and collimate the laser beam. The interference pattern of the plane waves is recorded on the photographic plate. The normal of the plate bisects the angle θ between the two plane waves. The spatial frequency of the fringes, determined by the angle θ, is called the offset frequency of the recorded grating. We controlled the ratio of reference-to-signal beam intensity by inserting neutral density filters in either beam.

We also used this setup for measuring the relevant readout parameters, except that only one beam was used in the reconstruction process. To perform the measurements, we first used a readout beam from the direction of I_r and then used a beam from the direction I_s to check the measurements.

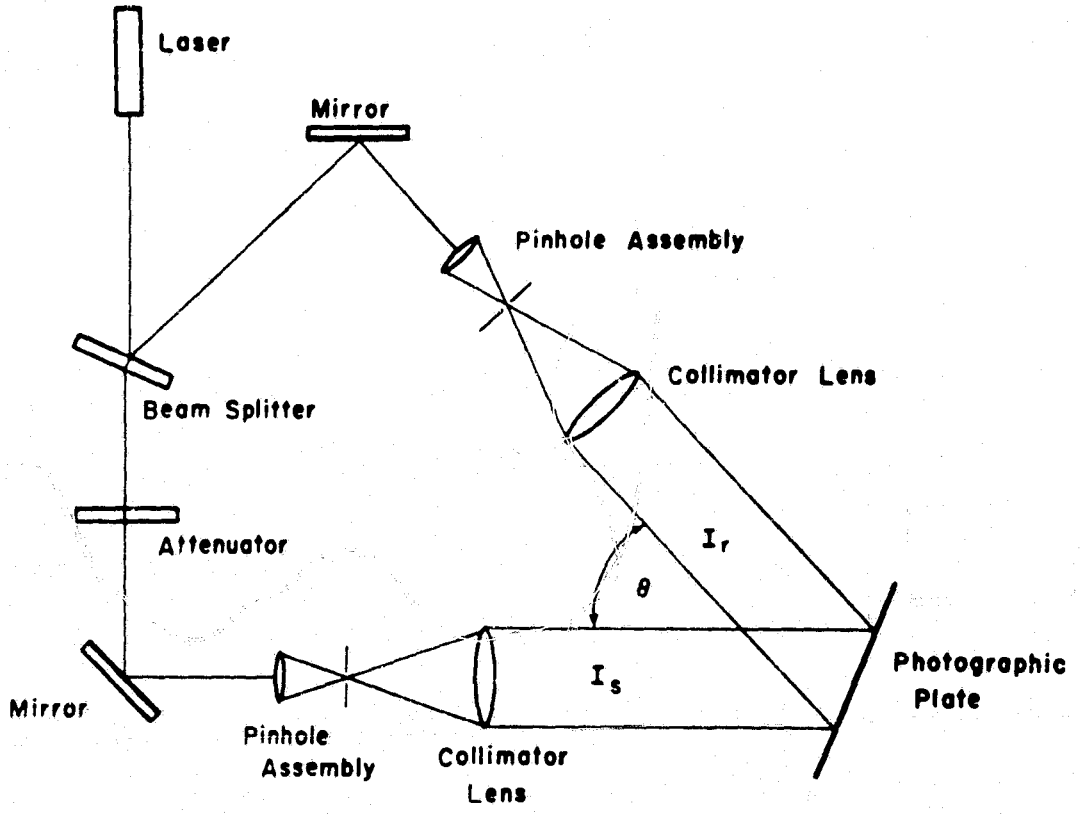

FIGURE 3-1. SETUP FOR DIFFRACTION EFFICIENCY MEASUREMENTS

In most instances, the measured results agreed within 10 percent.

The diffraction efficiency was determined by using the following relation

$$\text{Diffraction Efficiency} = \frac{I_d}{I_i - I_e}$$

We measured the diffraction efficiencies of different recording materials as a function of exposure levels and reference beam to signal beam intensity ratios. The results of these measurements will be described separately for the different materials.

3.3.1.3 Experimental Procedure for Determining the Angular Discrimination

The experimental set-up for recording and subsequently for measuring the angular orientation sensitivity of simple holograms is shown in Fig. 3-2. Light from the laser is split into two paths by the beam splitter, and diverted by the mirrors to the recording material. The interference pattern is recorded for various values of the angle θ between the two beams and for various angular orientations of the recording material with respect to the light beams. The orientation is adjusted by means of a motor driven platform, and the angle θ is changed by relocating the optical components.

During readout only I_r is incident on the recording material. The output of a photomultiplier, used to measure the intensity of the diffracted beam, is fed into a chart recorder through a logarithmic amplifier. By rotating the hologram at a constant rate, we can plot the relative intensity of the diffracted light as a function of the incidence angle of the readout wave.

We have experimentally listed the angular discrimination of photochromic and lithium niobate materials and the results are given paragraphs 3.3.4 and 3.3.5.

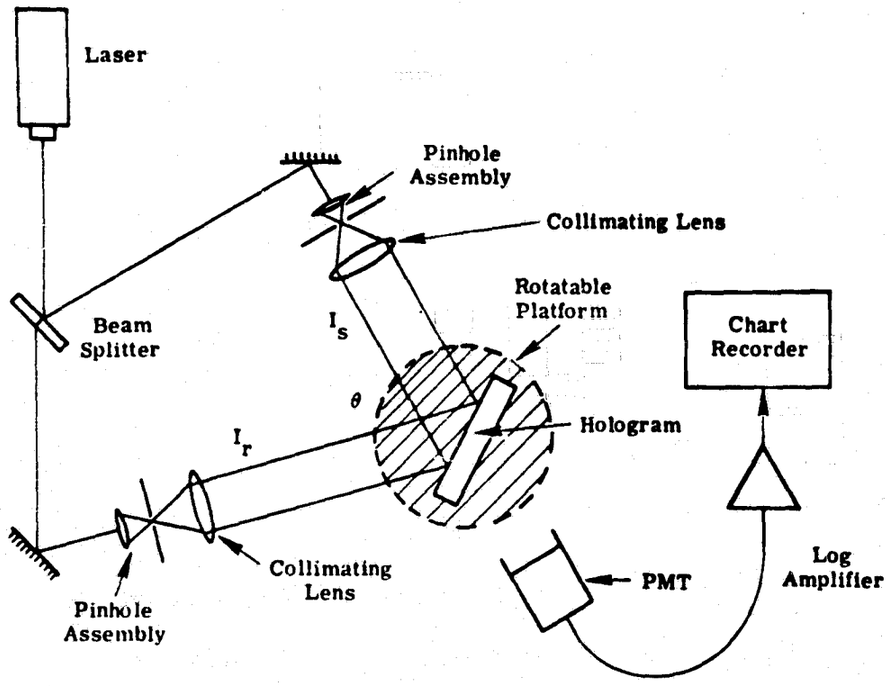

FIGURE 3-2. SETUP FOR ANGULAR ORIENTATION SENSITIVITY MEASUREMENTS

3.3.2 Photographic Emulsions

Photographic emulsions are the most common recording materials used in holography. In dense data storage applications only a small number of the available emulsions are suitable. These are referred to as high resolution or Lippmann emulsions. These emulsions are characterized as having high resolving power, extremely small grain size, and low exposure sensitivity. A brief summary of the advantages and disadvantages of fine-grain photographic emulsion is given in the following. The advantages are:

(1) very high resolution; many commercially available photographic emulsions have a resolving power in excess of 3,000 lines/mm. The latest Lippmann emulsions have an extremely small grain size and a resolving power which approaches that of photochromic crystals,

(2) relatively high speed; even very fine grain emulsions, considered to be slow by ordinary standards, require exposures that are orders of magnitude less than most of the other materials tested for use in optical memories,

(3) a large dynamic range; it is not uncommon for high resolution emulsions to have an 80 dB dynamic range,

(4) broadband spectral sensitivity; many high resolution photographic emulsions are available with uniform spectral sensitivity extending from 400 to 700 nm, and

(5) stability; these materials are archival if kept under suitable environmental conditions.

The disadvantages of photographic emulsions are:

(1) low diffraction efficiency; as with all absorption type materials, the maximum diffraction efficiency is only a few percent (chemical bleaching processes exist which can increase the practical diffraction efficiency to about twenty percent),

(2) chemical development; most photographic emulsions require a lengthy and sometimes complex developing process to make the stored information permanent, and

(3) limited thickness; the thickness is generally limited to 100 microns because of the dimensional stability of photographic emulsions and the difficulty associated with chemically developing through the entire thickness of emulsions; this imposes a limitation on the available storage capacity.

3.3.2.1 Experimental Results

The main emphasis in our investigations is to determine whether photographic emulsions are suitable for holographic recording in the UV light. The reason for using UV illumination is that the shorter wavelengths allow higher packing densities. We measured the exposure sensitivities and diffraction efficiencies for Kodak HR and 649 emulsions and Agfa Lippmann emulsions.

The UV illumination is derived from an argon laser by using specially coated reflecting mirrors and high plasma tube currents. Two spectral lines are emitted simultaneously, 351.1 nm and 363.8 nm. These lines were separated by means of an external 60° spectroscope prism. Because the 363.8 nm line has approximately three times more power than the 351.1 nm line we used it exclusively in our experiments.

We used the experimental procedure described in Section 3.3.1.1 to measure the exposure characteristics of the photographic emulsions; the results are shown in Figs. 3-3 and 3-4. The curves shown in Fig. 3-3 are the optical density variations as a function of exposure, whereas the curves in Fig. 3-4 are given as amplitude transmittance variations as a function of exposure. The trend for the exposure characteristics curves is similar to the conventional curves obtained with visible light. However, the

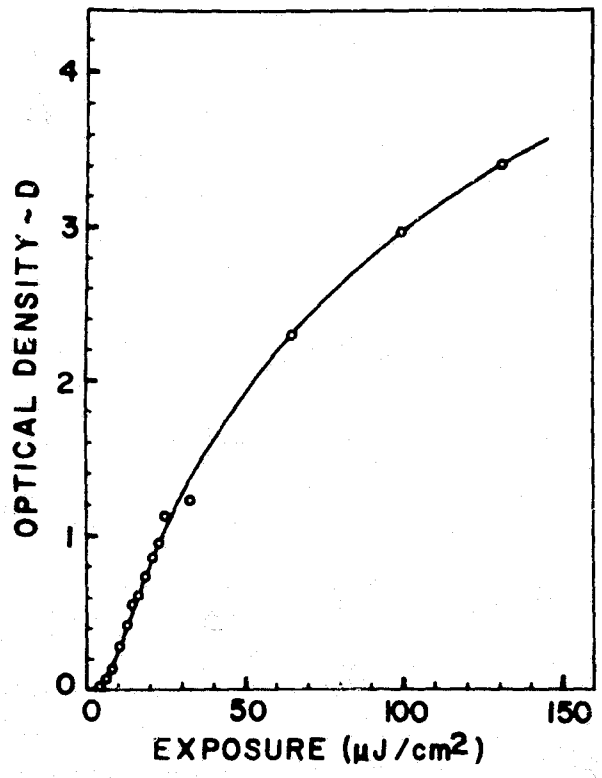

(a) HR Plate

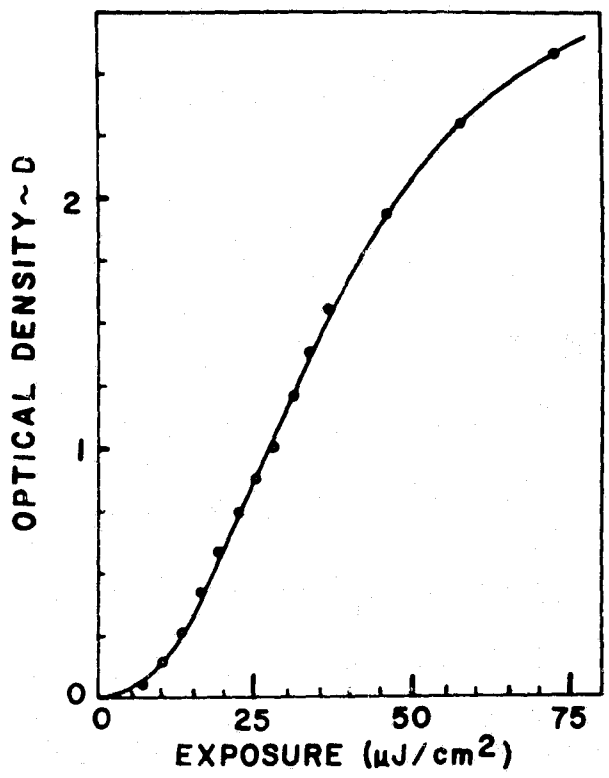

(b) 649F Film

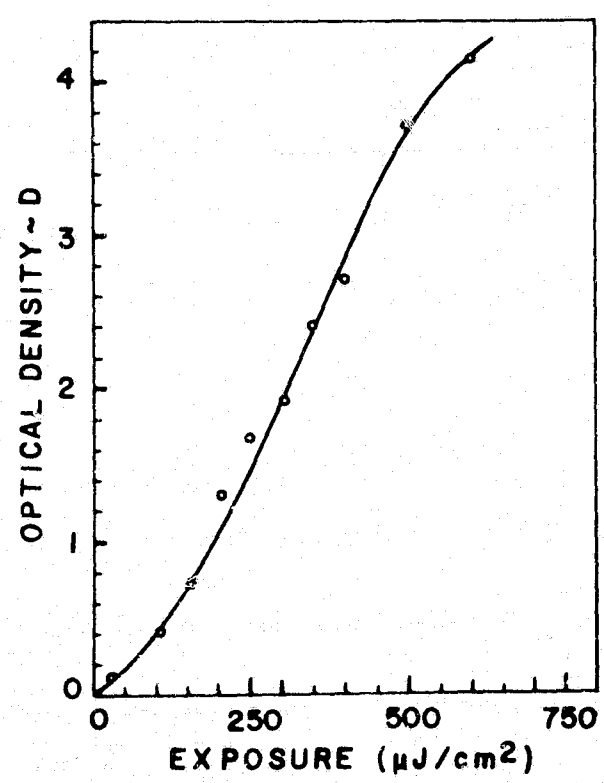

(c) Lippmann Emulsion

FIGURE 3-3. OPTICAL DENSITY VERSUS EXPOSURE FOR PHOTOGRAPHIC EMULSIONS

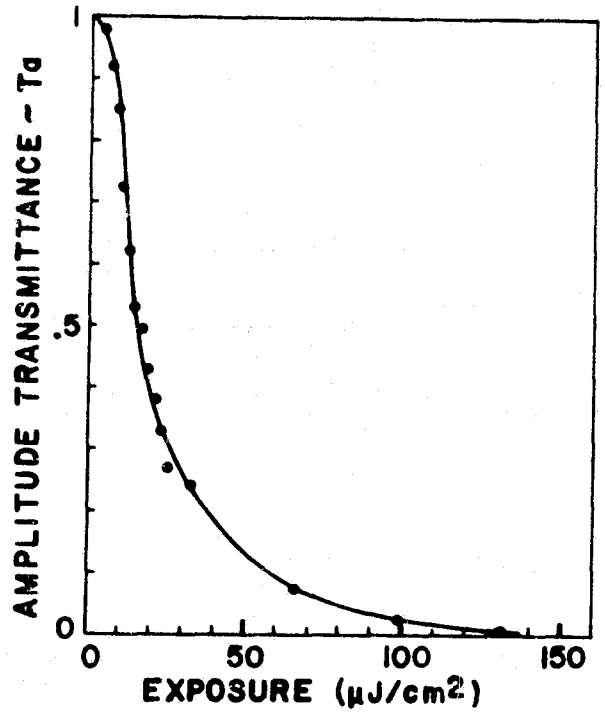

(a) HR Plate

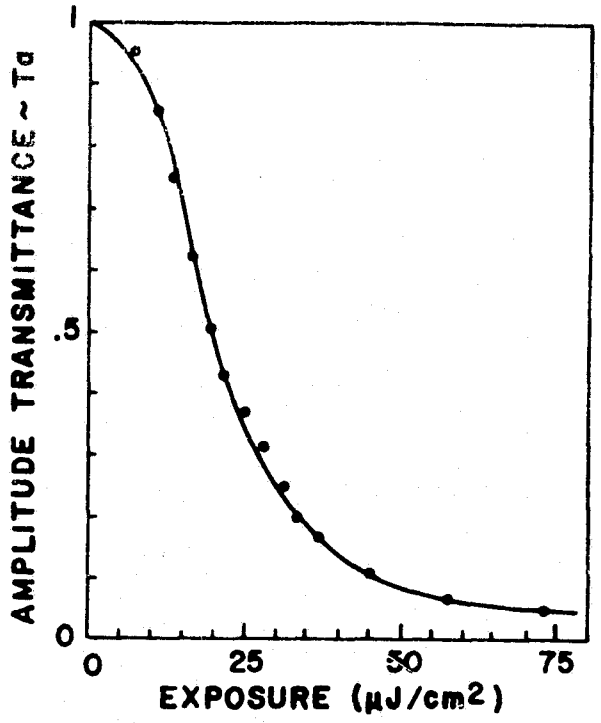

(b) 649F Film

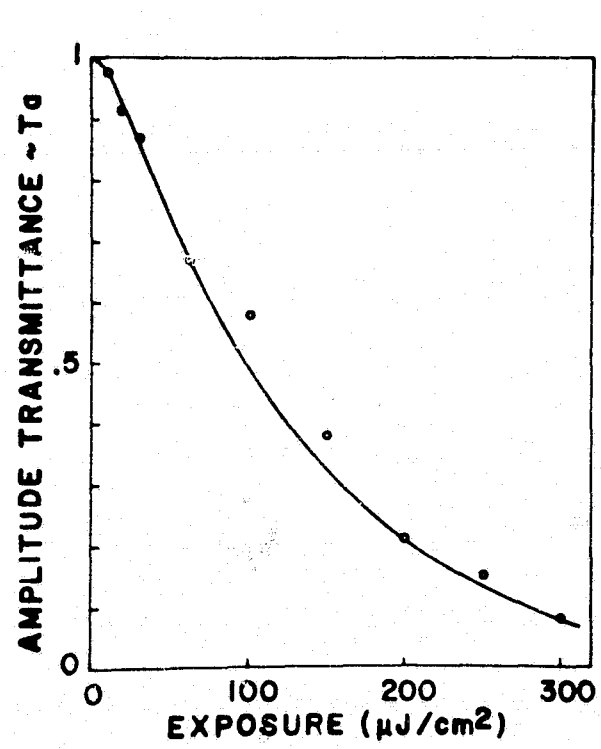

(c) Lippmann Emulsion

FIGURE 3-4. AMPLITUDE TRANSMITTANCE VERSUS EXPOSURE FOR PHOTOGRAPHIC EMULSIONS

exposure sensitivity has increased by a factor of five. We also note that the exposure sensitivity of the Agfa Lippmann emulsions is lower than that for the Kodak HR and 649F emulsions; this is due to the smaller grain size of the Agfa emulsions.

We also measured the diffraction efficiencies for the three emulsions by using the experimental arrangement and procedure described in paragraph 3.3.1.2. Fig. 3-5 shows the diffraction efficiencies as a function of exposure. In all cases the diffraction efficiency is lower than the efficiency of the same emulsions at visible light. This decrease in efficiency is primarily due to increased scattering in the emulsions at the lower wavelengths.

3.3.3 Thick Dichromated Gelatin

Recent work has shown that high quality holograms can be recorded in hardened gelatin films sensitized with dichromate solutions. Since the holograms are recorded as dielectric phase gratings, high diffraction efficiencies can be attained. Furthermore, light scattering from such materials is so low that relatively high signal-to-noise ratios can be achieved in the reconstructed image. The preparations of such materials for holographic recording is fairly straightforward; all that is necessary is to treat gelatin with a dichromate solution (either ammonium dichromate or potassium dichromate are suitable) for several minutes prior to exposure. The development process is also relatively simple. The advantages of dichromated gelatin are:

(1) it is pure phase material; losses due to absorption and scattering are typically only a few percent,
(2) high diffraction efficiency; hologram gratings have been recorded with diffraction efficiencies exceeding 85 percent.

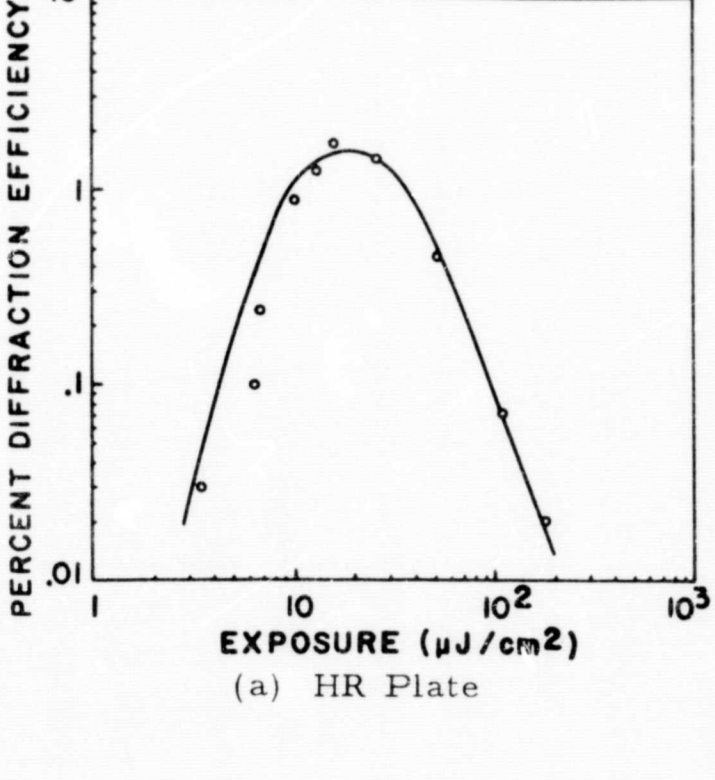

(a) HR Plate

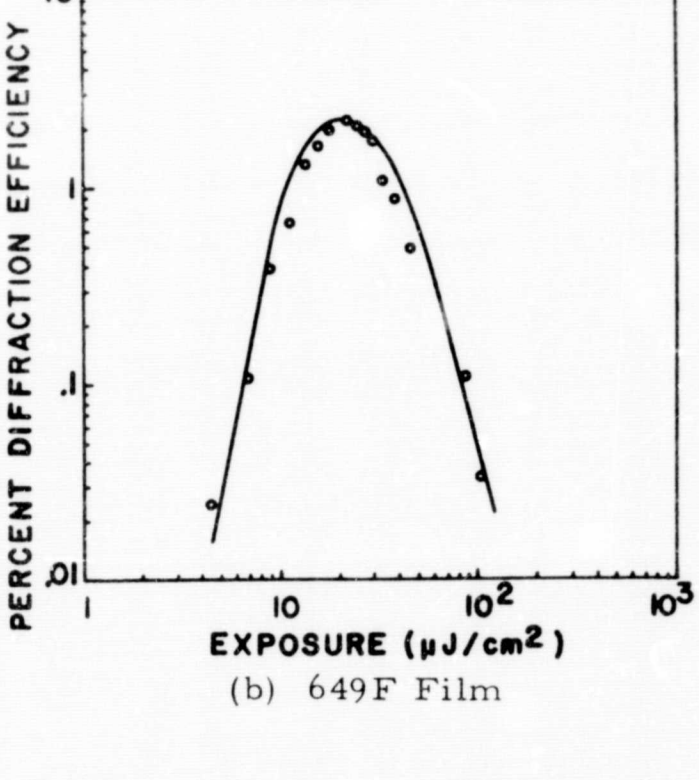

(b) 649F Film

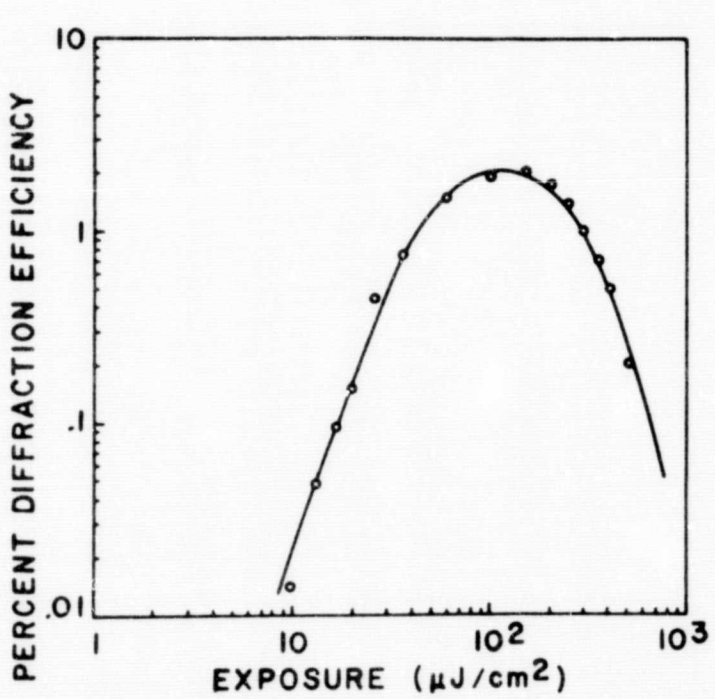

(c) Lippmann Emulsion

FIGURE 3-5. DIFFRACTION EFFICIENCY VERSUS EXPOSURE FOR PHOTOGRAPHIC EMULSIONS

(3) very high resolution; the resolution of dichromated gelatin has been experimentally shown to be in excess of 5,000 lines/mm,

(4) ease of preparation and processing; for preparation, a gelatin plate is soaked in a dilute solution of a dichromate salt and dried; development requires only a treatment with water and alcohol, and

(5) stability; the hologram recording is archival if the gelatin is kept in a low humidity atmosphere.

The disadvantages of dichromated gelatin are:

(1) limited spectral response; although dichromated gelatin is not sensitive to light whose wavelength is greater than about 520 nm, it may be possible to use dye sensitizers to extend the sensitivity to about 650 nm,

(2) short shelf life; after sensitization with the dichromate salt the gelatin undergoes a dark reaction so that the exposure must be made within one or two days (cold storage, however, may increase shelf life to many months),

(3) relatively poor exposure sensitivity; between two and three orders of magnitude less sensitive than photographic emulsions (exposure range is between 30 to 100 mJ/cm^2); however, it appears possible that with other development procedures the sensitivity can be increased by a factor of ten,

(4) environment sensitivity; if holograms recorded in dichromated gelatin materials are exposed to a high humidity atmosphere, a significant reduction in diffraction efficiency results and the imagery will suffer a loss of quality, and

(5) limited thickness; the thickness is generally limited to 100 microns because of the dimensional stability of the gelatin, thus imposing a limitation on the available storage capacity.

3.3.3.1 Experimental Results

We performed a series of experiments for investigating the merits of different gelatins; three types of gelatins of differing "hardness" were dichromated and the diffracting capabilities of each type were determined. Using the experimental arrangement and procedure described in paragraph 3.3.1.2, we measured the diffraction efficiencies of these materials as a function of exposure and reference-to-signal beam intensity ratios. The results are shown in Figs. 3-6 through 3-8. The results for the "soft" gelatin are shown in Fig. 3-6, the results for the "moderately hard" gelatin are shown in Fig. 3-7 and the results for the "hard" gelatin are shown in Fig. 3-8. Each curve in the figures is for a different reference beam to signal beam intensity ratio K; the offset angle is 30 degrees and the illumination wavelength is 488 nm. Note that the diffraction efficiencies are relatively high and that, in some instances, they approach the theoretical limit of 100 percent. Also note that we can achieve high diffraction efficiencies with a K value of 7 where the nonlinearities are not as severe as with K equal to 1; this yields high diffraction efficiencies with relatively higher S/N ratios. The high efficiencies which can be achieved with dichromated gelatin materials make them attractive for read-only holographic memories.

3.3.4 Photochromic Materials

Photochromic materials such as alkali halides glasses, potassium bromide (KBr) and potassium chloride (KCL) crystals, strontium titanate ($SrTiO_3$) crystals doped with Fe-Mo and Ni-Mo, calcium fluoride, and a variety of photochromic plastics have been successfully used to record holograms. These photochromics are absorptive materials that change color when illuminated with light of a suitable wavelength; this color change may be a permanent coloration (photocolor) or a permanent discoloration (photo-bleach), but in general the color changes are reversible either with light or heat. The advantages of photochromics are:

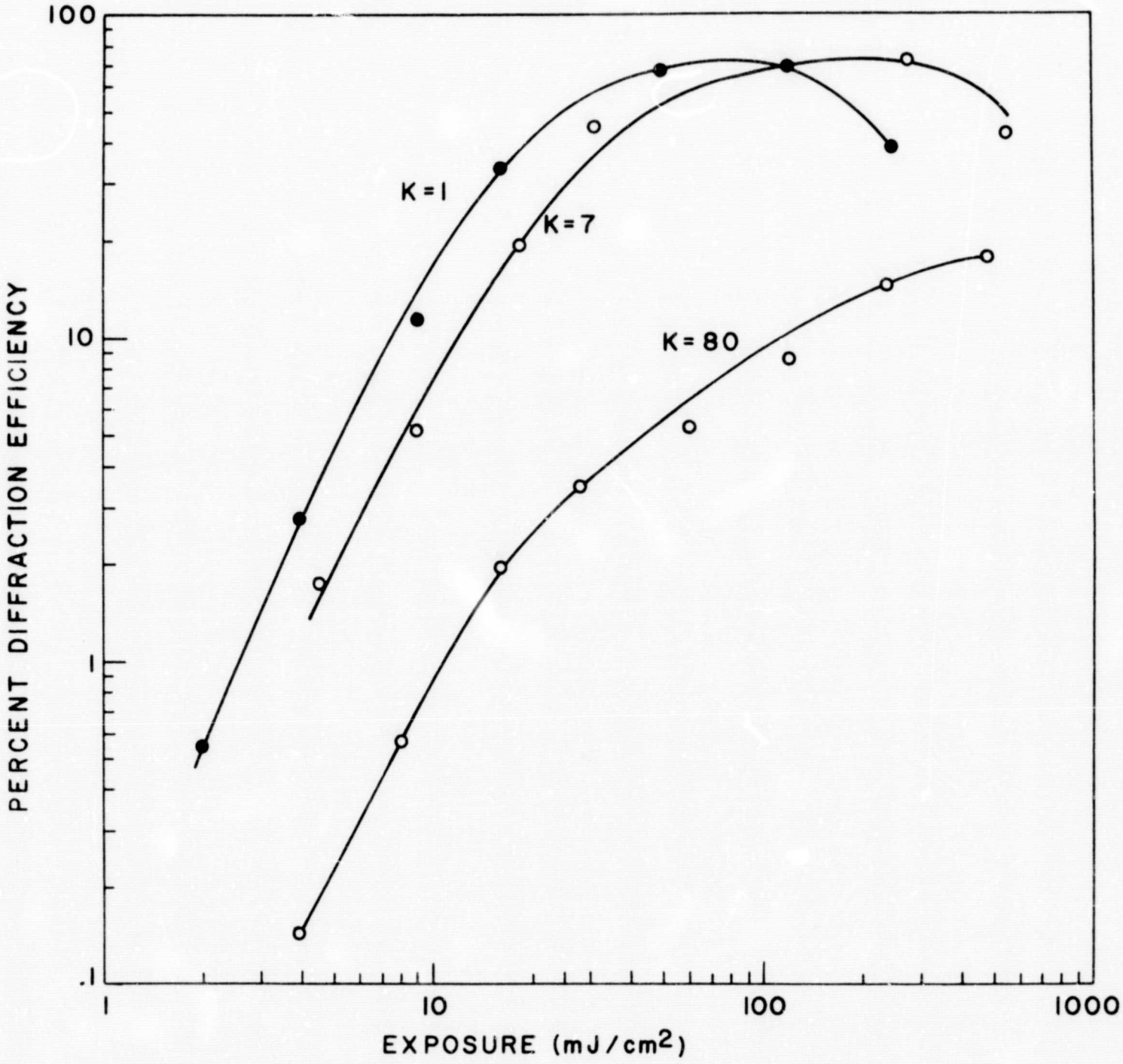

FIGURE 3-6. DIFFRACTION EFFICIENCY VERSUS EXPOSURE FOR "SOFT" DICHROMATED GELATIN

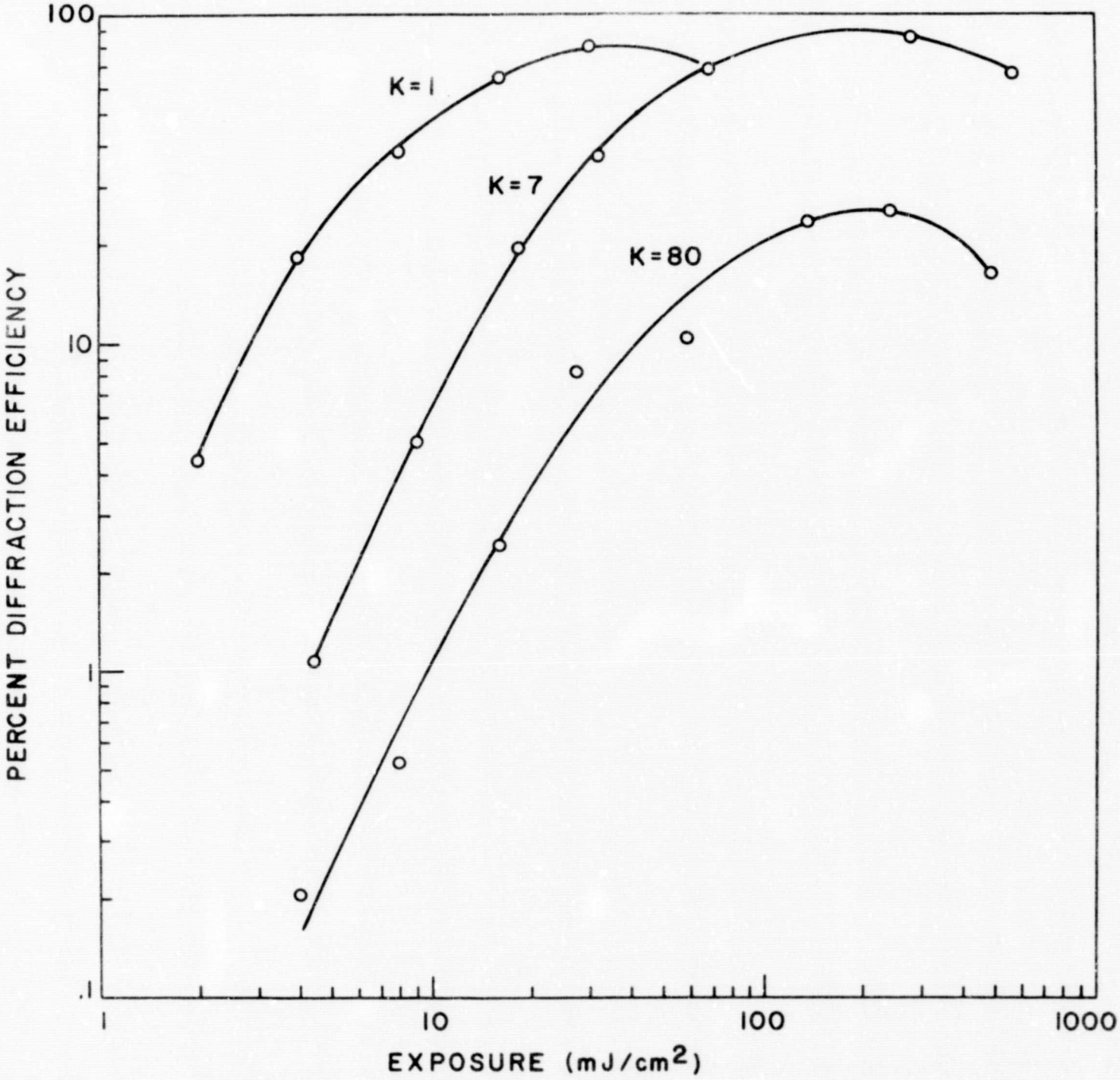

FIGURE 3-7. DIFFRACTION EFFICIENCY VERSUS EXPOSURE FOR "MODERATELY HARD" DICHROMATED GELATIN

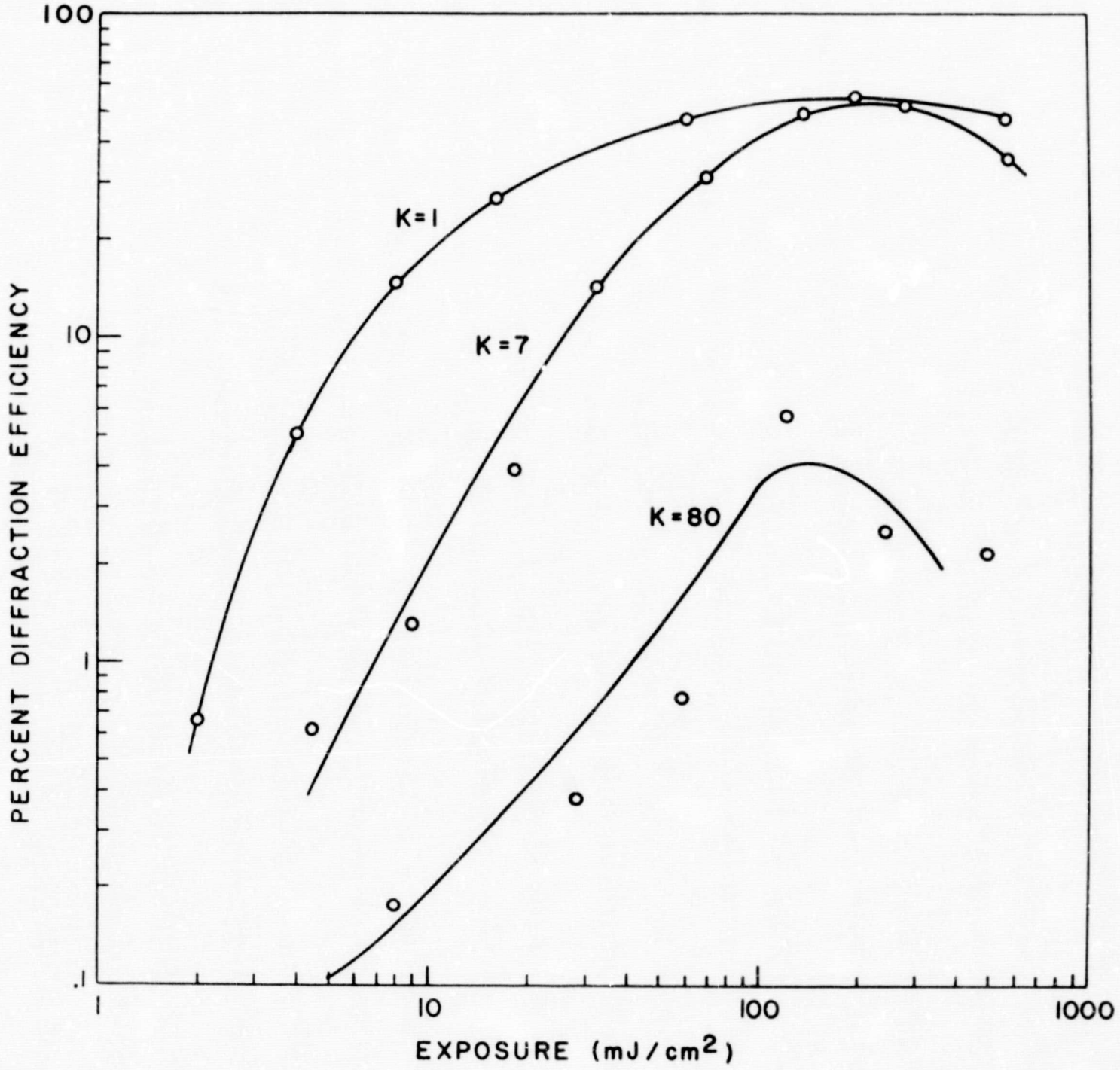

FIGURE 3-8. DIFFRACTION EFFICIENCY VERSUS EXPOSURE FOR "HARD" DICHROMATED GELATIN

(1) high resolution; resolution greater than 3000 lines/mm have been achieved and, because of its molecular structure, the attained resolution can be much higher than with conventional films whose silver grains are much greater than the size of photochromic molecules,

(2) reversability; some photochromics such as silver halide glasses can be recycled indefinitely,

(3) reasonable stability; exposure to light causes degradation of the recording but this is a relatively slow process at low ambient temperatures,

(4) high angular and wavelength sensitivities; the great thickness, e.g., 1 mm or greater, results in high angular and wavelength sensitivities on readout, thus allowing a large number of holograms to be recorded in the same volume but read out selectively, and

(5) no processing is required.

The disadvantages of photochromics are:

(1) very slow sensitivity; most inorganic photochromic materials are several orders of magnitude less sensitive than conventional photographic emulsions,

(2) low diffraction efficiency; generally less than one percent,

(3) poor thermal stability; the information is rapidly erased at temperatures ranging from 50° to 100° C, and

(4) poor spectral response; most photochromics are sensitive to only one or two of the primary colors.

3.3.4.1 Experimental Results

Our main motivation for investigating photochromic materials was to verify our theoretical angular discrimination predictions and determine what diffraction efficiencies are possible.

Using the experimental arrangement and procedure described in paragraph 3.3.1.3, we measured the angular orientation sensitivity of a 1.6 mm thick silver halide photochromic glass. The offset angle was 30 degrees with $\theta_r = \theta_s$, and the illumination wavelength was 488 nm. Fig. 3-9 shows the relative diffracted intensity as a function of incidence angle of the readout beam. The expected sinc function behavior is clearly evident in this experimental curve. The half power width of the angular orientation sensitivity curves was determined from the experimental data and compared with results calculated by using Eq. (3-6). In all cases good agreement between calculated and experimental results was observed. For the example of Fig. 3-9 the experimental half power width of the angular orientation is 2.9 minutes of arc whereas the calculated value is 2.91 minutes of arc.

We also measured the diffraction efficiency as a function of exposure levels and offset angles. The diffraction efficiency was relatively low and under no conditions did it exceed 0.3 percent.

3.3.5 Ferroelectric Materials

The ferroelectric materials, which include lithium niobate, barium titanate, and strontium barium niobate, offer several attractive features as a holographic storage medium. The ferroelectric material undergoes a change in refractive index upon exposure to relatively intense light and behaves as a pure phase, volume holographic recording. No processing is required and the recording can be thermally erased. High diffraction efficiency can be obtained but the material is relatively insensitive. The advantages of ferroelectric materials are:

(1) high resolution; recordings of up to 4000 lines/mm have been made;

(2) reversability; heating the material to about 170° C causes the recording to disappear and the material can be recycled (extensive data on fatigue effects, if any, is not yet available),

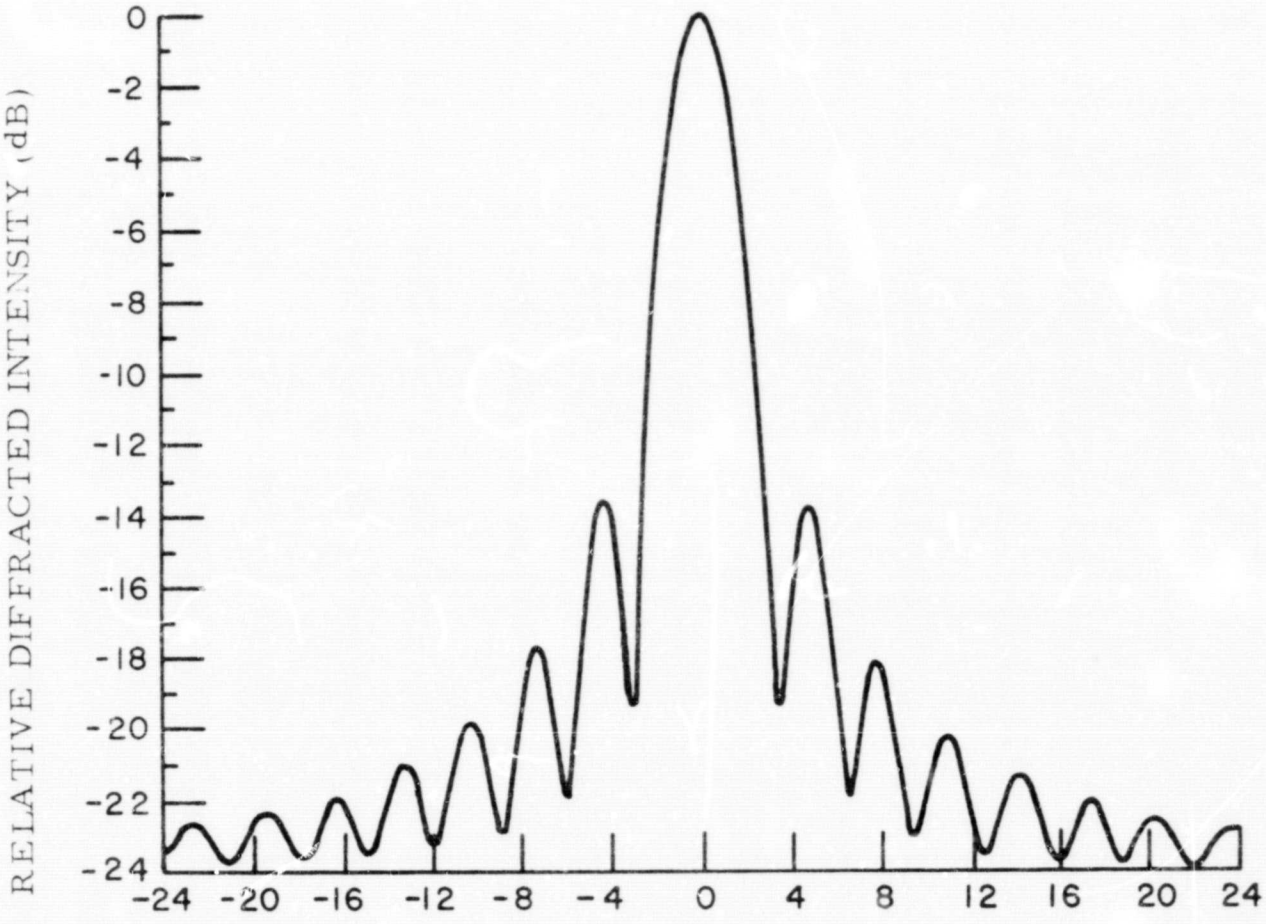

FIGURE 3-9. ANGULAR ORIENTATION SENSITIVITY MEASUREMENTS FOR PHOTOCHROMICS

Thickness = 1.6 mm Offset Angle = 30°

(3) erasability; light can also be used for erasing selected volumes in a crystal,

(4) reasonable stability; exposure to light causes a degradation of the recording but this is a relatively slow process at moderate-to-low light levels,

(5) high efficiency; since this is a phase recording material very high efficiency of reconstruction can be obtained (up to 40 percent has been reported with lithium niobate),

(6) high angular sensitivity of read-out; the great thickness (e.g., 1 cm) results in very high angular sensitivity on read-out thus allowing a large number of holograms to be recorded in the same volume but read out selectively, and

(7) no processing is required.

The disadvantages of ferroelectric materials are:

(1) very low sensitivity; exposures of 100 J/cm^2 are required to record holograms in lithium niobate, and

(2) although the ferroelectric materials appear to respond to all wavelengths in the visible spectrum, their spectral sensitivity is not uniform, requiring compensation of the intensity levels of the various colors of the recording beams.

3.3.5.1 Experimental Results

We have tested two samples of lithium niobate crystals , with thicknesses of 2 mm and 5 mm, to determine their angular orientation sensitivity and also their diffraction efficiencies.

Using the experimental arrangement and procedure described in paragraph 3.3.1.3, we measure the angular orientation sensitivity of the two samples as a function of offset angle. Fig. 3-10 shows two representative results of the relative diffracted intensity as a function of incidence angle of the

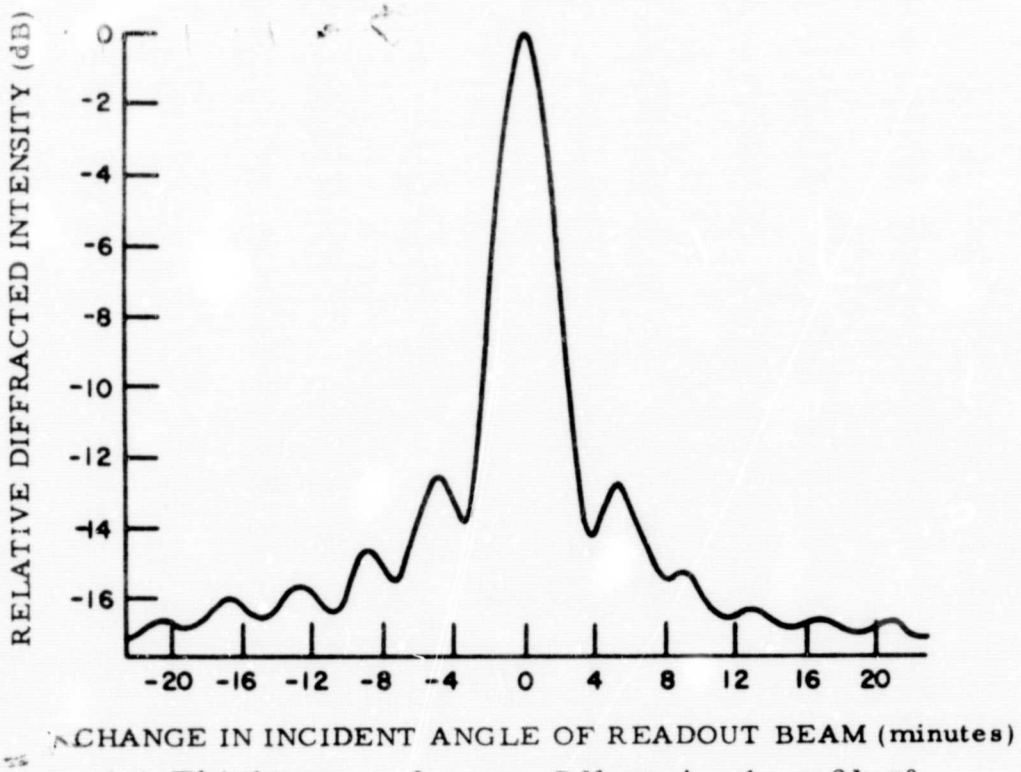

(a) Thickness = 2 mm, Offset Angle = 31.5°

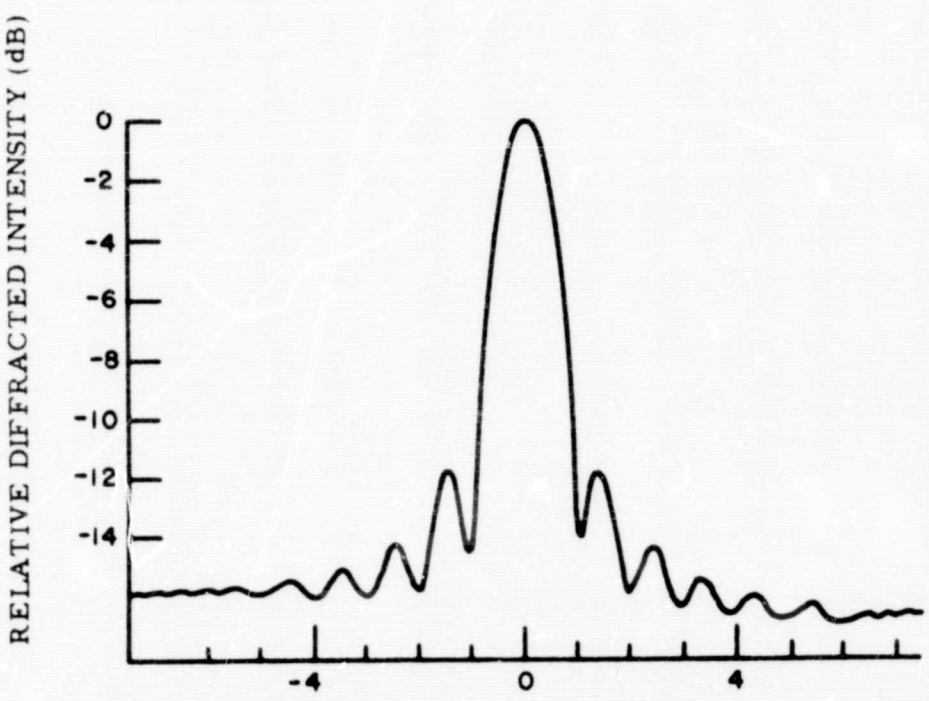

(b) Thickness = 5 mm, Offset Angle = 40°.

FIGURE 3-10. ANGULAR ORIENTATION SENSITIVITY MEASUREMENTS FOR LITHIUM NIOBATE

relative diffracted intensity as a function of incidence angle of the readout beam. The curve shown in Fig. 3-10(a) was for a hologram recorded in the 2 mm thick sample, with an offset angle of 31.5 degrees ($\theta_r = \theta_s$) and an illumination wavelength of 488 nm. The curve shown in Fig. 3-10(b) was for a hologram recorded in the 5 mm thick sample, with an offset angle of 40 degrees ($\theta_r = \theta_s$) and an illumination wavelength of 488 nm. The half power width of the angular orientation sensitivity curves was determined from these experimental curves and the results were in good agreement with the values calculated by using Eq. (3-6).

We also measured the diffraction efficiency for these materials as a function of exposure levels and offset angles. As for photochromics the maximum diffraction efficiency was less than 1 percent which is significantly lower than the 40 percent efficiency reported in the literature (Ref. 10). This discrepancy may be due to improper "poling" of the crystals.

3.3.6 Manganese Bismuth Materials

Manganese bismuth (MnBi) is an erasable hologram recording material. It is a ferromagnetic compound having a strong uniaxial magnetic anisotropy which can be epitaxially oriented normal to a thin film of the material. Thin films of MnBi are typically coated on mica substrates to produce epitaxial crystal growth. Formation of a MnBi film is accomplished by vacuum deposition of separate layers of manganese and bismuth followed by prolonged annealing. The MnBi films are typically from 500-1000 Å thick and have a polished, metallic appearance similar to aluminum. A MnBi film deteriorates in a few weeks time if left exposed to the atmosphere; a silicon monoxide overcoating is sometimes applied to reduce this deterioration to a minimum.

Hologram recording (and also bit or spot recording) on MnBi is accomplished by means of Curie-point writing. MnBi has a saturation

magnetization (M_s) of about 500 Gauss and a saturation field of roughly 5,000 Oersteds at room temperature for a typical coating thickness. If completely magnetized MnBi is heated to 360° C (the Curie temperature) the magnetization of the material goes to zero. If the temperature is increased to about 450° C (the peritectic temperature) the compound decomposes into liquid bismuth and solid α-manganese. The useful magnetic properties of MnBi are therefore lost at temperatures greater than or equal to the peritectic temperature. The useful writing temperature range of MnBi therefore lies between 360° C and 450° C. MnBi cooled from this range regains its ferromagnetic properties slightly below the Curie temperature. If cooled in the presence of a strong magnetic field, the MnBi can be magnetized to its original saturation level M_s.

MnBi has a number of advantages and disadvantages for data storage applications. The advantages are:

(1) high resolution; the theoretical resolution limit is determined by the size of the magnetic domains which is about 0.5 micron for MnBi; recording of gratings finer than 1000 ℓ/mm has been demonstrated,

(2) reversability; the recording can be erased by temporarily impressing a magnetic field on the film of 400 Oersteds; the material is free of fatigue and can be recycled indefinitely,

(3) stability; the recording is stable if the Curie point is not exceeded or a magnetic field capable of erasure is not applied; readout is nondestructive if the intensity of the read beam is not sufficient to heat the film above the Curie point,

(4) readout can be made by reflection or transmission; the reconstructed image can be formed by either reflected light (the Kerr effect) or transmitted light(Faraday effect),

(5) fast response; exposure times as short as 1 nsec can be used, and

(6) no processing; once the film has been prepared by saturating it magnetically no further processing is required and no chemical reactions are involved.

The disadvantages are:

(1) low sensitivity; the energy density required for exposure is on the order of 10 mJ/cm^2 as compared to 0.1 mJ/cm^2 for 649F emulsion,

(2) sensitivity to thermal damage; the film will decompose if heated beyond a certain point (450° C), and

(3) low diffraction efficiency; the most serious drawback of MnBi may be the low diffraction efficiency demonstrated to date; efficiencies on the order of 0.01 percent and 0.001 percent have been measured for Kerr and Faraday readout modes, respectively,

3.3.6.1 Experimental Procedure

Because the experimental procedure and geometry used for our investigation of MnBi differ from that paragraph 3.3.1.2, we describe them separately here. We performed our experimental work on MnBi films using a pulsed ruby laser. The laser was operated in a single transverse mode (TEM_{oo}) and a single longitudinal mode. Output of the laser is variable from from 0-30 mJ at 694.3 nm with a nominal pulse duration of 30 nsec. The experimental geometry is shown in Fig. 3-11. Due to the high peak powers from the pulsed laser (on the order of 1 megawatt) special precautions were used to avoid damage to the optical components. Some important features of this system are the use of a prism for directing the beams, a coated beamsplitter to provide both the signal and reference beam, and an uncoated lens to expand the laser beam. Prior to exposure, a CW He-Ne laser and glass beamsplitter were used to align the pulsed laser and the hologram recording system. The output of the pulsed laser was monitored with a

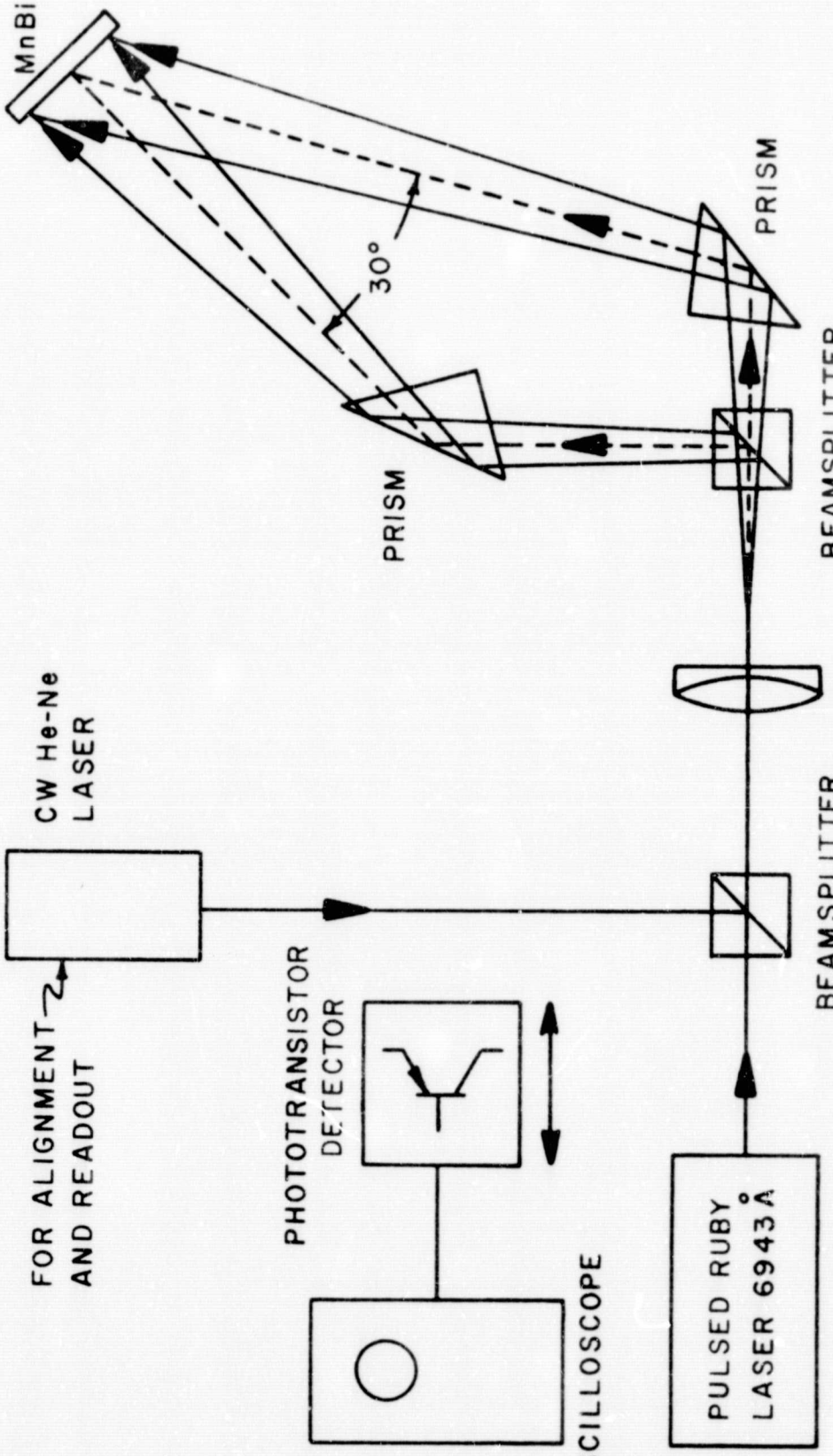

FIGURE 3-11. EXPERIMENTAL SETUP FOR MnBi TESTS

photodetector and a storage-type oscilloscope to obtain data about pulse bandwidth, number of pulses, and energy output during each exposure. An offset angle of 30 degrees and a reference-to-signal beam intensity ratio of 2 was throughout the experiments.

The main objective of our experimental investigation of MnBi was to determine basic recording parameters such as exposure sensitivity and diffraction efficiency. A more extensive investigation was precluded by the limited availability of MnBi films. Experimental data was obtained mainly by recording plane wave gratings.

3.3.6.2 Experimental Results

We tested a number of samples of MnBi materials which we obtained from the Honeywell Company and the Jet Propulsion Laboratories (JPL). A representative sample of our results with hologram gratings recorded on one of the MnBi samples is shown in Table 3-1. In the table, λ refers to the readout wavelength while η_1, η_2, η_3, and η_4 are the first, second, third, and fourth order diffraction efficiencies, respectively. In Table 3-2, we list the transmittance (T_λ), reflectance (R_λ), and absorptance (A_λ) as a function of wavelength for this particular sample.

We also noticed that sometimes the intensity of the diffracted wavefront from a hologram grating can be varied by the application of an external magnetic field. The reason for this is that when the MnBi is optically damaged, a partially etched grating structure is formed. The external magnetic field effects only the undamaged MnBi and causes the effective modulation of the grating structure to change. A hologram recorded in this manner cannot be fully erased.

Our experience with a number of MnBi samples prompted the following comments:

	FARADAY				KERR			
λ	η_1	η_2	η_3	η_4	η_1	η_2	η_3	η_4
6471Å	2.85×10^{-5}	1.35×10^{-5}	3.88×10^{-6}	0	5.05×10^{-5}	2.44×10^{-5}	7.2×10^{-6}	0
5682	3.1×10^{-5}	1.13×10^{-5}	3.06×10^{-6}	0	4.4×10^{-5}	1.16×10^{-5}	4.85×10^{-6}	0
5208	3.0×10^{-5}	1.22×10^{-5}	4.65×10^{-6}	0	4.0×10^{-5}	1.0×10^{-5}	3.67×10^{-6}	0
4765	1.17×10^{-5}	0.535×10^{-5}	2.5×10^{-6}	1.08×10^{-6}	1.75×10^{-5}	$.92\times10^{-5}$	3.66×10^{-6}	1.25×10^{-6}

TABLE 3-1

Diffraction Efficiency vs. Wavelength

λ	T_λ	R_λ	A_λ
6471Å	.035	.40	.565
5682Å	.049	.244	.707
5208Å	.0575	.182	.761
4765	.0386	.158	.803

TABLE 3-2

Transmittance, Reflectance, and Absorptance vs. Wavelength

(1) MnBi films require carefully controlled exposures to prevent permanent optical damage,

(2) erasable holograms can be recorded on MnBi with a maximum diffraction efficiencies of at least 10^{-4} percent,

(3) it is possible to record holograms in a partially erasable mode with diffraction efficiencies on the order of 3×10^{-3} percent; the diffraction efficiency of a hologram recorded in this manner can be varied by an external magnetic field, and thus has the properties of a magneto-optical modulator,

(4) permanently damaged, nonerasable holograms can be recorded with diffraction efficiencies on the order of 10^{-1} percent,

(5) the resolving power of MnBi is at least 800 lines/mm,

(6) the exposure range for erasable MnBi holograms is in the range of 5-30 mJ/cm^2, and

(7) the properties of MnBi vary significantly over the area of the samples tested, probably due to nonuniform coating of the thin films.

3.3.7 Photopolymer Materials

Photosensitive materials based on photo-induced polymerization have been successfully used to record holograms. The major effect appears to be a change in the index of refraction of the material; correspondingly high diffraction efficiencies have been reported (up to 45 percent) for films 10 to 20μ in thickness. The material is "developed" by brief exposure to ultraviolet radiation; no chemical processing is required. Exposures of 1 to 30 mJ/cm^2 are required and the resolution exceeds 1000 lines/mm.

The components of the materials we used are quite stable separately, but have a useful life of only a few hours when mixed to form a photosensitive film. The optically processed hologram is quite stable. The presence of light scattering polymer particles causes a significant amount of noise in

the reconstruction. The materials cannot be recycled. The advantages of photopolymer materials are:

(1) high resolution; over 1000 lines/mm,

(2) stability; recordings appear to last indefinitely and can be non-destructively read out,

(3) rapid processing; limited by the rate of the photochemical reactions to a few milliseconds (exact requirements are not known),

(4) low cost material; and

(5) high efficiency; since this is a phase material, high diffracting efficiencies can be obtained (up to 45 percent efficiency under suitable conditions have been reported).

The advantages of photopolymer materials are:

(1) low sensitivity; 1 to 30 mJ/cm^2 required for exposure,

(2) high noise level due to scattering particles,

(3) lifetime; limited lifetime of prepared photosensitive material,

(4) read-only; the materials tested cannot be recycled,

(5) nonlinearity; the linear range of the amplitude transmission versus exposure curve is quite limited and linear amplitude recording would be difficult; however, since the most important phenomena appears to be a phase effect, this nonlinearity may not be of particular importance, and

(6) although the photopolymer material can be made as a thick volume material, multiple hologram storage is complicated by the surface effects and self-developing nature of the material.

3.3.7.1 Experimental Results

Using the experimental arrangement and procedure described in paragraph 3.3.1.2 we measured the diffraction efficiency of photopolymer samples as a function of exposure and reference-to-signal beam intensity ratios. The results of these measurements are shown in Fig. 3-12.

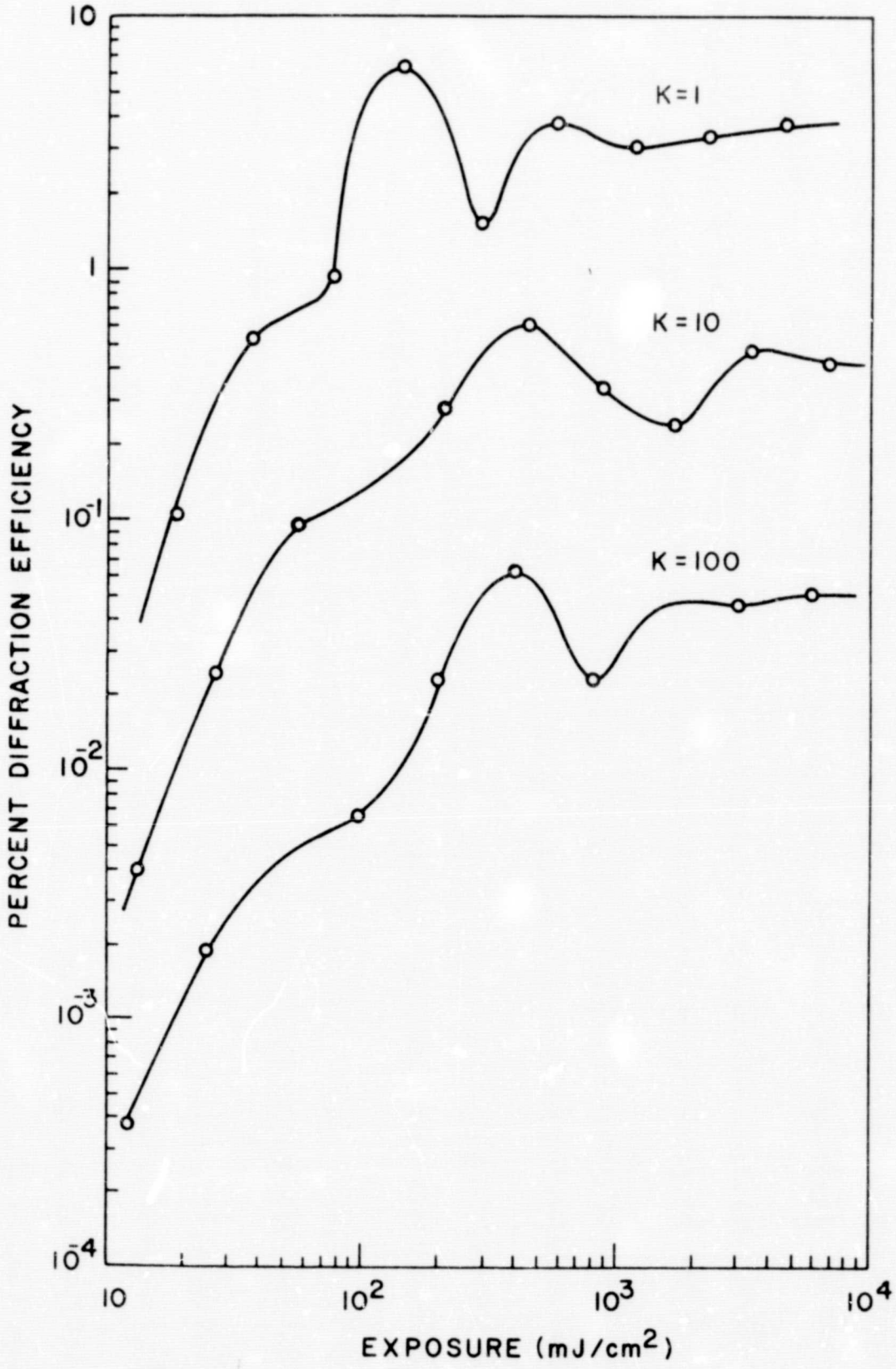

FIGURE 3-12. DIFFRACTION EFFICIENCY VERSUS EXPOSURE FOR PHOTOPOLYMERS

Throughout the experiments the offset angle was held constant at 40 degrees ($\theta_r = \theta_s$) and the illumination wavelength was 488 nm; the recorded spatial frequency was therefore 1400 lines/mm. We note, in all the experimental curves, a peculiar "dipping" phenomena. That is, diffraction efficiencies as a function of exposure monotonically increase to a maximum value, then decrease, and then increase again to a saturation level. This phenomenon, which is not clearly understood, is probably associated with the chemistry of the materials. Although the diffraction efficiencies that were measured are not high, they are adequate for the holographic storage application; this, in conjunction with dry processing, make photopolymer materials attractive for holographic memories.

3.3.8 Photo-Resist Materials

Photo-resist materials such as Kodak ortho resist have been used to record holograms. The index of refraction of the resist changes upon exposure and no processing is required to make this index change permanent. The material is inherently insensitive and cannot be recycled. The advantages of photo-resists are:

(1) high resolution; the resolution of resists typically approach 1000 lines/mm, and

(2) no processing, at least for the phenomena described here.

The advantages of photo-resists are:

(1) they are very insensitive,

(2) unstable; read-out should cause degradation,

(3) cannot be recycled, and

(4) they have poor signal-to-noise ratio.

3.3.8.1 Experimental Results

Using the experimental arrangement and procedure described in

paragraph 3.3.1.2 we measured the diffraction efficiency of several samples of Kodak Orthoresist (KOR) and Kodak Metal Etch Resist (KMER). The offset angle was 30 degrees and the illumination wavelength was 363.8 nm. The reference-to-signal beam intensity ratio K was unity in all the experiments. Fig. 3-13(a) shows the diffraction efficiency as a function of exposure for KOR materials. Fig. 3-13(b) shows the diffraction efficiency as a function of exposure for KMER materials. The diffraction efficiency of both KOR and KMER is relatively poor, and both have low exposure sensitivity. Furthermore, although not evident from results shown in Fig. 3-13, we noted that the scatter noise from these materials is relatively high. We conclude that if the efficiencies and noise characteristics do not improve, these materials are not suitable for dense holographic storage applications.

3.3.9 Photoplastics

Photoplastic recording materials consist of a conducting substrate and layers of photoconductive and thermoplastic materials. A corona discharge is used to place a charge on the thermoplastic materials, and a subsequent illumination with light causes the material to discharge locally. Upon recharging and heating, the thermoplastic layer deforms as a function of the distribution of the surface charge density. These surface deformations are stable until reheating the thermoplastic erases the recorded image. The advantages of photoplastics are:

(1) high resolution; resolution of over 1000 lines/mm is possible,

(2) reversibility; presently available materials have been successfully recycled up to 10 times without significant deterioration,

(3) diffraction efficiency; should be relatively high since this is a phase material,

(4) stability; the uncharged material is stable if not heated to plasticity, and

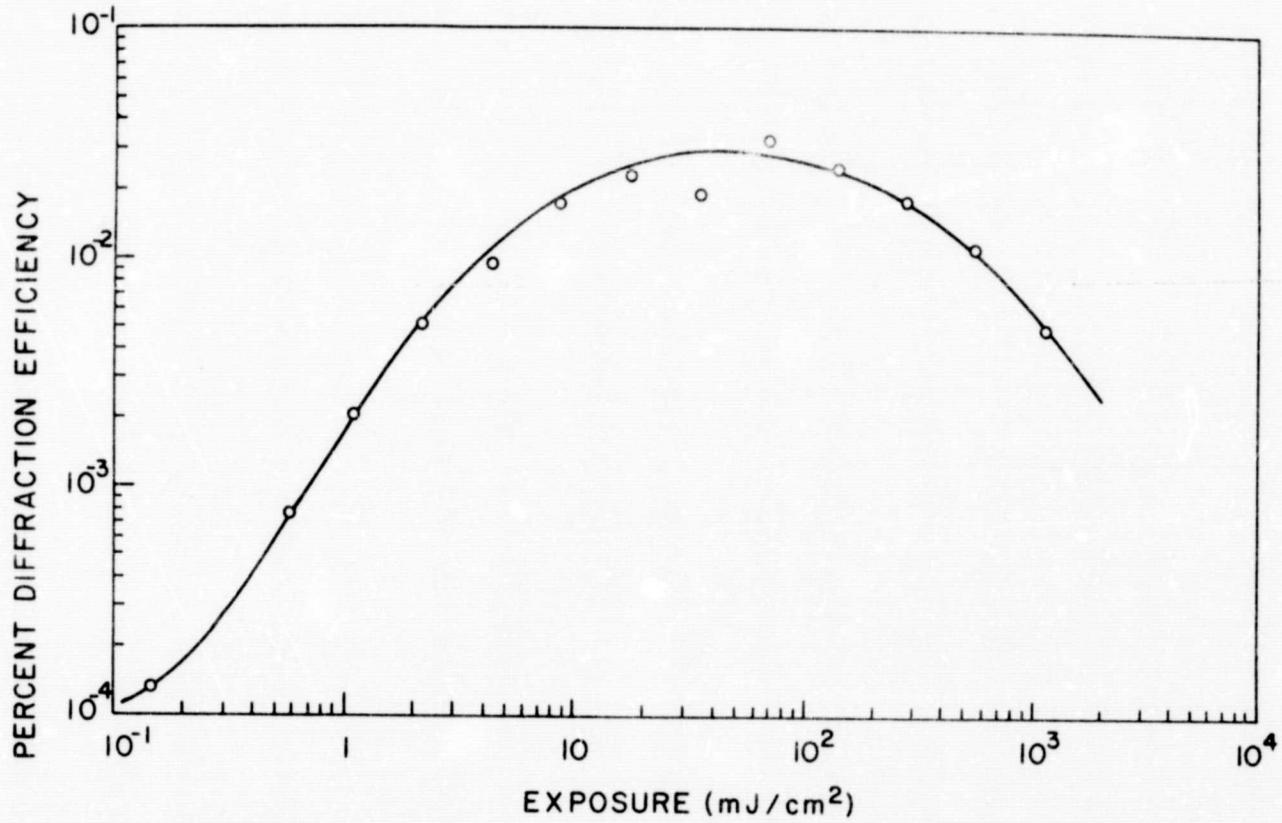

(a) KOR

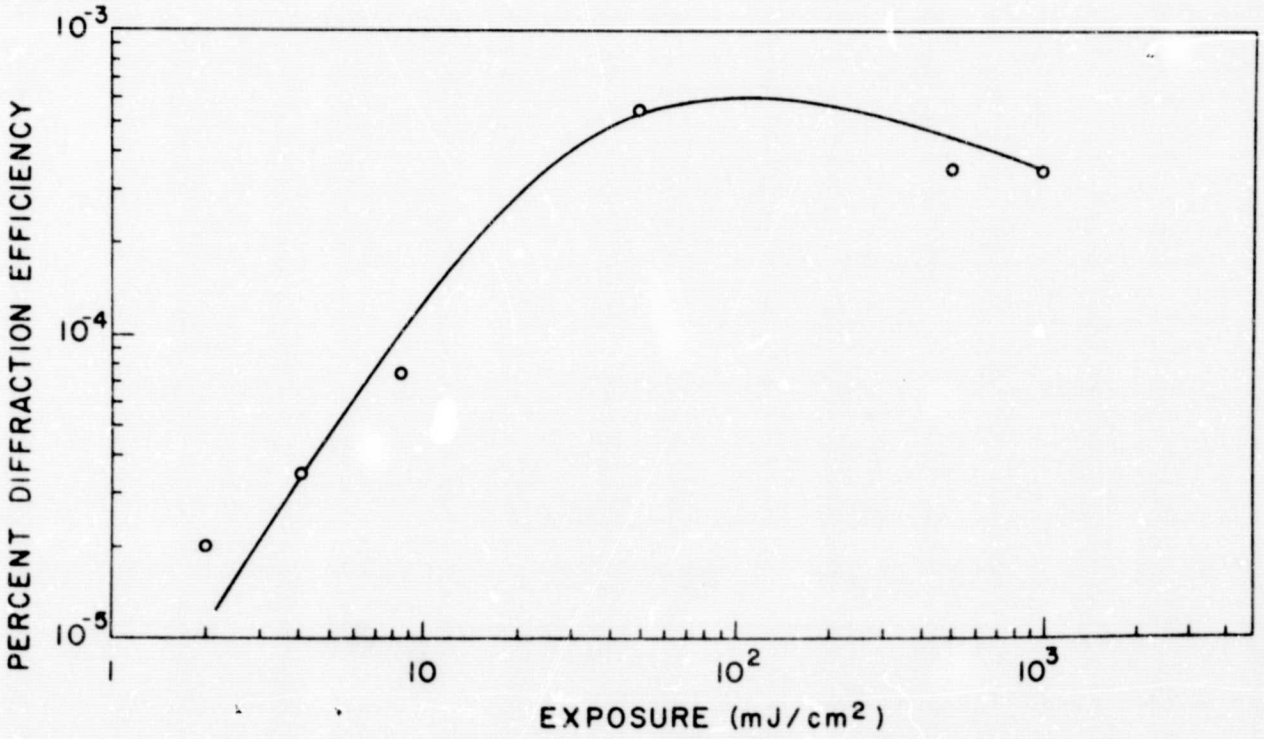

(b) KMER

FIGURE 3-13. DIFFRACTION EFFICIENCY VERSUS EXPOSURE FOR PHOTORESISTS

(5) sensitivity; some red sensitive photoplastic films have been used to make recordings with exposures comparable to conventional photographic emulsions.

The disadvantages of photoplastics are:

(1) complexity; equipment is required to provide a corona discharge and heating,
(2) limited reusability; at present, there appears to be a limit to the number of recycles possible, and
(3) limited bandwidth; these materials only respond to a band of spatial frequencies which is centered at some fixed frequency.

3.3.9.1 Experiments

During the last part of the contract period we began to construct photoplastic devices. The photoplastics are coated on a glass substrate onto which a thin film of transparent conductor (generally tin oxide) has been deposited. Although the photoplastic may be a mixture of photoconductors and thermoplastics, we found that separate layers of a photoconductive material and a thermoplastic is more effective for holographic recording. The photoconductor layer is coated onto the tin oxide and the thermoplastic material is then coated onto the photoconductor layer. The recording process requires that the photoplastics be corona charged; after exposure to a light image, it is recharged so that the potential on the surface is constant but the charge density, in the areas exposed to light, becomes relatively high. When the thermoplastic is heated to its softening point (typically 80° C) and then quickly cooled, surface deformations are produced which correspond to the light image. These deformations produce a phase hologram which is stable at room temperature until erased by applying a higher temperature. Erasure usually causes a complete neutralization of the electrostatic charges, after which the recording

process can be repeated.

We began by electrolytically etching commerically available tin oxide coated glass to leave a number of isolated squares, and then fixing electrodes along opposite edges of each square. A pulsed a-c voltage applied between each set of electrodes generates resistive heating to heat the thermoplastic during recording and erasure. Using dip coating techniques, we coated layers (1μ to 3μ thick) of photoconductive and thermoplastic materials on the glass substrates.

We tested some of these photoplastic devices to determine their exposure sensitivities and diffracting capabilities using the experimental arrangement and procedure described in paragraph 3.3.1.2. The offset angles were 30 and 40 degrees and the illumination, derived from a He-Ne laser, was 632.8 nm. Preliminary results indicate that the exposure sensitivities and diffraction efficiencies are comparable to Kodak high resolution photographic emulsions.

3.3.10 Comments

The investigations of the materials described above were sufficient to show that none of the tested materials possess all the characteristics necessary for a read/write storage material that can be used in the final system. A list of these desired characteristics will be given in Section VII. Some of the tested materials could serve as interim devices for checking the remaining components of the holographic memory and verifying some of the concepts proposed in this study. In particular, either the thick photographic emulsions or thick dichromated gelatin materials could be used to test the angular and wavelength discrimination of read-only memories, and the photoplastics could serve as interim thin read/write storage materials.

3.4 NOISE CHARACTERISTICS OF HOLOGRAPHIC RECORDING MATERIALS

3.4.1 Introduction

In this part we characterize recording materials so that we can determine the effects of noise produced by the material in a holographic memory. The methods used to determine the noise characteristics are general in nature and can be applied to nay recording material. In this study, photographic emulsions are used for our analysis and experimental work by way of an example. Besides being dependent on various recording parameters, the quality of a reconstructed signal from a hologram is dependent on two kinds of noise produced by the photographic emulsion. One source of noise is the intermodulation noise which arises from the nonlinearity of the characteristic curve of the recording material. For photographic emulsions, this type of noise is determined by the shape of the T_a-E curve, the ratio of the reference-to-signal beam intensity K, the bias transmittance t_b, and the nature of the signal itself. The second source of noise is random noise caused by scattering centers within the recording material. For photographic emulsion, the noise arises from the granular structure of the emulsion. A measure of the degradations in the reconstruction caused by the two noise sources is given by the ratio of the signal intensity to the average noise intensity ($\overline{I}/\overline{I}_n$) in the reconstructed image. This ratio can be obtained experimentally by using simple input objects such as a point source or a diffusely illuminated transparent aperture.

We use a model for the photographic emulsion to determine analytically the $\overline{I}/\overline{I}_n$ ratio in the reconstruction and compare experimental results with the theoretical results. An example is given to show how the experimental results can be used for evaluating the performance of the recording material in a holographic memory.

3.4.2 Signal and Noise in the Reconstructed Image

To derive the $\overline{I}/\overline{I}_n$ ratio in the reconstructed image, we assume that the T_a-E curve (about a bias exposure E_o) can be adequately represented by a second order polynomial. The amplitude transmittance of the film, developed to a given bias exposure is then

$$T(E)-t_b = s_1 \Delta E + s_2 \Delta E^2, \tag{3-8}$$

where t_b is the transmittance due to E_o, ΔE is the variation in the exposure and s_1 and s_2 are coefficients determed from the T_a-E curve.

3.4.2.1 Intermodulation Noise

In recording a thin amplitude hologram, the intensity of the light distribution at the hologram plane is

$$I(x, y) = \left|a(x, y) \exp [j\theta (x, y)] + a_r \exp (j2\pi\alpha x)\right|^2 \tag{3-9}$$

The functions $a(x, y) \exp [j\theta(x, y)]$ and $a_r \exp (j\pi\alpha x)$ are the wavefronts caused by the object and the reference source, respectively. If we define

$$b^2 = \frac{1}{A_t} \int\int a^2(x, y)dx\, dy \tag{310}$$

$$K = \frac{a_r^2}{b^2} \tag{3-11}$$

and $$I_o = a_r^2 + b^2 = b^2 (K+1) = a_r^2(K+1)/K, \tag{3-12}$$

the function I(x, y) may be written as

$$I(x, y) = I_o + \Delta I(x, y),$$

$$\Delta I(x, y) = \frac{I_o}{(K+1)} \left\{ -1 + \left[\frac{a^2(x, y)}{b^2} \right] \right.$$

$$\left. + 2\sqrt{K} \left[\frac{a(x, y)}{b} \right] \cos \left[2\pi \alpha x - \theta(x, y) \right] \right\} . \qquad (3-13)$$

The constant A_t in Eq. (3-10) is the area of the hologram, the constant b^2 is the average signal intensity at the hologram plane, and K is the ratio of the reference-to-signal beam intensity. The amplitude transmittance of the developed hologram is

$$T_a(x, y) - t_b = s_1 t \Delta I(x, y) + s_2 t^2 \Delta I^2(x, y) \quad , \qquad (3-14)$$

where t is the time of exposure. If we substitute Eq. (3-13) into Eq. (3-14), the amplitude transmittance becomes

$$T_a(x, y) - t_b = T_o(x, y) + T_1(x, y) + T_2(x, y), \qquad (3-15)$$

where

$$T_o(x, y) = \frac{-s_1 E_o}{(K+1)} + \frac{s_2 E_o^2}{(K+1)^2} + \frac{E_o}{(K+1)} \left[\frac{a^2(x, y)}{b^2} \right] \left\{ s_1 + \frac{2(K-1) E_o s_2}{(K+1)} + \right.$$

$$\left. \frac{E_o s_2}{(K+1)} \left[\frac{a^2(x, y)}{b^2} \right] \right\} , \qquad (3-16)$$

$$T_1(x, y) = \left\{ 1 + \frac{2E_o s_2}{(K+1)s_1} \left(\frac{a^2(x, y)}{b^2} - 1 \right) \right\} \frac{2\sqrt{K} E_o s_1}{(K+1)} \left[\frac{a(x, y)}{b} \right] \cos[2\pi \alpha x - \theta(x, y)] ,$$

(3-17)

$$T_2(x,y) = \frac{2KE_0^2 s_2}{(K+1)^2} \left[\frac{a^2(x,y)}{b^2}\right] \cos 2[2\pi\alpha x - \theta(x,y)] \qquad (3\text{-}18)$$

and

$$E_0 = I_0 t.$$

The degradation due to the film nonlinearity is given by the term

$$T_n(x,y) = \frac{4E_0^2 s_2\sqrt{K}}{(K+1)^2} \left[\frac{a(x,y)}{b}\right] \left\{\left[\frac{a^2(x,y)}{b^2}\right] - 1\right\} \cos[2\pi\alpha x - \theta(x,y)]. \qquad (3\text{-}19)$$

Using a statistical approach, Goodman and Knight (Ref. 10) have shown that, if the signal is diffusely illuminated, the average intensity of the spurious images in the reconstruction, due to the film nonlinearity, is proportional to a triple convolution of the intensity of the signal. Similar results were also obtained by Kozma, et.al. (Ref. 11).

In general it is difficult to define a unique $\overline{I}/\overline{I}_n$ ratio for the intermodulation noise because of its object dependent characteristics. However, from Eq. (3-19) we note that the intensity of the spurious images reconstructed from $T_n(x,y)$ depends on the coefficient $4E_0^2 s_2\sqrt{K}/(K+1)^2$ as well as the structure of the object. A ratio $\overline{I}/\overline{I}_n$ for the intermodulation noise can be given by

$$S_1 = \frac{1}{\gamma}\left[\frac{2E_0 s_2}{(K+1)s_1}\right]^{-2} \qquad (3\text{-}20)$$

where the parameter γ is the signal dependent factor. The ratio S_1 is proportional to the square of the ratio of the coefficient of the signal to the coefficient of the nonlinear degradation. For a given object, the parameter

γ can be determined from $T_n(x,y)$ at any desired location in the reconstructed image. From Eq. (3-20) we note that the $\overline{I}/\overline{I}_n$ ratio due to film nonlinearity can be improved by using a larger reference-to-signal beam intensity ratio K or by reducing the bias exposure E_o.

3.4.2.2 Film Grain Noise

We shall now derive the $\overline{I}/\overline{I}_n$ ratio for the film grain noise. Suppose that the signal recorded on the hologram consists of N point sources. The wavefront of the signal at the hologram plane is

$$a(x,y)\exp[j\theta(x,y)] = \sum_{m=1}^{N} a_o \exp\left[-j\theta_m - \frac{j2\pi}{\lambda d}\left\{(x-u_m)^2 + (y-v_m)^2\right\}\right], \quad (3\text{-}21)$$

and

$$a^2(x,y) = Na_o^2 + 2a_o^2 \sum_{m=1}^{N-1}\sum_{n=m+1}^{N} \cos\left[\theta_n - \theta_m + \frac{2\pi}{\lambda d}\left\{(x-u_n)^2 - (x-u_m)^2 + (y-v_n)^2 - (y-v_m)^2\right\}\right], \quad (3\text{-}22)$$

where a_o^2 is the intensity of each of N equal point sources, d is the distance between the hologram and the object planes, and u_m, v_m are the positions of the point sources in the object plane. If each point source has a random phase, the average of the second term in Eq. (3-22) is zero and we have that

$$b^2 = Na_o^2 . \quad (3\text{-}23)$$

Suppose that the hologram is linearly recorded. When the hologram is illuminated by the original reference beam, the complex amplitude of the real image reconstructed from the hologram is

$$h(u,v) = \frac{\sqrt{K}\,(E_o s_1)h_p}{\lambda d(K+1)a_o\sqrt{N}} \iint_{A_t} a(x,y)\exp\left[j\theta(x,y) - j\frac{2\pi}{\lambda d}\left\{(x-u)^2+(y-v)^2\right\}\right]dx\,dy, \tag{3-24}$$

which is the Fresnel approximation to the Kirchhoff diffraction integral. The constant h_p is the complex amplitude of the reconstruction beam and d is the distance between the hologram and the real image of the signal. Upon substituting Eq. (3-21) into h(u, v), we find that the complex amplitude of any one of the point sources reconstructed is approximately equal to

$$h(u_m, v_m) = \frac{\sqrt{K}\,(E_o s_1)h_p F A_t}{\lambda d(K+1)\sqrt{N}} \tag{3-25}$$

The parameter F is a spatial frequency dependent factor which is determined by the modulation transfer function (MTF) of the photographic emulsion (Ref. 8). Although the detailed effects of the modulation transfer function upon the complex amplitude of the reconstructed image cannot be predicted by our simple analysis, these details of the effects of MTF on wavefront reconstruction can be found in a recent paper by Kozma and Zelenka (Ref. 3). Using $h(u_m, v_m)$, we find that the intensity of any one of the point sources is equal to

$$I_s = \frac{F^2 K(E_o s_1)^2 A_t^2 I_p}{(K+1)^2(\lambda d)^2 N}, \tag{3-26}$$

where

$$I_p = |h_p|^2.$$

Kozma (Ref. 8) showed that the average intensity produced by the film grain noise is equal to

$$I_g = \frac{A_t \Phi_{\tau'\tau'}(p_o, q_o) I_p}{(\lambda d)^2} \qquad (3\text{-}27)$$

where $\Phi_{\tau'\tau'}(p_o, q_o)$ is the Wiener spectrum of the film grain noise at a suitably chosen spatial frequency within the bandwidth of interest. Therefore, the ratio of the signal intensity to the average intensity due to the film grain noise is given by

$$S_2 = \frac{I_s}{I_g} = \frac{F^2 K A_t (s_1 E_o)^2}{(K+1)^2 \Phi_{\tau'\tau'}(p_o, q_o) N} \qquad (3\text{-}28)$$

If the N point sources are replaced by a diffusely illuminated object, the parameter N must be replaced by $A_o A_t/(\lambda d)^2$, where A_o is the area occupied by the signal. In such a case, the parameter N represents the total number of resolution elements in the signal.

3.4.2.3 Combined Ratio of Signal Intensity to Average Noise Intensity

Because the processes in the photographic emulsion that produce the film grain noise and the intermodulation noise are nearly independent, the total $\overline{I}/\overline{I}_n$ ratio can be written as

$$\frac{\overline{I}}{\overline{I}_n} = \frac{1}{\frac{1}{S_1} + \frac{1}{S_2}} = \frac{1}{\gamma \left[\frac{2E_o s_2}{(K+1)s_1}\right]^2 + \frac{(K+1)^2 \Phi_{\tau'\tau'}(p_o, q_o) N}{F^2 K A_t (s_1 E_o)^2}} . \qquad (3\text{-}29)$$

To illustrate the dependence of $\overline{I}/\overline{I}_n$ on the recording parameters, we now find the $\overline{I}/\overline{I}_n$ ratio for a specific example. We assume that the granular structure in the photographic emulsion is represented by the checkerboard model; the Wiener spectrum of this film grain is equal to (Ref. 13)

$$\Phi_{\tau'\tau'}(p,q) = t_b(1-t_b)\, G(p,q),$$

where

$$G(p,q) = r^2 \,\mathrm{sinc}^2(pr/\lambda d)\,\mathrm{sinc}^2(qr/\lambda d). \qquad (3\text{-}20)$$

The parameter t_b in Eq. (3-29) is the bias transmittance of the film and r^2 is the area of a film grain. In this example we also assume that the T_a - E curve of the film is given by

$$T(E) = \frac{\beta^2}{E^2 + \beta^2}\ , \qquad (3\text{-}31)$$

where β is a parameter used to fit T(E) to the experimentally derived data. Fig. 3-14 shows the function T(E) as well as the T_a -E curve measured experimentally for Kodak 649F film. It can be seen that T(E) is in close agreement with the experimental T_a-E curve over the range shown. Using the theoretical T_a-E curve, we find that the coeffecients s_1 and s_2 are given by

$$s_1 = \left.\frac{dT}{dE}\right|_{E_o} = \frac{-2E_o t_b^2}{\beta^2} \qquad (3\text{-}32)$$

and

$$s_2 = \tfrac{1}{2}\left.\frac{d^2T}{dE^2}\right|_{E_o} = -\frac{t_b^2}{\beta^2}(4t_b - 3)\ , \qquad (3\text{-}33)$$

where

$$t_b = \frac{\beta^2}{\beta^2 + E_o^2}\ .$$

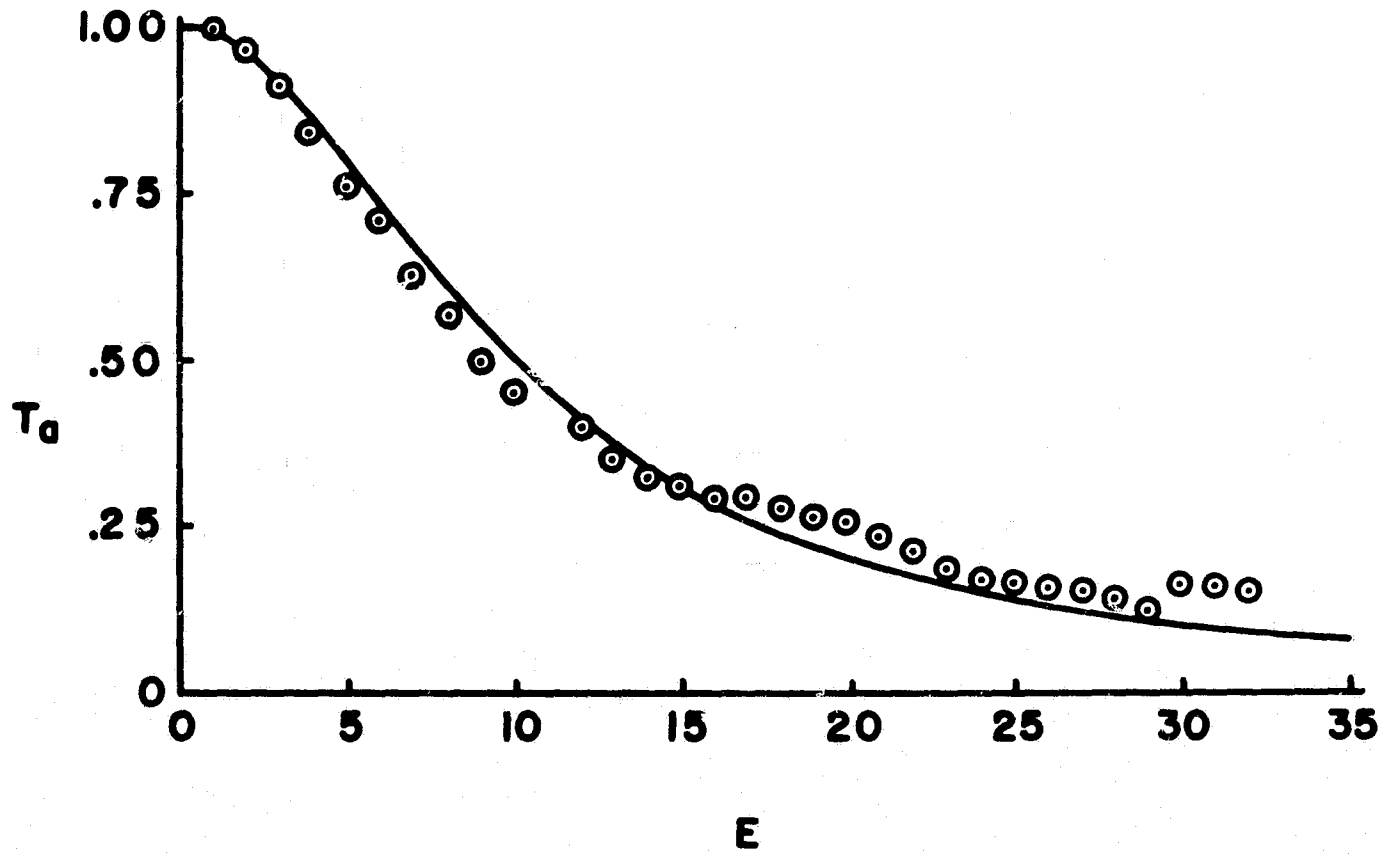

O Experimental

—— Calculated Curve

FIGURE 3-14. AMPLITUDE TRANSMITTANCE VERSUS EXPOSURE FOR 649F EMULSIONS

Substituting s_1 and s_2 into Eq. (3-28) we obtain

$$\overline{I}/\overline{I}_n = \frac{1}{\left[\frac{(4t_b-3)^2\gamma}{(K+1)^2} + \frac{(K+1)^2\, G(p_o, q_o)\, N}{F^2 t_b(1-t_b)\, KA_t}\right]} \quad . \tag{3-34}$$

If we define

$$R = \frac{F^2 A_t}{G(p_o, q_o)\, N} \quad , \tag{3-35}$$

then $\overline{I}/\overline{I}_n$ becomes

$$\overline{I}/\overline{I}_n = \frac{R}{\left[\frac{R\gamma(4t_b-3)^2}{(K+1)^2} + \frac{(K+1)^2}{t_b(1-t_b)K}\right]} \quad . \tag{3-36}$$

If $R\gamma$ is very small, the ratio $\overline{I}/\overline{I}_n$ will be dominated by S_2. In this case the $\overline{I}/\overline{I}_n$ ratio will be mostly due to film grain noise. In general R can be made small by increasing the number of resolution elements per unit area of the hologram, as it is evident from Eq. (3-35). Therefore, we deduce that the fundamental restriction on the performance of the photographic emulsion in an optical memory is the film grain noise because we generally want to store large amounts of data in a small area of the recording material.

The geometry for recording and reconstruction holograms is illustrated in Fig. 3-15. The dependence of the ratio $\overline{I}_s/\overline{I}_n$ on the reference-to-signal beam ratio K and the bias transmittance t_b is shown in Fig. 3-16 and

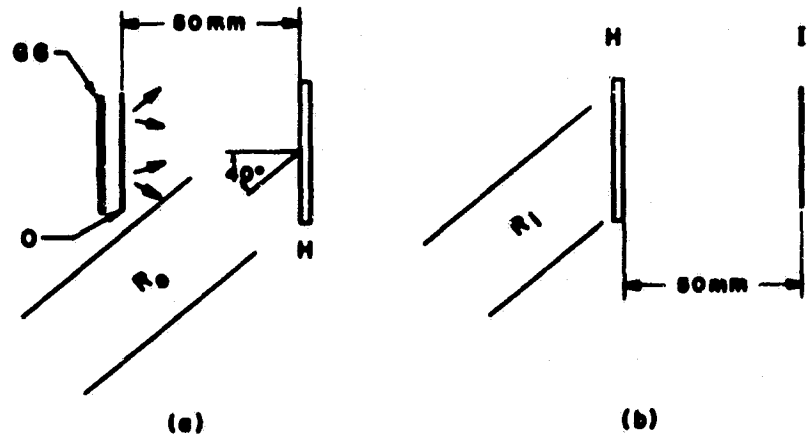

FIGURE 3-15. READ-IN AND READ-OUT ARRANGEMENTS FOR FRESNEL HOLOGRAMS
O = Object, R_o = Reference Beam, H = Hologram,
GG = Ground Glass, R_i = Reconstruction Beam,
I = Image

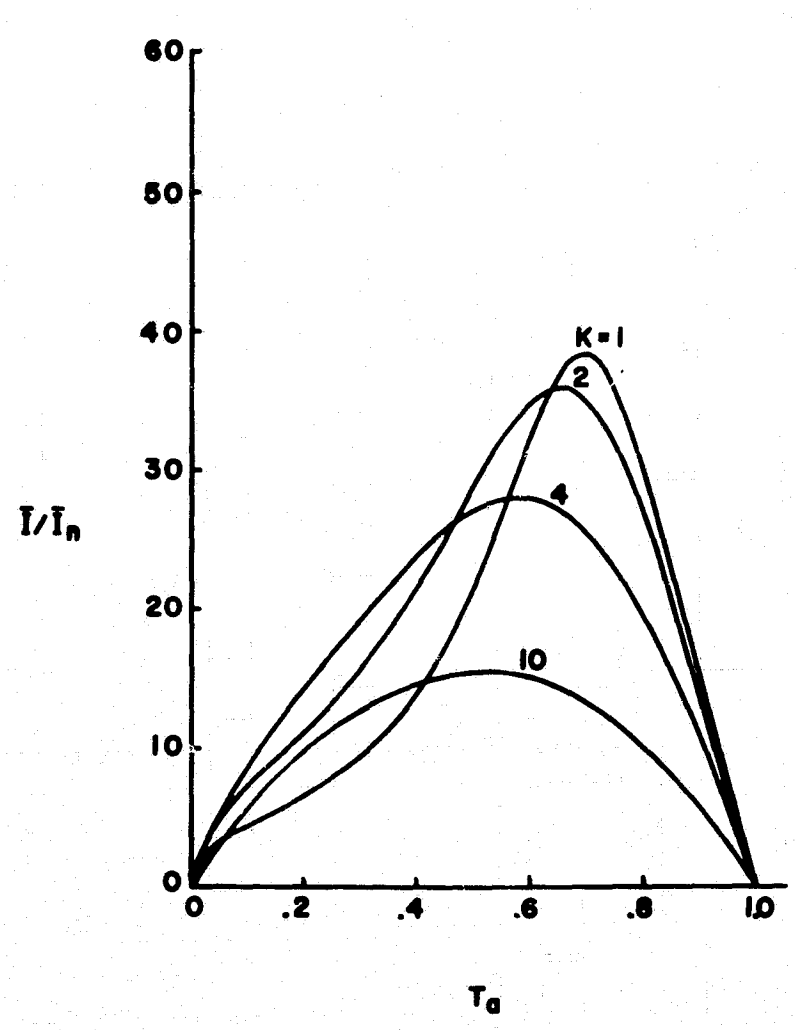

FIGURE 3-16. SIGNAL-TO-AVERAGE NOISE INTENSITY RATIO VERSUS AMPLITUDE TRANSMITTANCE FOR DIFFERENT BEAM RATIOS

Fig. 3-17. In obtaining these curves, we assumed that the area of a typical film grain is about $.25 \times 10^{-8}$ mm^2 which is the average size of a silver halide particle in the Kodak high resolution photographic emulsion (Ref. 14). The value of γ is chosen to be 0.1 to fit the experimental data shown later. From Eq. (3-36) we expect that for small values of K both the grain noise and the intermodulation will play a role in determining the ratio $\bar{I}/\bar{I}_n$ in the reconstructed image. But when there are fewer resolvable points per unit area of the hologram, the intermodulation noise will predominate because the factor R is increased by the reduction of the N/A_t ratio. From Eq. (3-36) we also observe that when the value of K increases, the recording will become more nearly linear and the intermodulation noise will start to diminish. With K=10 the hologram is almost linearly recorded. Therefore, the ratio $\bar{I}/\bar{I}_n$ plotted in Fig. 3-16 as a function of t_b for K=10 displays the characteristics of the ratio of signal intensity to the average noise intensity due to the film grain noise alone. For K less than 10 the curves show a combination of the intermodulation noise and the film grain noise.

In Fig. 3-16 the ratio $\bar{I}/\bar{I}_n$ is plotted as a function of K for different numbers of resolvable points in the signal. From our analysis we expect that the film grain noise will dominate the noise process when K is large or when there is a large number of reslovable points recorded in the hologram. For large K, the ratio $\bar{I}/\bar{I}_n$ is inversely proportional to K. However, for large N the ratio $\bar{I}/\bar{I}_n$ is proportional to $K/(K+1)^2$ for all values of K. This property of the ratio $\bar{I}/\bar{I}_n$ is illustrated in Fig. 3-17. The curves are normalized so that the ratio is equal to 1 at K=1000. As can be seen, the curve for $N=4 \times 10^7$ closely approximates the curve of the function $K/(K+1)^2$, the dominate source of noise is therefore due to film grains. However, as we reduce the value of N, the shape of the curve starts to deviate from the curve which shows predominantly grain noise since the nonlinearity effects are not negligible. This phenomenon occurs only when K is less than 20, because for

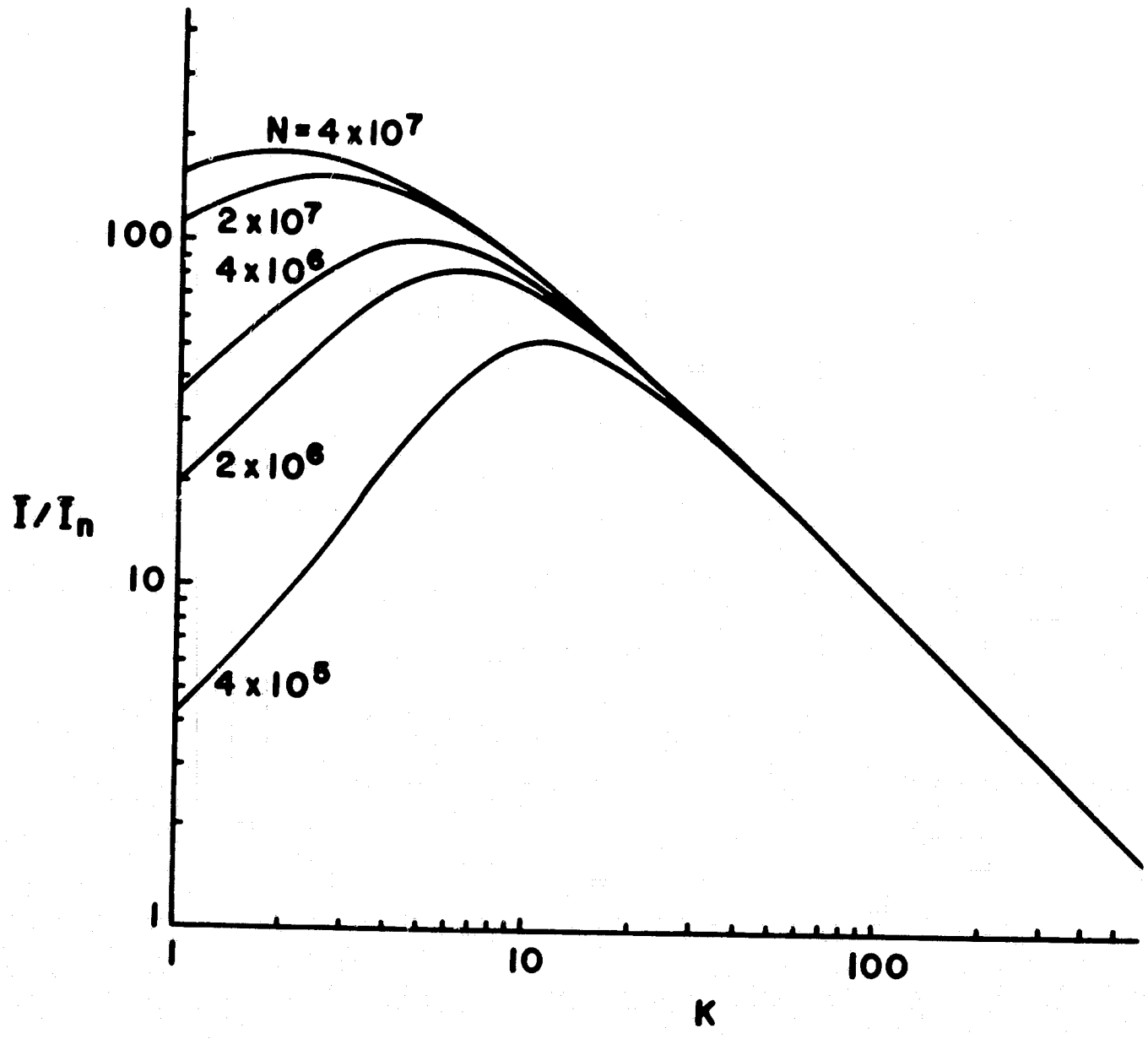

FIGURE 3-17. SIGNAL-TO-AVERAGE NOISE INTENSITY RATIO VERSUS BEAM RATIO FOR DIFFERENT VALUES OF RESOLUTION ELEMENTS

greater values of K the recording is linear for all values of N. In the following section we shall compare these results to experimental data.

3.4.3 Experimental Results

We performed a series of experiments, using the configuration shown in Fig. 3-15, in which we determined the noise characteristics of the holographic recording process. We recorded holograms on Kodak 649F plates which were developed in D-19 for five minutes. The object of the experiments is to (1) determine the best recording parameters for recording digital data with the best signal-to-noise ratio and (2) compare the experimental results with the theoretical results based on the above analysis.

We measured the ratio $\bar{I}/\bar{I}_n$ as a function of reference-to-signal beam ratio K, amplitude transmittance and aperture size to determine the optimum operating parameters. The average scattered noise of a series of holograms at different transmittances was compared to the scattered light of a uniformly exposed plate.

The ratio $\bar{I}/\bar{I}_n$ of the reconstruction from a hologram of a point object was measured as a function of the reference-to-signal beam intensity ratio K. A single point object was chosen so that the intermodulation noise would not be present; the grain noise caused by the photographic emulsion is therefore the only noise source. The point object was located 50 mm from the hologram recording plane and a plane wave was used as a reference beam. We made a series of holograms for which K was varied over a 70 dB range, the exposure being held fixed. Fig. 3-18 shows the signal-to-average noise $\bar{I}/\bar{I}_n$ as a function of K for $T_a=0.5$. Note that, in the absence of intermodulation noise, the logarithm of the ratio $\bar{I}/\bar{I}_n$ is a linear function of the logarithm of the reference-to-signal beam irradiance ratio. This curve can also be used to estimate the ratio $\bar{I}/\bar{I}_n$ for N points linearly recorded

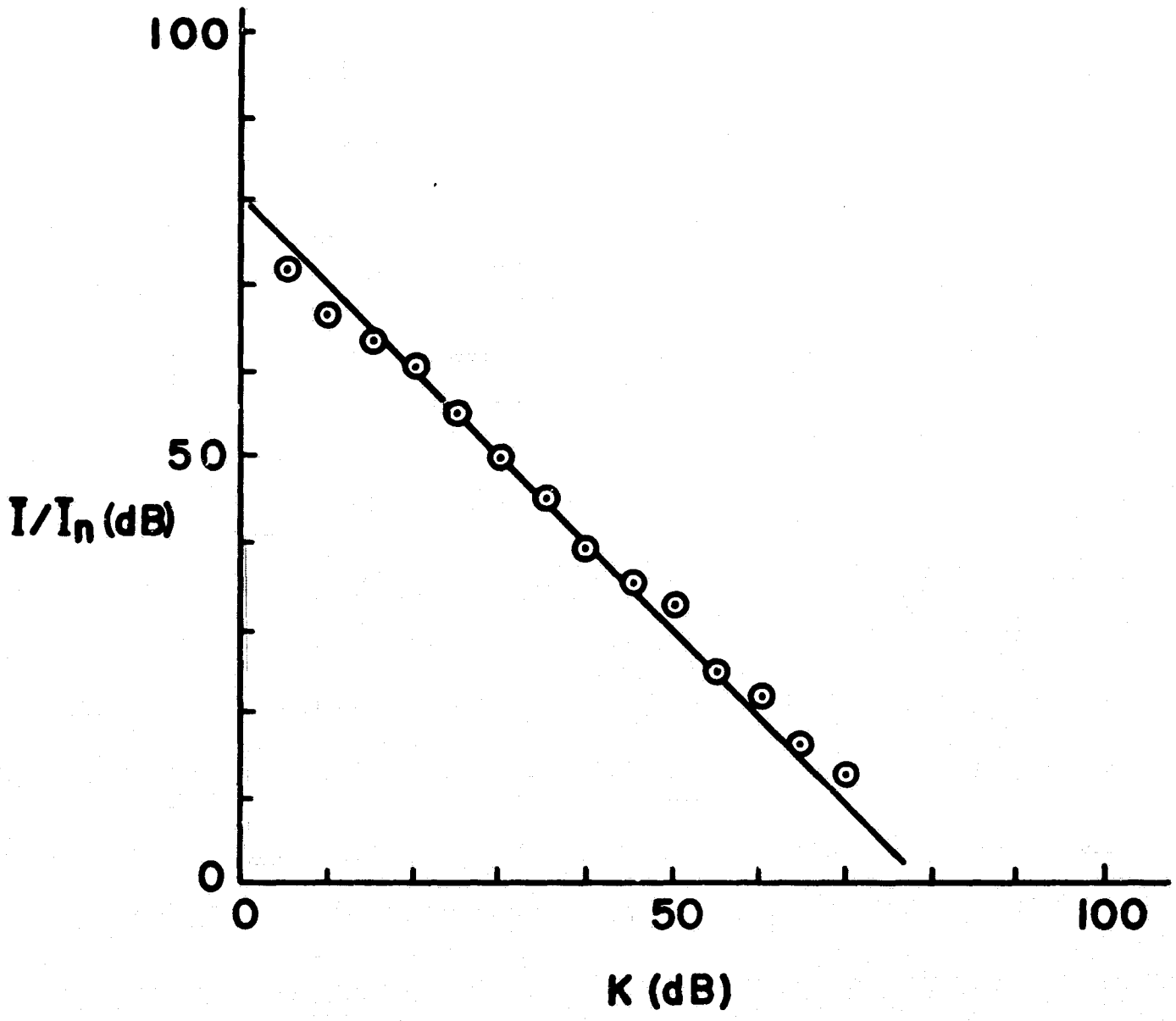

FIGURE 3-18. SIGNAL-TO-AVERAGE NOISE INTENSITY RATIO FOR A POINT SOURCE

by changing the abscissa to read 10 $\log_{10}(NK)$, where N is the number of resolution elements in the object. We see that to achieve a $\overline{I}/\overline{I}_n$ ratio of 10 for a given recording area, we can record 10^6 resolution elements with K=10, or we can record 10^7 resolution elements with K=1.

The above experiment was repeated using the two different objects shown in Fig. 3-19 a "dark square" object containing approximately 2×10^7 resolvable points and a digital array containing approximately 4×10^6 resolvable points in the reconstructed image. The ratio $\overline{I}/\overline{I}_n$, as a function of K, is shown in Fig. 3-20. The experimental data clearly shows that the ratio $\overline{I}/\overline{I}_n$ is inversely proportional to K for large K and the form of the data is independent of the number of resolvable points in the signal. However, for small K, the form of the relationship is dependent on the number of resolvable points as predicted by Eq. (3-36).

We calculated these curves from the analysis by substituting the hologram aperture size, the number of points, the bias transmittance and other pertinent data into Eq. (3-36). The experimental data and the calculated curves are in close agreement. These curves suggest that small K values should be used when a large number of data points are recorded coherently to optimize the $\overline{I}/\overline{I}_n$ ratio. However, as the number of points is reduced, the value of K must be increased to obtain the maximum $\overline{I}/\overline{I}_n$ ratio.

The measured $\overline{I}/\overline{I}_n$ ratio as a function of amplitude transmittance for the dark square object and the digital array is shown in Fig. 3-21. The reference-to-signal beam ratio K was 1 for the dark square object and 20 for the 10^4 array. The effect of linear and nonlinear recording on the ratio $\overline{I}/\overline{I}_n$ can be seen here; at the lower K value the intermodulation noise causes the peak of the $\overline{I}/\overline{I}_n$ curve to occur at higher transmittances, whereas for linear recording the ratio $\overline{I}/\overline{I}_n$ reaches a maximum near a bias transmittance of 0.5. We see that the calculated curves are in agreement with the

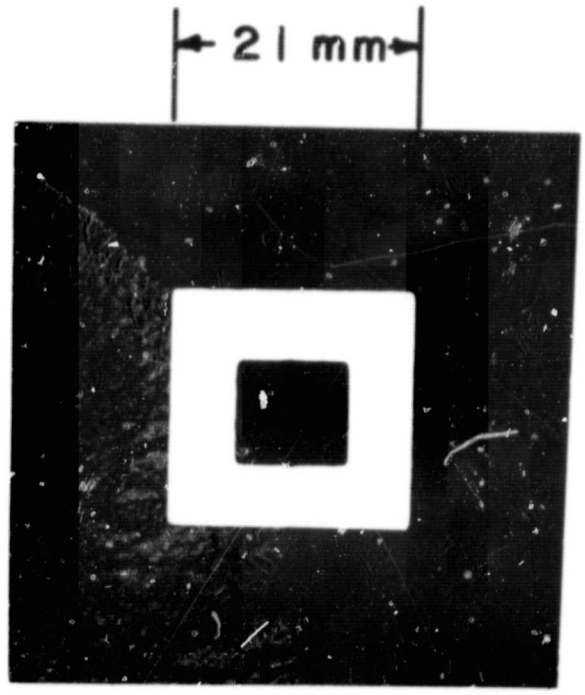

DARK SQUARE OBJECT

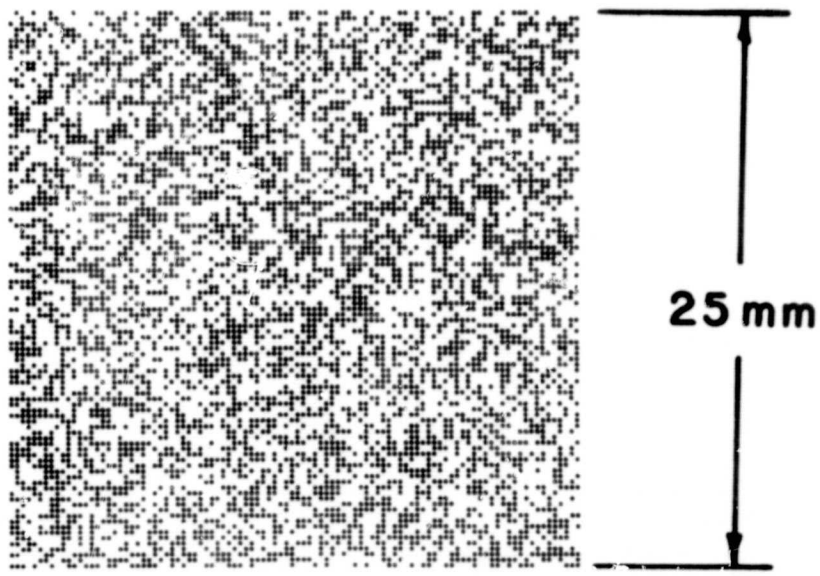

10^4 ARRAY OBJECT

FIGURE 3-19 INPUT SIGNALS USED FOR NOISE STUDIES

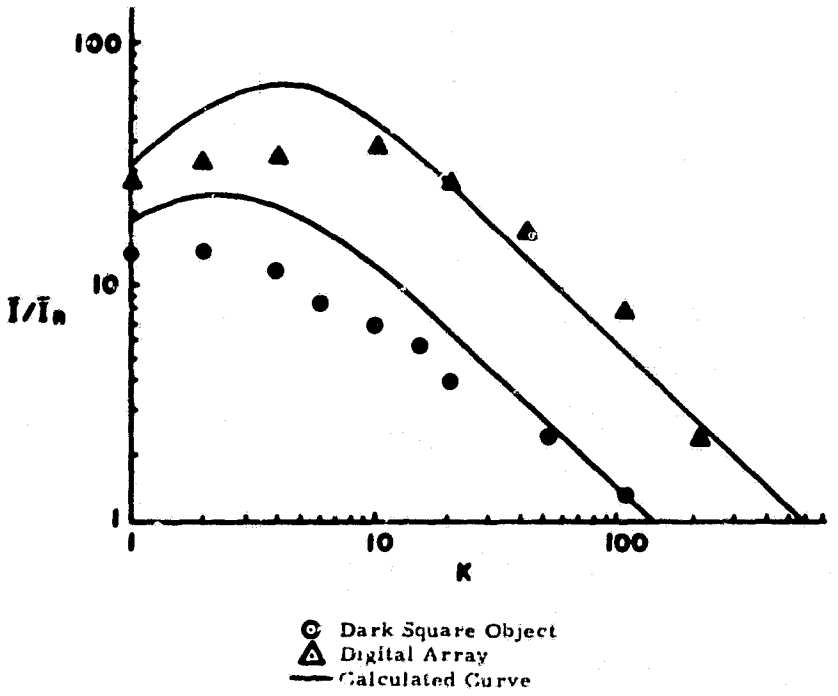

FIGURE 3-20. SIGNAL-TO-AVERAGE NOISE INTENSITY RATIO VERSUS BEAM RATIO

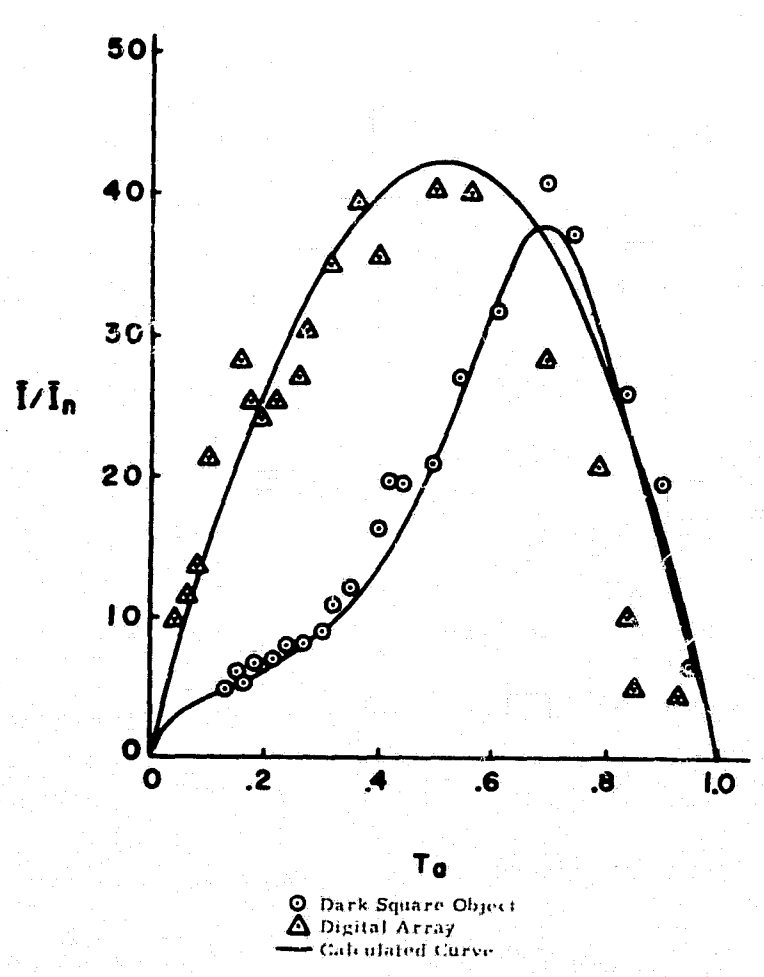

FIGURE 3-21. SIGNAL-TO-AVERAGE NOISE INTENSITY RATIO VERSUS AMPLITUDE TRANSMITTANCE

experimental values. These results suggest that, when recording nonlinearly, operating at higher amplitude transmittances will produce the maximum $\bar{I}/\bar{I}_n$ ratio.

The measured $\bar{I}/\bar{I}_n$ ratio as a function of the hologram aperture size is shown in Fig. 3-22. Both the dark square and the digital array objects were used; the hologram parameters were $T_a = 0.5$ and K=4. We found the ratio $\bar{I}/\bar{I}_n$ to be fairly independent of the hologram aperture (Ref. 8 and 12); however, the variance of the noise becomes greater as the aperture size is decreased. The standard deviation of $\bar{I}/\bar{I}_n$ is shown for the case of the dark square. There is marked improvement in the resolution of the image as the aperture is increased, but little change in $\bar{I}/\bar{I}_n$ ratio, until the aperture size of the hologram is large enough to resolve the highest spatial frequency of the ground glass diffuser used to back the object (Ref. 12). Beyond this point, the number of resolvable points in the reconstruction will be independent of the area of the hologram. Then the $\bar{I}/\bar{I}_n$ ratio, which depends on the ratio A_t/N, should increase as the area A_t increases further.

The average noise scattered from a uniformly exposed plate was compared to that scattered by a hologram for various amplitude transmittance values. The normalized average noise intensity from holograms of the dark square object is shown in Fig. 3-23 along with the average noise from a uniformly exposed plate. Both the hologram and the uniformly exposed plate were recorded on Kodak 649F emulsion and similarly processed.

Fig. 3-23 shows that the average noise intensity of a uniformly exposed plate was considerably higher than the average noise from a hologram, each having an average amplitude transmittance of 0.5. The difference is attributed to the fringe structure of the hologram; even though the average amplitude transmittance is 0.5 dark and bright fringes will have amplitude transmittances that are less than and greater than 0.5. The film grain noise of a uniformly exposed plate reaches a maximum at an amplitude

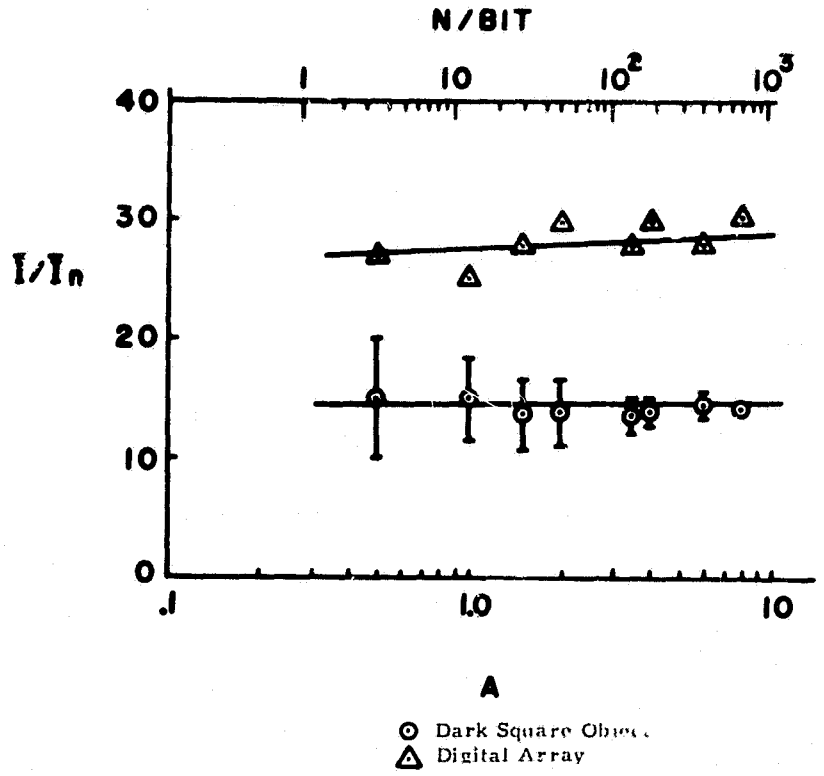

FIGURE 3-22. SIGNAL-TO-AVERAGE NOISE INTENSITY RATIO VERSUS HOLOGRAM APERTURE

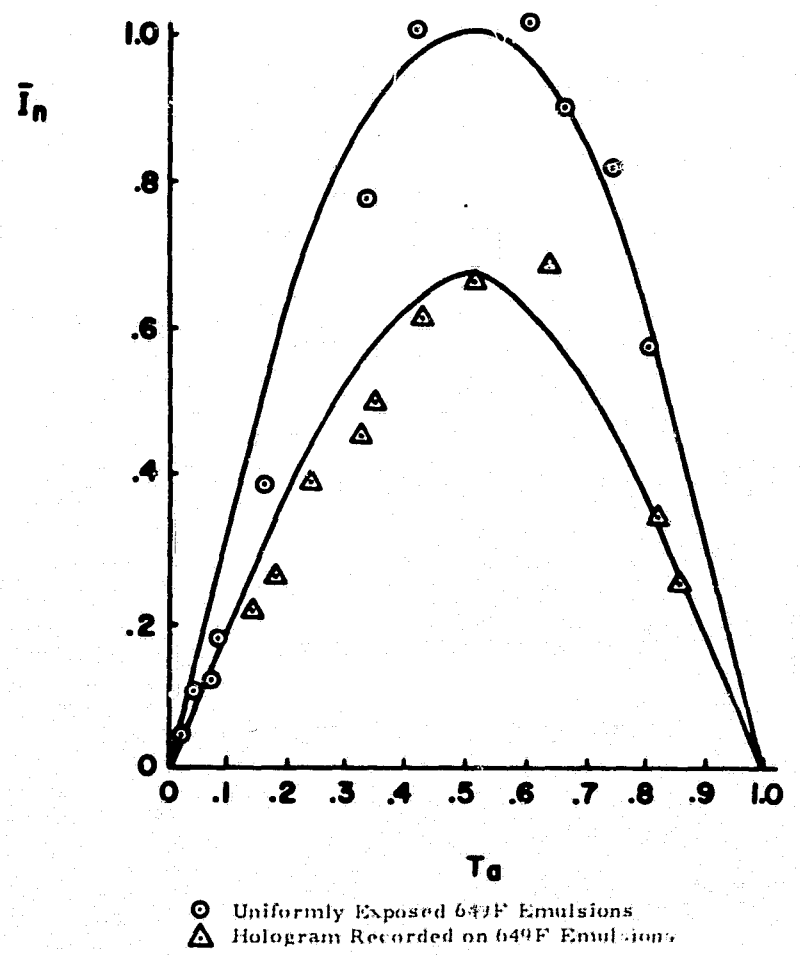

FIGURE 3-23. NORMALIZED NOISE INTENSITY VERSUS AMPLITUDE TRANSMITTANCE

transmittance of about 0.5 and falls off sharply for higher and lower values of transmittance. Therefore, the fringe structure of a hologram having regions of less and greater transmittance than the measured average value will scatter less light than a uniformly exposed plate of the same average value. Also shown in Fig. 3-23 are the calculated curves report by Goodman (Ref. 12), for the checkerboard model. We see from this and previous curves that the checkerboard model is a good approximation to the film grain noise.

The diffraction efficiency of a recording material can be calculated from Eq. (3-25) where

$$D.E. = \frac{I_s (\lambda d)^2}{I_p A_t} = \frac{K(E_0 s_1)^2}{(K+1)^2} \quad \frac{F^2}{N} \tag{3-37}$$

for a linearly recorded hologram. We experimentally determined the diffraction efficiency of a hologram made of a point object as a function of the bias transmittance. We compared these data with a curve calculated from Eq. (3-37) for a value of $F^2 = 1$. These results are shown in Fig. 3-24.

3.4.4 Discussion

The signal-to-average-noise intensity ratio as a function of the various recording parameters has been determined analytically and experimentally in previous sections. Here we want to point out that this ratio can also be used to estimate the recording capacity of the photographic film. From a theoretical point of view the recording capacity of the photographic film in a holographic memory should be determined by the signal-to-noise ratio in the reconstruction of the hologram. The signal-to-noise ratio is generally defined as the ratio of the average intensity of the signal to the variance of the random fluctuation of the noise process. The nature of the intermodulation noise makes it difficult to find the variance of the fluctuation of the noise

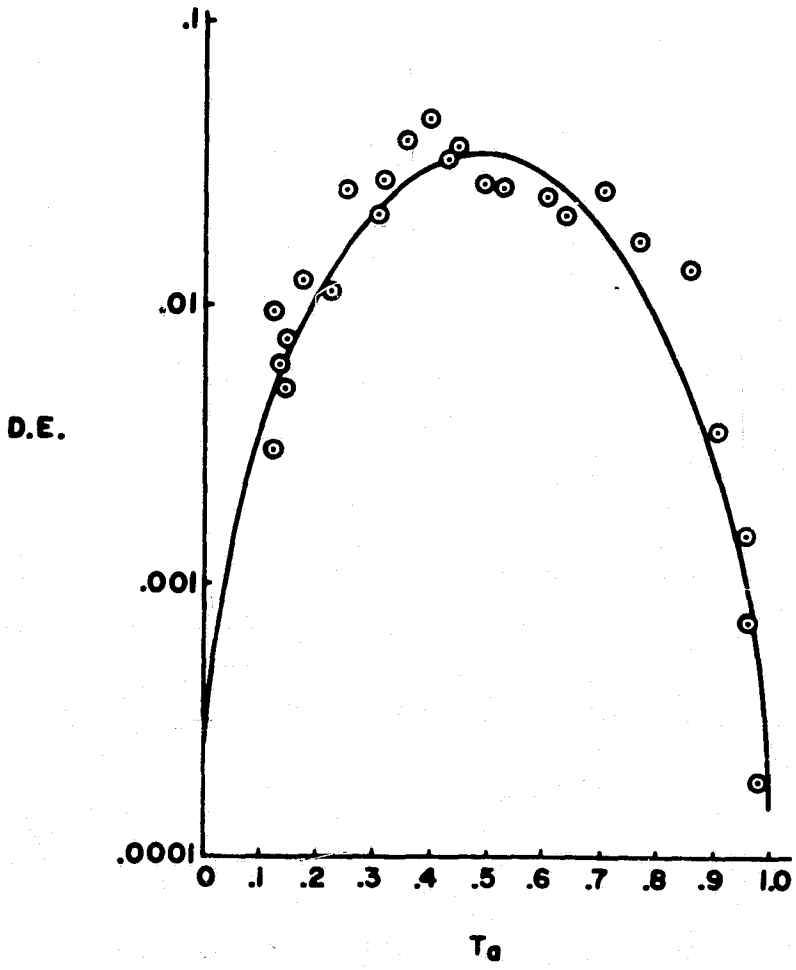

FIGURE 3-24. DIFFRACTION EFFICIENCY VERSUS AMPLITUDE TRANSMITTANCE

in a generalized reconstructed image. However, there are two approaches for developing a criterion for determining the recording capacity of the photographic emulsion. In the first approach, we assume that the hologram is linearly recorded and that the noise caused by the granular structure in the film is a Gaussian random process so that the variance of the noise is equal to one-half the average noise intensity. In this case a signal-to-noise ratio can be obtained directly, and it is proportional to $\bar{I}/\bar{I}_n$ ratio discussed previously. In the second approach we simply use the $\bar{I}/\bar{I}_n$ ratio as the criterion to determine the storage capacity of the photographic emulsion. This criterion may be called the level of detectability since its value is determined by the readout detectors. Once this value is shown, we can use an experimental curve, similar to the one shown in Fig. 3-18, to determine the maximum number of points that can be recorded and read out correctly for linearly recorded information. This number will then define the recording capacity of the recording material.

As an example of the recording capacity, suppose that the detecting system will perform satisfactorily if the $\bar{I}/\bar{I}_n$ ratio is 10 dB. From Fig. 3-18 the number of resolution elements that can be coherently recorded is given by 10 log NK, where K is assumed to be large enough to provide a linear recording. Let us assume that K=10; we therefore see that 10^6 resolution elements can be recorded with a $\bar{I}/\bar{I}_n$ ratio of 10 dB. Now suppose that 10 resolution elements constitute one bit of stored data, we see that the storage capacity is approximately 10^5 bits if the hologram is made with the same geometry as shown in Fig. 3-4. Therefore, 10^5 bits could be recorded on a 4.5 mm^2 hologram with a $\bar{I}/\bar{I}_n$ ratio, for each resolution element, of about 10 dB. The storage capacity can be increased by having each bit contain less than 10 resolution cells; however, the variance of the signal detected by the photodetector will increase, placing an eventual limitation on the number of resolution cells per bit.

3.5 ERROR RATES AND STORAGE CAPACITIES OF HOLOGRAPHIC MEMORIES

3.5.1 Introduction

When retrieving information from a holographic memory, a beam of coherent light illuminates the hologram so that a real image of the stored information appears at the plane of a detector. The information is converted into electronic signals by using, for example, an array of photodiodes or phototransistors. Because the holograms may be recorded on photographic materials, the complex amplitude of the image at the plane of the detector will contain additive noise which may be caused by combinations of the film grain noise, the surface relief noise, or the nonlinear characteristics of the photographic material. In the present study we use a model for the random noise to find the error probabilities and the storage capacities of the holographic memory system. In our model for the random noise we assume that the noise is primarily caused by the granular structure of the photographic material. Noise caused by the surface relief and the nonlinearity of the photographic film is assumed to be suppressed sufficiently by controlling the holographic recording parameters (Ref 15). In modeling the behavior of the random noise in the reconstruction, we assume that the spatial fluctuation of the complex amplitude of the noise is a stationary, Gaussian random process. Therefore, the joint probability density of the real part and the imaginary part of the noise at a point in the reconstructed image is given by

$$p(n_r, n_i) = \left(\frac{1}{2\pi\sigma^2} \right) \exp\left[-(n_r^2 + n_i^2)/2\sigma^2 \right] \qquad (3\text{-}38)$$

where n_r and n_i are the real and imaginary parts of the random noise. The constant σ^2 is the variance of the noise.

Using this model for the random noise in the reconstruction, we can find the error rate and the storage capacity for holographic memories which

uses one of two different data formats for storing information on the holograms. In one format the information is a sequence of binary digits represented by an array of point sources. In the second data format the binary digits are represented by an array of square apertures. Fig. 3-25 shows examples of these data formats. In this analysis we asuume that intensity of each element of the data format has one of two possible fixed values.

3.5.2 Array of Point Sources

We begin by assuming that the photodiodes have infinitesimal areas. The signal detected by a photodiode at the detector plane (the reconstruction plane of the hologram) will be proportional to

$$I_1 = |s + n|^2, \tag{3-39}$$

where s is the complex amplitude of a point source reconstructed from the hologram and n is the complex amplitude of the random noise at the position of the photodiode. Because the data is binary, the signal s is euqal to either $\sqrt{E}\ \exp(j\theta)$ or 0, where E is the intensity of the point source. The phase angle θ of the signal is assumed to be unknown. We want to determine, from the photodetector output I_1, whether a signal has occurred; this problem is a hypothesis testing problem. In one hypothesis, which we call H_1, the parameter I_1 is given by

$$I_1 = |\sqrt{E}\ \exp(j\theta) + n|^2 \tag{3-40}$$

In the second hypothesis, which we call H_0, the parameter I_1 is simply

$$I_1 = |n|^2 \tag{3-41}$$

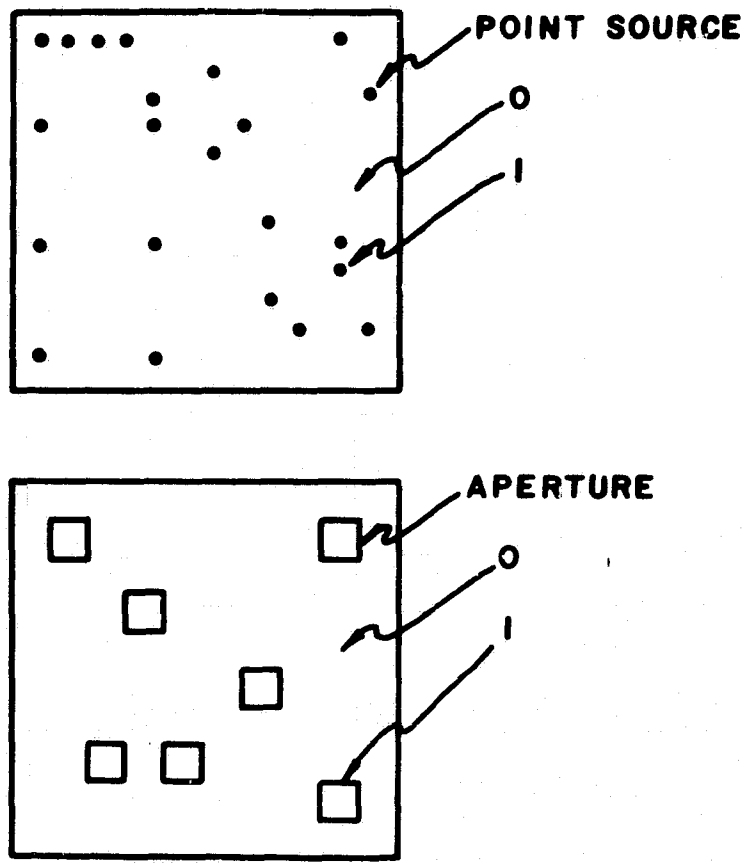

FIGURE 3-25. INPUT DATA FORMATS

We can determine whether I_1 comes from hypothesis H_1 or hypothesis H_0 with minimum error by using the likelihood ratio.

$$L(I_1) = p_1(I_1)/p_0(I_1) \quad . \tag{3-42}$$

The functions $p_1(I_1)$ and $p_0(I_1)$ are the probability density functions of I_1 under the two hypotheses. From the received value of I_1, we compute the likelihood ratio $L(I_1)$ and compare it to a predetermined threshold γ. If $L(I_1)$ exceeds the threshold, we say that I_1 comes from the hypothesis H_1 and $s = \sqrt{E}\exp(j\theta)$; otherwise we assume that hypothesis H_0 is true and $s=0$. The threshold is determined by the costs that we assign to the possible outcomes of each test, but if we assign equal costs for making incorrect decisions, the threshold is equal to 1. This problem as formulated is similar to the problem of target detection by pulse radar studied by Marcum (Ref. 16).

The probability density functions $p_1(I_1)$ and $p_0(I_1)$ can be found from the probability density of the noise as given in Eq. (3-38). Moreover, the probability density $p_0(I_1)$ can be obtained as a special case of $p_1(I_1)$ by setting $E=0$. If we let

$$b = \sqrt{E}\ \exp(j\theta) + n \tag{3-43}$$

and if we substitute Eq. (3-43) into Eq. (3-40), the parameter I_1 equals $|b|^2$. Because n is a Gaussian random variable, b is also a Gaussian random variable and its probability density function is given by

$$p(b_r, b_i) = \left(\frac{1}{2\pi\sigma^2}\right) \exp\left\{-\frac{1}{2\sigma^2}\left[(b_r - \sqrt{E}\cos\theta)^2 + (b_i - \sqrt{E}\sin\theta)^2\right]\right\}, \tag{3-44}$$

where b_r and b_i are the real and imaginary parts of b. We can express the probability density function of b in terms of its amplitude $|b|$ and

phase ϕ by using a simple transformation; the probability density function of b then becomes

$$p(|b|,\phi)=\begin{cases}(|b|/2\pi\sigma^2)\ \exp -\frac{1}{2\sigma^2}\left[|b|^2+E-2|b|\sqrt{E}\cos(\phi-\theta)\right] \text{ for } |b|\geq 0;\\ 0 \text{ for } |b|<0.\end{cases} \tag{3-45}$$

Finally, we obtain the probability density function of $|b|$ by integrating over the variable ϕ.

$$p(|b|)=\begin{cases}(|b|/\sigma^2)\ \exp\left[-(|b|^2+E)/2\sigma^2\right] I_0\left(|b|\sqrt{E}/\sigma^2\right) \text{ for } |b|\geq 0;\\ 0 \text{ for } |b|<0,\end{cases} \tag{3-46}$$

where the $I_0(x)$ is a modified Bessel function. Because I_1 is equal to $|b|^2$ under hypothesis H_1, the probability density function $p_1(I_1)$ is

$$p_1(I_1)=\begin{cases}\left(\frac{1}{2\sigma^2}\right)\exp\left[-(I_1+E)/2\sigma^2\right] I_0\left(\sqrt{I_1 E}/\sigma^2\right) \text{ for } I_1\geq 0;\\ 0 \text{ for } I_1<0.\end{cases} \tag{3-47}$$

and we note that the probability density function $p_1(I_1)$ does not depend upon the phase angle θ. If we set $E=0$ in Eq. (3-47), we obtain

$$p_0(I)=\begin{cases}\left(\frac{1}{2\sigma^2}\right)\exp\left(\frac{-I_1}{2\sigma^2}\right) \text{ for } I_1\geq 0;\\ 0 \text{ for } I_1<0.\end{cases} \tag{3-48}$$

If we substitute Eq. (3-47) and Eq. (3-48) into Eq. (3-42), the likelihood ratio becomes

$$L(I_1) = \exp\left(\frac{-E}{2\sigma^2}\right) I_0\left(\frac{\sqrt{I_1 E}}{\sigma^2}\right) . \qquad (3\text{-}49)$$

The output from the photodiode is used to calculate the likelihood ratio $L(I_1)$ which is then compared with a threshold γ. Because the likelihood ratio is a monotonically increasing function of I_1, the detection can also be performed using I_1 directly. The new detection threshold γ' is the solution of the equation

$$L_1(\gamma') = \gamma \qquad (3\text{-}50)$$

In Fig. 3-26 we have plotted $p_1(I_1)$ for three values of E/σ^2. As we have indicated previously, the function $p_1(I_1)$ is equal to $p_0(I_1)$ when $E/\sigma^2 = 0$. Therefore, the curve corresponding to $E/\sigma^2 = 0$ in Fig. 3-26 shows the functional forms of $p_0(I_1)$. The intersection of the curve $p_1(I_1)$ with the curve $p_0(I_1)$ gives us the threshold γ'.

In using the likelihood ratio to determine the binary data stored in the hologram, we may make two kinds of errors. One error is to decide that the binary digit is 1 when, in fact, its value is 0. The probability of making such an error is

$$\begin{aligned} P_1(F) &= \int_{\gamma'}^{\infty} p_1(I_1)\, dI_1 \\ &= \int_{\gamma'}^{\infty} \frac{1}{2\sigma^2} \exp\left(-\frac{I_1}{2\sigma^2}\right) dI_1 \\ &= \exp\left(-\frac{\gamma'}{2\sigma^2}\right) \end{aligned} \qquad (3\text{-}51)$$

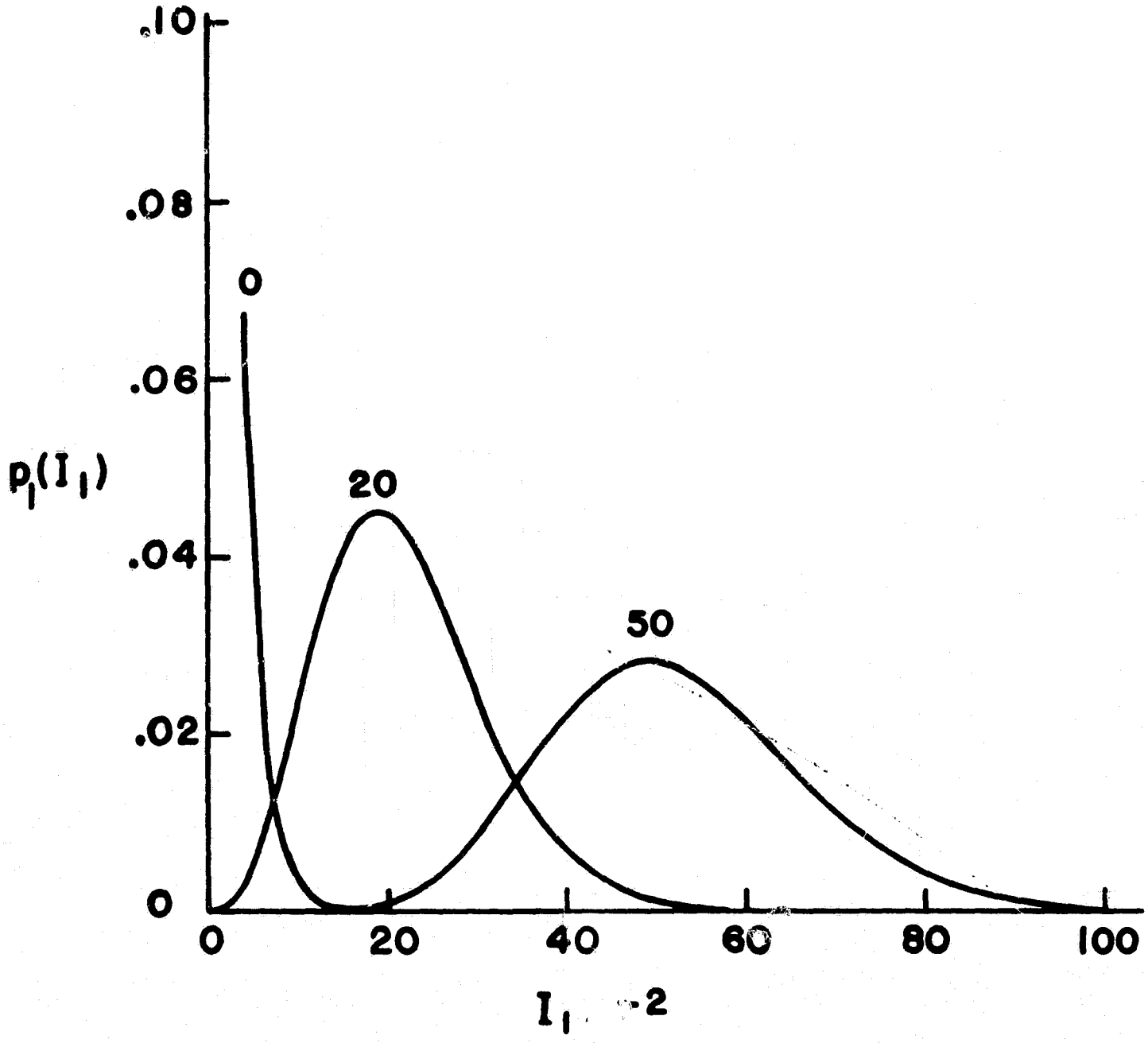

FIGURE 3-26. PROBABILITY DENSITY FUNCTION FOR DIFFERENT SNR

We also make an error if we decide that the binary digit is 0 when the actual binary digit is 1. The probability of making this error is

$$P_1(M) = \int_0^{\gamma'} p_0(I_1)\, dI_1$$

$$= \frac{1}{2\sigma^2} \exp(-E/2\sigma^2) \int_0^{\gamma'} I_0(\sqrt{I_1/E}\sigma^2) \exp(-I_1/2\sigma^2)\, dI_1 \quad (3\text{-}52)$$

If $\frac{I_1}{2\sigma^2}$ is replaced by y^2, Eq. (3-52) may be written

$$P_1(M) = \frac{1}{2\sigma^2} \exp(-E/2\sigma^2) \int_0^{\gamma'} y I_0(y\sqrt{E}/\sigma^2) \exp\left[-\frac{y^2}{2\sigma^2}\right] dy$$

$$= \exp - \left(\frac{E}{2\sigma^2}\right) \int_0^{\sqrt{\frac{\gamma}{\sigma^2}}} y\, I_0\left(y\sqrt{\frac{E}{\sigma^2}}\right) \exp\left(-\frac{y^2}{2}\right) dy$$

$$= 1 - Q\left(\sqrt{\frac{E}{\sigma^2}},\ \sqrt{\frac{\gamma'}{\sigma^2}}\right) \quad (3\text{-}53)$$

where $Q(\alpha, \beta)$ is defined as

$$Q(\alpha, \beta) = \int_p^{\infty} \nu \exp\left(-\frac{\nu^2 + \alpha^2}{2}\right) I_0(\alpha, \nu)\, d\nu \quad (3\text{-}54)$$

Using the Gaussian model for the film grain noise, we can show that the average noise intensity is equal to $2\sigma^2$. The signal-to-noise

ratio E/σ^2 is, therefore, equal to one-half the ratio of the signal intensity to the average film grain noise intensity. Given some needed error probability for the holographic memory we can use Fig. 3-27 or Table 3-3 to determine the E/σ^2 ratio to achieve such performance. From the dependence of E/σ^2 ratio on the hologram parameters we can find the storage capacity of the holographic memory. The dependence of the signal-to-noise ratio on the hologram parameters has been found by Goodman (Ref. 12) and also by Kozma (Ref. 8). Using Eq. (3-46) from Ref. 8, we find that the signal-to-noise ratio E/σ^2, in terms of the hologram parameters, is given by

$$SNR_1 = E/\sigma^2 = \frac{2F^2\eta^2 K A_t}{\Phi_{\tau'\tau'}(p_o, q_o)(K+1)^2 N}, \qquad (3\text{-}55)$$

where F is a spatial frequency dependent factor, K is the reference-to-signal beam ration, $\Phi_{\tau'\tau'}(p_o, q_o)$ is the Wiener spectrum of the film grain noise, N is the total number of point sources recorded on the hologram, and η is the normalized slope of the T_a versus E curve.

The storage capacity per unit area of the recording material can be defined as

$$C_1 = N/A_t$$

$$= \frac{2F^2\eta^2 K}{\Phi_{\tau'\tau'}(p_o, q_o)(K+1)^2 SNR_1} \text{ bits/mm}^2 \qquad (3\text{-}56)$$

As an example, suppose that an error rate of 3×10^{-6} is adequate for a holographic memory. The corresponding SNR_1 is found from Table 3-3 to

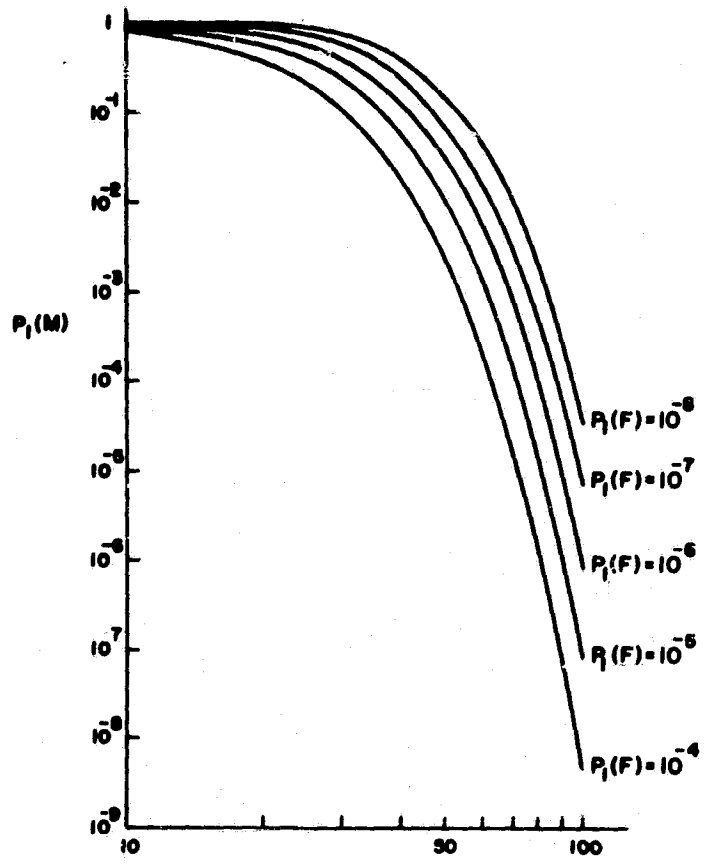

E/σ²

FIGURE 3-27. ERROR PROBABILITY VERSUS SNR

SNR	p_1 (E)	p_2 (E)M = 10
10	0.106	0.255
20	0.269×10^{-1}	0.120
30	0.709×10^{-2}	0.53×10^{-1}
40	0.191×10^{-2}	0.224×10^{-1}
50	0.522×10^{-3}	0.913×10^{-2}
60	0.144×10^{-3}	0.361×10^{-2}
70	0.398×10^{-4}	0.139×10^{-2}
80	0.111×10^{-4}	0.525×10^{-3}
90	0.308×10^{-5}	0.195×10^{-3}
100	0.862×10^{-6}	0.711×10^{-4}
110	0.242×10^{-6}	0.256×10^{-4}
120	0.678×10^{-7}	0.909×10^{-5}
130	0.191×10^{-7}	0.319×10^{-5}

TABLE 3-3: ERROR RATES vs S/N RATIO

The parameters p_1 (E) and p_2 (E) are the minimum error probabilities for point source array and aperture array respectively.

be 90. If the hologram parameters are chosen so that F = .81, K = 4, $\eta = 0.55$ and $\Phi_{\tau'\tau'} = 1.38 \times 10^{-9}$, the storage capacity, calculated using Eq. (3-56), is equal to 3.9×10^{7} bits/cm^2. The values of the hologram parameters used in calculating the storage capacity are those typically used for holographic recording on a Kodak 649F plate. This value of the storage capacity is close to the value commonly predicted for photographic materials using less exact analyses.

3.5.3 Array of Apertures

We shall now remove the restriction concerning the area of the photodiodes. With this restriction removed, the output from the photodiode under hypotheses H_1 is

$$I_2 = \sum_{m=1}^{M} \left| \sqrt{I_s}\ \exp^{j\theta_m} + n_m \right|^2 , \qquad (3\text{-}57)$$

where $I_s = E/A_d$, M is the number of resolution elements within the light sensitive area of the detector, and A_d is the area of both the detector and the aperture. In Eq. (3-57) we have normalized the intensity of the light within the aperture so that the total energy entering the detector is equal to E. Under hypothesis H_0 we have

$$I_2 = \sum_{m=1}^{M} |n_m|^2 . \qquad (3\text{-}58)$$

Here we shall assume that the noise samples in Eqs. (3-57) and (3-58) are statistically independent Gaussian random variables. Each term in

Eq. (3-57) will then have a probability density function similar to Eq. (3-47) and each term in Eq. (3-59) will have a probability function similar to Eq. (3-48). The probability density functions $p_0(I_2)$ are found in paragraph 3.5.4 to be

$$p_1(I_2) = \begin{cases} (1/2\sigma^2)\exp\left[-(I_2 + MI_s)/2\sigma^2\right]\left(\sqrt{\frac{I_2}{MI_s}}\right)^{M-1} I_{M-1}(\sqrt{MI_sI_2}/\sigma^2) \text{ for } I_2 > 0, \\ 0, \quad I_2 < 0 . \end{cases} \tag{3-59}$$

and

$$p_0(I_2) = \begin{cases} (1/2\sigma^2)^M \frac{I_2^{M-1}}{(M-1)!} \exp\left[-I_2/2\sigma^2\right] \text{ for } I_2 \geq 0 ; \\ 0 \text{ for } I_2 < 0 . \end{cases} \tag{3-60}$$

The likelihood ratio is, therefore,

$$L_2(I_2) = \frac{p_1(I_2)}{p_0(I_2)} = (M-1)!\left(\frac{2\sigma^2}{\sqrt{MI_sI_2}}\right)^{M-1} \exp\left[-\frac{MI_s}{2\sigma^2}\right] I_{M-1}(\sqrt{MI_sI_2}/\sigma^2). \tag{3-61}$$

Since the likelihood ratio $L_2(I_2)$ is also a monotonically increasing function of I_2, the photodetector output I_2 can again be used for detection. The probability densities $p_1(I_2)$ are shown in Figure 3-28 for three different ratios of MI_s/σ^2 and M = 10.

The error probabilities obtainable are given by

$$P_2(F) = \int_{\gamma_{2'}}^{\infty} p_0(I_2)\, dI_2 \tag{3-62}$$

and

$$p_2(M) = 1 - \int_{\gamma_2}^{\infty} p_1(I_2)\, dI_2 \tag{3-63}$$

where γ_2' is solution of the equation

$$L_2(I_2) = 1 \quad . \tag{3-64}$$

In Section 3.5.5 we find that

$$p_2(F) = \exp\left[\frac{-\gamma_2'}{2\sigma^2}\right] \sum_{k=0}^{M-1} \frac{1}{k!} \left(\frac{\gamma_2'}{2\sigma^2}\right)^k \tag{3-65}$$

and

$$p_2(M) = 1 - Q_M\left(\sqrt{\frac{MI_s}{\sigma^2}}\,,\ \sqrt{\frac{\gamma_2'}{\sigma^2}}\right) \tag{3-66}$$

where $Q_M(\alpha, \beta)$ is the generalization of the Q-function (Ref. 18). The error probability $p_2(M)$ as a function of the signal-to-noise ratio MI_s/σ^2 and for various values of $p_2(F)$ is shown in Fig. 3-29. The minimum error probability for this case is listed in the third column in Table 3-3.

We can also find the storage capacity of this holographic memory. Using again Eq. (3-46) from Ref. 8, we find that the signal-to-noise ratio MI_s/σ^2 becomes

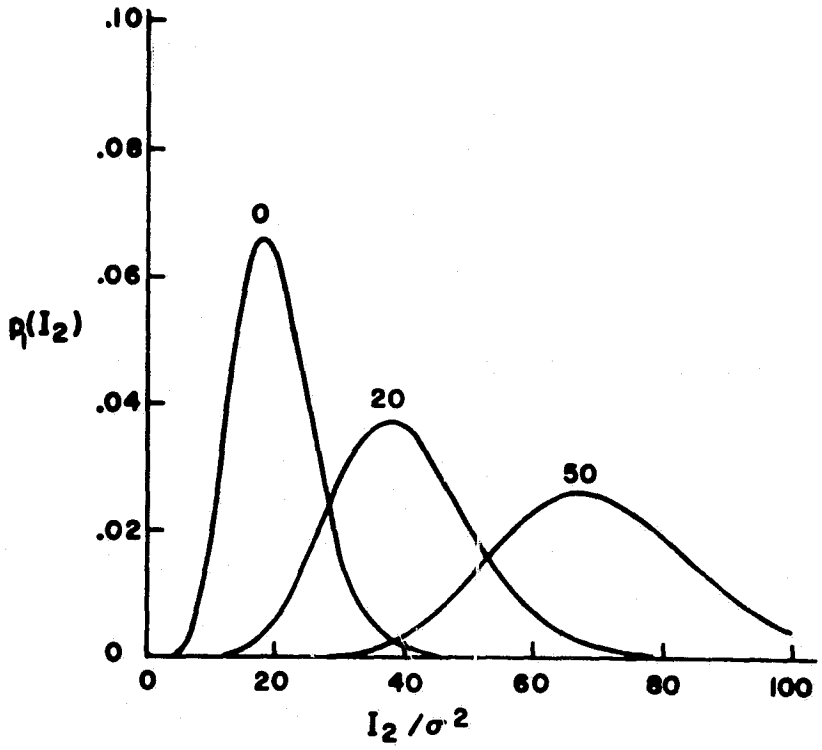

FIGURE 3-28. PROBABILITY DENSITY FUNCTION FOR DIFFERENT SNR

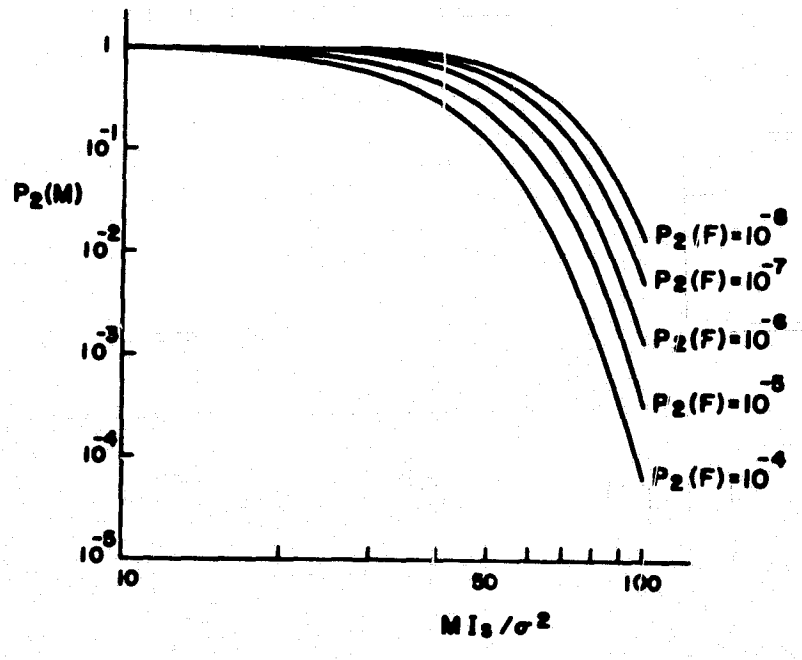

FIGURE 3-29. ERROR PROBABILITY VERSUS SNR

$$SNR_2 = \frac{2F^2K\eta^2A_t}{\Phi_{\tau'\tau'}(p_o, q_o)(K+1)^2(N/M)} \tag{3-67}$$

where N is the total number of resolution elements in the reconstructed image and M is the number of resolution elements per bit. The storage capacity is then

$$C_2 = \frac{\left(\frac{N}{M}\right)}{A_t}$$

$$= \frac{2F^2\eta^2K}{\Phi_{\tau'\tau'}(p_o, q_o)(K+1)^2SNR_2} \quad \text{bits/mm}^2 . \tag{3-68}$$

On comparing the storage capacities C_1 and C_2, we find that the storage capacity of a recording material is dependent on the signal-to-noise ratio SNR but independent of the data format. However, the error probability is dependent both on the signal-to-noise ratio and the data format. Following the numerical example given previously, we find that for the same minimum error probability, the storage capacity of the holographic memory using large detectors and apertures is 2.7×10^7 bits/cm^2. The reduction in performance of the present system is mainly due to the collection of more noise by the larger photodetectors.

3.5.4 Derivations of the Probability Density Functions $p_1(I_2)$ and $p_0(I_2)$

The probability density functions $p_1(I_2)$ and $p_0(I_2)$ of the variable I_2 given in Eq. (3-58) and Eq. (3-59) are equal to the M^{th} power of the characteristic function associated with $p_1(I_1)$ and $p_0(I_1)$ with E being substituted by MI_s. The characteristic function associated with $p_1(I_1)$ is

$$M_1(w) = \int_0^\infty \left(\frac{1}{2\sigma^2}\right) \exp\left[-(I_1 + I_s)/2\sigma^2\right] I_0(\sqrt{I_1 I_s}/\sigma^2) \exp\left[-jwI_1\right] dI_1. \quad (3\text{-}69)$$

When the series form of $I_0(\sqrt{I_1 I_s}/\sigma^2)$ is used in Eq. (3-69), we obtain

$$M_1(w) = \left(\frac{1}{2\sigma^2}\right) \exp\left[-(I_s/2\sigma^2)\right] \sum_{m=0}^{\infty} \frac{1}{m!} \left(\frac{I_s}{4\sigma^4}\right)^m \int_0^\infty \frac{I_1^m}{m!} \exp\left[-(jw+\frac{1}{2\sigma^2})I_1\right] dI_1 . \quad (3\text{-}70)$$

We can solve Eq. (3-70) by using the relationship (Ref. 19)

$$\int_0^\infty \frac{x^m}{m!} \exp\left[-qx\right] dx = \frac{1}{q^{m+1}} \quad (3\text{-}71)$$

We then find that

$$M_1(w) = \left(\frac{1}{2\sigma^2}\right)\left[jw + \frac{1}{2\sigma^2}\right]^{-1} \exp(-I_s/2\sigma^2) \sum_{m=0}^{\infty} \frac{1}{m!} \left(\frac{I_s}{4\sigma^4}\right)^m \left[jw + \frac{1}{2\sigma^2}\right]^{-m} \quad (3\text{-}72)$$

The summation in Eq. (3-72) is the series form of the exponential function $\exp \frac{I_s}{(jw + 1/2\sigma^2)4\sigma^4}$. Therefore,

$$M_1(w) = (1/2\sigma^2)(jw + 1/2\sigma^2)^{-1} \exp\left[-\frac{I_s}{2\sigma^2} + \frac{I_s}{4\sigma^4(jw + \frac{1}{2\sigma^2})}\right]. \quad (3\text{-}73)$$

By letting $I_s = 0$, we obtain the characteristic function of $p_0(I_1)$:

$$M_0(w) = (1/2\sigma^2)(jw + 1/2\sigma^2)^{-1} \tag{3-74}$$

The characteristic function of $p_1(I_2)$, which is the M^{th} power of $M_1(w)$ is

$$V_1(w) = \left(\frac{1}{2\sigma^2}\right)^M \left[jw + \frac{1}{2\sigma^2}\right]^{-M} \exp\left[-\frac{MI_s}{2\sigma^2} + \frac{MI_s}{4\sigma^4(jw + \frac{1}{2\sigma^2})}\right] \tag{3-75}$$

Similarly, the characteristic function of $p_0(I_2)$ is

$$V_0(w) = (1/2\sigma^2)^M (jw + 1/2\sigma^2)^{-M} \tag{3-76}$$

The probability density function $p_1(I_2)$ can be found from the inverse Fourier transform of $V_1(w)$:

$$\begin{aligned} p_1(I_2) &= (1/2\pi) \int_{-\infty}^{\infty} V_1(w) \exp(jwI_2)\, dw \\ &= (1/2\sigma^2)^M \exp[-MI_s/2\sigma^2] \\ &\quad \int_{-\infty}^{\infty} (jw+1/2\sigma^2)^{-1} \exp\left[\frac{MI_s}{4\sigma^4(jw+1/2\sigma^2)} + jwI_2\right] \frac{dw}{2\pi}. \end{aligned} \tag{3-77}$$

Before carrying out the integration in Eq. (3-77) we substitute the series form of the exponential function into the integrand. The integral $p_1(I_2)$ can now be written as

$$p_1(I_2) = (1/2\sigma^2)\exp[-MI_s/2\sigma^2]\sum_{m=0}^{\infty}\frac{1}{m!}\left(\frac{MI_s}{4\sigma^4}\right)^m\int_{-\infty}^{\infty}\frac{\exp[jwI_2]}{(jw+1/\sigma^2)^{m+M}}\frac{dw}{2\pi}\,. \tag{3-78}$$

The integral in Eq. (3-78) can be found by using contour integration. For $I_2 > 0$

$$\int_{-\infty}^{\infty}\frac{[\exp jwI_2]}{2\pi(jw+1/2\sigma^2)^{m+M}}\frac{dw}{2\pi} = \frac{I_2^{m+M-1}}{(M+m-1)}\exp(-I_2/2\sigma^2). \tag{3-79}$$

Substituting this result into Eq. (3-78) we find that

$$p_1(I_2) = (1/2\sigma^2)\exp[-(MI_s+I_2)/2\sigma^2]\left(\sqrt{\frac{I_2}{MI_s}}\right)^{M-1}\sum_{m=0}^{\infty}\frac{\left(\sqrt{\frac{MI_sI_2}{2\sigma^2}}\right)^{2m+m-1}}{m!(m+M-1)!}$$

$$= (I/2\sigma^2)\exp[-(I_2+MI_s)/2\sigma^2]\left(\sqrt{\frac{I_2}{MI_s}}\right)^{M-1} I_{M-1}(\sqrt{MI_sI_2}/\sigma^2)$$

for $I_2 \geq 0$, (3-80)

and

$$p_1(I_2) = 0 \text{ for } I_2 < 0\,.$$

The probability density $p_0(I_2)$ can be found similarly from

$$p_0 I_2 = \frac{1}{2\pi (2\sigma^2)^M} \int_{-\infty}^{\infty} \frac{\exp[jwI_2]}{(jw+1/2\sigma^2)^M} \, dw \ . \qquad (3\text{-}81)$$

Using the identity given in Eq. (3-79) once again, we find that

$$p_0(I_2) = \begin{cases} (1/2\sigma^2)^M \ \dfrac{I_2{}^{M-1}}{(M-2)!} \ \exp[-I_2/2\sigma^2] \text{ for } I_2 \geq 0; \\ 0 \text{ for } I_2 < 0. \end{cases} \qquad (3\text{-}82)$$

3.5.5 Derivations of Error Probabilities $P_2(F)$ and $P_2(M)$

The error probability $P_2(F)$ can be written as

$$P_2(F) = 1 - \int_0^{\gamma_2'} p_0(I_2) \, dI_2$$

$$= -(1/2\sigma^2)^M \int_0^{\gamma_2'} \frac{I_2{}^{M-1}}{(M-1)!} \exp\left[\frac{I_2}{2\sigma^2}\right] dI_2 \ . \qquad (3\text{-}83)$$

In Ref. 19, p. 317, we find the following identity:

$$\int_o^u \frac{x^{M-1}}{(M-1)!} \exp[-x] \, dx = \exp[-u] \sum_{k=0}^{\infty} \frac{u^{k+M}}{(k+M)!} \ . \qquad (3\text{-}84)$$

Upon using this identity in Eq. (3-83) we obtain

$$P_2(F) = 1 - \exp\left[-\frac{\gamma_2'}{2\sigma^2}\right] \sum_{k=0}^{\infty} \frac{\left(\frac{\gamma_2'}{2\sigma^2}\right)^{k+M}}{(k+M)!}$$

$$= \exp\left(-\frac{\gamma_2'}{2\sigma^2}\right) \sum_{k=0}^{m-1} \frac{\left(\frac{\gamma_2}{2\sigma^2}\right)^{k}}{k!} \quad . \qquad (3\text{-}85)$$

The error probability $P_2(M)$ is given by

$$P_2(M) = 1 - \int_{\gamma_2'}^{\infty} p_1(I_2)dI_2$$

$$= 1 - \frac{1}{2\sigma^2} \int_{\gamma_2'}^{\infty} \left(\sqrt{\frac{I_2}{MI_s}}\right)^{M-1} \exp\left[-(I_2+MI_s)/2\sigma^2\right] I_{M-1}\left(\sqrt{MI_s I_2/\sigma^2}\right) dI_2 \qquad (3\text{-}86)$$

Replacing I_2/σ^2 by y^2 and MI_s/σ^2 by α^2, we obtain

$$P_2(M) = 1 - \int_{\sqrt{\frac{\gamma_2'}{\sigma^2}}}^{\infty} y \left(\frac{y}{\alpha}\right)^{M-1} \exp\left[-(y^2+\alpha^2)/2\right] I_{M-1}(\alpha y)\, dy$$

$$= 1 - Q_M\left(\sqrt{MI_s/\sigma^2}, \sqrt{\frac{\gamma_2'}{\sigma^2}}\right) \qquad (3\text{-}87)$$

where $Q_M(\alpha, \beta)$ which is the generalization of the Q-function is defined by

$$Q_M(\alpha, \beta) = \int_\beta^\infty y \left[\frac{y}{\alpha}\right]^{M-1} \exp\left[-(y^2 + \alpha^2)/2\right] I_{M-1}(ay)\, dy$$

$$= Q(\alpha, \beta) + \exp\left[-(a^2 + \beta^2)/2\right] \sum_{k=1}^{M-1} \left(\frac{\beta}{\alpha}\right)^k I_k(\alpha\beta) \quad . \tag{3-88}$$

SECTION IV

COMPUTER SIMULATION OF HOLOGRAPHIC MEMORY

4.1 INTRODUCTION

The purpose of the computer simulation is to analyze the achievable performance of a memory system based on presently available storage materials, and to determine the needed performance of the recording material when other system components have been specified. The major components in the holographic memory that we shall consider in the computer simulation are (1) the laser, (2) the beam deflector, (3) the block data composer, (4) the recording material and (5) the detector array. The operating parameters of each of the components interact so that the selection of these parameters cannot be made individually. For example, if we know the diffraction efficiency of the recording material, the efficiency of the beam deflector, and the spectral response of the output detector, we can determine the power and wavelength requirements of the laser. Similarly, knowing the size of the detectors, their separation, and the geometry of the system, we can determine the accuracy required of the beam deflectors. These considerations, in turn, influence the requirements on the recording material. The computer can be used for balancing the requirements of the five major system components in terms of the requirements on the optical design itself.

We have investigated a number of holographic materials and storage formats; these investigations have led to the formulation of a model which adequately characterizes the behavior of thin absorptive materials. This model has been used to determine the diffraction efficiency and the signal-to-noise ratio (SNR) of holograms recorded on photographic emulsions. As demonstrated in Paragraph 3.4, the predicted values of these parameters

are in good agreement with experimental measurements. Using the same model, we can also simulate the response of the material to any given signal and analyze the individual effects of the intermodulation noise caused by the nonlinearity and the grain noise of the recording material on the reconstructed image from this signal. The procedure and results of such simulation will be presented in Paragraph 4.2.

We also used the computer to analyze the imaging properties of holograms. Questions such as the tolerance on the repeatability of the beam deflector, and bounds on the accuracies of components, such as input block data composer, output detector array and laser wavelength, can be answered by studying the holographic imaging properties. We wrote a computer program in Fortran IV using the time sharing computer facility in our laboratory. The details relating to the analysis carried out by the computer program are presented in Paragraph 4.3. A listing of the computer program is given in Paragraph 4.4.

4.2 COMPUTER SIMULATION OF HOLOGRAPHIC RECORDING MEDIA

During the past year we initiated a computer simulation program for characterizing holographic storage materials. In this section, we shall describe our preliminary investigations in simulating the holographic recording material and present some representative results. Although these basic methods can be used to treat a broad class of recording materials, we use photographic emulsions in this study by way of an example.

In this study we assumed that the amplitude transmittance versus exposure characteristics of a thin absorptive recording medium can be represented by

$$T(E) = \frac{\beta^2}{E^2 + \beta^2} \qquad (4\text{-}1)$$

In earlier investigations we found that this function provided a good fit to the experimental data obtained for Kodak 649F photographic emulsion. To carry out the simulation of film nonlinearity, we first expand the amplitude transmittance function T(E) in a Taylor series expansion about a bias exposure E_o;

$$T(E) - t_b = \sum_{m=1}^{\infty} s_m (E-E_o)^m , \qquad (4-2)$$

where

$$s_m = \frac{1}{m!} \left. \frac{dT}{dE} \right|_{E_o}$$

In calculating the amplitude transmittance of the developed hologram, we use an exposing intensity

$$I(x) = \left| ke^{j2\pi ax} + a(x)e^{j\theta(x)} \right|^2 , \qquad (4-3)$$

where the functions $ke^{j2\pi ax}$ and $a(x)e^{j\theta(x)}$ are the wavefronts coming from the reference source and the object, respectively. For convenience, a one-dimensional signal was used; this simplification should have little bearing on the outcome of the simulation. We used a Fourier transform hologram for simulation so that $a(x)e^{j\theta(x)}$ is the Fourier transform of the signal. Upon substituting Eq. (4-3) into Eq. (4-1), we can show that the amplitude transmittance of the hologram is

$$T_a(x) = P_o(x) + P_1(x) \frac{2s_1 E_o \sqrt{K}}{(K+1)} \left(\frac{a(x)}{b}\right) \cos \left(2\pi ax - \theta(x)\right)$$

$$+P_2(x) \frac{Ks_2 E_o}{(K+1)} \left(\frac{a(x)}{b}\right)^2 \cos \left\{2 \left(2\pi ax - \theta(x)\right)\right\} + \ldots , \qquad (4-4)$$

where $b^2 = \langle a^2(x) \rangle$.

The functions $P_m(x)$ are polynomials in $\frac{a(x)}{b}$ whose coefficients are determined by the parameters $\{s_m\}$ of Eq. (4-2), the bias exposure E_o, and the reference-to-signal beam ratio K. The function $P_o(x)$ is the low spatial frequency term recorded in the hologram, so that the light distribution due to $P_o(x)$, in the reconstruction, is close to the optical axis. The second term in Eq. (4-4) is associated with the reconstructed signal. Because the carrier frequencies of the various terms in Eq. (4-4) are different, there will be no interference among the signals reconstructed from these terms. Therefore, the only term which is important for our simulation experiment is the second term of Eq. (4-4). We find $P_1(x)$ in terms of the recording signal and recording parameters:

$$P_1(x) = \Bigg[\left(1 + \frac{s_3}{s_1} \frac{3KE_o^2}{(K+1)^2} + \frac{s_5}{s_1} \frac{10K^2E_o^4}{(K+1)^4} + \cdots \right)$$

$$+ \left(\frac{a^2(x)}{b^2} - 1 \right) \left(\frac{s_2}{s_1} \frac{2E_o}{K+1} + \frac{s_3}{s_1} \frac{3KE_o^2}{(K+1)^2} \right. \qquad (4\text{-}5)$$

$$\left. + \frac{s_4}{s_1} \frac{12KE_o^3}{(K+1)^3} + \frac{s_5}{s_1} \frac{20K^2E_o^4}{(K+1)^4} + \cdots \right) + \cdots \Bigg]$$

In the simulation, Eq. (4-2) is approximated by a fifth order polynomial. We also assume that $P_1(x)$ can be approximated by its first two terms. With such an approximation the second term in Eq. (4-4) becomes

$$T_s(x) = \frac{2s_1 E_o \sqrt{K}}{(K+1)} G_1 \left[\frac{a(x)}{b}\right] \cos\left[2\pi\alpha x - \theta(x)\right] + \frac{2s_1 E_o \sqrt{K}}{(K+1)} G_2 \left[\left(\frac{a(x)}{b}\right)^2 - 1\right]\left(\frac{a(x)}{b}\right) \cos\left[2\pi\alpha x - \theta(x)\right] \tag{4-6}$$

where G_1 and G_2 are the first two coefficients of $P_1(x)$. The first term in Eq. (4-6) contains the information of the original signal. The second term, which we call a noise term, represents an additive degradation of the signal in the reconstruction.

The procedure for simulating the film nonlinearity is schematically illustrated in Fig. 4-1. Figure 4-2 shows the intensity distribution of the test signal. Each pulse in this signal contained 44 resolution elements. The complex amplitude of the test signal was first multiplied by a random phase function generated by a random number generator in the computer. The signal was then normalized so that its total energy is equal to unity. The Fourier transform of the signal was computed using a fast-Fourier transform program. A nonlinear operation was performed on the Fourier transform of the signal to simulate the nonlinear noise characteristics of the film. An inverse Fourier transform operation then transfers this noise into the image plane. The noise was combined with the linearly recorded signal. At point A we introduced into the computer the different system parameters such as the reference-to-signal beam ratio K, the bias exposure E_o, and the aperture size of the detector. For each set of system parameters, the intensity of the simulated output signal was plotted on a Calcomp plotter.

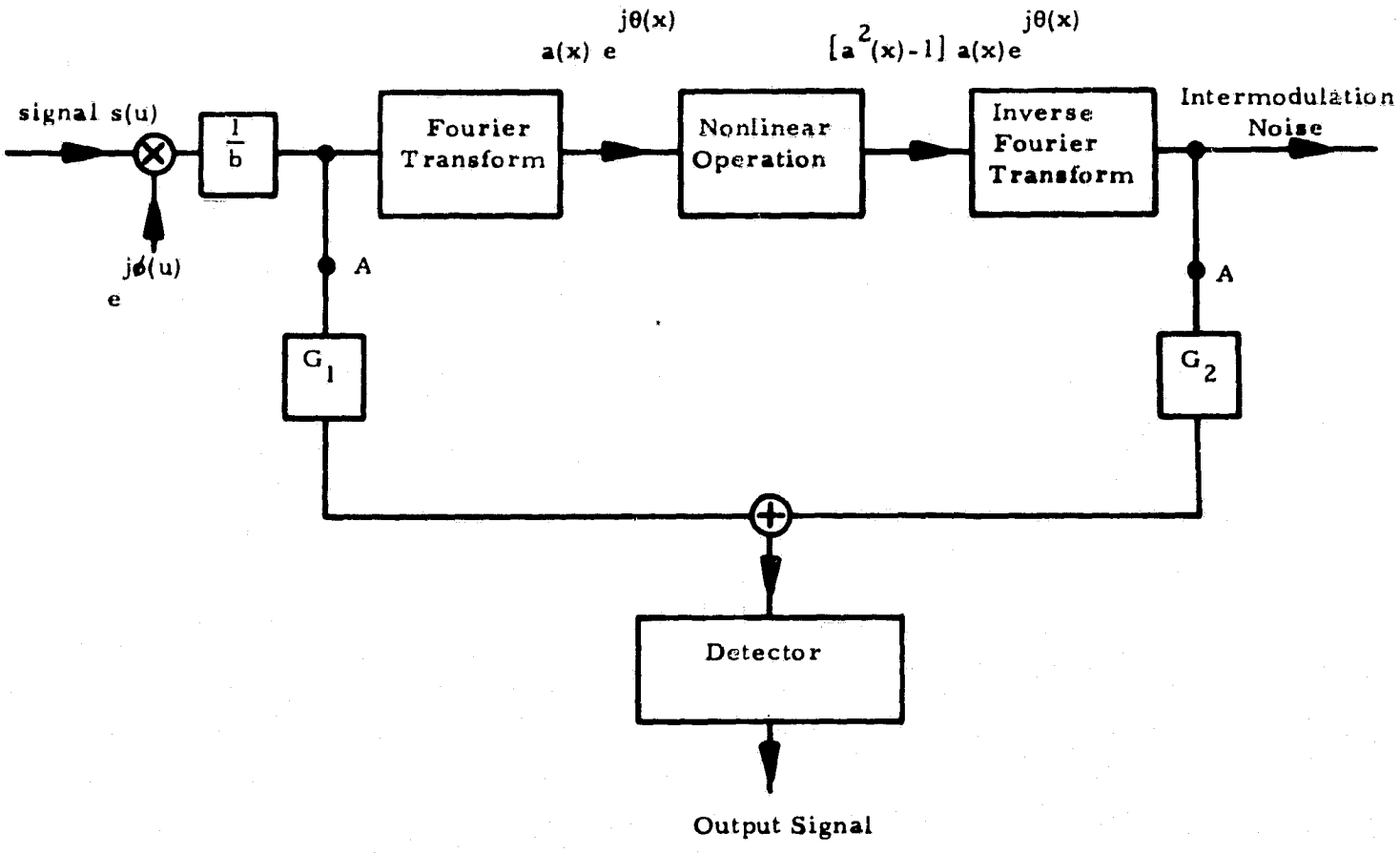

FIGURE 4-1. COMPUTER SIMULATION OF FILM NONLINEARITY

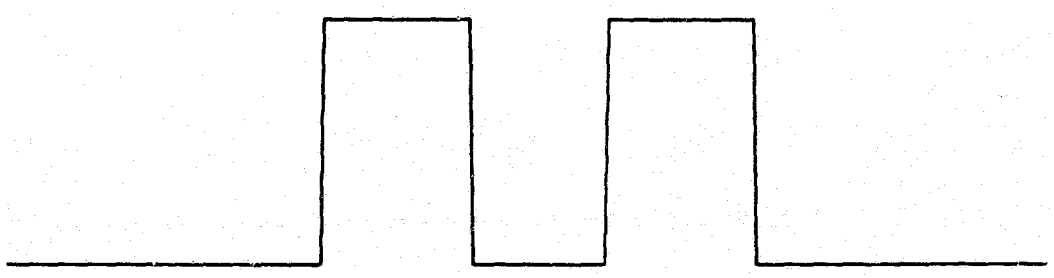

FIGURE 4-2. INPUT SIGNAL FOR SIMULATION EXPERIMENTS

Representative samples of the simulated results are given in Fig. 4-3 where we show the intensity distribution of the output signal for various reference-to-signal beam ratios and detector apertures. The relative sizes of the detector apertures were 1, 3 and 5, respectively; the beam ratio K was 2, 4, 8, and 16. For each plot the intensity of the linear signal without noise added was normalized to a fixed value. Note that the randomness of the output signal can be reduced by using a large detector aperture. We also note that the film nonlinearities introduce large fluctuations into the output signals. These fluctuations are reduced for larger beam ratios K. The inter-modulation noise is generally dependent on the structure of the signal. To investigate this aspect of the inter-modulation noise, we carried out a simulation using the signal in Fig. 4-2, adding a constant bias to the signal. The result of the simulation is shown in Fig. 4-4. No significant differences can be noted in the random fluctuation in the detector output because the constant bias does not significantly change the structure of the signal.

We also simulated the effect of film grain noise on the reconstructed image. The film grain noise in the output plane is assumed to be Gaussian noise with independent real and imaginary parts. The simulated film grain noise was generated by a subroutine and the procedure for obtaining the detector output is schematically illustrated in Fig. 4-5. The signal, at the plane of detector, is given simply by the sum of the original signal and the simulated film grain noise. The SNR, determined by the ratio of the intensity of the signal to the variance of the noise, ranged from 5 to 30 in the simulation experiment. Representative samples of the simulated results are shown in Figs. 4-6 to 4-8. Figure 4-6 shows the intensity distribution of the output signal as a function of the SNR for a detector

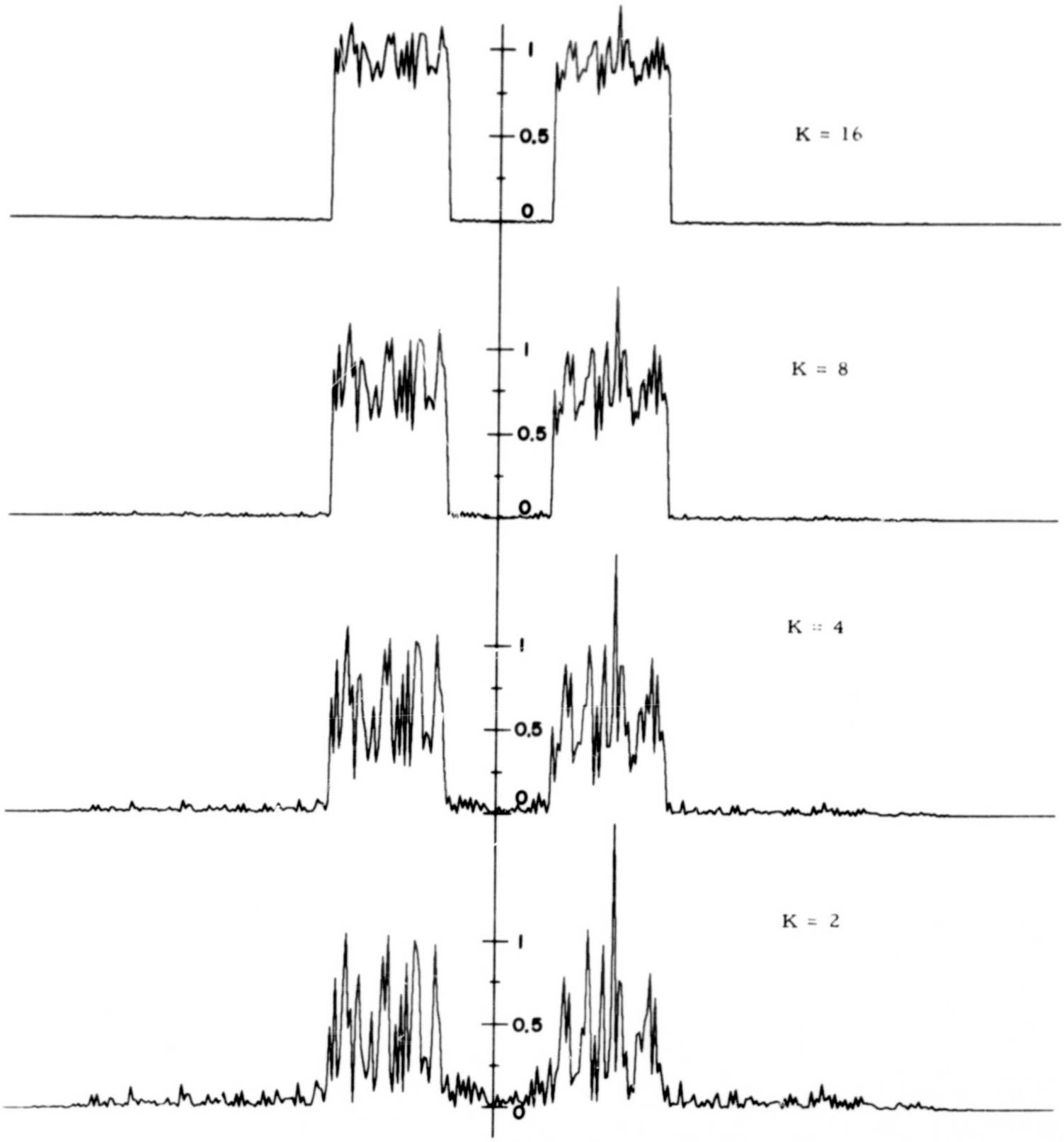

FIGURE 4-3(a). OUTPUT SIGNALS: RELATIVE DETECTOR APERTURE = 1

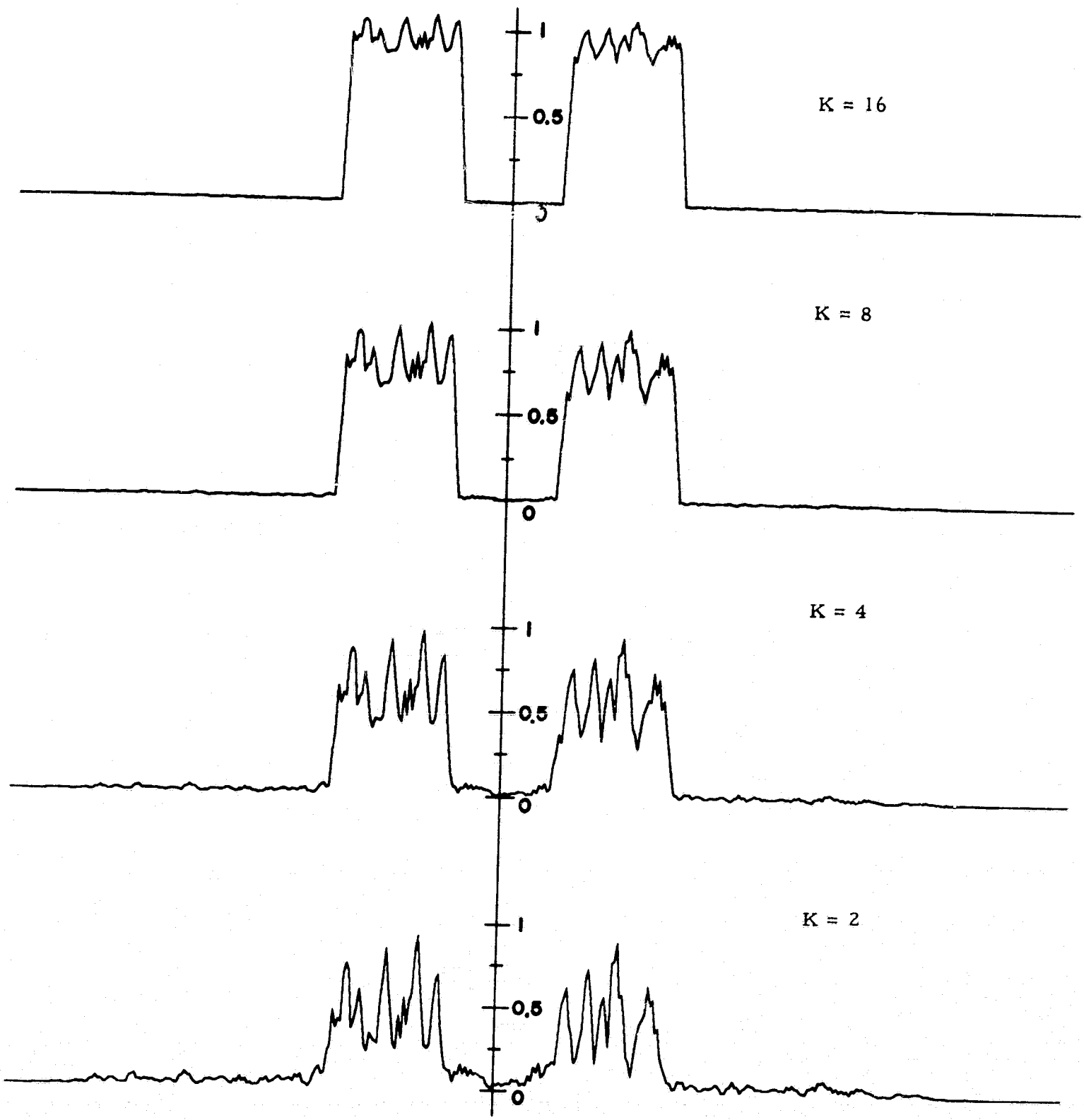

FIGURE 4-3(b). OUTPUT SIGNALS: RELATIVE DETECTOR APERTURE = 3

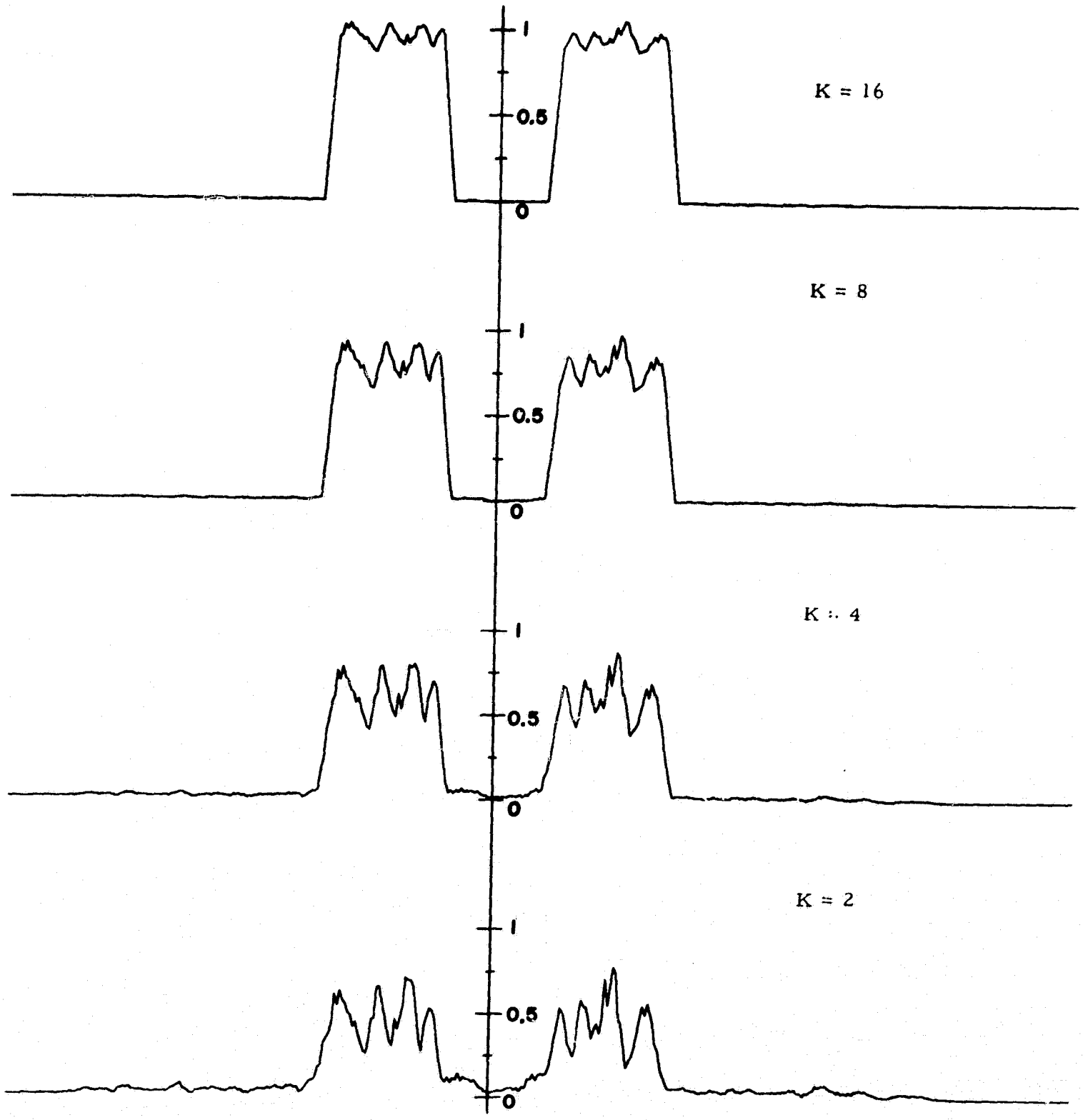

FIGURE 4-3(c). OUTPUT SIGNALS: RELATIVE DETECTOR APERTURE = 5

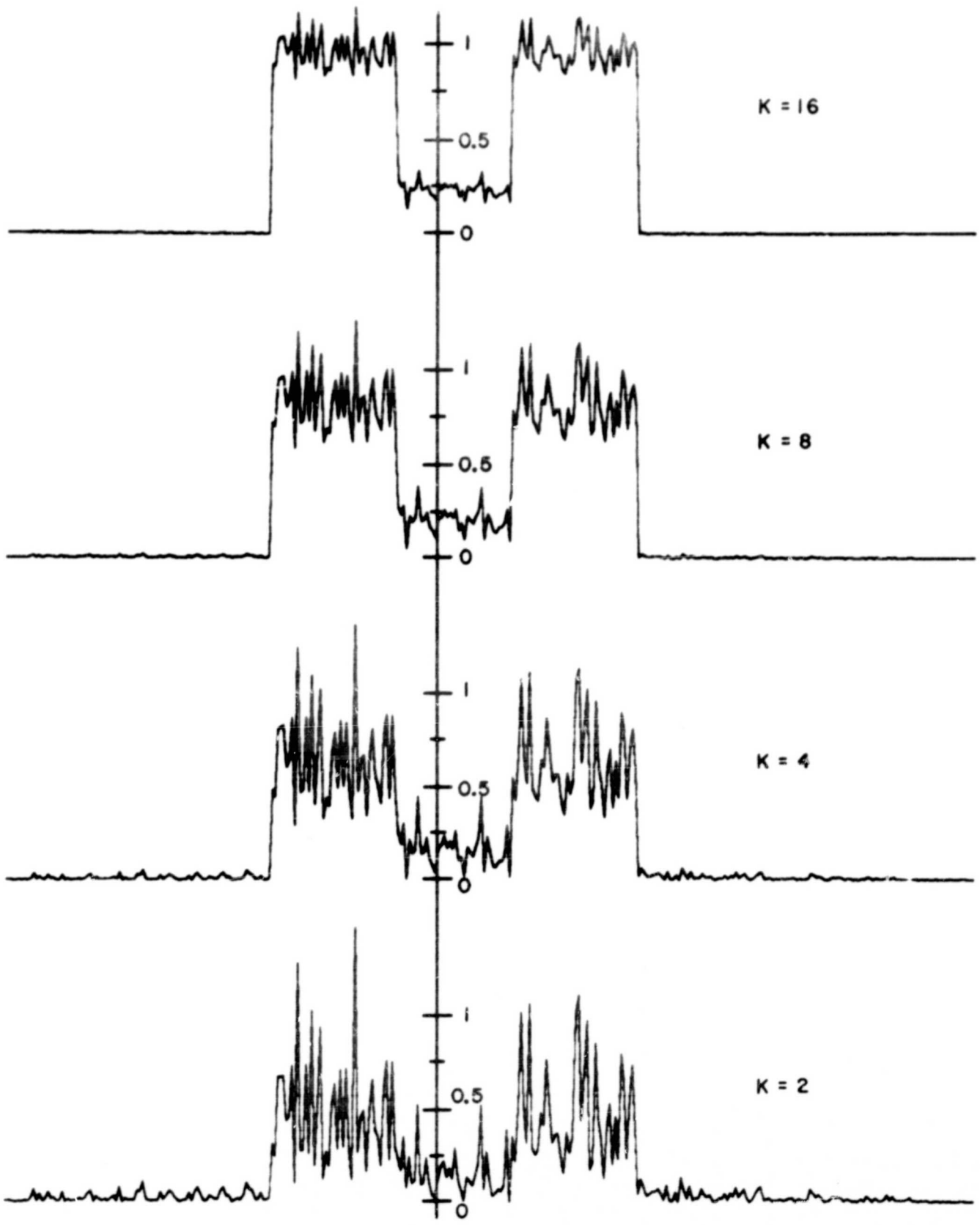

FIGURE 4-4. OUTPUT SIGNALS: ORIGINAL INPUT SIGNAL CONTAINS A CONSTANT BIAS

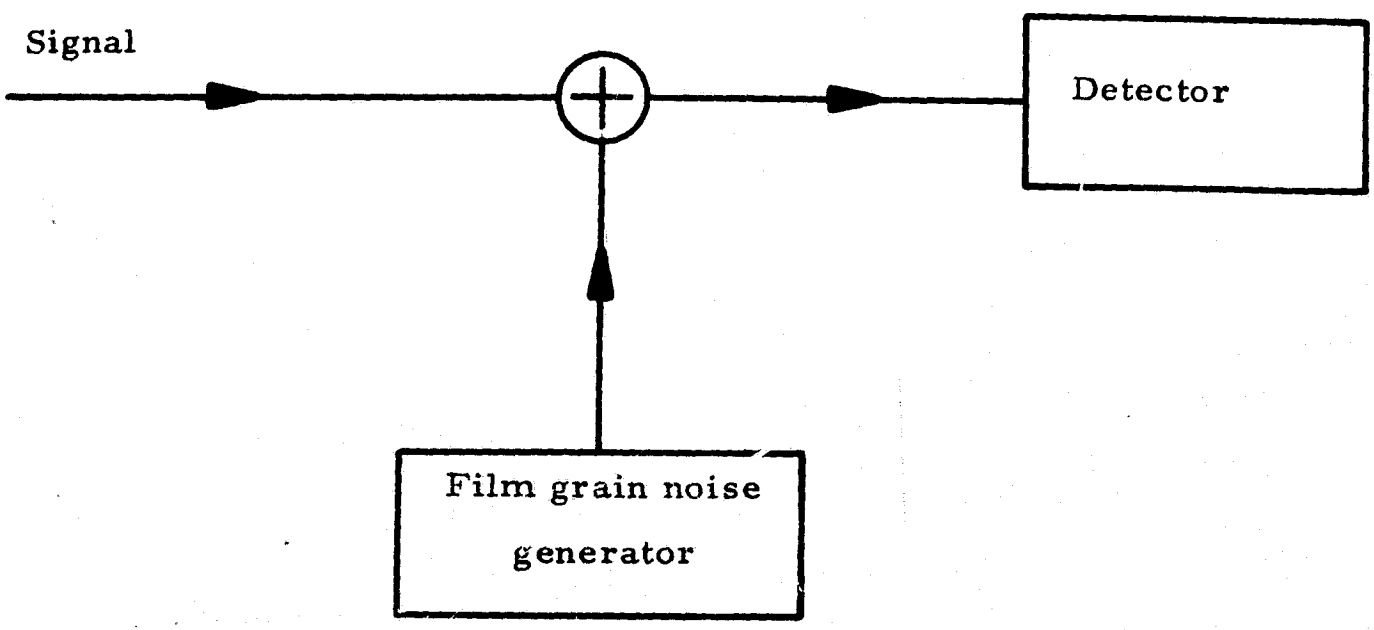

FIGURE 4-5. COMPUTER SIMULATION OF FILM GRAIN NOISE

aperture of 1. The SNR in Figs. 4-6(a) to 4-6(f) are 30, 25, 20, 15, 10 and 5, respectively. Figure 4-7 and 4-8 again show the intensity distribution of the output signal but the relative sizes of the apertures were 3 and 5, respectively. Because the Gaussian noise can assume large values, occasional large fluctuations are observed in the detector output shown in Fig. 4-6; this fluctuation is greatly reduced when the SNR is 15 or larger. The smoothing effect of the aperture can be observed in the simulated results shown in Figs. 4-7 and 4-8.

4.3 COMPUTER ANALYSIS OF HOLOGRAPHIC IMAGING

The operating parameters of the major components of the holographic memory are determined by the imaging properties of the hologram. For example, if the deflection of the readout beam does not accurately duplicate the deflection of the reference beam, the reconstructed image will be displaced and aberrated, and will be misaligned in relation to the photodetector array. Similarly, a displacement of the input block data composer will result in output misalignments. These geometrical errors increase the detection errors in the readout process.

A number of investigations dealing with the properties of holographic imaging have been reported (Ref. 21-27); the analysis of Champagne is most applicable to our situation. We have adapted his results and used a high speed digital computer to establish tolerances on the stability of the major components of the holographic memory.

Figure 4-9 shows the geometry used for the analysis of the imaging properties of holograms. The hologram is positioned at the x-y plane and the object point source O is located to the left of the x-y plane. The distance from the point O to the center of the hologram is R_O. The projection

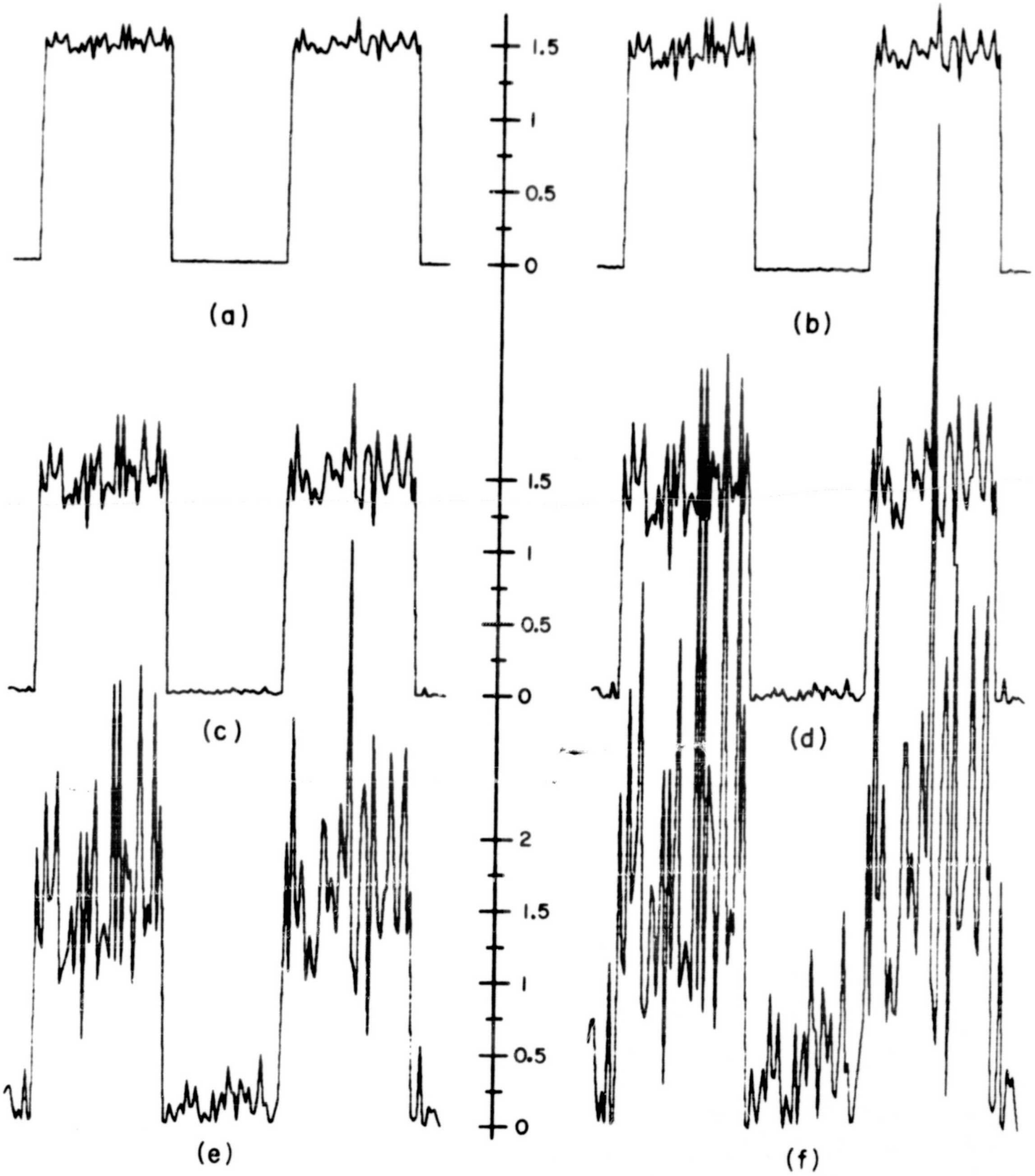

FIGURE 4-6. OUTPUT SIGNALS: RELATIVE DETECTOR APERTURE = 1

Input SNR in (a) to (f) are respectively: 30, 25, 20, 15, 10, and 5

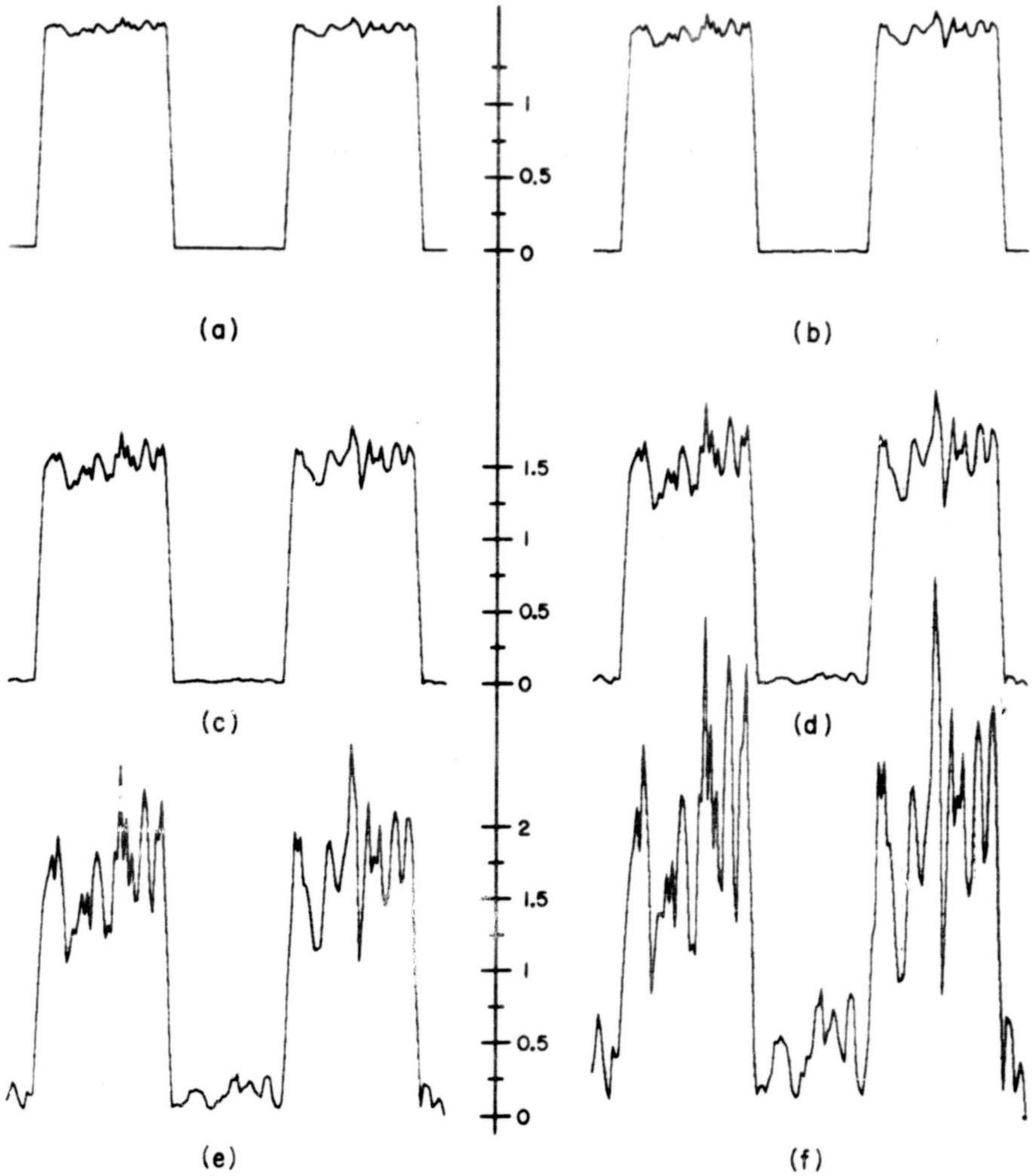

FIGURE 4-7. OUTPUT SIGNALS: RELATIVE DETECTOR APERTURE = 3

Input SNR in (a) to (f) are respectively: 30, 25, 20, 15, 10, and 5

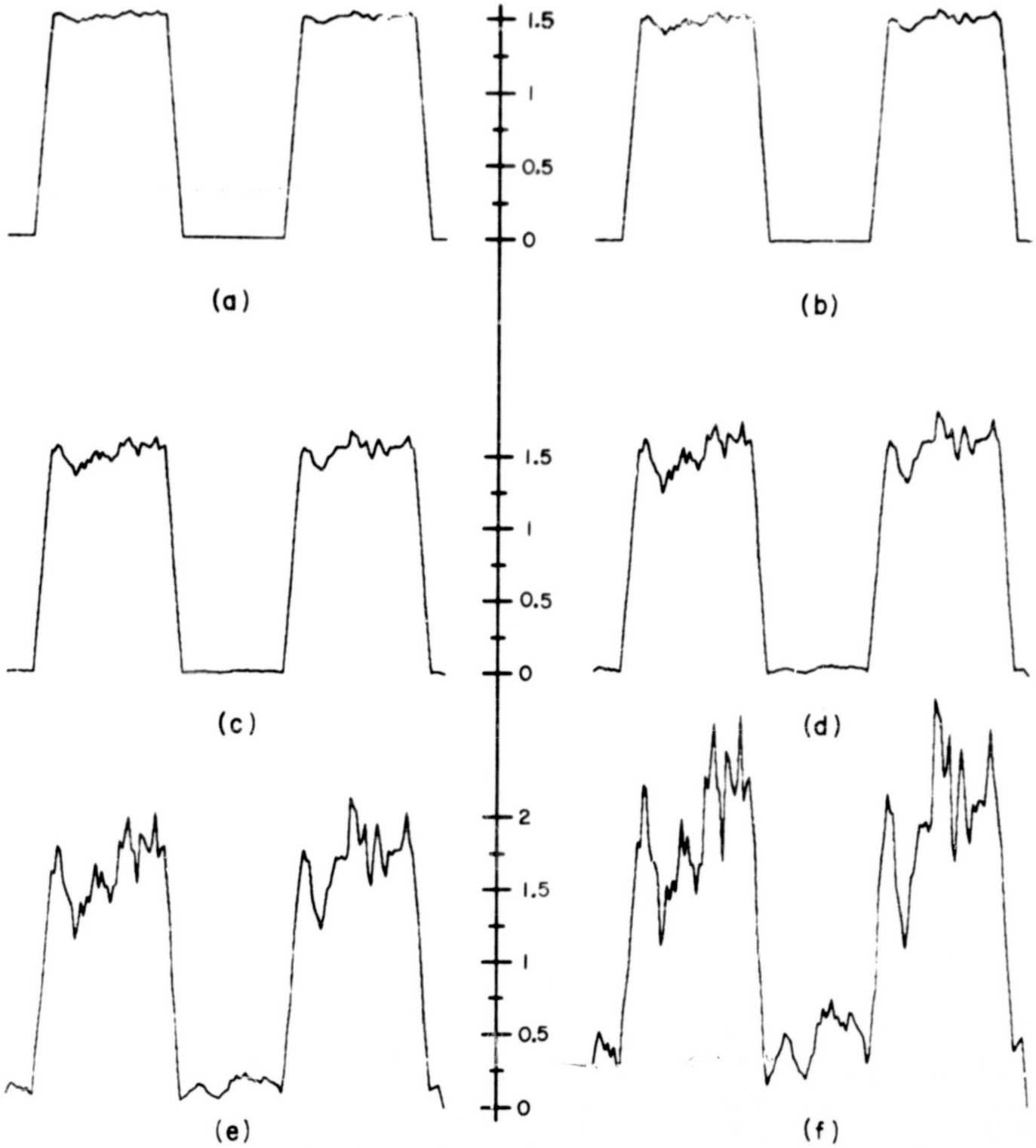

FIGURE 4-8. OUTPUT SIGNALS: RELATIVE DETECTOR APERTURE = 5

Input SNR in (a) to (f) are respectively: 30, 25, 20, 15, 10, and 5

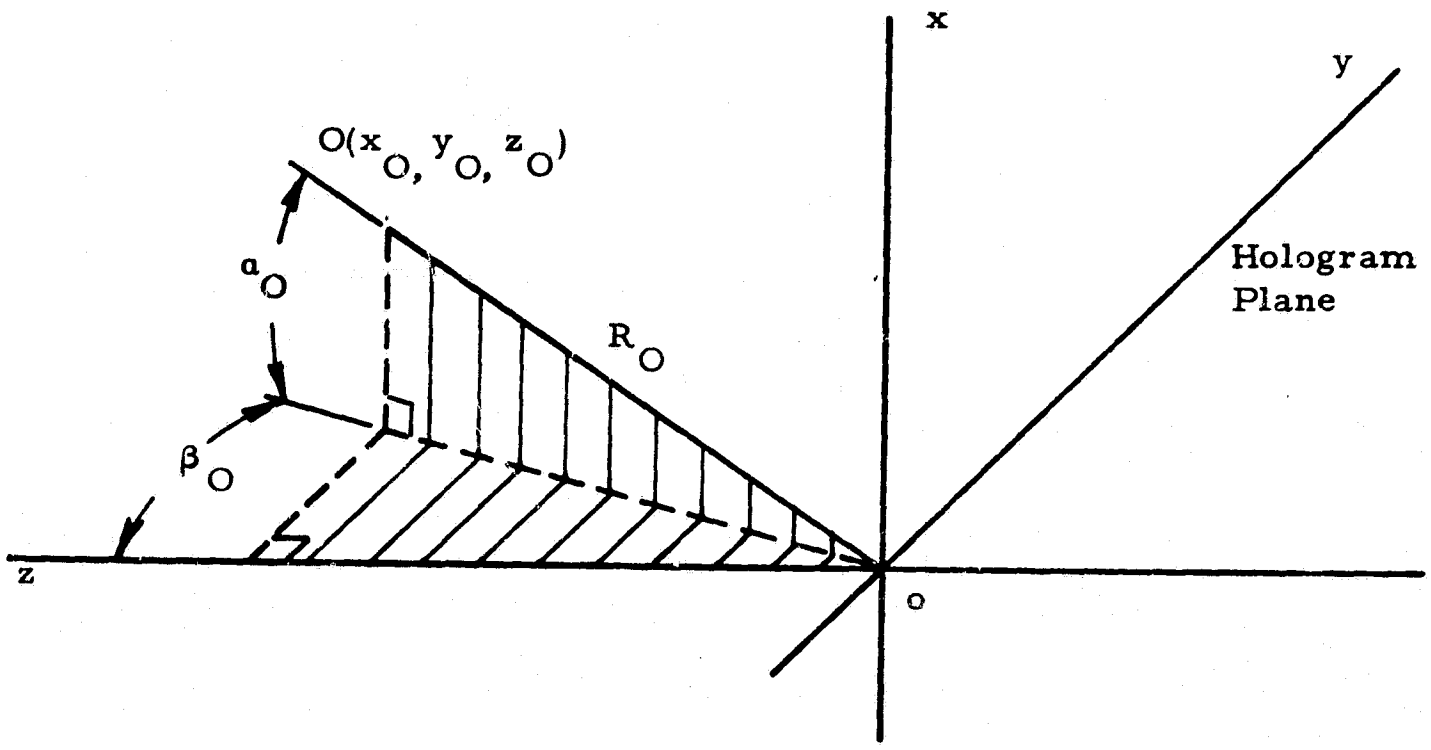

FIGURE 4-9. COORDINATE SYSTEM FOR ANALYZING HOLOGRAPHIC IMAGING

of the line R_O onto the y-z plane forms an angle β_O with respect to the x-z plane; and likewise the projection of the line R_O forms an angle α_O with respect to the y-z plane. As can be seen, the location of the point can be defined with respect to the hologram surface by the parameters R_O, α_O, and β_O. In terms of the recording and reconstruction geometries, the reference, reconstruction, and image points can be defined similarly. However the subscript O in the parameters R_O, α_O, and β_O will be replaced by R, C, and I to denote reference, reconstruction, and image points respectively; this notation is the same as the notation used in Champagne's work. The Gaussian imaging properties of the hologram are

$$\frac{1}{R_I} = \frac{1}{R_C} \pm \frac{\mu}{m^2} \left(\frac{1}{R_O} - \frac{1}{R_R} \right) \qquad (4\text{-}7)$$

$$\sin \alpha_I = \sin \alpha_C \pm \frac{\mu}{m} (\sin \alpha_O - \sin \alpha_R) \qquad (4\text{-}8)$$

$$\cos \alpha_I \sin \beta_I = \cos \alpha_C \sin \alpha_C \pm \frac{\mu}{m} (\cos \alpha_O \sin \beta_O - \cos \alpha_R \sin \beta_R) \qquad (4\text{-}9)$$

where

$$\mu = \frac{\lambda_C}{\lambda_O} \qquad (4\text{-}10)$$

and m is the scaling factor of the hologram. The plus sign is used with the virtual image and the negative sign with the real image. Since the object which represents the signal to be recorded in a holographic memory is usually planar, we find that it is more convenient to express the location of a point in Cartesian coordinates. From Eq. (4-7) to (4-9), we can obtain the position of the image in terms of its x, y, z coordinates which are given by

$$x_I = R_I(\sin \alpha_C \pm \frac{\mu}{m} \sin \alpha_R) \pm \frac{\mu}{m}\left(\frac{R_I}{R_O}\right) x_O \qquad (4\text{-}11)$$

$$y_I = R_I(\cos \alpha_C \sin \beta_C \pm \frac{\mu}{m} \cos \alpha_R \sin \beta_C) \pm \frac{\mu}{m}\left(\frac{R_I}{R_O}\right) y_O \qquad (4\text{-}12)$$

and

$$z_I = (R_I^2 - x_I^2 - y_I^2)^{\frac{1}{2}} \qquad (4\text{-}13)$$

If R_I^2 is less than $(x_I^2 + y_I^2)$, Eq. (4-13) implies that images cannot be reconstructed with the conditions provided in the reconstruction geometry. When the reconstruction duplicates the recording geometry, it is obvious from previous equations that the following conditions must be satisfied:

$$\begin{aligned} x_I &= x_O \\ y_I &= y_O \\ z_I &= z_O \end{aligned} \qquad (4\text{-}14)$$

Generally the parameters used in recording and reconstructing the hologram cannot be exactly controlled. As a result, errors in the positioning

of the image will inevitably occur. As an example, let us holographically record two points located in the same plane, one at $(0,\ 0,\ z_O)$ and the other at $(x_O,\ y_O,\ z_O)$. In reading out this hologram we shall use a reconstruction geometry which is slightly different from the recording geometry and determine the resulting shift and distortions of the images. Using Eqs. (4-7) to (4-13), we can find that the position of the image of the point located at $(0,\ 0,\ z_O)$ is given by

$$\frac{1}{R'_I} = \frac{1}{R_C} \pm \frac{\mu}{m^2}\frac{1}{z_O} - \frac{1}{R_R} \tag{4-15}$$

$$\Delta x_1 = R'_I\left(\sin\alpha_C \pm \frac{\mu}{m}\sin\alpha_R\right)$$

$$\Delta y_1 = R'^{\,2}_I\left(\cos\alpha_C \sin\beta_C \pm \frac{\mu}{m}\cos\alpha_R \sin\beta_R\right) \tag{4-16}$$

$$z_1 = R'^{\,2}_I - \Delta x_1^{\,2} - \Delta y_1^{\,2} \tag{4-17}$$

The position of the image of the object point located at $(x_o,\ y_o,\ z_o)$ can be written as

$$x_I = \frac{\mu}{m}\, x_O + \Delta x_1 + \Delta x_2 \tag{4-18}$$

$$y_I = \frac{\mu}{m}\, y_O + \Delta y_1 + \Delta y_2 \tag{4-19}$$

$$z_I = z_1 + \Delta z \tag{4-20}$$

where

$$\Delta x_2 = \pm \frac{\mu}{m} \left(\frac{R_I - R_O}{R_O} \right) x_O + (R_I - R'_I)(\sin \alpha_C \pm \frac{\mu}{m} \sin \alpha_R) \quad (4\text{-}21)$$

$$\Delta y_2 = \pm \frac{\mu}{m} \left(\frac{R_I - R_O}{R_O} \right) y_O + (R_I - R'_I) \cos \alpha_C \sin \beta_C \pm \frac{\mu}{m} \cos \alpha_R \sin \beta_R \quad (4\text{-}22)$$

$$\Delta z = \left(R_I^2 - x_I^2 - y_I^2 \right)^{\frac{1}{2}} - z_1 \quad (4\text{-}23)$$

In the equations above, the parameters Δx_1 and Δy_1 represents a uniform shifting of all the image points lying on the same plane. The parameters Δx_2, Δy_2 and Δz, which are dependent on the position of the object, represent the geometric distortion in the image.

Using Champagne's analytical results we can also calculate the maximum aberrations associated with any reconstruction geometry. The aberrations are given in terms of the wavefront deviations from a Gaussian sphere. The respective phase errors due to spherical, comatic and astigmatic aberrations are given as:

$$\Delta_S = \frac{1}{8\lambda_C} (x^2 + y^2)^2 \, S$$

$$\Delta_C = \frac{1}{2\lambda_C} (x^2 + y^2)(xC_x + yC_y) \quad (4\text{-}24)$$

$$\Delta_A = \frac{1}{2\lambda_C} (x^2 A_x + y^2 A_y + xyA_{xy})$$

where x, y are the hologram coordinates and S, C_x, C_y, A_x, A_y and A_{xy} are the aberration coefficients. The aberration coefficients are

$$S = \frac{1}{R_C^3} - \frac{1}{R_I^3} \pm \frac{\mu}{m^4}\left(\frac{1}{R_O^3} - \frac{1}{R_R^3}\right)$$

$$C_x = \frac{\sin\alpha_C}{R_C^2} - \frac{\sin\alpha_I}{R_I^2} \pm \frac{\mu}{m^3}\left(\frac{\sin\alpha_O}{R_O^2} - \frac{\sin\alpha_R}{R_R^2}\right)$$

$$C_y = \frac{\cos\alpha_C \sin\beta_C}{R_C^2} - \frac{\cos\alpha_I \sin\beta_I}{R_I^2} \pm \frac{\mu}{m^3}\left(\frac{\cos\alpha_O \sin\beta_O}{R_O^2} - \frac{\cos\alpha_R \sin\beta_R}{R_R^2}\right)$$

$$A_x = \frac{\sin^2\alpha_C}{R_C} - \frac{\sin^2\alpha_I}{R_I} \pm \frac{\mu}{m^2}\left(\frac{\sin^2\alpha_O}{R_O} - \frac{\sin^2\alpha_R}{R_R}\right) \qquad (4\text{-}25)$$

$$A_y = \frac{\cos^2\alpha_C \sin^2\beta_C}{R_C} - \frac{\cos^2\alpha_I \sin^2\beta_I}{R_I}$$

$$\pm \frac{\mu}{m^2}\left(\frac{\cos^2\alpha_O \sin^2\beta_O}{R_O} - \frac{\cos^2\alpha_R \sin^2\beta_R}{R_R}\right)$$

$$A_{xy} = \frac{\sin\alpha_C \cos\alpha_C \sin\beta_C}{R_C} - \frac{\sin\alpha_I \cos\alpha_I \sin\beta_I}{R_I}$$

$$\pm \frac{\mu}{m^2} \left(\frac{\sin \alpha_O \cos \alpha_O \sin \beta_O}{R_O} - \frac{\sin \alpha_R \cos \alpha_R \sin \beta_R}{R_R} \right)$$

In discussing the maximum aberration of the hologram one additional parameter of interest is the F# of the hologram which is defined as

$$F\# = \frac{f}{2\zeta} \tag{4-26}$$

where

$$\frac{1}{f} = \frac{\mu}{m^2} \left(\frac{1}{R_O} - \frac{1}{R_R} \right)$$

and ζ is the radius of the hologram. The parameter f is essentially the hologram focal length. The maximum phase errors due to the three types of aberrations can be shown to be

$$\Delta_s(\max) = \frac{1}{128\lambda_C} \left(\frac{f}{F\#} \right)^4 S$$

$$\Delta_c(\max) = \frac{1}{16\lambda_C} \left(\frac{f}{F\#} \right)^3 \left(c_x^2 + c_y^2 \right) \tag{4-27}$$

$$\Delta_A(\max) = \pm \frac{1}{8\lambda_C} \left(\frac{f}{F\#} \right)^2 \left[\frac{1}{2} | A_x + A_y | + \sqrt{\frac{(A_x - A_y)^2}{4} + A_{xy}^2} \right]$$

The sign in $\Delta_A(\max)$ depends on the sign of $A_x + A_y$. The - sign in $\Delta_A(\max)$ will be used if the sign of $A_x + A_y$ is positive; otherwise the + sign in $\Delta_A(\max)$ will be used.

A computer program including all the equations described above was written in Fortran IV and is included in Paragraph 4.4. In using the program the user supplies the values of (x_O, y_O, z_O), (R_R, α_R, β_R), (R_C, α_C, β_C), λ_O, λ_C, m, and F# to the computer. Upon receiving the data the computer will use the various equations to calculate and subsequently print out the parameters of interest such as the image position, the uniform shifting in position of all image points, the geometric distortion, and the maximum phase error of the three types of aberrations. In the following two examples we will show how to use the computer program to analyze the defects in the image introduced by the major components. In the first example, we assume that the beam deflector causes an error of 5×10^{-4} degrees in the orientation of the reconstructed beam. This error in the reconstruction beam angle is about one percent of the deflection angle of the laser beam. The other pertinent data needed in the calculation are given below

$(x_O, y_O, z_O) = (10, 10, 100)$ mm

$R_R = R_C = \infty$

$\alpha_R = 40$ degrees

$\beta_R = 0$ degrees

$\alpha_C = (40 + 5 \times 10^{-4})$ degrees

$\beta_C = 5 \times 10^{-4}$ degrees

F# = 1

and $\lambda_C = \lambda_O = .5 \times 10^{-3}$ mm. The computer supplies us with the following information about the reconstructed image

uniform shift

$$\begin{cases} \Delta x_1 = 6.7 \times 10^{-4} \text{ mm} \\ \Delta y_1 = 6.7 \times 10^{-4} \text{ mm} \end{cases}$$

geometric distortion

$$\begin{cases} \Delta x_2 = 6.4 \times 10^{-6} \text{ mm} \\ \Delta y_2 = 6.7 \times 10^{-6} \text{ mm} \end{cases}$$

$\Delta_S(\max) = 0$

$\Delta_C(\max) = 0$

$\Delta_A(\max) = 0$

The error in the beam deflector caused the image at the detector plane to move by a distance of 6.7×10^{-4} mm. This shift in position is significantly smaller than the distance between adjacent photodetectors. Furthermore, only a very small amount of geometric distortion appears in the reconstructed image.

In the second example we consider the case where the reconstruction beam is not a collimating beam. This may be caused by a slight change in the position of the collimating lens in the holographic memory. To analyze this situation we supply the computer with the following data:

$(x_O, y_O, z_O) = (10, 10, 100)$ mm

$R_R = \infty$

$R_C = 10000$ mm

$\alpha_C = \alpha_R = 40$ degrees

$\alpha_C = \beta_R = 0$ degrees

F# = 50

and $\lambda_C = \lambda_O = .5 \times 10^{-3}$ mm.

The information we obtain from the computer is as follows:

$\Delta z = .99$ mm

Lateral magnification = .99

$\Delta_S = -.74 \times 10^{-5}$ wavelength

$\Delta_C = 0$

$\Delta_A = -0.041$ wavelength

The image plane was shifted by a distance of .99 mm, and there is a slight demagnification of the image; for this application, however, the amount of lateral magnification must be reduced to less than 0.999. The result provided by the computer also indicates that a slight amount of aberration is present.

With such a computer program we can, in the future, find out the tolerances of all the major components in the holographic memory.

4.4 COMPUTER PROGRAM FOR HOLOGRAPHIC IMAGE ANALYSIS

```
00100 DIMENSION X0(3),XR(3),XC(3),XI(3),A(3),D(3),S(3),W(2)
00110 200 TYPE1
00120 1 FORMAT(1X,'SUPPLY THE PROPER DATA AFTER EACH ?; ANGLE IN DEGREE,
00130&DISTANCE IN MM')
00140 TYPE2
00150 2 FORMAT(1X,'X0,Y0,Z0 OF OBJECT POINT?',/)
00160 ACCEPT,X0
00170 TYPE3
00180 3 FORMAT(1X,'R(RADIUS),AR,BR OF REFERENCE;IF PLANE WAVE,SET R=0
00190& ?',/)
00200 ACCEPT,XR
00210 TYPE4
00220 4 FORMAT(1X,'R(RADIUS),AC,BC OF RECONST.;IF PLANE WAVE,SET R=0
00230& ?',/)
00240 ACCEPT,XC
00250 TYPE5
00260 5 FORMAT(1X,'WR,RECORDING WAVELENGTH; WC,RECONST. WAVELENGTH=?',/)
00270 ACCEPT,W
00280 TYPE6
00290 6 FORMAT(1X,'TYPE 1 IF IMAGE=VIRTUAL; TYPE -1 IF IMAGE=REAL?',/)
00300 ACCEPT,I
00310 TYPE7
00320 7 FORMAT(1X,'HOLOGRAM MAGNIFICATION=?',/)
00330 ACCEPT,AM
00340 TYPE8
00350 8 FORMAT(1X,'F-NUMBER OF HOLOGRAM=?',/)
00360 ACCEPT,F
00370 CALL HCOMP(X0,XR,XC,XI,A,D,S,W,F,I,AMAG1,AMAG2,AM)
00380 TYPE9,X0
00390 9 FORMAT(1H1 ,'POSITION OF OBJECT:',2X,'X=',E10.3,' MM',2X,'Y=',
00400&E10.3,' MM',2X,'Z=',E10.3,' MM')
00410 IF(XR(1).EQ.0) TYPE10,XR(2),XR(3)
00420 IF(XR(1).NE.0.) TYPE11,XR
00430 10 FORMAT(1X,'REFERENCE BEAM:      AR=',E10.3,'  DEGREE',
00440&6X,'BR=',E10.3,'  DEGREE'
00450&)
00460 11 FORMAT(1X,'REFERENCE POINT:  XR=',E10.3,' MM',2X,'YR=',
00470&E10.3,' MM',2X,'ZR=',E10.3,' MM')
00480 IF(XC(1).EQ.0.) TYPE12,XC(2),XC(3)
00490 12 FORMAT(1X,'RECONST. BEAM:  AC=',E11.5,' DEGREE',4X,'BC=',
00500&E11.5,' DEGREE')
00510 IF(XC(1).NE.0.) TYPE13,XC
00520 13 FORMAT(1X,'RECONST. POINT:  XC=',E10.3,' MM',2X,'YC=',
00530&E10.3,' MM',2X,'ZC=',E10.3,' MM')
00540 TYPE14,W
00550 14 FORMAT(1X,'RECORDING WAVELENGTH=',E10.4,' MM',4X,
00560&'RECONST. WAVELENGTH=',E10.4,' MM')
00570 TYPE15,AM,F,I
00580 15 FORMAT(1X,'HOLOGRAM MAGNIFICATION=',E10.3,/,1X,'F-NUMBER=',
00590&E10.3,/,1X,'IMAGE=',I3,4X,10HO=NO IMAGE,' ; 1=VIRTOAL;  -1= REAL')
```

```
00600 IF(I.EQ.0) GØ TØ 293
00610 TYPE16,XI
00620 16 FØRMAT(1H1 ,'PØSITIØN ØF IMAGE:',2X,'X=',E10.3,
00630&' MM',2X,'Y=',E10.3,' MM',2X,'Z=',E10.3,' MM')
00640 TYPE171,AMAG1,AMAG2
00650 171 FØRMAT(1X,'LATERAL MAGNIFICATIØN=',E11.4,/,1X,
00660&'LØNGITUDINAL MAGNIFICATIØN=',E11.4)
00670 TYPE17,S
00680 17 FØRMAT(1X,'UNIFØRM SHIFT:','X=',E10.3,' MM  ','Y=',E10.3,
00690&' MM  ','Z=',E10.3,' MM  ')
00700 TYPE18,D
00710 18 FØRMAT(1X,'GEØMETRIC DISTØRTIØN:',2X,'X=',E10.3,' MM',2X,
00720&'Y=',E10.3,' MM',2X,'Z=',E10.3,' MM')
00730 TYPE19,A
00740 19 FØRMAT(1X,'SPHERICAL ABERRATIØN=',E10.3,'  WAVELENGTH',/,1X
00750&,'CØMA=',E10.3,'  WAVELENGTH',/,1X,'ASTIGMATISM=',E10.3,
00760&'  WAVELENGTH')
00770 293 TYPE20
00780 20 FØRMAT(1H1,1X,' TYPE 0 TØ END PRØGRAM; TYPE 1 TØ CØNTINUE',/)
00790 ACCEPT,NT
00800 IF(NT) 100,100,200
00810 100 STØP
00820 END
```

```
00100 SUBRØUTINE HCØMP(XØ,XR,XC,XI,A,D,S,W,F,I,AMAG1,AMAG2,AM)
00110 DIMENSIØN XØ(3),XR(3),XC(3),XI(3),A(3),D(3),S(3),W(2)
00120 U=W(1)/W(2)
00130 PI=3.1415926536/180.
00140 IF(XR(1).EQ.0.) GØ TØ 20
00150 RQ=XR(1)
00160 XR(1)=RQ*SIN(PI*XR(2))
00170 XR(2)=RQ*CØS(PI*XR(2))*SIN(PI*XR(3))
00180 XR(3)=SQRT(RQ**2-XR(1)**2-XR(2)**2)
00190 20 IF(XC(1).EQ.0.) GØ TØ 21
00200 RQ1=XC(1)
00210 XC(1)=RQ1*SIN(PI*XC(2))
00220 XC(2)=RQ1*CØS(PI*XC(2))*SIN(PI*XC(3))
00230 XC(3)=SQRT(RQ1**2-XC(1)**2-XC(2)**2)
00240 21 CØNTINUE
00250C
00260C
00270C       CØMPUTE R AND 1/R
00280C
00290C
00300 RØ=SQRT(XØ(1)**2+XØ(2)**2+XØ(3)**2)
00310 RR=SQRT(XR(1)**2+XR(2)**2+XR(3)**2)
00320 RC=SQRT(XC(1)**2+XC(2)**2+XC(3)**2)
00330C
00340C
00350 RØ1=1/RØ
00360 RR1=1./RR
00370 RC1=1./RC
00380 IF(XR(1).EQ.0.) RR1=0.
00390 IF(XC(1).EQ.0.) RC1=0.
00400C
00410C
00420C
00430C        MAGNIFICATIØN
00440C
00450 AMAG1=AM/(1.+I*(AM*AM*RØ*RC1/U-RØ*RR1))
00460 AMAG2=I/U*AMAG1**2
00470C
00480C
00490C        SET UP PARAMETERS TØ FIND PØSITIØN ØF IMAGE
00500C
00510C
00520 RI1=RC1+I*(U/AM**2)*(RØ1-RR1)
00530 RI=1./RI1
00540C
00550C
00560 IF(XR(1).EQ.0.) GØ TØ 1
00570 VR1=XR(1)*RR1
00580 VR2=XR(2)*RR1
00590 GØ TØ 2
```

```
00600 1 VR1=SIN(XR(2)*PI)
00610 VR2=C0S(XR(2)*PI)*SIN(XR(3)*PI)
00620C
00630C
00640 2 IF(XC(1).EQ.0.) G0 T0 3
00650 VC1=XC(1)*RC1
00660 VC2=XC(2)*RC1
00670 G0 T0 4
00680 3 VC1=SIN(XC(2)*PI)
00690 VC2=C0S(XC(2)*PI)*SIN(XC(3)*PI)
00700C
00710C
00720C        IMAGE P0SITI0N
00730C
00740C
00750 4 XI(1)=RI*(VC1+I*(U/AM)*(X0(1)*R01-VR1))
00760 XI(2)=RI*(VC2+I*(U/AM)*(X0(2)*R01-VR2))
00770 X0=RI**2-XI(1)**2-XI(2)**2
00780 IF(X0.LT.0) G0 T0 10
00790 XI(3)=SQRT(RI**2-XI(1)**2-XI(2)**2)
00800 XI(3)=SIGN(XI(3),RI)
00810C
00820C
00830C        UNIF0RM SHIFT IS DETERMINED BY A P0INT X=0,Y=0,Z0
00840C
00850C
00860 RII=1./(RC1+I*(U/AM**2)*(1./X0(3)-RR1))
00870 S(1)=RII*(VC1-I*(U/AM)*VR1)
00880 S(2)=RII*(VC2-I*(U/AM)*VR2)
00890 S(3)=SQRT(RII**2-S(1)**2-S(2)**2)- X0(3)
00900 S(3)=SIGN(S(3),RII)
00910C
00920C
00930C        GE0METRIC DIST0RTI0N
00940C
00950C
00960 D0 5 J=1,3
00970 YM=AMAG1
00980 IF(J.EQ.3) YM=SIGN(1.,RI)
00990 D(J)=XI(J)-YM*X0(J)-S(J)
01000 T=D(J)/XI(J)
01010 5 IF(T.LT.1.E-7) D(J)=0.
01020C
01030C
01040C      SPHERICAL ABERRATI0N
01050C
01060C
01070C         ZZ=F0CAL LENGTH 0F H0L0GRAM
01080C
01090 ZZ=(AM*AM/U)/(1./X0(3)-RR1)
```

```
01100C
01110 SS=RC1**3+I*(U/AM**4)*(R01**3-RR1**3)-RI1**3
01120C
01130 A(1)=(1./(128.*W(2)))*(ZZ/F)**4*SS
01140C
01150C
01160C       SET UP PARAMETERS TO CALCULATE MAX. COMA AND ASTIGMATISM
01170C
01180C
01190 IF(XR(1).EQ.0.) GO TO 6
01200 QR1=XR(1)*RR1**3
01210 QR2=XR(2)*RR1**3
01220 GO TO 7
01230 6 QR1=0.
01240 QR2=0.
01250C
01260C
01270 7 IF(XC(1).EQ.0.) GO TO 8
01280 QC1=XC(1)*RC1**3
01290 QC2=XC(2)*RC1**3
01300 GO TO 9
01310 8 QC1=0.
01320 QC2=0.
01330C
01340C
01350C         COMA
01360 9 E1=I*U/AM**3-(XI(1)/X0(I))*(RI1/R01)**3
01370 E2=I*U/AM**3-(XI(2)/X0(2))*(RI1/R01)**3
01380 IF(E1.LE.1.E-8) E1=0.
01390 IF(E2.LE.1.E-8) E2=0.
01400 CX=QC1-I*U*QR1/AM**3+X0(1)*R01**3*E1
01410 CY=QC2-I*U*QR2/AM**3+X0(2)*R01**3*E2
01420 IF(CX.LE.1.E-8) CX=0.
01430 IF(CY.LE.1.E-8) CY=0.
01440 A(2)=(1./16./W(2))*(ZZ/F)**3*SQRT(CX*CX+CY*CY)
01450C
01460C
01470C         ASTIGMATISM
01480C
01490C
01500 E3=I*U/AM**2-(XI(1)/X0(1))**2*(RI1/R01)**3
01510 E4=I*U/AM**2-(XI(2)/X0(2))**2*(RI1/R01)**3
01520 IF(E3.LE.1.E-8) E3=0.
01530 IF(E4.LE.1.E-8) E4=0.
01540 AX=QC1*XC(1)-I*U/AM**2*QR1*XR(1)+X0(1)**2*R01**3*E3
01550 AY=QC2*XC(2)-I*U/AM**2*QR2*XR(2)+X0(2)**2*R01**3*E4
01560 E5=I*U/AM**2-(XI(1)*XI(2))/(X0(1)*X0(2))*(RI1/R01)**3
01570 IF(E5.LE.1.E-8) E5=0.
01580 AXY=QC1*XC(2)-I*U/AM**2*QR1*XR(2)+X0(1)*X0(2)*R01**3*E5
01590 IF(AX.LE.1.E-8) AX=0.
```

```
01600 IF(AY.LE.1.E-8) AY=0.
01610 IF(AXY.LE.1.E-8) AXY=0.
01620 ISN=(AX+AY)/ABS(AX+AY)
01630C
01640C
01650 AZ=.25*(AX-AY)**2+AXY**2
01660 A(3)=-ISN*(1./8./W(2))*(ZZ/F)**2*(.5*(AX+AY)+SQRT(AZ))
01670 GØ TØ 12
01680 10 TYPE11
01690 11 FØRMAT(1X,'IMAGE CAN NØT BE RECØNSTRUCTED WITH CØNDITIØNS
01700& GIVEN')
01710 I=0
01720 12 RETURN
01730 END
```

SECTION V

INVESTIGATION OF SYSTEMS CONCEPTS AND MAJOR COMPONENTS

5.1 INTRODUCTION

One of the objectives of this study is to investigate system concepts and approaches useful for implementing a workable configuration of a 10^{10} to 10^{12} bit read/write memory. Although the main emphasis is to study potential read/write materials and various holographic recording techniques, these studies can be guided by an investigation of the overall system requirements which affect available trade-off parameters. The parameters associated with both the input and output interfaces of this data storage and retrieval system are not yet completely defined. We can, however, analyze some of the system components to see how they influence the overall system design.

A block diagram of an optical memory system is shown in Fig. 5-1. The major elements of the system are (1) a read/write storage material, (2) the block data composer which converts an input electrical signal to an optical signal, (3) the coherent light sources used for recording and retrieving the optical signals, (4) the devices used to deflect the reference, signal and readout beams, (5) the block data readout detectors which convert the optical readout data to an output electrical signal, and (6) the associated electronic, synchronization, and data conditioning drives. In this section we shall separately discuss the important considerations for each of these system elements and suggest approaches for implementing them in the memory system. The specific designs for including all the elements in an overall system will be presented in Section VI.

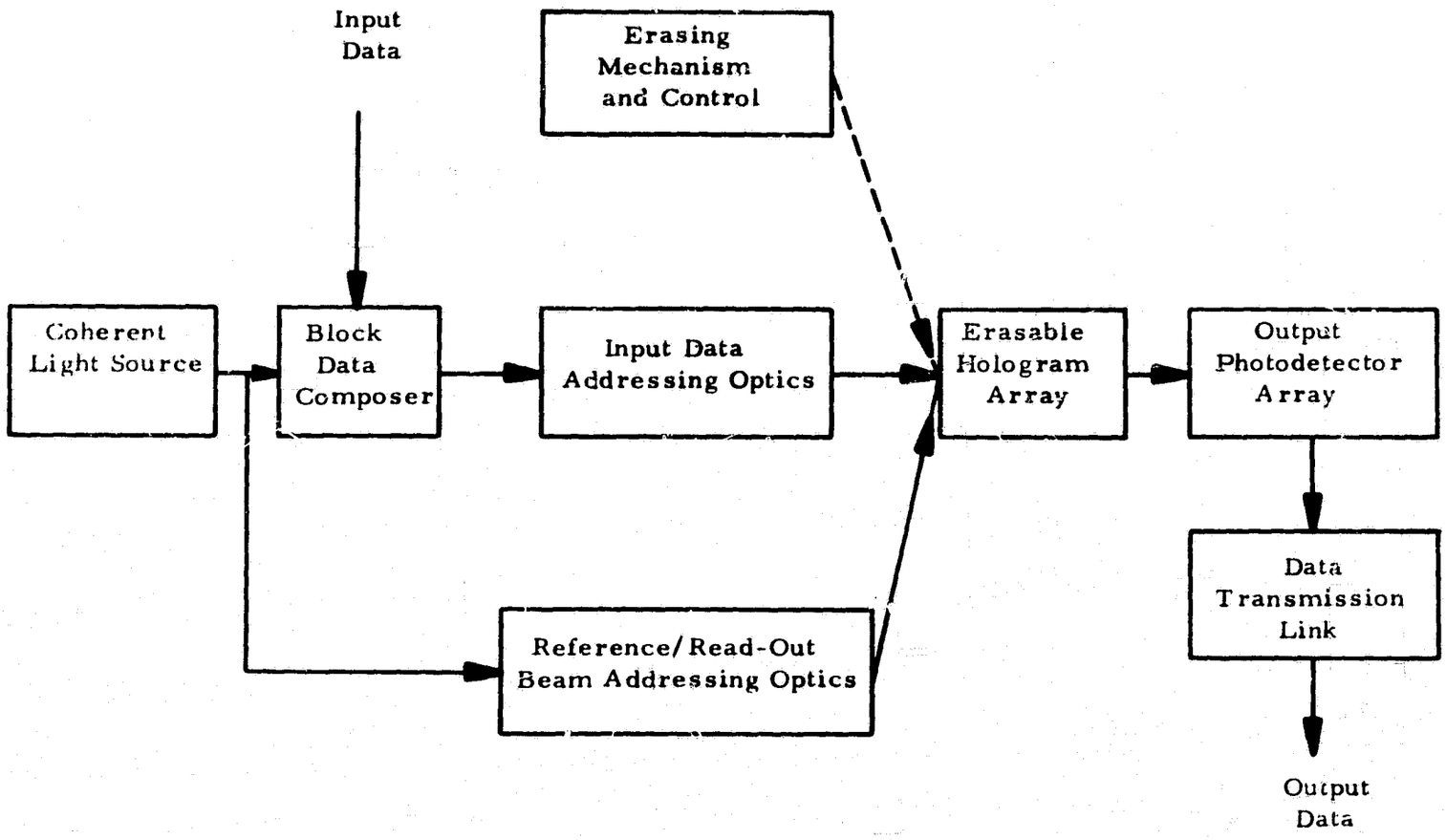

FIGURE 5-1. BLOCK DIAGRAM FOR HOLOGRAPHIC MEMORY SYSTEM

5.2 STORAGE MEDIUM

The most important constraint imposed by the overall system on the storage material is the capacity requirement of 10^{10} - 10^{12} bits. The maximum area in which this data can be stored will be constrained by limitations on the lens system and beam deflector designs. The minimum area will be determined mainly by the spatial resolution of the storage material and the number of incoherent additions of multiple holograms at each storage location in a thick hologram. Tradeoffs between the high packing densities and the SNR in the reconstructed imagery must also be examined for determining the minimum size of the storage material. Error rates are strongly dependent on the SNR; see Paragraph 3.5, Page 3-73, for details of these relationships.

The prospect of exploiting the wavelength or angular selectivity of a thick recording material for incoherent addition of many holograms at each storage location must be considered; the spectral sensitivity of the storage material will affect the extent to which wavelength variations can be employed in the design of a system. A tradeoff between the recording sensitivity of the storage material and the laser power required for data storage (at each wavelength) also exists.

The diffraction efficiency of the recorded holograms partly determines the laser power levels required for adequately retrieving the stored data. If many holograms are incoherently added at each storage location, each hologram must share the available diffraction efficiency and the laser power required for readout is affected.

The changes in storage material parameters as a function of exposure level and of reference to signal beam ratio can strongly affect the signal-to-noise ratio and therefore the readout error rates. Furthermore, optimization of the SNR may be inconsistent with optimization of the

diffraction efficiency; clearly the tradeoffs must be examined and compromises reached consistent with overall system requirements.

No erasable storage material is known to exist at this time with those characteristics needed for the 10^{10} - 10^{12} bit read/write holographic memory. Some candidate materials and the more important problems associated with each are listed here:

(1) manganese bismuth (or other ferromagnetic materials): useful only as thin films; very low diffraction efficiency; high exposure levels required (Ref. 28),

(2) lithium niobate (or other ferroelectric crystals): low diffraction efficiency; very high exposure levels required,

(3) photochromics: amplitude (rather than phase) variations are recorded so that the diffraction efficiency is low; high exposure levels required, and

(4) photoplastics: applicable only for thin (planar) holographic storage; spatial resolution is somewhat limited; acts as a bandpass spatial filter.

Based on various overall system constraints, the following storage material characteristics appear to be essential:

(1) phase (rather than amplitude) variations must occur as a function of exposure for a 200 nm range of visible wavelengths;

(2) thicknesses up to 3 mm are needed for sufficient wavelength selectivity;

(3) spatial frequency response must extend beyond 2000 lines/mm; and

(4) complete erasure without loss of sensitivity or resolution is needed to provide a large number of cycles.

Other storage material characteristics which are desirable but which may be relaxed if the performance of other system components improves include the following:

(1) energy density required to generate an optimum diffraction efficiency of at least 50 percent, for a single hologram, should be about $10^4 ergs/cm^2$,

(2) linear incoherent addition of at least 20 holograms in one location should be possible, and

(3) noise levels should be consistent with the required SNR for a given error rate at the data packing density used.

Clearly other characteristics must be considered; these include the stability of the material in the expected environment, the tolerance of the memory readin and readout functions to dimensional variations, and the techniques required for erasing the material. Although these environmental characteristics are important for the final system, the oth : characteristics must be emphasized in the initial material development efforts. The system can be modified to accommodate a broad range of environmental and other peripheral requirements.

5.3 STORAGE AND RETRIEVAL FORMAT

The physical dimensions and the geometrical arrangement of the various system components will be determined by several factors. The dominant factor is the overall memory capacity which is dependent on the number of bits in each hologram and the number of holograms in each storage location. Other factors include the spatial resolution of the storage material, the temporal and spatial coherence of the laser output, the hologram format (Fresnel or Fourier transform), and the resolvable angular increments of the beam deflectors. A displacement of the

reconstructed image and image aberrations can be avoided only if the readout beam duplicates the recording beam in both orientation and wavelength. The problem of providing clearance along all possible optical paths through the system must also be considered.

The basic functions of the storage format are (1) to direct a portion of the laser output through the block data composer which modulates the beam, (2) to direct the modulated beam toward any one of the storage locations, and (3) to direct the reference beam toward the same storage location. The system must function equally well for all storage locations, for all laser wavelengths, and for all angular orientations of the reference beams. The basic function of the retrieval format is to direct a readout beam having a particular wavelength and angular orientation toward any one storage location so that an aerial reconstructed image of a particular hologram is projected onto an array of detectors.

The physical dimensions of the storage material will be established by the required memory capacity, by the spatial resolution of the storage material, and by the number of incoherent additions of holograms which are permitted at each storage location. Examples showing how to determine storage medium dimensions and how to select specific geometries will be described in Section VI.

5.4 INPUT BLOCK DATA COMPOSER

The block data composer (BDC) provides the holographic system with a spatial array of successive blocks of data taken from the electronic data. Each block of data must spatially modulate an expanded laser beam so that its intensity variations represent the bit pattern displayed on the BDC. This spatially modulated beam (the signal beam) is directed to a particular storage location where it interferes with the reference beam to form a hologram.

Two general types of BDC's can be distinguished: those in which the array of data is established in direct response to an electrical signal, and those in which the array of data is established by a scanned and modulated light or electron beam. In either case, an optically detectable change must result in response to the optical or electrical signal; and this induced optical change must persist after the driving signal is removed. The BDC material must be erasable and must be capable of being recycled many times since each time the 10^{10} - 10^{12} bit holographic memory is filled, the BDC composer must recycle 10^{5} to 10^{7} times. The BDC material should be reasonably sensitive so that practical electrical or optical drive signal power levels can be used to generate each array of data, and its light modulation efficiency should be maximized so that the energy requirements on the laser can be minimized. The BDC material must be uniformly effective in spatially modulating laser beams at all wavelengths used. Since the data composed by the BDC has a relatively low density, the resolution of the material need not be high, but the spatial array of data on the BDC must have a direct correspondence with the array of light detectors used in the output plane. Since fabrication technology is expected to limit the minimum spacing between adjacent photodetectors to about 50 microns, the spacing between adjacent bits in the BDC will also be in the 50 micron range. Magnification between the input plane (the BDC) and the output plane (the photodetector array) can be used if necessary, but unity magnification appears to be a desirable design feature.

The ratio of the energy transmitted at each bit location in the ON state (bit = 1) to that transmitted in the OFF state (bit = 0) is the contrast ratio for the BDC. The contrast ratio available from the BDC affects the exposure level and reference-to-signal beam ratio, and it affects the threshold conditions established at the photodetector array. The difference between the average signal intensities for a "1" and for a "0" at the photo-

detector array during readout will be low for a poor contrast ratio so that noise and random fluctuations in laser power are more significant.

The rate at which data can be composed in the BDC and the time required to reset or erase the BDC must be compatible with input data rates. If the permitted writing speeds are not sufficient, the incoming data must be buffered, rescaled in time, and split into many channels which drive parallel inputs to the BDC. The full BDC array could then be activated at a rate which keeps pace with the incoming data. The time interval required for the reset or erasing operation can be obtained by making the BDC data rate during composition faster than the incoming data rate; the lull time between data blocks while fresh data is accumulating in the buffer can then be used for erasure.

At least seven types of materials have been considered for the BDC. These materials are listed here with notations which describe the switching techniques required, the type of optical change induced, the typical light efficiencies expected, and the erasing techniques required:

(1) PLZT (or other ferroelectric ceramics): switched with voltage pulses through an electrode matrix; polarization rotation or scattering changes induced; up to 90 percent light efficiency with polarization rotation, up to 20 percent with scattering; erased by applying a fixed voltage across all matrix intersections (Refs. 29-33),

(2) Manganese bismuth (or other ferromagnetic materials): switched with a modulated light beam; polarization rotation changes incuded; up to 10 percent light efficiency; erased with a pulsed magnetic field (Ref. 28),

(3) Photoplastics: switched with voltage pulses through an electrode matrix (fixed illumination during scanning required); phase changes induced; light efficiencies undetermined but over 30

percent is theoretically possible; erased by heating.

(4) Photochromics: switched with a modulated light beam; amplitude changes induced; up to 75 percent light efficiency; erased with relatively strong illumination (different wavelength than that used for writing),

(5) KD*P (or other electro-optic crystals): switched by a modulated electron beam; polarization rotation changes induced; up to 10 percent light efficiency; erased by discharging the electron accumulating layer,

(6) Lithium niobate (or other optically damageable crystals): switched by a modulated light beam; phase changes induced; light efficiencies undetermined but over 50 percent is theoretically possible; erased by heating, and

(7) Nickel-iron (or other magneto-optic materials): switched with current pulses through a conductor matrix; polarization rotation changes induced; up to 10 percent efficiency; erased by driving a fixed current through all pairs of conductors in the matrix.

High sensitivities to the switching pulses are not as important for the BDC as for the storage material since all the power available from the switching mechanism can be sequentially applied to each position. The light efficiencies noted above are not diffraction efficiencies but the percentage of the incident light passed in the ON state. The relative thicknesses of the various materials are important only in optimizing light efficiency, switching sensitivity, and contrast.

The physical dimensions of each element within the BDC will be determined by the nature of the optical design. No major difficulties are expected in constructing a BDC of any reasonable size which may be established by considering other system constraints.

The electronics for switching the array of positions will depend largely on the switching mode required. Switching with modulated light or electron beams requires a high data-rate beam modulator driven by a signal directly proportional to the data in the incoming data stream, along with synchronized beam scanning devices. Switching with electrical signals requires matrix accessing electronics which sequentially apply signals corresponding to bit states in the incoming data stream to each matrix position. In both cases means to reset or erase the array in preparation for new data must be included.

5.5 LASER

In this section we examine the important properties of the laser needed to read data into and out of the holographic memory. Other lasers might be required in the system (for example, to provide optical switching of certain block data composer materials or to provide erasing illumination for certain types of storage materials); these laser requirements are not considered here.

The data readin and readout functions may require significantly different laser output characteristics. It is presumed that any particular hologram will be read in and read out with the same wavelength. The readin and readout operations may require that the laser have different power levels or different pulse widths or both. Such controls are relatively simple to implement and are definitely more desirable than designing and incorporating two lasers into the system.

To achieve a memory capacity in excess of 10^{10} bits will probably require the use of more than one wavelength; incoherent addition of more than one hologram at each storage location is one important technique that may require several wavelengths. In the following paragraphs several operating constraints and requirements of the laser are discussed; these

constraints and requirements apply for each wavelength.

The energy per pulse supplied for reading data into the holographic memory will depend mainly on the efficiency of the block data composer, the efficiency of the beam deflectors, the losses through the passive optical components, and the sensitivity of the recording material. The energy per pulse required for reading data out of the memory will depend mainly on the efficiency of the beam deflectors, the diffraction efficiency of the holograms, the losses through the passive optical components, and the sensitivity of the photodetectors.

Three operating conditions establish the primary constraints on the laser pulse width for readin; the laser pulse width must be compatible with all three, and the constraints must be compatible with each other. The first constraint is the time interval between successive compositions of data blocks; this time interval will depend directly on the input bit rate. The second constraint is the rate at which energy must be supplied to the storage material to achieve the required exposure level; this rate may be established either by limitations on the peak power available or by the instantaneous power levels permitted by the storage material. The third constraint is the requirement that the hologram interference fringes during each recording interval be stable; if the pulse width is too long, the temporal frequency difference between the signal and reference beams (such as that caused by an uncompensated acousto-optic beam deflector) would destroy the interference patterns.

Three other conditions establish the important constraints on the laser pulse width for readout; again, mutual compatibility is needed. The first constraint is the time interval permitted for the photodetectors to accumulate a sufficient number of photons; this time interval will depend directly on the output bit rate, and on the time response and sensitivity of the photodetectors. The second constraint is the rate at which energy

can be supplied to each photodetector to accumulate the required number of photons; this rate may be established either by limitations on the peak power available or by the instantaneous power levels permitted by the detectors. The third constraint is the time interval before access to the next storage location to be read out must begin; this time interval will very likely be the least restrictive.

The temporal coherence required of the laser illumination is determined by the largest optical path length difference between the signal and reference beams. The average offset angle between the reference and signal beams, the distance between the block data composer and the hologram array, and the largest dimensions of the block data composer and the hologram array affect this difference. In Fig. 5-2 the largest dimensions of the block data composer and the holographic storage medium are L and D, respectively, the average offset angle is ϕ_o and the separation between the block data composer and the storage medium is z_o. The geometry can be arranged so that a zero path length difference exists between the central ray in the signal beam and the central ray in the reference beam directed toward the center of the hologram array. The largest path length difference between extreme rays in the signal and reference beams is given approximately by

$$\Delta = \left[z_o^2 + \left(\tfrac{1}{2} L + \; \right)^2\right]^{\frac{1}{2}} - z_o + \tfrac{1}{2} D \sin \phi_o ,$$

assuming the maximum reference beam deflection angle is less than about 15 degrees. For typical geometries, $z_o \approx D$, $L \approx 0.3D$, and $\phi_o \approx 45$ degrees. With these numbers we get $\Delta \approx 0.9D$. The largest hologram dimension is not likely to be smaller than 110 mm for a 10^{10} - 10^{12} bits memory; therefore, a minimum laser coherence length of about $(0.9)(110) \approx 100$ mm is required. The spectral width $\delta\lambda$ associated with a coherence length Δ is given approximately by

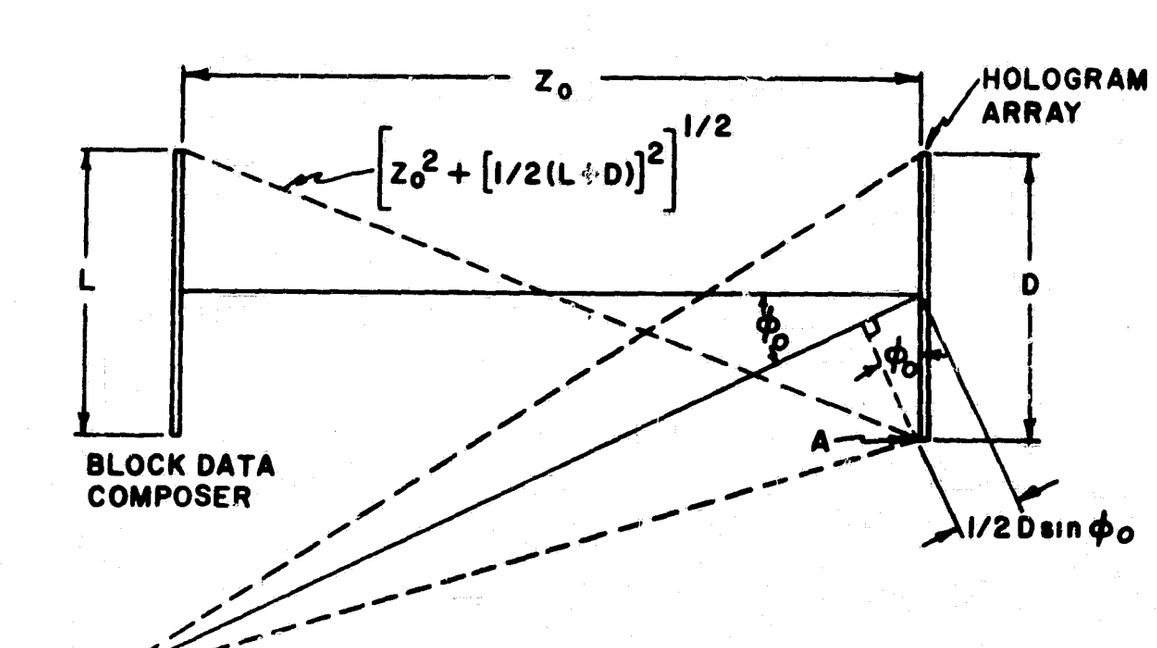

FIGURE 5-2. PATH LENGTH DIFFERENCES BETWEEN REFERENCE AND SIGNAL BEAMS

$$\delta\lambda = \frac{\lambda_o^2}{\Delta} ,$$

where λ_o is the wavelength. Taking $\lambda_o = 0.5 \times 10^{-3}$ mm (green) and $\Delta = 100$ mm, we get $\delta\lambda = 0.0025$ mm. Such spectral widths are readily obtainable with many presently available lasers. The smallest spectral width reported to date for tunable liquid dye lasers is about 0.05 nm (Ref. 34); parametrically tuned gas lasers can have spectral widths narrower than 0.0025 nm (Ref. 35). Spatial coherence requirements can be readily met by operating the laser optical resonator in a TEM_{oo} mode.

Variations of the output power or the output wavelength of the laser with time, temperature, or other environmental parameters can adversely affect overall system operation. Variations in power will affect exposure levels during readin and threshold conditions in the photodetectors during readout. Slight variations in wavelength between readin and readout beams will introduce errors in the registration and the diffraction efficiency of the data projected from the storage medium toward the photodetector array during readout; these errors will be quite sensitive to wavelength variations if a large number of holograms are incoherently added at each storage location. Tolerances on these power and wavelength variations are established by the permitted variations in exposure during readin, by the detection threshold conditions imposed by the photodetector array, and by the thickness selected for the storage medium.

The overall electrical to optical energy conversion efficiency of the laser is expected to be rather low (probably less than 0.5 percent. Techniques for removing (and perhaps partially reclaiming) the excess energy consumed by the laser will be an important overall system consideration.

Three approaches for implementing a feasible laser scheme can be identified at present. The most promising approach involves the use of one or more tunable liquid dye lasers with electronic tuning devices. The entire visible spectrum and segments of the UV and IR can be covered with various combinations of dyes and solvents; any single dye-solvent combination can cover up to a 50 nm range. Output spectral widths narrowed to 0.05 nm have been obtained with a blazed reflection grating replacing one of the optical resonator mirrors; tuning is accomplished by rotating the blazed grating with as much as 70 percent of the original power being retained (Ref. 34). The energy available per pulse from current lasers of this type are marginally acceptable; however, significant improvements have been made in the past several months and further improvements are expected.

Another possible scheme involves the use of one or more parametrically tunable lasers. The nonlinear interaction of coherent laser light (the pump wavelength) with certain crystals, maintained at a carefully controlled temperature, results in the generation of light at different wavelengths (the pump and idler wavelengths); the new wavelengths are a function of the angle of arrival of the original light and of the temperature of the crystal. Therefore, tuning over a wavelength range can be accomplished by varying the relative orientation or temperature (or both) of the nonlinear crystal. Conversion efficiencies of 50 percent have been measured. Spectral widths of the tuned output light are typically in the 0.001 to 0.5 nm range. Tuning throughout the visible range, and well into the IR, can be accomplished by varying the temperature of a single nonlinear crystal (such as lithium niobate) from 150°C to about 500°C (Ref. 35).

A third approach is to use one or more lasers, each of which is capable of operating at several discrete wavelengths. A combination of an argon laser and a krypton laser would provide at least ten discrete wavelengths in the visible range. Variations in power at each wavelength would have to be accommodated by designing each laser to provide adequate power at its weakest output wavelength. The lasers could be designed to operate in a pulse mode with provisions for electronically changing wavelengths between successive pulses. This approach could be implemented with existing technology to meet the requirements of several possible system configurations; the limitations on the total number of wavelengths and on the distribution (spacing) of these wavelengths are major shortcomings of this approach.

Another approach for implementing this third scheme is to use a Nd-YAG laser with intracavity frequency doubling, with the Nd-YAG rod maintained at a temperature of about -40°C. The cooling of the laser rod permits at least 13 discrete infrared wavelengths between 946 nm and 1358 nm to be generated (one at a time with intracavity tuning). Intracavity frequency doubling provides 13 discrete visible wavelengths between 473 nm and 679 nm. A second benefit of cooling is to narrow the spectral width of each output wavelength to about 0.1 nm (at room temperature, these widths are about 5 nm). The prospect of further spectral narrowing with an intracavity etalon also exists; coherence lengths of several hundreds of millimeters appear to be feasible with this approach. In a randomly pulsed mode, such a laser appears to be capable of providing about 1000 ergs per pulse at each output wavelength.

5.6 BEAM DEFLECTORS

The function of a beam deflector is to direct the laser illumination to each holographic memory storage location during both readin and readout. The reference beams and the readout beams must either be identical or exact conjugates, depending on the hologram storage format selected. The beam deflectors must operate equally well for all laser wavelengths used in the system. If angle of arrival changes are incorporated to provide unambiguous separation of incoherently added holograms, the beam deflectors must simultaneously provide access to and arrival angle changes at each storage location.

For flexible application of the holographic memory, the beam deflectors must operate in a random access mode. Random reposition times are dependent on input and output data rates, on the required hologram exposure time, and on the sensitivity and time response of the array of readout photodetectors. For example, at a bit rate of 10^8 bits/second with 10^6 bits/hologram, an interval of 10^{-3} seconds is available between storage operations for exposing the recording material, for repositioning the laser beam, and for preparing a new array of data on the BDC. Exposure times must be minimized to relieve the data buffering and time rescaling which may be required by the BDC. Suppose that a 10^{-5} second exposure time is permitted; the 0.99×10^{-3} seconds remaining can be used to reposition the laser beam with the beam deflectors. Such an interval is more than 100 times longer than typical reposition times for either acousto-optic or electro-optic devices. In fact, some mechanical devices can be operated in a random access mode with such reposition intervals. The access time requirement is, therefore, not a major problem.

Beam deflector design complexity depends on the number of positions to be accessed. For an acousto-optic device, factors such as material dimensions, acoustic attenuation, and electrical drive bandwidths limit the design as larger numbers of accessible positions are required. For an electro-optic device, factors such as material dimensions, material availability, and drive voltage levels limit the design.

Acousto-optic beam deflectors are promising candidates for use in the holographic memory system; recent improvements in electro-acoustic transducer fabrication technology and the availability of relatively large and high quality acousto-optic crystals are the major factors which affect this judgment. Other important advantages of acousto-optic over electro-optic beam deflectors include the more modest drive power and voltages needed, the smaller quantities of high quality polished optical crystals required, and the simpler techniques needed for accommodating many laser wavelengths. Developments in electro-optic beam deflection techniques should be continuously monitored, however. New techniques should be evaluated and compared to acousto-optic approaches, and updated judgments should be made.

The deflection efficiency (ratio of the useful to the incident light intensity) must be maximized to relax laser output power requirements. Repositioning errors resulting from slight changes in electrical drive signals, in ambient temperature, or in other parameters must be held within limits set by the storage and readout geometries. Image position shift errors of more than about 20 percent of a bit dimension cannot be tolerated. For thick holographic storage angular errors also reduce the output signal intensity. The amount of electrical and temperature stabilization required for a specific set of beam deflector characteristics and for a specific geometrical arrangement can be determined with relative ease.

All acousto-optic and some electro-optic beam deflectors provide a change in propagation direction (incremental angle change) to deflect a laser beam from one position to another. The magnitude of this incremental angle change is typically quite small (10^{-4} radians or less) and must be magnified to match practical holographic memory dimensions. Also, the diameter of the deflected beam must match the dimensions of each hologram in the array (i.e., the deflected beam must fully illuminate any selected hologram but must not overlap onto adjacent holograms). Standard optical beam-shaping techniques can be used to satisfy these requirements, but the optical configuration must also be consistent with the readin/readout geometry. Additional problems arise if the readout operation calls for beam directions that are conjugate to those used for readin. A set of readout beams conjugate to a set of reference beams can, in principle, be generated with a combination of passive and active optical components (lenses, mirrors, electro-optic shutters, etc.) using the same beam deflectors that were used for readin. Otherwise, a second combination of beam deflectors and passive optics could be incorporated to provide the conjugate readout beams.

The electrical drive requirements for an acousto-optic beam deflector (AOBD) will depend largely on the acousto-optic material used, the efficiency of the electro-acoustic transducer, and the bandwidth and center frequency selected. The material and the transducer efficiency will determine the power level at which the AOBD must be driven over the operating bandwidth to achieve the highest practical light deflection efficiency. For water or other liquids, center frequencies will be in the 15 to 40 MHz range. For crystalline acousto-optic materials such as lead molybdate ($PbMoO_4$), the center frequencies may be as high as 500 MHz; more typically they will be between 50 and 200 MHz for single crystal transducers, such as lithium niobate ($LiNbO_3$). The bandwidths

will typically be about 50 percent of the center frequency, although fractional bandwidths as high as 67 percent can be used if necessary. Bandwidth may be traded for optical efficiency if smaller bandwidths can be tolerated. The practical number of accessible output positions is about $0.5\tau_d\Delta f_d$ where Δf_d is the bandwidth and τ_d is the time required for an acoustic beam to propagate across the AOBD. The lowest tolerable bandwidth can be obtained with the longest τ_d's (longest AOBD's), but acoustic attenuation affects and limitations on acoustic material dimensions place bounds on τ_d. More detailed design relations for a pair of orthogonally oriented AOBD's are developed in the following paragraphs.

The acousto-optic approach for the beam deflecting function is more amenable to compensation for laser wavelength changes than any conceivable electro-optic approach. The reason for this can be seen from the following brief discussion. Recall that the Bragg condition for an AOBD operating in the Bragg mode is (Ref. 36-38),

$$\sin \tfrac{1}{2}\theta_B \approx \tfrac{1}{2}\theta_B = \tfrac{1}{2}\frac{\lambda}{\Lambda} \qquad (5\text{-}1)$$

where θ_B is the full Bragg angle, λ is the light wavelength, and Λ is the acoustic wavelength. A finite acoustic aperture of width W generates an acoustic energy pattern distributed angularly about the normal to the electro-acoustic transducer face. The range of acoustic wave components, with intensities within 4dB of the normally directed wave component, is given by

$$\delta\theta = \frac{n\Lambda}{W} \qquad (5\text{-}2)$$

where n is the index of refraction of the acousto-optic material.

Equation (5-1) can be written as

$$\theta_B = \frac{\lambda}{v} f \tag{5-3}$$

where $\Lambda = v/f$ was used; v is the acoustic propagation speed and f is the electrical drive frequency. A change in θ_B resulting from a change in f is given in a similar fashion by

$$\Delta\theta_B = \frac{\lambda}{v} \Delta f. \tag{5-4}$$

Equation (5-3) indicates that the optimum (or center) Bragg angle varies directly with λ; Eq. (5-4) indicates a similar variation of $\Delta\theta_B$ with λ. Furthermore, Eq. (5-3) indicates that the center Bragg angle condition can be met for different λ's by making a proportional change in θ_B or in f. If a different center frequency is established for each λ used, with a fixed θ_B, the electrical bandwidth of the electro-acoustic transducer must be correspondingly increased. However, if properly chosen wavelength dispersive elements (such as prisms) are positioned just before and after the AOBD, the Bragg angle θ_B can be caused to vary with λ so that a fixed center frequency f can be used, as illustrated in Fig. 5-3 (Ref. 39).

It must be emphasized, however, that the simple scheme shown in Fig. 5-3 can provide exact compensation only for the center drive frequency. As indicated by Eq. (5-4), the incremental angle changes $\Delta\theta_B$ corresponding to incremental frequency changes Δf will still be scaled by λ. It may be possible to compensate over the full electrical bandwidth with properly chosen combinations of dispersive optical elements (lenses and prisms). If such a technique can be implemented, the AOBD could be driven by a highly stabilized set of drive frequencies given by $f_o \pm m(\Delta f_o)$ where $m = 1, 2, 3, \ldots$ and where f_o is a fixed center frequency and Δf_o is a fixed frequency increment. A relatively simple and easy to stabilize frequency synthesizer could then be used instead of a continuously tunable

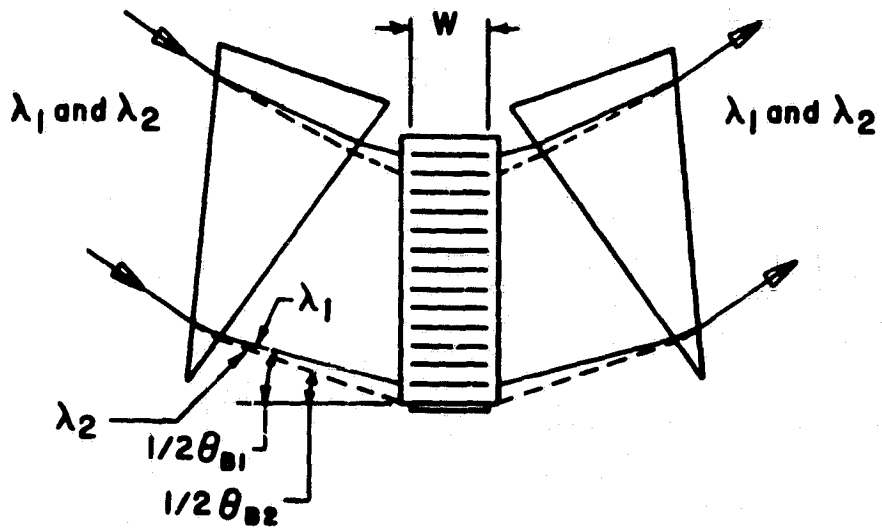

FIGURE 5-3. OPTICAL COMPENSATION FOR WAVELENGTH CHANGES IN ACOUSTIC BRAGG CELL

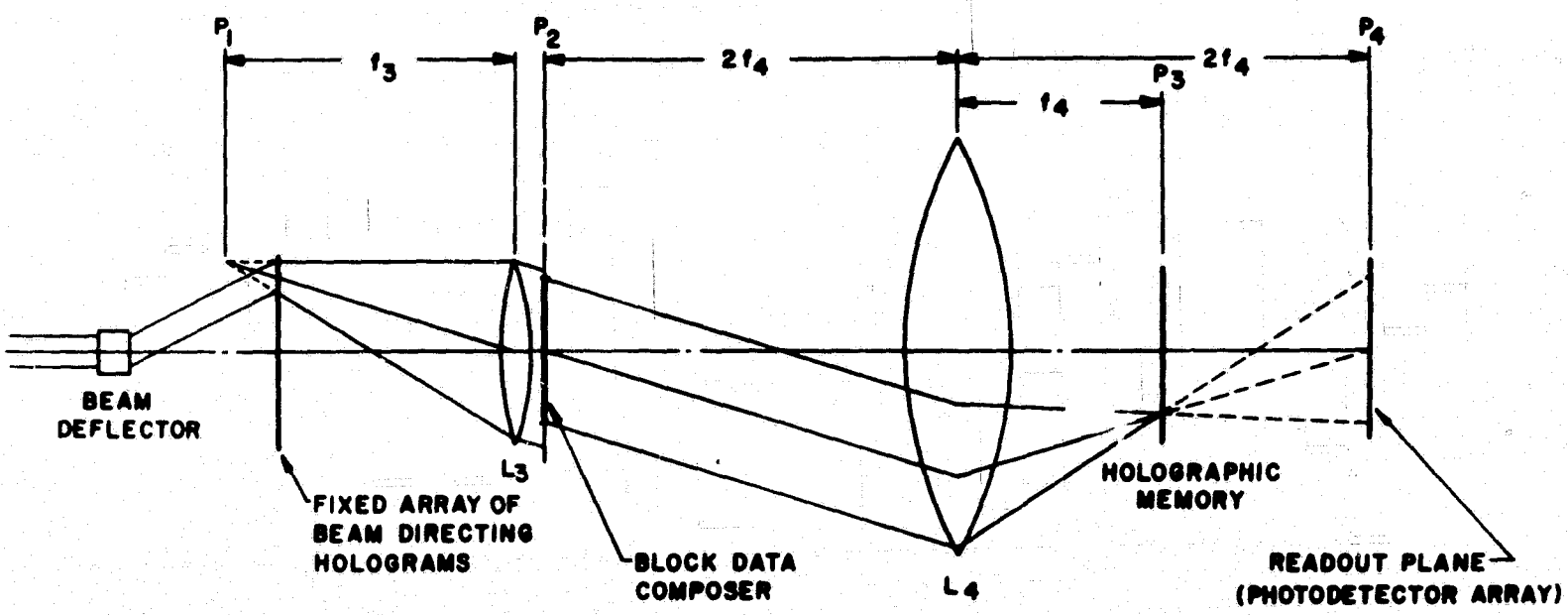

FIGURE 5-4. BEAM DIRECTING WITH FIXED ARRAY OF HOLOGRAMS

oscillator. Also, the logic required to select a specific drive frequency would be greatly simplified since only M different frequencies would be required instead of $\rho_z M$, where M is the number of holograms per dimension and ρ_z is the number of laser wavelengths used.

An important type of beam directing (not deflecting) may be required in system configurations where Fourier transform holograms are formed. The function of this beam directing array is illustrated in Fig. 5-4. The beam directing device is a fixed array of holograms. In this array there is one hologram for each storage location and, therefore, one fixed hologram for each beam deflector output position. In Fig. 5-4 only the signal beam path is indicated; the reference beams can be derived from the same deflected beams by using suitable optics. Along the signal path deflected beam from the beam deflector illuminates a separate fixed hologram in the beam directing array. Each fixed hologram projects a wavefront along the signal path which appears to emanate from a point source just behind the fixed hologram array in plane P_1. These spherical wavefronts are collimated by L_3 and directed through the BDC in plane P_2, where the collimated beam is spatially modulated. Note that the central ray of this modulated beam propagates in a direction which is angularly displaced from the optical axis of the signal path; the amount of angular displacement is directly proportional to the displacement from the axis of the corresponding effective point source in plane P_1.

Lens L_4 simultaneously images plane P_1 into plane P_3 and plane P_2 into plane P_4 so that the light distribution in plane P_3 is proportional to the Fourier transform of the data in plane P_2 (in the BDC) and an image of the array of data in the BDC is formed at plane P_4. The data is holographically recorded in plane P_3; each member of the stored array of holograms is therefore a Fourier transform hologram of the corresponding block of data from the BDC. An image of each block of data can be

projected onto plane P_4 by illuminating each hologram with the readout beam. Note that as each hologram in the memory is interrogated with the proper readout beam, each corresponding image is formed in the same relative position in plane P_4 so that a fixed array of readout photodetectors can be located in plane P_4.

The array of beam directing holograms (referred to in the literature as an array of Fresnel lens segments or a "hololens" array) generates an array of point sources in plane P_1 which has a one-to-one correspondence to the array of Fourier transform holograms recorded in plane P_4 (Ref. 40). This fixed hologram array can be constructed as an array of thick phase holograms with efficiencies approaching 100 percent. If multiple wavelength incoherent hologram addition is used in the holographic memory, multiple beam directing holograms can be formed but with reduced efficiencies. A more detailed analysis of an optical system similar to the one illustrated in Fig. 5-4 will be given in Section VI.

5.7 BLOCK DATA READOUT DETECTORS

The function of the readout detectors is to sense the binary data in the two-dimensional images retrieved from the holographic memory and to convert the two-dimensional spatial data into time varying electrical signals. A photosensitive detector array (PDA) and circuitry for electronically scanning and interrogating the PDA are the major components of the block data readout device. The hologram array, addressed by the deflected laser beam, produces a reconstructed image of the stored data pattern. The presence or absence of light dots is detected by the PDA with one photodetecting element corresponding to each bit in the digital data pattern.

A one-to-one correspondence must exist between the elements in the BDC and the individual detecting elements in the PDA. Magnification between the BDC and the PDA may be necessary (or convenient), but it is not likely that the absolute value of the magnification will exceed three. Thus the PDA center spacings may be larger than the BDC center spacings by a factor of three. The optical arrangement in Fig. 5-4 illustrates a unity magnification situation. It can be seen that magnification can be achieved by adjusting the positions of the object and image planes (P_2 and P_4) relative to lens L_4.

With present PDA technology, linear arrays with several hundred detectors on a line can be constructed with center spacings ranging from 0.05 mm to 0.5 mm. Two-dimensional arrays with up to 16 x 16 elements with center spacings ranging from 0.2 to 0.5 mm are presently available. These dimensions are compatible with preliminary requirements for fully populated two-dimensional PDA's with 300 x 300 to 500 x 500 elements. A fully populated array with 300 x 300 detectors on 0.2 mm centers would have a total size of about 60 x 60 mm.

If the detecting elements of the PDA are operated in a charge storage mode, the PDA can be illuminated for a brief interval (1 to 100μ sec) and then electronically interrogated during a 100 to 1000μ sec interval. This mode of operation permits the beam deflectors to be repositioned during the interrogation interval and minimizes the dead time between blocks of data being read out. Sufficient laser energy must be supplied during the illumination to provide a high probability of correct detection at all PDA elements. Furthermore, the energized detectors (those receiving "ones") must be capable of holding the accumulated charge for at least the full interrogation interval and must be discharged (set to "zero") by the interrogating electronics (or a combination of electronics and special illumination devices) to prepare the PDA for detecting the next block of data.

Tradeoffs exist between SNR and variations in image intensity and in detector responsitivity. If wide variations occur in either image intensity (from image to image or from position to position in one image) or detector responsitivity, the threshold conditions must be broadened thereby consuming part of the available SNR. Some electronic compensation for such effects might be obtained (e.g., by individually biasing each detector in the PDA), but such schemes would add to the complexity of the PDA drive circuitry. The alternative is to provide a high SNR and good uniformity of image intensities.

The absolute sensitivity and time response of the detectors in the PDA will determine the readout laser power level and pulse duration. Pulse durations in the 1 to 100μ sec range are feasible and laser power levels for readout are not expected to exceed those needed for reading. As noted above, the energy delivered per readout is established by the SNR and the detector threshold conditions. If necessary, a feedback loop can be established to provide continuous control of the laser intensity.

Typical PDA's use silicon photodetecting elements which have a peak spectral response at about 900 nm. Typical relative responses at various visible wavelengths are 0.62 at 700 nm, 0.42 at 600 nm, 0.32 at 500 nm, and 0.15 at 450nm. To compensate for the change in detector responsitivity with wavelength, the available laser energy must be inversely related to these relative spectral responses. Approximately three times as much energy must be delivered to the PDA at 450 nm relative to that at 600 nm.

A solid state PDA is most suitable as a readout device because it has those advantages attributed to integrated circuit devices; i.e., reduced weight, volume, and power consumption, plus greatly increased reliability and environmental immunity. Solid state PDA's perform the functions of

a pickup tube without the necessity for high voltages, magnetic fields, vacuum envelopes, filament power, and protection against mechanical shock. The addressing of individual portions of the photosensitive array can be facilitated by random or sequential digital address of rows and columns in the array.

The most attractive current approaches to solid state detection use arrays of diodes, diode-diodes, diode-transistors or hybrid elements consisting of MOS devices and transistors The advantages of the single diode approach lie primarily in the ease of fabrication of diode arrays, high packing densities and relatively good uniformity of response between elements. Unfortunately, simple diode structures exhibit two problems. First, unless all unaddressed rows and columns terminate in zero impedence, there are multiple photoconductive crosstalk paths through the various rows and columns which preclude use of diodes for multiple spot imaging applications. Secondly, a sequentially-read diode array cannot be operated in the charge-storage, light-integration mode. The output signal level is therefore strictly a function of the light incident on the element during the readout time at the instant of interrogation with a resultant loss of overall light collection efficiency.

The next simplest configuration is the diode-diode structure which provides several advantages over the simple diode array. If a back-biased photodiode is used as a light sensor, charge-storage (light integration) can be used. Although the diode-diode structure has a light integration capability, the low output signal available from the diodes needed for large area arrays makes direct readout of such a device difficult. Conceptually, the diode-diode structure offers the advantage that the commutating diodes can be made using one material technology while the sensing diodes can be matched to the particular spectral response desired. Recent work using this approach (Ref. 41) consisted of using hpa 4207 diodes as

the light sensitive elements and hpa 1006 high conductance diodes as the switching elements. The minimum detectable signal using these diodes was found to be 0.025 picojoules (pJ) This corresponds to a 0.25μ w signal (at 800 nm) of 100 nsec duration which procudes an error rate of 10^{-8} at a signal-to-noise ratio 10:1.

A phototransistor array is a form of the diode-diode configuration in which the structure is fabricated to produce transistor action through the two junctions. The structure is nearly identical to a diode-diode arrangement and the readout approach is similar. In general, the addressing rows of transistor elements have a common low impedance collector strip and the emitters are connected in a column by a metalized strip and attached to sense amplifier inputs. With phototransistor arrays, the variation in current gain of the devices produces the effect of varying responsitivity between elements of the array; as noted earlier, individual electrical biasing of each element might be required to compensate for this effect. The inherent current gain at the amplifying junction of the transistor is expected to improve the SNR at the output of the array Another configuration for the phototransistor array consists of fabricating a dual emitter device with the collectors of all transistors attached to a common substrate. One set of emitters is attached to the rows for addressing the array while the other set of emitters is attached to the columns for readout. This approach minimizes the effects of current gain variations and permits switching times in the 50 to 100 nanosecond range.

Recent work with phototransistor area arrays (Ref. 42), operating in the charge storage mode, indicates that detection of 0.4 pJ light pulses at 600 nm with 2μ sec access time is possible. The stored charge could be held for at least 80μ sec in a 16 x 16 array. The operation of

the system is slightly complicated by the fact that a three-step word-line interrogation sequence is required to operate in the charge storage mode.

Another array to be considered is the diode light sensor-FET isolation element array. Two configurations for these devices are possible. The diode may be connected in series with a voltage source and the gate of an FET which serves as a high input impedence amplifier. In this case, the diode operates as a steady state light sensor and the element is addressed by biasing a particular row of interconnected sources and sampling the various elements along the row. It is expected that the uniformity and reproduceability of this light sensing element should be very good and reasonable compatability exists between the various processes needed to fabricate the structure. The other configuration consists of the diode or transistor as a light sensor and its associated FET as a communicating device (Ref. 43). In this case, the diode or transistor has one terminal in common with the substrate which can be used as the output terminal. In this mode of operation, the sampling elements can be operated in the charge-storage, light-integration mode. Using transistor-FET mechani zation, one source of interraction can be reduced (namely, emitter bus cross-talk); however, parasitic coupling of the switch impulses into the output circuit through the interconnecting bus to substrate capacitances, and variations in the sampling switch characteristics are new sources of interaction. Also, increased fabrication complexity is experience in the transistor-FET array.

In addition to the approaches suggested above, which depend on the use of a p-n semiconductor function as the sensing device in an array, a new semiconductor device concept has been developed (Refs. 44 and 45) which shows promise as an optical detector and could be fabricated as an area array. The device operates by storing charge in potential wells created

at the surface of a semiconductor, and moving the charge over the surface by moving the potential well. The production and motion of charge is accomplished by forming an array of conductor-insulator-semiconductor capacitors which are used to transfer charge by the application of appropriate voltages to the conductors. An important feature of this device concept is that it does not require the fabrication of p-n junctions thereby offering significant advantages for obtaining high manufacturing yields. An optical detecting device may be made by imaging light onto the substrate, thereby creating electron-hole pairs which diffuse to the conducting electrode and are stored in potential wells created by the electrodes. After an integration period, the signal is read out by shift register action.

The design of the circuitry for electronically scanning and interrogating the PDA will depend largely on the memory organization (word lengths) and on the desired output bit rates. It is expected that 10 to 20 bit words will be read out at 5 to 10 million words per second so that a 10^{10} to 10^{12} bit memory could be completely accessed in 10^{2} to 10^{4} seconds. Sense amplifiers, NAND gate word transfer elements, buffer registers, timing clocks, and associated AND and OR logic gates are presently capable of operating at a 10^{7} bit per second rate. For example, a 256 x 256 element PDA could be connected to 256 row enabling switches and 256 column level sensing amplifiers. The 256 level sensing amplifiers could be arranged as sixteen 16-bit words driving 16 NAND gates. The outputs of the 16 NAND gates feed a 16-bit buffer register, connected to 16 AND gates, synchronized to read pulses from a timing clock. With such an arrangement, 16-bit words could be read out at 6×10^{6} words per second for a 96×10^{6} bit per second readout rate. Electronics to perform these operations are not far from present state-of-the-art. The major problems to be addressed in implementing such circuitry include

impedance matching of the PDA elements to the enabling switches and to the sense amplifiers, minimizing switching transient cross-coupling effects, minimizing effects of any RFI or other electrical interference, and maximizing the reliability of the large number of integrated circuit elements. The problems associated with implementing the PDA itself are expected to be more serious and to require more engineering development than the interrogating circuitry.

5.8 SYSTEM ELECTRONICS

The system electronics will include a prime power source, the specialized drive circuitry for each system component and a special purpose central processor which controls and synchronizes the overall system operation. We cannot, at this time, be specific about these electronic assemblies, but some general comments can be made.

It appears that the laser will consume the bulk of the energy available to the system. The capacity of the prime power source will, therefore, be strongly affected by laser output power requirements and by the overall laser efficiency. The operating power levels expected for the BDC, the beam deflectors, the PDA, and a central processing unit will probably be in the 10 to 100 watt range; the laser may require several hundred watts.

Each system component will require specialized drive circuitry. For example, acousto-optic beam deflectors will require two electronically tunable oscillators and two broadband power amplifiers, each with interface logic for control inputs from the central processor. In contrast, the PDA will require word oriented digital logic circuitry with electronic line scanning; techniques for time scaling and data multiplexing might also be required. From a systems viewpoint, it is essential that all of these specialized drive circuits be compatible with control commands

issued by a central processing unit. Therefore, in all cases circuitry interfacing with the central processor must be provided.

The central processing unit includes a special purpose computer and associated software and system interface equipment. The specific order, speed, and complexity of control commands issued from this unit to the several system components will depend on the system configuration, on the input/output data rates, and on the number of possible commands each component must receive.

SECTION VI

SYSTEM DESIGN AND SYNTHESIS

Several important relations among the parameters of a holographic memory system can be developed without fixing the exact geometries or techniques. A set of general relations is developed in this section; these relations can be considered a first edition of an overall set of systems design equations. This development is followed by the application of these design equations in synthesizing two system; in each system a hologram format is selected, along with specific techniques for the major system components, and performance criteria are established for the storage material and for the system components.

6.1 GENERAL SYSTEM DESIGN RELATIONS

Many factors must be considered in relating the quantities which affect the system design. The fact that these quantities are interrelated prevents them from being neatly categorized. The definitions of these quantities and the derivation of the design equations is begun by considering a general geometry. As other system features are examined, these initially defined quantities will reappear.

6.1.1 Geometric Features

The following quantities are defined with reference to Fig. 6-1. For the block data composer we have:

L = side dimension of the BDC;

ℓ = side dimension of a bit in the BDC;

N = number of bits per dimension in the BDC and in the PDA;

k_1 = BDC center spacing parameter; so that

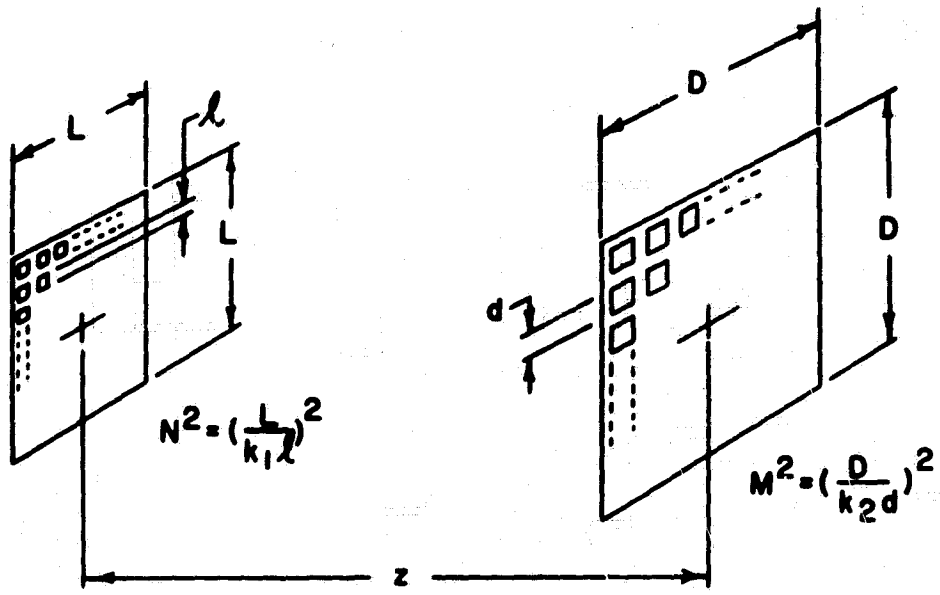

FIGURE 6-1. GEOMETRY FOR ANALYZING CAPACITY

$$N = \frac{L}{k_1 \ell} \tag{6-1}$$

For the hologram array we have:

D = side dimension of holographic memory;

d = side dimension of each hologram storage location;

M = number of storage locations per dimension;

k_2 = holographic memory center spacing parameters; so that

$$M = \frac{D}{k_2 d} \quad . \tag{6-2}$$

Further, we have:

z = separation between the holographic memory and the BDC; if a lens is used between the BDC and the memory, z can be replaced by the separation between the lens and the memory (typically, $z \rightarrow f$ where f is the focal length of the lens)

δ = Rayleigh resolution limit for the hologram aperture d at the BDC;

λ = wavelength of laser illumination; so that

$$\delta = \frac{\lambda z}{d} \quad . \tag{6-3}$$

If k_3 is the resolution redundancy parameter for each storage location, we have

$$\ell = k_3 \delta = \frac{k_3 \lambda_z}{d} \quad , \tag{6-4}$$

and

$$k_4 = \frac{D}{z} \quad . \tag{6-5}$$

We also make the following definitions:

C_o = memory bit capacity with one hologram per storage location;

C = total memory bit capacity;

ρ_z = number of incoherently added holograms per storage location;

ρ_{xy} = maximum useful bit packing density in bits per unit area; so that the following relationships hold

$$C_o = N^2M^2 = \left(\frac{k_4}{k_1 k_2 k_3} \quad \frac{L}{\lambda}\right)^2 , \tag{6-6}$$

$$C = C_o \rho_z , \tag{6-7}$$

$$C_o \leq M^2 d^2 \rho_{xy} = \frac{D^2 \rho_{xy}}{k_2^2} , \tag{6-8}$$

and

$$D \geq k_2 \left(\frac{C_o}{\rho_{xy}}\right)^{\frac{1}{2}} \tag{6-9}$$

The quantity ρ_z is proportional to the thickness b_o of the storage material. With either wavelength or reference beam angle discrimination between incoherently added holograms, ρ_z will be given by

$$\rho_z = \Gamma_z b_o \tag{6-10}$$

where Γ_z is a measure of the number of equally spaced wavelength or angle resolvable elements in the wavelength or angle band available. For example, with wavelength discrimination and an average angle between signal and reference beams of 30 degrees, Γ_z is given approximately by (Ref. 6)

$$\Gamma_z \approx \frac{\lambda_2 - \lambda_1}{5\lambda_o^2} , \tag{6-11}$$

where λ_2 and λ_1 are the longest and shortest wavelengths in the available band, respectively λ_0 is a wavelength near the center of the band.

6.1.2 Optical Loss Parameters

The laser output in any system will be divided between the signal and reference paths during read-in with some fraction of the energy directed initially along each path being received at the storage material. All of the available laser energy can, in principle, be directed along the read-out path; however, many practical configurations will not permit this. The more important optical transmissivity factors are defined and related as follows (refer to Fig. 6-2):

T_s = fraction of the laser energy initially directed along the signal beam path which reaches any one storage location during read-in;

T_w = same for reference beam path;

T_r = same for read-out beam path;

t_s = transmissivity of passive optical components in the signal path (excluding a diffuser, if one is used);

t_w = same for reference path;

t_r = same for read-out path;

t_d = fraction of the energy from a signal path diffuser directed toward any one storage location;

η_d = optical efficiency of the beam deflector;

η_b = optical efficiency of the block data composer;

T_i = transmissivity of the passive optical components preceding the beamsplitter, including the effects of beamsplitter losses.

With these definitions we can obtain the following relations:

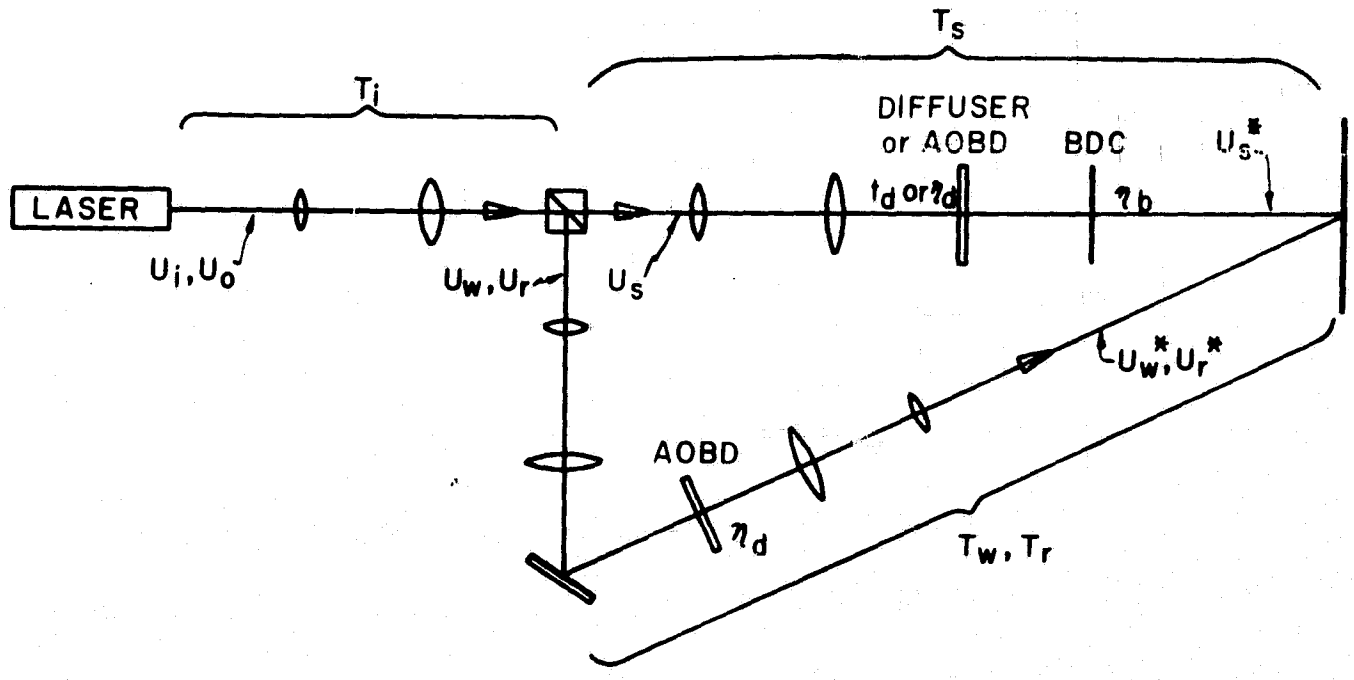

FIGURE 6-2. OPTICAL LOSS PARAMETERS

$$T_s = \begin{cases} t_s t_d \eta_b , & \text{Fresnel geometry} \\ t_s \eta_d \eta_b , & \text{Fourier transform geometry} \end{cases} \tag{6-12}$$

$$T_w = t_w \eta_d , \tag{6-13}$$

and

$$T_r = t_r \eta_d . \tag{6-14}$$

Consider a read-in situation having a reference-to-signal beam intensity ratio at the storage location of K; the total energy reaching the storage location U_t^* is given by

$$U_t^* = U_s^* + U_w^* = (1+K)\ U_s^* \tag{6-15}$$

where U_s^* and U_w^* are the amounts of signal and reference beam energy reaching the storage location, respectively (see Fig. 6-2). We may also write that

$$U_t^* = T_s U_s + T_w U_w , \tag{6-16}$$

where U_s and U_w are the amounts of energy initially directed along the signal and reference paths, respectively. Also,

$$T_i U_i = U_s + U_w \tag{6-17}$$

where U_i is the total available laser output energy per pulse. These relations lead to

$$U_i = \frac{1 + KT_s/T_w}{(1+K)\ T_i T_s}\ U_t^* . \tag{6-18}$$

We can define the energy per unit area required to optimally expose the storage material by S_r. Then for a hologram area d^2 we get

$$U_i = \frac{1 + KT_s/T_w}{(1+K)\, T_i T_s} \; d^2 S_r . \qquad (6\text{-}19)$$

Given a material sensitivity, a hologram size, and the system losses, the required laser energy per read-in pulse can be determined from Eq. (6-19).

The optical losses for read-out must include the effects of the hologram diffraction efficiency, defined as η_h. If each detector in the PDA must receive an amount of energy u_d to achieve a given SNR and error rate, the laser must supply an output energy U_o for read-out given by

$$U_o = \frac{N^2 u_d}{\eta_h T_r} . \qquad (6\text{-}20)$$

6.1.3 Laser Power, Pulse Width and Pulse Rate Factors

The laser is assumed to operate in a pulsed mode for both read-in and read-out. The peak and average laser power and the pulse width and pulse spacing might be different for the read-in and read-out operations. The following quantities are defined:

P_{pi} = peak laser output power during read-in;

P_{ai} = average laser output power during read-in;

P_{po} = peak laser output power during read-out;

P_{ao} = average laser output power during read-out;

P_{Ti} = total prime power supplied to laser during read-in;

P_{To} = total prime power supplied to laser during read-out;

τ_{pi} = laser pulse width during read-in;

ν_{qi} = laser pulse rate during read-in;

τ_{po} = laser pulse width during read-out;

ν_{qo} = laser pulse rate during read-out;

ν_i = input bit rate;

ν_o = output bit rate;

η_ℓ = overall electrical to optical laser power conversion efficiency.

These quantities can be related to each other and to other system quantities as follows:

$$P_{pi} = \frac{U_i}{\tau_{pi}} \tag{6-21}$$

and

$$P_{ai} = U_i \nu_{qi} = \left(\frac{U_i}{N^2}\right) \nu_i \tag{6-22}$$

In Eq. (6-22) the quantity in parentheses represents the amount of laser energy which must be supplied per input bit. We also have that

$$P_{Ti} = \frac{P_{ai}}{\eta_\ell} = \frac{\nu_i}{N^2 \eta_\ell} \frac{1+K\frac{T_s}{T_w}}{(1+K)\, T_i T_s} \, d^2 S_r \,, \tag{6-23}$$

$$P_{po} = \frac{U_o}{\tau_{po}} \,, \tag{6-24}$$

and

$$P_{ao} = U_o \nu_{qo} = \left(\frac{U_o}{N^2}\right) \nu_o \quad . \tag{6-25}$$

In Eq. (6-25) the quantity in parentheses represents the amount of laser energy which must be supplied per output bit. Finally,

$$P_{To} = \frac{P_{ao}}{\eta_\ell} = \frac{u_d \nu_o}{\eta_\ell \eta_h T_r} \quad . \tag{6-26}$$

6.1.4 Important BDC Relations

The effect of the BDC on the overall system was partially described in Eq. (6-25), which includes the effect of the BDC optical efficiency η_b. Another important BDC parameter is the contract ratio ψ_b, defined as the ratio of the light intensity transmitted by ON positions to that transmitted by OFF positions. If we define the signal to noise ratio which the storage material will provide for a given optical arrangement to be $(SNR)_s$, then the effective overall signal-to-noise $(SNR)_T$ is given by

$$(SNR)_T = \frac{(SNR)_s \psi_b}{(f + \psi_b)} \tag{6-27}$$

where f is the ratio of the area occupied by the OFF signals to that by the ON signals.

The prime power requirements of the BDC will be determined mainly by the requirements of the logical drive circuitry and by the input bit rate. The magnitude of the power required by the BDC is not expected to be a significant factor in the overall system design.

6.1.5 Important Beam Deflector Relations

The beam deflectors must provide access to each of the M^2 hologram storage locations for each wavelength used or for each reference beam angle used. Present indications are that acousto-optic beam deflectors (AOBD's) will be used in the holographic memory system. An electro-optic deflector (split-angle type) might be used on combination with a primary pair of AOBD's if reference beam angle changes at each storage location are required, but the more important system design conditions will involve the AOBD's. The following quantities and relations are important for the design of an AOBD:

τ_d = time required for an acoustic wave to propagate across the useful aperture of the AOBD;

L_d = useful length (aperture) of an AOBD;

v_d = acoustic propagation speed in the AOBD material;

θ_B = acoustic Bragg angle;

Δf_d = electrical bandwidth over which the AOBD can be operated;

f_{cd} = center frequency;

k_d = number of Rayleigh resolution elements assigned to each AOBD accessible position;

k_λ = parameter accounting for increased AOBD performance requirements resulting from the use of more than one laser wavelength.

The AOBD optical efficiency η_d was defined and used earlier in Eqs. (6-12) thru (6-14). Also, the number of positions M per dimension that the deflectors must access was defined and used in Eqs. (6-2), (6-6), and (6-8). Other important relations for the design of an AOBD for this system are given as follows:

$$M = \frac{\tau_d \Delta f_d}{k_d k_\lambda} \quad , \tag{6-28}$$

and

$$\tau_d = \frac{L_d}{v_d} \quad . \tag{6-29}$$

The acoustic Bragg angle condition and incremental angular change are

$$\theta_B = \frac{\lambda f_{cd}}{v_d} \quad , \tag{6-30}$$

and

$$\delta\theta_B = \frac{\lambda}{v_d} \quad \delta f_d \quad . \tag{6-31}$$

In Eq. (6-31), $\delta\theta_B$ is an incremental AOBD output angle change resulting from an incremental frequency change δf_d.

The parameter k_λ may be unity if some optical scheme is used to compensate for the required changes in θ_B for changes in λ at a fixed center frequency f_{cd}, as described by Eq. (6-30). If no optical compensation is provided and if the AOBD's must operate at all wavelengths between λ_1 and λ_2 ($\lambda_2 > \lambda_1$), then the center frequency f_{cd} is broadened to a band Δf_{cd} given by

$$\Delta f_{cd} = \frac{\lambda_2 - \lambda_1}{\lambda_o} \quad f_{cdo} \quad , \tag{6-32}$$

where λ_o is the median wavelength and f_{cdo} is the center frequency at λ_o. The factor k_λ is given by

$$k_\lambda = \frac{1}{1 - \frac{\Delta f_{cd}}{\Delta f_d}} \quad . \tag{6-33}$$

For this case, that portion Δf_d^* of the full bandwidth Δf_d available for accessing the M output positions per dimension is given by

$$\Delta f_d^* = \frac{\Delta f_d}{k_f} = \Delta f_d - \Delta f_{cd} \quad . \tag{6-34}$$

It is apparent from Eqs. (6-32) - (6-34) that compensation for λ changes with changes in f_{cd} can place rather strong requirements on the bandwidth of the AOBD's. For example, with $\lambda_2 - \lambda_1 = 200$ nm at $\lambda_o = 500$ nm, a 100 percent overall fractional bandwidth ($\Delta f_d / f_{cdo}$) is necessary to achieve a 60 percent fractional bandwidth ($\Delta f_d^* / f_{cdo}$) at each wavelength in the band.

6.2 SYNTHESIS OF A HOLOGRAPHIC MEMORY WITH A THIN PLANAR STORAGE MATERIAL AND A FRESNEL GEOMETRY

A simplified layout of a holographic memory using a thin planar storage material and a Fresnel hologram geometry is shown in Fig. 6-3. This holographic memory approach should not be considered optimum; it is chosen to illustrate important system tradeoffs. As the synthesis develops, we shall see that the power requirements for the Fresnel geometry are much to high; in a subsequent synthesis, we shall show how the power requirements can be reduced to more reasonable levels. Angular conjugate reference and readout beams are used in this system, as indicated. This selection is permitted only for truly thin storage materials; the maximum thickness must be less than about one holographic fringe spacing (typically less than 0.5 microns). With this readout scheme no lenses are required between the BDC (or the PDA) and the storage

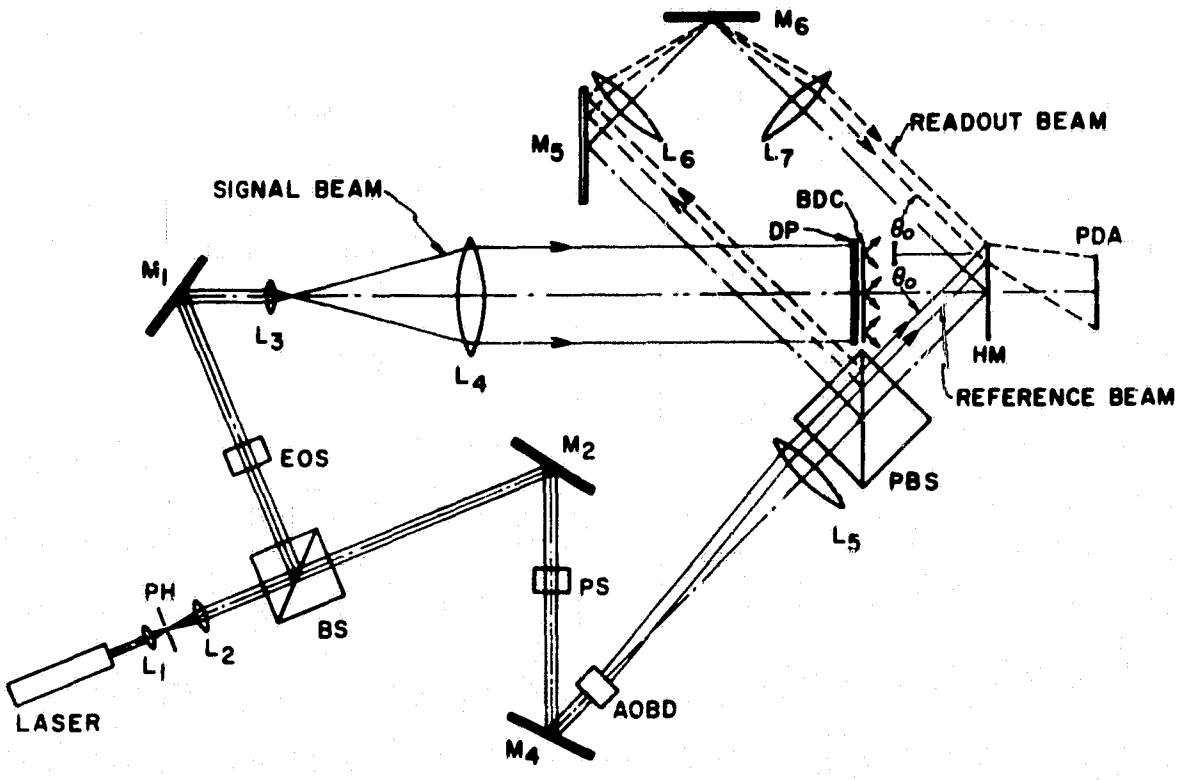

FIGURE 6-3. CONFIGURATION OF 10^9 BIT READ/WRITE HOLOGRAPHIC MEMORY

medium. A real image of the input data (the BDC) is generated behind the storage material in a plane which is conjugate to the input plane; the PDA is located in this output plane.

The reference and readout beam paths are created from a common beam by the polarizing beamsplitter PBS. The polarization switch PS in this path can be electronically activated to rotate the plane of polarization of the incident beam by 90 degrees so that the PBS will either totally transmit or totally reflect this beam (with slight losses). For readin the PS does not alter the incident beam and the PBS totally transmits. For readout the PS rotates the beam 90 degrees and the PBS totally reflects. The AOBD's in this path can be made polarization insensitive with either a liquid media or an acousto-optic crystal such as lead molybdate (PbM_oO_4).

Lens L_5 is positioned one focal length from the AOBD's and provides reference beams that are parallel in direction but converging to spatially separated points. Lenses L_6 and L_7 in the readout path invert the beam positions to provide the required reference/readout beam tracking; these lenses simultaneously provide an image of the PBS reflection plane at the conjugate plane between L_7 and the storage medium HM. This latter feature matches the sizes and wavefront curvatures of the reference and readout beams at the storage material to minimize aberrations in the reconstructed bit patterns.

The electro-optic switch (EOS) in the signal beam path is activated to extinguish the signal beam during readout. Lenses L_3 and L_4 expand and collimate the signal beam. The diffuser plate (DP) is chosen to provide reasonably uniform contributions from each point in the BDC at each point in the holographic memory HM. Since the diffuser efficiency t_d decreases with increasing illumination uniformity the need for a compromise is indicated. In the remainder of this synthesis we shall often refer

to and use the definitions and relations provided earlier in this section.

The diameter of lens L_4 must be at least $\sqrt{2}$ L; the diameters of lenses L_5, L_6 and L_7 must be at least $\sqrt{2}$ D. The width and height of the PBS must be at least DxD for the arrangement shown in Fig. 6-3. The dimensions of the PBS can be reduced by separating the reference/readout beam on a smaller scale, followed by an optical expansion to the required dimensions of the memory. In either case lenses with apertures of at least $\sqrt{2}$ D are required in each path.

The first quantitative constraint can be set by maximizing the apertures of the reference/readout path lenses. Although the maximum practical aperture is subject to question, we will assume a 12-inch (300 mm) upper limit for this example so that D ≤ 212 mm; we choose D = 210 mm. We further assume that $k_2 = 1.3$ is a practical choice; the specifications for the storage material will be established, as this synthesis develops, to be consistant with this choice. Using these selections and Eq. (6-8), we get

$$C_o = C \leq 2.61 \times 10^4 \rho_{xy} .$$

To achieve a capacity of $C = 10^9$ bits the storage material must support a cholographic bit packing density of $\rho_{xy} = 3.84 \times 10^4$ bits/mm^2. This packing density can be obtained with the best available high resolution films at signal-to-noise ratios of the order of 300 or 25 dB. No thin erasable material is known to have such a packing density, but MnBi and photoplastics are prospects. In this system the center spacing of the detecting elements in the PDA and of the bit positions in the BDC will be identical; therefore $k_1 = k_2 = 1.3$. The smallest practical PDA center spacing is expected to be about $k_1 \ell = 0.05$mm so that $\ell = 0.0385$ mm. We set $k_4 = 1$ so that $z = D = 210$ mm and the resolution redundancy

factor is set at $k_3 = 3$. At this point we assume that a pulsed ruby laser with $\lambda = 694.3$ nm will be a suitable laser. With these numbers we get, from Eq. (6-4), that d = 11.35 mm. From Eq. (6-2) we have that M = 14 which leads to N = 2255. The prospect of constructing a BDC or a PDA with $N^2 = 5 \times 10^6$ elements is very poor, mainly because of the complexity of the logic circuitry which would be required. We must seek other criteria for choosing d, ℓ, M, and N.

A practical choice for N appears to be N = 256 lines. An N x N matrix could be arranged with sixteen 16-bit words per line on 256 lines. From Eq. (6-6) we than have that M = 124; Eq. (6-2) gives d = 1.3 mm for the hologram size. By substituting these values in Eq. (6-4) we get $\ell = 0.336$ mm. The BDC side dimension is obtained from Eq. (6-1) to be L = 112 mm. These results appear reasonable. A pair of AOBD's providing access to 124 x 124 positions with a beam size of d = 1.3 mm area can be fabricated with PLZT ferroelectric ceramics if present development trends are indicative of the capabilities of these ceramics. Center spacings of 0.44 mm can be achieved with several classes of PDA's; array sizes of 256 x 256 are expected to be achievable within three years, at the latest.

The laser power requirements for readin and readout can be estimated by assuming some reasonable optical loss and efficiency parameters. With reference to Fig. 6-3 and to the earlier definitions, we make the following transmissivity and efficiency parameter estimations:

$$\eta_b = \tfrac{1}{2}(0.8) = 0.4 \qquad \text{(BDC efficiency)}$$

The factor $\frac{1}{2}$ accounts for only about $\frac{1}{2}$ of the bits in a block being "ones."

$$\eta_d = 0.5 \qquad \text{(AOBD efficiency)}$$

$$t_s = t_w = t_r = 0.3$$

$$t_d = 10^{-5}$$

The diffused light reaching any one hologram in this system is less than $(k_2 M)^{-2} = 6.5 \times 10^{-4}$ because of area ratios. With these choices we get, from Eqs. (6-12) - (6-14), that $T_s = 1.2 \times 10^{-6}$, $T_w = 0.15$, $T_r = 0.15$, $T_i = 0.9$ (assumed). With a beam ratio K = 4, we can now get from Eq. (6-18) that, $U_t^*/U_i = 5.4 \times 10^{-6}$. An achievable amount of energy per pulse, from a ruby laser pulsed at kilohertz rates, is $U_i = 6.25 \times 10^{-3}$ joules/pulse. Therefore, the energy received at the storage material per hologram per pulse must be $U_t^* = 3.38 \times 10^{-8}$ joules. Since the hologram area is $d^2 = 1.69$ mm^2, the energy density requirement of the storage material for optimum exposure is $S_r = U_t^*/d^2 = 20$ ergs/cm^2. This energy density is about the same as the requirements for recording on some high resolution photographic emulsions. It is about 50 times lower than the requirements of Kodak 649-F high resolution film

For readout each detector in the PDA must receive an energy of $u_d = 3 \times 10^{-12}$ joules. If we assume that the hologram diffraction efficiency is $\eta_h = 0.01$, Eq. (6-20) yields $U_o = 0.15 \times 10^{-3}$ joules which is about $0.025\, U_i$. However, the energy initially directed along the reference/readout path by the beamsplitter BS will be only $4 \times 10^{-5} U_i$ because of the relatively large signal path losses. An optical scheme which directs a higher fraction of U_i along the reference/readout path during readout must be added to the system. One possible scheme is to insert a second polarizing beam splitter PBS_2 and polarizing switch PS_2 between L_2 and BS in Fig. 6-3. A third polarizing beamsplitter PBS_3 is inserted between BS and M_2 in the reference/readout path. Additional

mirrors could direct the energy reflected by PBS_2 into PBS_3 with the polarization adjusted so that this energy is reflected toward M_2 along the reference/readout path.

The laser pulse width, along with U_i, will determine the peak laser output power. For example, if a pulse width of $\tau_{pi} = 10^{-7}$ seconds is used for the readin operation, then Eq. (6-21) shows that $P_{pi} = 62.5 \times 10^3$ watts. A more important quantity is the average laser output power, P_{ai} and P_{ao}. The energy required per bit from the laser during readin is $U_i/N^2 = 9.5 \times 10^{-8}$ joule/bit, and Eq. (6-22) shows that $P_{ai} = 9.5 \times 10^{-8}\nu_i$. For $\nu_i = 10^8$ bits/second, $P_{ai} = 9.5$ watts. If the overall laser efficiency is $\eta_\ell = 10^{-3}$, then the prime power required for the laser at $\nu_i = 10^8$ bits/second is $P_{Ti} = 9500$ watts. Lower peak and average powers can be tolerated during readout if a large fraction of the laser output can be directed along the readout path.

In assuming that the storage material could support a bit density $\rho_{xy} = 3.84 \times 10^4$ bits/mm^2, we noted that existing nonerasable materials can operate at this storage density with $(SNR)_s \approx 300$, or 25 dB. In selecting PLZT as the material for the BDC we have a potential contrast ratio $\Psi_b = 1000$, or 30 dB. A more realistic estimate of the achievable contrast is believed to be $\Psi_b = 100$, or 20 dB. With these estimates we get from Eq. (6-27) that $(SNR)_T \approx 300$, or 25 dB with f, the ratio of the areas of the ON and OFF signals, being 1:1.

The two orthogonal AOBD's must each access M = 124 positions at only one wavelength ($k_\lambda = 1$). We take $k_d = 2$ as a reasonable spot resolvability factor so that Eq. (6-28) yields $\tau_d \Delta f_d = 248$. If we select water as the acousto-optic medium, we must hold the maximum frequency $f_{cd} + \frac{1}{2}\Delta f_d$ below about 30 MHz to prevent excessive acoustic attenuation. Assuming that the bandwidth is $\Delta f_d = 0.5 f_{cd}$, we have $f_{cd} = 24$ MHz,

Δf_d = 12 MHz, and τ_d = 27 μ sec. Since v_d = 1.5 mm/μ sec for water, the total length L_d of each AOBD is, from Eq. (6-29), L_d = 18 mm. The acoustic attenuation A for water can be expressed by

$$A = \alpha f^2 L_d \tag{6-35}$$

where A is in dB when α is in dB/Hz^2-mm, f is in Hz, and L_d is in mm. For water at 70°C, $\alpha = 7.3 \times 10^{-17}$ dB/Hz^2-mm so that for f = 30 MHz and L_d = 18 mm we get A = 1.2 dB which is an acceptable attenuation.

Alternatively, if we select $PbMoO_4$ as the acousto-optic medium, we can operate at f_{cd} = 100 MHz with $\Delta f_d = 0.5 f_{cd}$ = 50 MHz which gives τ_d = 5 μ sec. Since v_d = 3.75 mm/μ sec in $PbMoO_4$, L_d = 18.8 mm. Attenuation effects on $PbMoO_4$ are negligible at these frequencies and lengths.

The AOBD length L_d can be under 20 mm for either choice. The AOBD thickness along the optical axis in $PbMoO_4$ can be about one-third of what it must be in water (because of the differences in f_{cd} and v_d) to operate in the Bragg deflection mode. The electro-acoustic coupling in $PbMoO_4$ is theoretically higher than for water, but the design and fabrication of transducers for water is expected to be simpler. It is not clear which AOBD technique should be chosen. Either approach may be successful; more detailed tradeoffs would have to be examined before making the final selection.

The design parameters for the system of Fig. 6-3 are summarized here with comments inserted for clarification:

1. Thin storage material (< 0.5 microns thick),
2. Diffuse image Fresnel hologram arrangement,
3. Angular conjugate readout beams,
4. Maximum lens apertures of 300 mm,

5. Storage material parameters:

$S_r \leq 20$ ergs cm^2 (optimum exposure)

$\rho_{xy} \geq 3.84 \times 10^4$ bits/mm^2

$\eta_h = 0.01$ (diffraction efficiency).

6 Holographic memory dimensions:

$C = 10^9$ bits (total capacity)

$M = 124$ holograms/dimension

$D = 210$ mm

$d = 1.3$ mm

$k_2 = 1.3$

$k_3 = 3$

7. BDC and PDA parameters:

$N = 256$ elements/dimension

$L = 112$ mm

$\ell = 0.336$ mm

$k_1 = 1.3$

BDC:	PDA:
$\eta_b = 0.4$	$u_d = 3 \times 10^{-12}$ joules/detector
$\Psi_b = 100$ or 20 dB	$(SNR)_T \approx 300$ or 25 dB

8. Optical Transmissivities:

$T_s = 1.2 \times 10^{-6}$; $t_d = 10^{-5}$ (diffuser)

$T_w = 0.15$

$T_r = 0.15$

$T_i = 0.9$

9. Pulsed ruby laser parameters:

$\lambda = 694.3$ nm

$U_i = 6.25 \times 10^{-3}$ joules/pulse

$P_{ai} = 9.5$ watts at $\nu_i = 10^8$ bits/second

$P_{Ti} = 9500$ watts at $\nu_i = 10^8$ bits/second

$\eta_\ell = 10^{-3}$

10. AOBD parameters:

$\tau_d \Delta f_d = 248$

$k_d = 2$

$k_\lambda = 1$

Water:	$PbMo_4$:
$\nu_d = 1.5$mm/μ sec	$\nu_d = 3.75$mm/μ sec
$f_{cd} = 24$ MHz	$f_{cd} = 100$ MHz
$\Delta f_d = 12$ MHz	$\Delta f_d = 50$ MHz
$\tau_d = 27$ μ sec	$\tau_d = 5$ μ sec
$L_d = 18$ mm	$L_d = 18.8$ mm
A = 1.2 dB (max)	A = negligible

The important results of this synthesis are the specifications for the storage material, the identification of the effects of the low optical efficiency (diffuse illumination) on the laser power and the storage material sensitivity, and the indication of the direct proportionality of the required average laser output power to the bit rates. The performance specifications for the BDC, the AOBD, and PDA appear to be reasonable for a system which might be scheduled for a breadboard phase in at most two or three years.

The storage material must also have a special property not yet mentioned. During each read-in operation, signal beam energy will reach all storage locations. Some threshold or control mechanisms must exist which prevents the $M^2 - 1$ unwanted signal contributions at each location during the M^2 read-in operations from adding to the total exposure. Otherwise, these contributions will partially expose the storage material. Both MnBi and photoplastics have such a mechanism. MnBi has a Curie temperature threshold which will permit a change only when signal plus reference beam energy is present. Photoplastics can be arranged such that a light signal affects the optical properties of the material only when a particular sequence of charges and voltages are applied.

We have seen that the major disadvantage of the Fresnel geometry is the low utilization of light, leading to excessively high prime power requirements. We shall now consider a system which is considerably more efficient in light useage, leading to reduced laser powers and reduced demands on the sensitivity of the storage material, even though the capacity of the system will be increased by an order of magnitude.

6.3 SYNTHESIS OF A HOLOGRAPHIC MEMORY WITH A THICK PHASE STORAGE MATERIAL AND AN IMAGING FOURIER TRANSFORM GEOMETRY

A simplified optical layout of a holographic memory which incorporates a thick phase storage material and an imaging Fourier transform geometry is shown in Fig. 6-4. The reference and read-out beams for this geometry are identical; an image of the data in plane P_2 (the BDC) is projected onto $Plane_4$ (the PDA) when a beam identical in all respects to the reference beam is directed at the corresponding hologram in plane P_3 (the holographic memory HM).

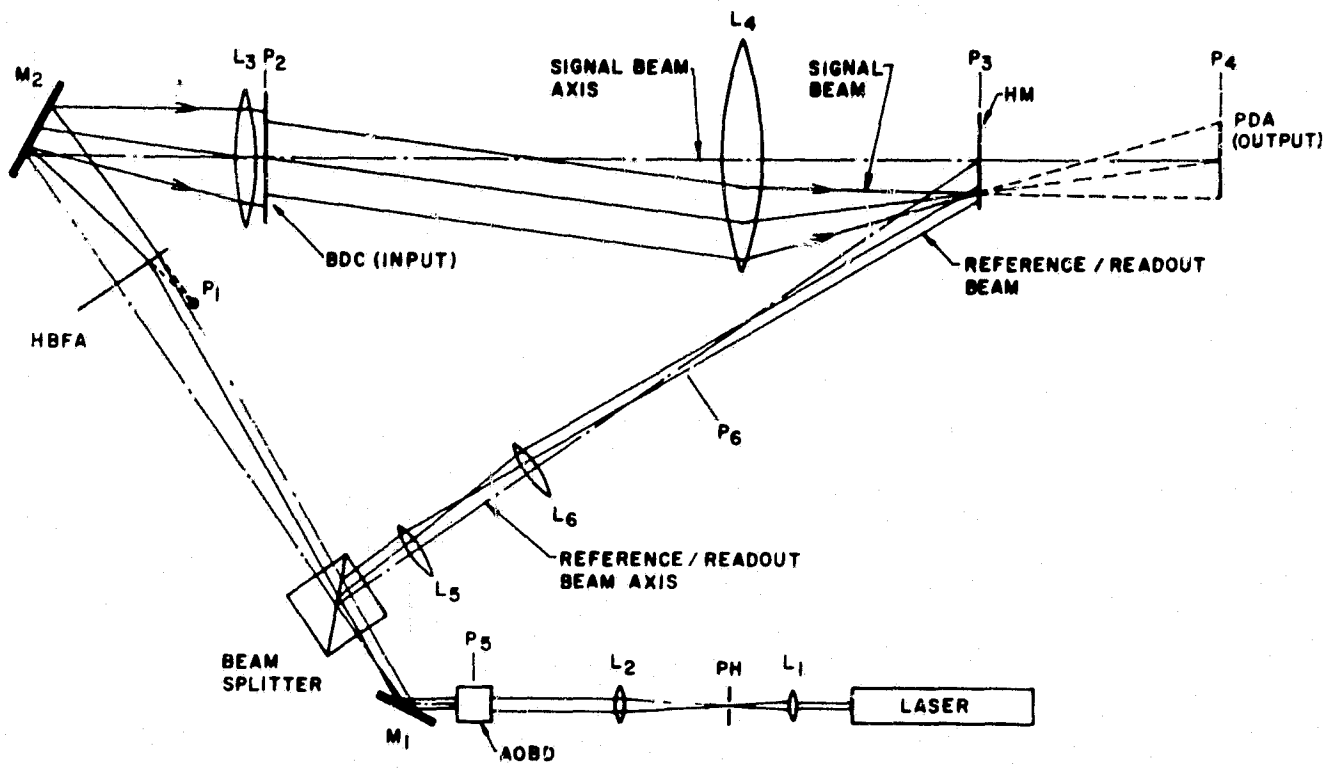

FIGURE 6-4. CONFIGURATION OF 10^{10} BIT READ/WRITE HOLOGRAPHIC MEMORY

In the system shown in Fig. 6-4, the AOBD's precede the reference/signal beamsplitter; both the signal and reference/readout beams are deflected. In the signal path a hologram beam forming array (HBFA) intercepts the deflected and collimated beams from the AOBD's. Each element in the HBFA corresponds to an AOBD output position and therefore to a hologram storage location in the HM. Each element of the HBFA array has the property that the output beam appears to come from a unique point in plane P_1. Therefore, the HBFA converts the angularly deflected beams into a set of point sources in plane P_1, one point source per AOBD output angle and storage location. Plane P_1 is one focal length from lens L_3 so that each apparent point source in plane P_1 generates a collimated beam to the right of L_3. Each collimated beam from L_3 propagates through the BDC and toward lens L_4 with a unique angle relative to the optical axis. The BDC in plane P_2 is two focal lengths from L_4. In plane P_3, one focal length behind L_4, a light distribution proportional to the Fourier transform of the data in the BDC is formed. The position of this light distribution is laterally displaced from the optical axis by an amount proportional to the angular deflection from the axis of the collimated beam from L_3. Appropriate choices of angular deflections will provide separation of each signal beam at the memory. The properties of lens L_4 are very important since it both transforms and images the data for each of the M^2 input images.

The reference/readout path is fairly simple. Lenses L_5 and L_6 image plane P_5 into plane P_6. The deflected beams pivot about the intersection point of the reference/readout axis with plane P_6.

The full aperture h_4 of lens L_4 can be related to other system parameters for the configuration in Fig. 6-4 by

$$h_4 \geq 2D + L + \frac{2f_4 \lambda}{\ell} \qquad (6\text{-}36)$$

where f_4 is the focal length of lens L_4. We can define the aperture ratio R_4 of lens L_4 by

$$R_4 = \frac{h_4}{f_4} \quad , \tag{6-37}$$

and get that

$$D \leq (\tfrac{1}{2} - \frac{\lambda}{R_4 \ell}) \; h_4 - \frac{L}{2} \quad . \tag{6-38}$$

Typically, $R_4 \geq 0.3$ and $\lambda/\ell \leq 0.01$; therefore,

$$D \leq \tfrac{1}{2} (h_4 - L) \quad . \tag{6-39}$$

The hologram aperture d must resolve ℓ in P_4. Thus, we get

$$d = k_3 \quad \delta = k_3 \frac{\lambda f_4}{\ell} \quad . \tag{6-40}$$

Using Eqs. (6-1) and (6-2), we get

$$LD = k_1 k_2 k_3 N M f_4 \lambda \tag{6-41}$$

which can be rewritten as

$$LD = k_1 k_2 k_3 C_0^{\frac{1}{2}} f_4 \lambda \tag{6-42}$$

Using Eq. (6-37), the equality of Eq. (6-39), and Eq. (6-42), we get that

$$D^2 - \tfrac{1}{2} R_4 f_4 D + \tfrac{1}{2} k_1 k_2 k_3 C_0^{\frac{1}{2}} \lambda f_4 = 0 \tag{6-43}$$

Solutions to Eq. (6-48) are that

$$D = \tfrac{1}{4} R_4 f_4 \pm \left[\frac{R_4^2 f_4^2}{16} - \tfrac{1}{2} k_1 k_2 k_3 C_0^{\frac{1}{2}} \lambda f_4 \right]^{\frac{1}{2}} \quad . \tag{6-44}$$

The term in brackets will be imaginary unless

$$\frac{R_4^2 f_4^2}{16} \geq \tfrac{1}{2} k_1 k_2 k_3 C_0^{\frac{1}{2}} \lambda f_4 \qquad (6\text{-}45)$$

or

$$C_0^{\frac{1}{2}} \leq \frac{R_4^2 f_4}{8 k_1 k_2 k_3 \lambda} \quad . \qquad (6\text{-}46)$$

We now choose $k_1 = k_2 = 1.3$, $k_3 = 2$, $\lambda = \lambda_{max} = 700$ nm, and $C_0 = 10^9$ bits and get, with the equality of Eq. (6-46), that

$$R_4^2 f_4 = 600 \text{ mm} \qquad (6\text{-}47)$$

or

$$h_4 = \frac{600}{R_4} \text{ mm} \quad . \qquad (6\text{-}48)$$

The largest lens aperture considered feasible is 24 inches (600 mm). Thus, to achieve $C_0 = N^2M^2 = 10^9$ bits with the arrangement in Fig. (6-4) and the parameters so far selected, we must choose

$h_4 = 600$ mm

$R_4 = 1$

$f_4 = h_4 = 600$ mm

$D = \frac{1}{4} R_4 f_4 = 150$ mm, from Eq. (6-44)

$L = h_4 - 2D = 300$ mm, from Eq. (6-39) with the equality.

We can now choose N and M; the choices N = 256 and M = 124 appear reasonable. The number of incoherent additions ρ_z is as yet unspecified; we choose $\rho_z = 10$ to get $C = C_0 \rho_z = 10^{10}$ bits. We can now get that $d = D/k_2M = 0.93$ mm and $\ell = L/k_1N = 0.90$ mm. The ℓ dimension is rather large; an imaging system with demagnification might have to be inserted after plane P_4 to reduce the size of the output image to make it compatible with more practical PDA dimensions.

From Eq. (6-8) we can not get $\rho_{xy} = 7.5 \times 10^4$ bits/mm^2, which is about twice the storage density of the first system. At this density, we can still expect to achieve $(SNR)_s = 100$, or 20 dB.

Since we have assumed $\rho_z = 10$, a laser which can provide ten discrete wavelengths with electronic wavelength selection means is required. A Nd-YAG laser, which can be operated in an intracavity frequency doubled mode to provide 13 discrete visible laser wavelength, is now commercially available. The distinguishing features of this laser were discussed in paragraph 5.4 We shall proceed with this synthesis assuming that such a laser could be designed with electronic wavelength selection, with sufficient coherence, and with sufficient peak and average power outputs. The performance required by the system will be compared to presently achievable performance levels.

From the 13 available discrete wavelengths between 473 nm and 679 nm, 10 can be selected so that the closest spacing between adjacent wavelengths is 3 nm. From Eqs. (6-10) and (6-11) we find that by setting $\lambda_2 - \lambda_1 = 3$ nm, $\lambda_0 = 500$ nm, and $\rho_z = 1$ (adjacent wavelengths), the storage material thickness must be at least $b_0 = 0.42$ mm. This result is compatible with the hologram dimension d = 0.93 mm.

The optical transmissivities and efficiencies will be similar to those in the first synthesis with one major exception: a diffuser is not used and a much larger fraction of the signal beam energy reaches the HM during each readin. We assume, therefore, that

$\eta_b = 0.4$

$\eta_d = 0.5$

$t_s = t_w = t_r = 0.3$

$t_d = 1.0$ (no diffuser)

With these values we get, from Eqs. (6-12) - (6-14), that

$$T_s = 0.06$$

$$T_w = T_r = 0.15$$

$$T_i = 0.9 \text{ (assumed)}$$

Using a beam ratio K = 4, we find from Eq. (6-18) that $U_t^*/U_i = 0.104$. If $d_2 = 0.865$ mm^2, we obtain from Eq. (6-19) that

$$S_r = 0.12U_i \tag{6-49}$$

where S_r will be in joules/mm^2 if U_i is in joules. The multiple visible wavelength Nd-YAG laser appears to be capable of supplying $U_i = 7 \times 10^{-5}$ joules = 700 ergs per pulse at a 4 KHz pulse rate. Therefore we can tolerate a film exposure energy density requirement of $S_r = 8400$ ergs/cm^2. Kodak 649-F high resolution films requires only 1000 ergs/cm^2.

For readout each detector in the PDA must receive about $u_d = 3 \times 10^{-1}$ joules. The amount of energy directed along the reference/readout path for K = 4, $T_s = 0.06$, and $T_t = 0.15$ is

$$U_r = \frac{T_i}{1+K\frac{T_s}{T_r}} U_i = 0.346\ U_i \ . \tag{6-50}$$

Thus the effective laser output energy $U_o = U_r = 0.346\ U_i$ and from Eq. (6-20) we get

$$\eta_h U_i = 3.8 \times 10^{-6} \text{ joules.} \tag{6-51}$$

For $U_i =$ x 10^{-5} joules, the hologram diffraction efficiency per hologram must be $\eta_h = 0.054$. This efficiency level is practical with $\rho_z = 10$ holograms per storage locations.

The peak laser power for $\tau_{pi} = 10^{-7}$ seconds is $P_{pi} = 700$ watts. The average laser power P_{ai} is more important; the energy per bit supplied for readin is $U_i/N^2 = 1.06 \times 10^{-9}$ joule/bit. From Eq. (6-22) we find that $P_{ai} = 1.06 \times 10^{-9} \nu_i$. For $\nu_i = 10^8$ bits/second, $P_{ai} = 0.106$ watts. The presently available Nd-YAG laser can operate at this average output power level in a repetitively pulsed mode at each of the 13 visible wavelengths. If the overall laser efficiency is $\eta_\ell = 10^{-3}$, the prime power requirement at $\nu_i = 10^8$ bits/second is $P_{Ti} = 106$ watts. We note that the power requirements for the Fourier transform approach are nearly two orders os magnitude less than those for the Fresnel approach discussed in the previous system and that the system capacity has been increased by a factor of ten.

In assuming the storage material could support a bit density of $\rho_{xy} = 7.5 \times 10^4$ bits/mm^2, we noted that $(SNR)_s = 100$, or 20 dB, appears feasible. With PLZT as the BDC material we again can expect $\Psi_b = 100$, or 20 dB. Thus, with Eq. (6-27) we can estimate that the PDA will observe $(SNR)_T \approx 100$ or 20 dB.

The two orthogonal AOBD's must each access M = 124 positions for $\rho_z = 10$ wavelengths in the band from $\lambda_1 = 473$ nm to $\lambda_2 = 679$ nm. If we assume that an optical Bragg angle compensation scheme such as the simple one illustrated in Fig. 5-3 is used, the center drive frequence f_{cd} will be approximately the same for each wavelength so that very little extra drive bandwidth will be required. However, the specific drive frequency which directs the beam to any specific storage location will be different for each wavelength (except at the zero incremental deflection position where $f = f_{cd}$). Therefore, the drive electronics must be capable of providing about $\rho_z M = 1240$ stable output frequencies within the bandwidth Δf_d instead of M = 124, as in the first system. Otherwise,

the AOBD's for this system can be identical to those characterized in the first system synthesis.

The design parameters synthesized for the system of Fig. 6-4 are summarized here with comments inserted for clarification.

1. Thick phase storage material.
2. Imaging Fourier transform hologram arrangement.
3. Identical reference and readout beams.
4. Fourier transforming lens parameters:

$h_4 = 600$ mm

$R_4 = 1$

$f_4 = 600$ mm

5. Storage material parameters:

$b_o \geq 0.42$ mm ($\Delta\lambda_{min} = 3$ nm)

$\rho_z = 10$ incoherent additions

$S_r \leq 8400$ ergs/cm^2

$\rho_{xy} \geq 7.5 \times 10^4$ bits/mm^2

$\eta_h \geq 0.054$ (diffraction efficiency)

6. Holographic memory parameters:

$C = 10^{10}$ bits (total capacity)

$M = 124$ storage locations/dimensions; $\rho_z = 10$

$d = 0.93$ mm

$k_2 = 1.3$

$k_3 = 2$

7. BDC and PDA parameters:

$N = 256$ elements/dimension

$L = 300$ mm

$\ell = 0.9$ mm

$k_1 = 1.3$

BDC:

$\eta_b = 0.4$

$\Psi_b = 100$ or 20 dB

PDA:

$u_d = 3 \times 10^{-12}$ joules/detector

$(SNR)_T \approx 100$ or 20 dB

8. Optical transmissivities:

$T_\varepsilon = 0.06$

$T_w = T_r = 0.15$

$T_i = 0.9$

9. Nd-YAG laser parameters:

$\rho_z = 10$ wavelengths from 473 nm to 679 nm

$U_i = 7 \times 10^{-5}$ joules per pulse

$P_{ai} = 0.106$ watts at $\nu_i = 10^8$ bits/second

$P_{Ti} = 106$ watts at $\nu_i = 10^8$ bits/second

$\eta_\ell = 10^{-3}$

Electronic wavelength selection means required.

10. AOBD parameters:

Optical compensation for the required Bragg angle changes with laser wavelength (fixed center drive frequency)

$\tau_d \Delta f_d = 248$

$k_d = 2$

$k_\lambda = 1$ (because of optical compensation)

water:	$PbMoO_4$:
v_d = 1.5mm/μsec	v_d = 3.75mm/μsec
f_{cd} = 24 MHz	f_{cd} = 100 MHz
Δf_d = 12 MHz	Δf_d = 50 MHz
τ_d = 27 μsec	τ_d = 5 μsec
L_d = 18 mm	L_d = 18.8 mm
A = 1.2 dB (max)	A = negligible

The important results of this synthesis are the specifications for the storage material, the specifications for the Fourier transforming lens, and the specifications for the multiple wavelength laser. The performance specifications for the BDC, the AOBD's, and the PDA appear to be reasonable for a system which might be scheduled for a breadboard phase in at most two to three years. The added feature of operation over a wide range of visible wavelengths will affect the design and operating complexity, but these are not expected to introduce insurmountable constraints.

The signal beam energy is highly localized during each readin in the Fourier transform geometry. The storage material will not require a threshold or control mechanism for desensitizing the M^2-1 other storage positions when one is being exposed if the slight amount of stray light in the vicinity of each readin signal can be tolerated.

The major implementation problems for this sytem would be obtaining a satisfactory read/write storage material, and a high quality lens with a unity relative aperture and a 600 mm focal length or its equivalent. The 2.4 meter space required between the input plane (the BDC) and the output plane (the PDA) might also present a problem

although the optics can be folded to preserve space. Furthermore, a proper optical design can reduce the total length of the system.

The two systems synthesized here should not be considered optimum. They were selected tc illustrate in detail the flavor of the systems design tradeoffs and constraints Further design efforts are needed to optimize the overall system performance. Nevertheless, it is clear from these two examples that a thick recording material is needed to achieve large storage capacities and that the Fourier transform geometry places a much lower requirement on the prime laser power.

SECTION VII

RECOMMENDATIONS

7.1 INTRODUCTION

In this section we give recommendations for continued efforts to develop a mass holographic memory system. These recommendations are based, in part, on the results of our exploratory studies during the past year and, in part, on our assessment of state-of-the-art technology in several key areas. A modifiable feasibility optical test bed should be designed and fabricated that is capable of using existing devices (such as acousto-optic beam deflectors, lasers, photodetector arrays, etc.) as well as improved versions of these devices as they become available. The recommended program could be accomplished within one year; the performance figures are consistent with this time scale. The ultimate performance needed of the various components to achieve a 10^{10} - 10^{12} bit read/write memory are also noted where appropriate.

We recommend that the test bed system be designed to operate in either of two modes. In the first mode, an interim read/write storage material (such as a photoplastic material) should be used so that the total memory system can be operated and tested under conditions similar to the intended application, but at a reduced total capacity. In the second mode, a thick semi-permanent recording material should be used so that incoherent addition can be demonstrated and tested; the total capacity in this second mode will be, therefore, higher than in the first mode.

We recommend that an extensive program be started to develop suitable recording materials for this application. A list of the requirements for this material is given in paragraph 7.4. We also recommend that a computer simulation program be started to assist in the optical

design; since the operating parameters of the major system components interact, it is difficult to optimize an optical design with so many free parameters. The characteristics of the storage material also strongly influence the system design. A part of the computer simulation should be to model the behavior of the photographic film so that the performance of the total memory system can be predicted. The recommendations are given in paragraph 7.5.

7.2 READ/WRITE MEMORY

The recommended performance figures for the major system components for the next phase are listed here with the ultimate performance figure needed to achieve a 10^{10} - 10^{12} bit memory. The capacity of this recommended system is rather modest (2.5×10^5 bits) but it is within state-of-the-art technology.

Laser - Commercially available lasers capable of providing 0.1 watt at each of at least two wavelengths will be adequate for both the read/write memory and the semi-permanent memory. For the final system an electronically tunable laser operable at 15 or more wavelengths in a 200 nm visible range will be needed. Final specifications for such a laser with power and pulse duration requirements compatible with updated system requirements remain to be determined.

Beam Deflectors - Beam deflectors capable of accessing any position in at least an 80 x 80 position format with a random access time of 30 to 60 microseconds are currently available. For the final system it is likely that a 300 x 300 position, 15 wavelength deflector will be needed to meet the system requirements. Final specifications for a 300 x 300 position deflector are to be determined.

Block Data Composer - As indicated in Section V, we believe that it is possible to fabricate a BDC, from PLZT or a similar material,

having 100 x 100 switchable elements in the near future. A 256 x 256 element BDC appears to be adequate for the final system based on our preliminary calculations.

Storage Material - Although we do not expect that photoplastics will be used as the storage material in the ultimate system, these materials appear to be the only reasonable sensitive erasable optical storage media which are presently available. It is reasonable to expect that a 5 x 5 array of holograms can be recorded on this material; this figure, combined with BDC capability of 100 x 100 = 10^4 bits/hologram, leads to a total storage capacity of 2.5 x 10^5 bits. The requirements on the storage material for use in the final system are probably more remote from state-of-the-art technology than any other component in the holographic memory. For this reason, we list the ultimate requirements for this material in paragraph 7.4.

Photodetector Array - Although it would be preferable to use a photodetector array having the same number of elements as the BDC, we believe it to be more feasible to begin with a partially populated array. Such an array would provide all the necessary functions for testing and exercising the memory. Ultimately the PDA must have the same number of elements as the BDC (256 x 256 elements). Fabrication techniques must be advanced and performance specifications established in this area.

7.3 SEMI-PERMANENT MEMORY

The major difference between the semi-permanent memory and the read/write memory is that the former will use more than one wavelength and a non-erasable thin storage material. Since the storage material for the semi-permanent memory may be photographic films or dichromated gelatins having a low noise figure, more holograms can be stored in a

memory system having fixed constructional parameters. If a 20 x 20 array of holograms and two wavelengths are used, the storage capacity of the semi-permanent memory will be 8×10^6 bits.

All of the requirements on the components of the read/write memory listed in paragraph 7.2 are the same, except that the beam deflector design is somewhat complicated by the need to operate at two wavelengths.

7.4 BASIC REQUIREMENTS FOR THE HOLOGRAPHIC MEMORY STORAGE MATERIAL

The basic requirements for any recording medium for this memory application is that it (1) has fast and localized read-write-erase capabilities, (2) is panchromatic over a suitable spectral range, (3) is capable of resolving over 2000 lines/mm, (4) has reasonable diffreaction efficiency, (5) has good noise characteristics, (6) can be nondestructively read out, (7) offers high density storage capabilities, and (8) be dimensionally stable for different environmental conditions. In the following we set forth our preliminary recommended specifications for the holographic storage materials and, where appropriate, we include a more detailed discussion of the requirements.

Phase Material - The recording media should be a material whose index of refraction changes as a function of an impinging spatially modulated laser light intensity. The peak (or maximum) index of refraction change, Δn, should be at least 0.001 at any wavelength in a 200 mm range. Furthermore, the material should not have absorption losses in excess of 5 percent of the incident illumination power at any incident angle. The choice of phase rather than absorptive material is advantageous because of its higher diffracting capabilities and relatively higher signal-to-noise ratio when a multiplicity of signals are incoherently superimposed in the

recording material. For the case of simple grating holograms recorded as fluctuations of the index of refraction in phase materials, the diffraction efficiency η is given as

$$\eta = \sin^2 \frac{\pi \Delta n t_o}{\lambda \cos \theta} \quad ,$$

where Δn is the fluctuations of the index of refraction, t_o is the thickness of the hologram, λ is the wavelength of the incident illumination, and θ is the Bragg angle. This equation shows that thick phase holograms can achieve a theoretical maximum diffraction efficiency of 100 percent when $\Delta n t_o = \frac{1}{2} \lambda \cos$. Using nominal values of $\lambda = 0.5$ micron, $t_o = 1$ mm, and $\theta = 30°$, we find that $\Delta n = 0.2165 \times 10^{-3}$. Allowing for incoherent superposition of signals and variations in both wavelength and Bragg angle, we expect that this value should be at least $\Delta n = 0.001$.

Linearity - The fluctuations of index of refraction of the material should be linearly related to the fluctuations of the incident light intensities over a range of $\Delta n = 0.001$. This requirement is designed to eliminate recording nonlinearities which tend to degrade the signal-to-noise ratio of the reconstructed imagery.

Thickness - The nominal thickness of the material over which the fluctuations in refractive index occur should be at least 1 mm. The dominant factor which dictates the desired thickness is the requirement for high angular orientation and wavelength discrimination. By using the wavelength discrimination property of thick holograms we could superimpose 20 signals, over a spectral range of 200 mm, by mearly separating the recording wavelength for each component hologram by 10 nm. For such a wavelength separation we can determine the thickness required to eliminate crosstalk between the component holograms by using the relation

recording material. For the case of simple grating holograms recorded as fluctuations of the index of refraction in phase materials, the diffraction efficiency η is given as

$$\eta = \sin^2 \frac{\pi \Delta n t_o}{\lambda \cos \theta} \quad ,$$

where Δn is the fluctuations of the index of refraction, t_o is the thickness of the hologram, λ is the wavelength of the incident illumination, and θ is the Bragg angle. This equation shows that thick phase holograms can achieve a theoretical maximum diffraction efficiency of 100 percent when $\Delta n t_o = \frac{1}{2} \lambda \cos$. Using nominal values of $\lambda = 0.5$ micron, $t_o = 1$ mm, and $\theta = 30°$, we find that $\Delta n = 0.2165 \times 10^{-3}$. Allowing for incoherent superposition of signals and variations in both wavelength and Bragg angle, we expect that this value should be at least $\Delta n = 0.001$.

Linearity - The fluctuations of index of refraction of the material should be linearly related to the fluctuations of the incident light intensities over a range of $\Delta n = 0.001$. This requirement is designed to eliminate recording nonlinearities which tend to degrade the signal-to-noise ratio of the reconstructed imagery.

Thickness - The nominal thickness of the material over which the fluctuations in refractive index occur should be at least 1 mm. The dominant factor which dictates the desired thickness is the requirement for high angular orientation and wavelength discrimination. By using the wavelength discrimination property of thick holograms we could superimpose 20 signals, over a spectral range of 200 mm, by mearly separating the recording wavelength for each component hologram by 10 nm. For such a wavelength separation we can determine the thickness required to eliminate crosstalk between the component holograms by using the relation

$$\Delta\lambda_{\frac{1}{2}} = \frac{.47\,\lambda^2\,(n^2 - \sin^2\theta_s)^{\frac{1}{2}}}{t_o\left[n^2 - (n^2 - \sin^2\theta_s)^{\frac{1}{2}}(n^2 - \sin^2\theta_r)^{\frac{1}{2}} + \sin\theta_s \sin\theta_r\right]} \quad ,$$

where n and t_o are the average index of refraction and thickness, respectively, of the recording medium, λ is the wavelength of illumination, and the incidence angles of the reference and signal beams relative to the hologram are denoted by θ_r and θ_s, respectively. We find that for offset angles $(\theta_r + \theta_s)$ exceeding 40° and nominal wavelength of 0.5 microns, a thickness of 1 mm is sufficient to avoid significant crosstalk between the component holograms.

Resolution - The material should respond uniformly to spatial variation of intensity over the range of 100 to 2200 lines/mm. Deviation from this response (i.e., index of refraction fluctuations) should not exceed ± 10 percent. The resolution of the recording material, which ultimately limits the storage capacity, can be related to the angle between the reference and signal beams, by the grating equation

$$d \sin \frac{\theta_r + \theta_s}{2} = \lambda \quad ,$$

where d is the distance between the recorded fringe surface, θ_r and θ_s are the angles of the reference and signal beam relative to the hologram, and λ is the wavelength of illumination. For this application we expect the illumination wavelength to vary from 400 mm to 750 mm, and the offset angle $(\theta_r + \theta_s)$ to vary from 5° to 90°. Using combinations of extreme values, we calculated that d_{min} = 10 microns and d_{max} = .45 microns. This leads to a spatial frequency range of 100 lines/mm to 2200 lines/mm.

Exposure and Erasure Sensitivity - On exposure to laser illumination of 100 milliwatts/mm^2 for a 0.1 millisecond duration, the material

should change its index of refraction by $\Delta n = 0.001$. We anticipate that multiwavelength lasers having output powers of 20 mJ/cm^2 will become available. Allowing for 50 percent efficiency for page composer, and 10 percent efficiency for deflection devices and optical components, the energy density impinging on the storage material is reduced to 10 $\mu J/mm^2$. If 10^5 bits of information can be recorded on each hologram in the array and if we assume that the desired data rate is 10^8 bits/sec, the maximum duration for exposing each hologram is 0.1 millisecond which leaves 0.9 milliseconds to compose the next block of data. Thus, the available intensity is 100 milliwatts/mm^2.

Spectral Response - The spectral response of the material should be uniform to within ±10 percent over a range of 200 nm. The center of this range could be at any wavelength within the band of 500 nm to 650 nm. The required spectral sensitivity of the material is established by the available laser sources and the spectral response of other components of the system. The response of the input block data composer, output photo-detector array, and optical components operate best at wavelengths greater than 450 nm. Since it is inconvenient to work with wavelengths greater than 750 nm, we limited the center of the tunable wavelength range to values between 500 nm and 650 nm.

Noise Characteristics - For a uniformly exposed recording resulting in a refractive index change ranging from 0 to 0.001, the ratio of scatter intensity over incident intensity should not exceed 10^{-8}. For an incident beam, impinging normally on the recording material and illuminating area of 1 cm^2, the scattered intensity measured at a distance of 100 mm from the recording material at an angle of 40° relative to the normal should not exceed 10^{-8} of the intensity measured along the normal at the same distance.

The quality of the image reconstructed from a hologram is dependent on the characteristics of the noise generated by the recording material. This noise, which is random in nature, is the scattered light caused by the granular structure of the recording materials. A measure of the severity of the noise in the reconstructed image is given by the signal-to-noise ratio, defined as the ratio of the average energy of the image to the variance of the fluctuation of the noise processes. For coherent optical systems, we find that a better measure is given by the ratio of the signal intensity to the average noise intensity. Because this ratio can be conveniently measured experimentally, it is the average noise intensity which we define in the specification above. Based on our earlier analysis and experimental results, we chose the value 10^{-8} for the ratio of scatter to incident intensity. This value is based on the need for a signal-to-noise ratio of 100 to get suitable error rates for a hologram with an area equal to 1 mm^2, a nominal diffraction efficiency of 50 percent, and 20 incoherent recordings.

Reversibility - The material should operate through repeated record-erase cycles, with no significant degradation between recordings, for a period of several years. The number of record-erase cycles is dependent on the exact function of the optical memory and whether the storage material can be periodically replaced.

Nondestructive Readout - The material should be capable of non-destructive readout of the recorded information with any wavelength in the wavelength range 4000Å to 7500Å. Degradation of the recorded fluctuations of the refractive index should not exceed 10 percent. We expect that these requirements could be satisfied with some means of external control, say the application of an electric or magnetic field.

Multiple Recordings - Superposition of twenty independent recordings should be possible. Later recordings in a sequence shall not adversely affect earlier recordings. This requirement is designed to assume that the material can support a multiplicity of superimposed recordings.

Localized Recording and Erasing - The material should have the capabilities for effectively partitioning it into independent cubes having 1 mm sides. Readin and erasure of the recorded information in each of these component cubes should not affect the recordings in adjacent cubes. The spacing between the centers of these cubes should not exceed 2 mm.

Environmental Effects - Limited environmental changes of temperature and humidity should have negligible effect on the dimensional stability of the material. Specifically, the termal coefficient of linear expansion should not exceed 1×10^{-6} cm/cm/°C, and the humidity coefficient of linear expansion should not exceed 10^{-6} cm/cm/1 percent change in relative humidity. Changes in temperature and humidity result in either shrinkage or expansion of the recording material. These in turn generally cause a change in both orientation and spacing of the fringe surfaces in holograms recorded in three dimensional media. As a consequence of this change, either the orientation or the wavelength of the reconstructing beam must be altered to maximize the diffracted intensity. In both instances, the location of the reconstructed image will also change resulting in poor registration with the output photodetector array.

In the following example we illustrate how to establish the required value for the termal coefficient of linear expansion (TCE). For simplicity we consider only simple grating holograms in which the fringe surfaces are perpendicular to the surface of the recording medium. The spacing d of the recorded fringes obeys the Bragg relation

$$d = \frac{\lambda}{2 \sin \theta}$$

where λ is the illumination wavelength, and θ is half the angle subtended between the reference and signal beams. If we allow for expansion or contraction due to a temperature difference (ΔT) between readin and readout, we find that the fringe spacing becomes

$$d' = d + \Delta d = [1 + (TCE)\ \Delta T] \frac{\lambda}{2 \sin \theta}$$

where $\Delta d = \pm (TCE)\ \Delta T d$, causing an angular change $\Delta\theta$ for satisfying the Bragg relation for the changed condition, where

$$\Delta\theta = \frac{1}{\frac{\partial d}{\partial \theta}}\ \Delta d$$

$$= - (TCE)\ \Delta T \tan \theta$$

and

$$TCE = \left| \frac{\Delta\theta}{\Delta T}\ \cot \theta \right| .$$

In an earlier paragraph we noted that in order to achieve proper wavelength discrimination we must resort to hologram thicknesses exceeding 1 mm. For this thickness the angular orientation discrimination is smaller than 3 minutes of arc. Consequently if we allow deviations of ±10 percent, $\Delta\theta$ cannot exceed ±0.3 minutes of arc or approximately $\pm 10^{-4}$ rad. Using this value for $\Delta\theta$ and $\theta = 45°$ and $\Delta T = 50\,°C$, we find that

$$TCE = 1 \times 10^{-6}\ cm/cm/\,°C.$$

This requirement can obviously be relaxed if some temperature control schemes are used. Similar procedures can be used to find the humidity coefficient of linear expansion.

7.5 SYSTEM ANALYSIS AND RECORDING MATERIALS SIMULATION WITH A COMPUTER

As a part of the computerized system studies a computer program to simulate the response of some idealized recording materials should be written. The purpose of this simulation study is to indicate what characteristics the recording material must have for a 10^{10}- 10^{12} bits holographic memory system. The idealized material is characterized by its

(1) thickness
(2) refractive index
(3) absorption coefficient
(4) modulation transfer function (MTF)
(5) exposure sensitivity
(6) wavelength sensitivity
(7) temperature and humidity dependence
(8) dynamic range
(9) noise characteristics

The response of the recording material should be investigated for various recording parameters such as

(1) types of holograms (Fresnel type, Fourier transform type, etc.)
(2) the incidence angles of the reference beam and signal beam
(3) angle of the readout beam
(4) recording and readout wavelengths
(5) reference-to-signal beam intensity ratio
(6) input data format, size and contrast

The parameters of interest in the response are

(1) diffraction efficiency
(2) aberrations

(3) signal-to-noise ratio

(4) angular orientation and wavelength discrimination

These parameters of the recording material will then be used in the overall system study. In the recording material simulation, the computer programs should have provisions to generate graphically the response of a specific signal recorded on the idealized material.

Equally important is the relationships among the operating parameters of the other major system components. Among these parameters are the following:

(1) the beam deflectors:

- (a) efficiency (electrical and optical)
- (b) random access time
- (c) number of randomly accessible positions per dimension and coupling between dimensions
- (d) repeatability
- (e) effects of temperature and wavelength variations
- (f) effects of drive power and frequency variations

(2) the block data composer:

- (a) efficiency
- (b) speed
- (c) contrast ratio
- (d) electrical drive requirements
- (e) effects of temperature and wavelength variations

(3) the laser:

- (a) efficiency
- (b) effect of output power fluctuations
- (c) coherence requirements

(3) (d) output power requirements

(e) number of wavelengths and tuning rates required

(f) effects of temperature on performance

(g) pulse rates and widths needed

(4) the output detector array:

(a) number of elements needed

(b) dimensions

(c) sensitivity versus wavelength

(d) response time to light and to electronic interrogation signals (output data rate)

(e) effects of temperature changes

(f) registration tolerances imposed on the output data

(5) the input/output interfaces:

(a) data rates to be accommodated

(b) signal levels

(c) buffer requirements

Other system requirements may be added to this list. The need for a computerized system analysis approach is clearly indicated by the number of system elements which interact. The choice of computer inputs and outputs will be determined mainly by examining those parameters which are amenable to change (outputs) and those which are not (inputs).

REFERENCES

1. J. Goodman, Introduction to Fourier Optics, McGraw-Hill Book Co., Inc., 1968.

2. H. Smith, Principles of Holography, John Wiley and Sons, Inc., 1969.

3. For example see F. M. Smits and L. E. Gallaher, "Design Considerations for a Semipermanent Optical Memory", Bell Systems Tech. J., 46, 1267 (1967).

4. P. J. vanHeerden, "Theory of Optical Information Storage in Solids", Appl. Opt., 2, 393 (1963).

5. A. A. Friesem, et. al., "Holographic Data Storage in Thick Recording Media", Proceedings of Northeast Electronics Research Engineering Meeting (NEREM), Boston, Mass., Nov. 1968.

6. A. A. Friesem and J. L. Walker, "Thick Absorbing Media in Holography", Appl. Opt., 9, 201 (1970).

7. A. A. Friesem, "Three Dimensional Recording Media in Holography", Ph. D. Thesis, University of Michigan, 1968.

8. A. Kozma, "Effect of Film Grain Noise in Holography", J. Opt. Soc. Am., 58, 436 (1968).

9. A. Kozma, "Analysis of the Film Nonlinearities in Hologram Recording", Optics Acta, 15, 527 (1968).

10. J. W. Goodman and G. R. Knight, "Effects of Film Nonlinearities on Wavefront-Reconstruction Images of Diffuse Objects", J. Opt. Soc. Am., 58, 1276 (1968).

11. A. Kozma, G. W. Jull and K. O. Hill, "An Analytical and Experimental Study of Nonlinearities in Hologram Recording", Appl. Opt., 9, 721 (1970).

12. J. Goodman, "Film Grain Noise in Wavefront-Reconstruction Imaging", J. Opt. Soc. Am., 57, 493 (1967).

13. E. L. O'Neill, Introduction to Statistical Optics, Addison-Wesley Publishing Co., Inc., Reading, Mass., 1963.

14. C. E. Kenneth Mees and T. H. James, The Theory of Photographic Process, Third Edition, MacMillian, Inc., 1966.

15. W-H. Lee and M. O. Greer, "Noise Characteristics of Photographic Emulsion Use in Holography", to be published.

16. J. I. Marcum and P. Swerling, "Studies of Target Detection by Pulsed Radar", IRE Trans. of Information Theory, 6, 145 (1960).

17. J. I. Marcum, "Table of Q-Function", Rand Corporation, Santa Monica, California, Report No. RM-339, January, 1950.

18. W. C. Lindsey, "Error Probabilities for Rician Fading Multichannel Reception", IEEE Trans. of Information Theory, IT-10, 339 (1964).

19. I. S. Gradshteyn and I. M. Ryzhik, Tables of Integrals, Series and Products, Academic Press, New York, 1965.

20. F. S. Chen, J. T. LaMachia and D. B. Fresen, "Holographic Storage in Lithium Niobate", Appl. Phys. Letters, 13, 223 (1968).

21. J. A. Armstrong, "Fresnel Holograms Their Imaging Properties and Aberrations", IBM J. Research and Development, 9, 171 (1965).

22. R. W. Meier, "Magnification and Third-Order Aberrations in Holography", J. Opt. Soc. Am., 55, 987 (1965).

23. E. N. Leith, J. Upatnieks, and K. A. Haines, "Microscopy by Wavefront Reconstruction", J. Opt. Soc. Am., 55, 981 (1965).

24. A. Offner, "Ray Tracing Through a Holographic System", J. Opt. Soc. Am., 56, 1509 (1966).

25. E. B. Champagne, "Nonparaxial Imaging, Magnification and Aberration Properties in Holography", J. Opt. Soc. Am., 57, 51 (1967).

26. I. A. Abramowitz and J. M. Ballantyne, "Evaluation of Hologram Aberrations by Ray Tracing", J. Opt. Soc. Am., 57, 1522 (1967).

27. I. A. Abramowitz, "Evaluation of Hologram Imaging by Ray Tracing", Appl. Opt., 8, 403 (1969).

28. R. S. Mezrich, "Curie-Point Writing of Magnetic Holograms and MnBi", Applied Physics Letters, 14, 132 (1969).

29. C. E. Land and G. H. Haertling, "Electro-Optic Ceramics: A Review of Materials and Applications", Bulletin of the American Ceramic Society, 49, 411 (1970).

30. G. H. Haertling and C. E. Land, "Hot-Pressed Ferroelectric Ceramics for Electro-Optics Applications", Bulletin of the American Ceramic Society, 49, 411 (1970).

31. J. R. Maldonado and A. H. Meitzler, "Ferroelectric Ceramic Light Gates Operated in a Voltage Controlled Mode", IEEE Transactions on Electron Devices", ED-17, 148 (1970).

32. C. E. Land and P. D. Thacher, "Ferroelectric Ceramic Electro-Optic Materials and Devices", Proceedings of IEEE, 57, 721 (1969).

33. D. B. Fraser and J. R. Maldonado, "Improved Aging and Switching of Lead Zirconate-Lead Titanate Ceramics with Indium Electrodes", Bulletin of the American Ceramic Society, 49, 412 (1970).

34. H. Kogelnik, C. V. Shank, T. P. Sosnowski, and A. Dienes, "Hologram Wavelength Selector for Dye Lasers", Applied Physics Letters, 16, 499 (1970).

35. S. E. Harris, "Tunable Optical Parametric Oscillators", Proceedings of the IEEE, 57, 2091 (1969).

36. W. R. Klein and D. B. Cook, "Unified Approach to Ultrasonic Light Diffraction", IEEE Transactions on Sonics and Ultrasonics, SU-14, 123 (1967).

37. I. E. Gordon, "A Review of Acousto-Optical Deflection and Modulation Devices", Proceedings of the IEEE, 54, 1393 (1966).

38. E. G. Lean, M. Dakss, and C. G. Powell, "Efficiencies and Bandwidths of Intracavity Acousto-Optics Devices", IBM J. Res. and Deve., 13, 184 (1969).

39. G. Hrbek, J. Lekavich, and W. Watson, "An Improved Laser Color TV System Using Acousto-Optic Interactions", IDEA Symposium of the Society for Information Display, New York, 40, May 1970.

40. J. A. Rajchman, "Promise of Optical Memories", J. of Appl. Physics, 41, 1376, (1970).

41. H. R. Vilkomerson, et. al., "Holographic Read-Only Memories Accessed by Light-Emitting Diodes", Proc. FJCC, San Francisco, 33, 1197 (1968).

42. M. Feldman and G. L. Heiter, "Low Level Binary Light Detection in Charge Storage Phototransistor Arrays", Solid State Sensors Symposium, Minneapolis, Minn., 10 (1970).

43. J. M. Assour and R. D. Lohman, "A Photodetector Array for Holographic Optical Memories", RCA Review, 30, 4 (1969).

44. W. S. Boyle and G. E. Smith, "Charge Coupled Semiconductor Devices", Bell System Tech. J., 49, 4 (1970).

45. G. F. Amelio, et. al., "Experimental Verification of the Charge Coupled Device Concept", Bell System Tech. J., 49, 4 (1970).